MIMICKING THE PRE-HAIRPIN INTERMEDIATE OF GP41

A screening platform based on coiled coil lipopeptides in artificial biomembranes

Dissertation zur Erlangung des Grades

"Doktor der Naturwissenschaften"

am Fachbereich

Chemie, Pharmazie und Geowissenschaften

der Johannes-Gutenberg Universität Mainz

vorgelegt von

Steffen Schuy

geboren in Homburg / Saar

Mainz 2008

Dekan: Prof. Dr. P. Langguth

Erster Gutachter: Prof. Dr. A. Janshoff

Zweiter Gutachter: Prof. Dr. R. Zentel

Tag der mündlichen Prüfung:

meinen Eltern und Brüdern

TABLE OF CONTENTS

ABSTRACT

A novel screening platform for potential retroviral fusion inhibitors on the basis of fully functional membrane-anchored coiled coil lipopeptide receptors has been established. The work comprises the scrutiny of lateral organization of functional lipids in phase separated bilayers and an in-depth investigation of the biophysical properties of lipopeptide-based receptors. Lateral sorting of lipids was detected by the recognition of streptavidin of biotinylated lipids in phase separated bilayers and by nanoscopic patterns in mixed fluorocarbon / hydrocarbon lipid bilayers, employing temperature controlled atomic force microscopy (AFM) as a versatile characterization method. Particular features of fluorocarbon bilayers were additionally investigated in great detail by means of ellipsometry and ATR-IR spectroscopy. Lipopeptide-receptors were synthesized on the basis of a robust and reliable in situ coupling reaction by coupling terminal cysteine modified receptor-peptides to a maleimide functionalized lipid bilayer. Receptor functionality of the lipopeptides was visualized by specific binding of vesicles and nanoparticles tracked by a multiplicity of characterization methods, such as AFM, ellipsometry, CLSM and fluorescence spectroscopy. Finally, in situ coupling of viral peptides, originating from the fusion protein of HIV resulted in a mimic of the pre-hairpin intermediate of gp41. Structural analysis of N36-lipopepides by means of CD-spectroscopy in combination with FT-IR spectroscopy revealed a coiled coil assembly of lipopeptides, which render the aggregates fully functional receptors for potent fusion inhibitors. Thereby, reversible inhibitor binding of T20 and the corresponding C-peptides was detected by AFM and ellipsometry, rendering coiled coil lipopeptides a new promising technique for screening of retroviral fusion inhibitors.

LIST OF FIGURES

LIST OF TABLES

ABBREVIATIONS

AcCN	Acetonitril
AFM	Atomic force microscopy
BisTris	Bis(2-hydroxyl)amino-tris(hydroxymethyl)methane
BODIPY	2-(4,4-difluoro-5-methyl-4-bora-3a,4a-diaza-s-indacene-3-dodecanoyl)-1-hexadecanoyl-sn-glycero-3-phosphocholine, β-BODIPY 500/510 C_{12}-HPC
BSA	Bovine serum albumin
CLSM	Confocal laser scanning microscopy
DCC	N,N'-Dicyclohexylcarbodiimide
DIEA	N,N'-Diisopropylethyl-amine
DMAP	4-(Dimethylamino)pyridine
DMF	N,N'-Dimethylformamide
DMPC	1,2-Dimyristoyl-sn-glycero-3-phosphocholine
DMSO	Dimethylsulfoxid
DOPC	1,2-Dioleoyl-sn-glycero-3-phosphocholine
DOPC*	DOPC mixed with 1-10 mol% of MCC-DOPE (maleimide functionalized DOPC)
DOPE	1,2-Dioleoyl-sn-glycero-3-phosphoethanolamine
DPPC	1,2-Dipalmitoyl-sn-glycero-3-phosphocholin
EDC	N-(3-Dimethyaminopropyl)-N'-ethyl-carbodiimide hydrochloride
EDT	Ethanedithiole
EDTA	Ethylene diamine tetracetic acid
FRAP	Fluorescese recovery after photobleaching
H6	His_6Tag peptide (CGGHHHHHH)
H6-TAMRA	TAMRA labelled His_6Tag peptide (CGGHHHHHH-TAMRA)
HBTU	O-Benzotriazole-N,N,N',N'-tetramethyl-uronium-hexafluoro-phosphate

FRET	Förster resonance energy transfer
HF	aqueous hydrofluoric acid (35 wt%)
H-N36 or H-C34	Viral peptides originating from the NHR or CHR region of gp41 from SIV, respectively
HOBT	1-Hydroxybenzotriazole
HPLC	High performance liquid chromatography
IEC	Ion exchange chromatography
IEC-A	20 mM Na_2HPO_4, pH = 4.0, solvent A for IEC
IEC-B	1 M NaCl, 20 mM Na_2HPO_4, pH = 4.0, solvent B for IEC
K8	HS-CGWKKKKKKKK-Ac
K8-TAMRA	HS-CGWKKKKKKKK-TAMRA
MCC-DOPE	1,2-Dioleoyl-sn-glycero-3-phosphoethanolamine-N-[4-(p-maleimidemethyl)cyclohexane-carboxamide]
MIMIC	Micromolding in capillaries
MLV	Multilamellar vesicles
NHS	N-Hydroxysuccinimide
PBS	Phosphate buffered saline
PDMS	Poly(dimethylsiloxane)
POPC	1-Palmitoyl-2-oleoyl-sn-glycero-3-phosphocholine
ROI	Region of interest
RP-A	aqueous solution of 1% AcCN/0.075% TFA (*v*/v), RP-HPLC solvent A
RP-B	10 % Milli-Q water, 90 % AcCN, 0.7 % TFA (*v*/v), RP-HPLC solvent B
RP-HPLC	Reversed phase – HPLC
S-N36 or S-C34	Viral peptides originating from the NHR or CHR region of gp41 from SIV, respectively
SSLB	Solid supported lipid bilayer
SUV	Small unilamellar lipid vesicles
T20	Fusion inhibitor (Roche Pharma, Mannheim)

TAMRA	5(6)-Carboxy-tetramethyl-rhodamine
Texas Red	Sulforhodamine 101 1,2-dihexadecyl-sn-glycero-3-phosphoethanol-amine (Triethylammonium Salt)
TFA	Trifluoroacetic acid
TIS	Triisopropylsilane
Tris/HCl	Tris-(hydroxymethyl)-aminomethan-hydrochlorid

CHAPTER I

1 INTRODUCTION

1.1 BIOLOGICAL MEMBRANES

The cell is the fundamental unit in biology, spatially confined by the plasma membrane, which is organized in terms of a lipid bilayer, composed of phospholipids, proteins and steroids. However, the complexity and the diversity of plasma membrane components complicate the investigation of single components. Artificial biomembranes, in which plasma membrane components can be individually incorporated, provide an appropriate system for studying the function of single proteins, ligand-receptor interactions and transport processes. Additionally, lipid sorting and lateral lipid segregation into domains is believed to play key roles in cellular signal transduction.

1.2 SOLID SUPPORTED LIPID BILAYERS: APPLICATIONS FOR BIOSENSORS

Over the last decades, solid supported lipid bilayers have been utilized as model systems for studying basic membrane processes or ligand-receptor interactions and were employed for biosensor applications.[1-3] Spreading of unilamellar vesicles on a solid support, as pioneered by McConnell et al. represents a versatile and attractive way for the deposition of bilayers on metal electrodes, silicon wafers, mica or glass.[3] Unlike vesicular systems or lipid monolayers on an air / water interface, investigation of solid supported lipid bilayer are accessible by a wealth of surface sensitive analytical methods, such as atomic force microscopy, quartz crystal microbalance, impedance spectroscopy, total internal reflection fluorescence (TIRF) or attenuated total internal reflection IR spectroscopy (ATR-IR). [4-7] A great benefit of SSLBs is the long term stability and the lateral mobility of the lipid molecules, whereby proteins are incorporated or adsorbed in a quasi-native environment. The lateral mobility is maintained by a 1 – 2 nm thick water layer, trapped between the bilayer and the solid support.

The development of microstructured solid supported lipid bilayers, as first envisioned by Boxer, Cremer and Janshoff combines the benefits of the applicable analytical methods with

biosensor applications, since several individual addressable lipid bilayer compartments can be fabricated and analyzed under identical experimental conditions.[8-10] Microstructured membranes render sensor arrays of individual addressable SSLBs feasible for the study of cell adhesion or molecular recognition events.[9, 11] Further, on-chip immunoassays were thereby realized for investigating the kinetics and thermodynamics of antibody binding to antigens, as well as bilayer coated functional microchannels utilized for the determination of enzyme kinetics.[12, 13] However, investigation of transmembrane proteins embedded in solid supported lipid bilayers is complicated by the interaction of the protein with the solid support. Therefore, a new route of investigation of was envisioned by the fabrication of arrays of mobile tethered vesicles, in which transmembrane proteins can be inserted and analyzed under quasi-native conditions.[14]

1.3 VIRAL MEMBRANE FUSION PROTEINS

Enveloped viruses are covered by a lipid bilayer, which protects the genetic material of the virus until delivery to the cytoplasm of the cell and infection results. Fusion proteins, presented on the surface of the virus membrane facilitate viral entry by viral mediated membrane fusion. This membrane fusion process is the crucial step in virus infection and understanding of the molecular mechanism is essential for the design and function of modern fusion inhibitors. In general, membrane fusion proteins undergo major conformational changes, triggered by specific interactions with the host membrane that mediate membrane fusion. Two types of fusion proteins, denoted as class I and class II fusion proteins are defined and distinguished by the predominant secondary structure element of the core structure.[15] In case of class I mediated membrane fusion, observed for the human immunodeficiency virus (HIV gp41 protein), influenza virus (HA2 protein), ebola virus (GP2 protein) or SARS virus (S2 protein) refolding of the central core structure of the fusion protein results in highly stable rod-like post fusion structures with a central trimeric α-helical coiled coil (trimer-of-hairpins).[16, 17] In the post fusion state of class II membrane fusion the central trimer-of-hairpins is composed of β-structures.

Human immunodeficiency viruses (HIV), as well as the simian immunodeficiency virus (SIV) belong to the family of enveloped viruses exhibiting class I fusion proteins.[18] The mechanism of viral mediated membrane fusion is shown in figure 1.1.

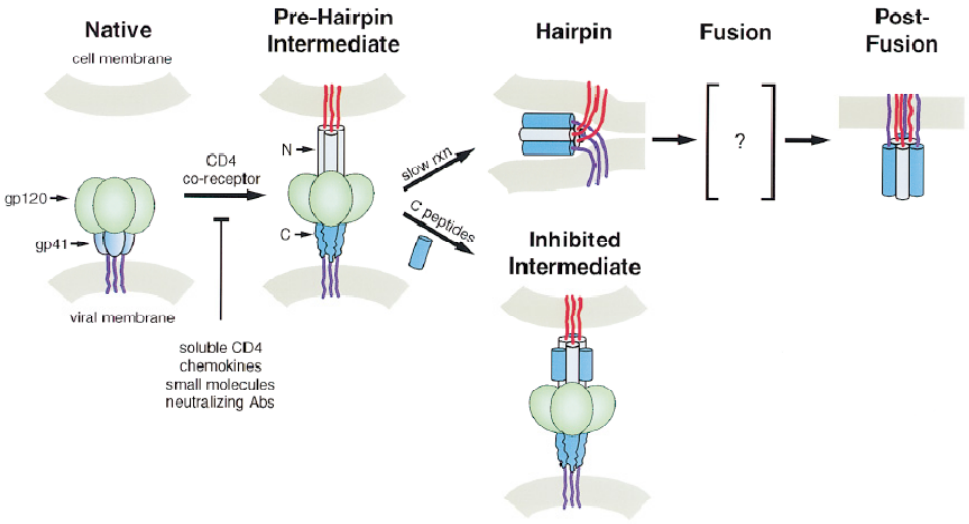

Figure 1.1. Model of HIV membrane fusion.[18]

The fusion proteins of HIV or, more specifically, enveloped glycoprotein complexes (Env) are homotrimeric integral proteins, consisting of non-covalently associated dimeric subunits, gp120 and gp41. Initially, hydrophobic fusion peptides (red) are inserted into the cell membrane and formation of the pre hairpin intermediate results. This process is triggered by binding of the gp120 to the CD4 chemokine receptors of the host cell, followed by conformational rearrangement of gp41.[16, 19, 20] Refolding of gp41 leads to the trimer-of-hairpins motive (post-fusion state) and membranes are brought into contact, whereby membrane fusion is induced. Fusion inhibitors can target the pre hairpin intermediate by packing into the conserved hydrophobic groves of the coiled coil core structure and refolding of gp41 is inhibited.[18, 21]

1.4 REFERENCES

[1] Sackmann, E. Supported Membranes: Scientific and Practical Applications. *Science* **1996**, 271, 43-48.

[2] Tamm, L. K. and McConnell, H. M. Supported phospholipid bilayers. *Biophys. J.* **1985**, 47, 105-113.

[3] Brian, A. A. and McConnell, H. M. Allogeneic Stimulation of Cytotoxic T Cells by Supported Planar Membranes. *PNAS* **1984**, 81, 6159-6163.

[4] Faiss, S.; Schuy, S.; Weiskopf, D.; Steinem, C. and Janshoff, A. Phase Transition of Individually Addressable Microstructured Membranes Visualized by Imaging Ellipsometry. *J. Phys. Chem. B* **2007**, 111, 13979-13986.

[5] Goormaghtigh, E.; Raussens, V. and Ruysschaert, J. M. Attenuated total reflection infrared spectroscopy of proteins and lipids in biological membranes. *Biochimica et biophysica acta* **1999**, 1422, 105-185.

[6] Janshoff, A.; Galla, H.-J. and Steinem, C. Piezoelectric Mass-Sensing Devices as Biosensors - An Alternative to Optical Biosensors? *Angewandte Chemie* **2000**, 39, 4004-4032.

[7] Janshoff, A.; Neitzert, M.; Oberdörfer, Y. and Fuchs, H. Force Spectroscopy of Molecular Systems - Single Molecule Spectroscopy of Polymers and Biomolecules. *Angewandte Chemie* **2000**, 39, 3212-3237.

[8] Cremer, P. S. and Yang, T. Creating Spatially Addressed Arrays of Planar Supported Fluid Phospholipid Membranes. *J. Am. Chem. Soc.* **1999**, 121, 8130-8131.

[9] Groves, J. T.; Ulman, N.; Cremer, P. S. and Boxer, S. G. Substrate-Membrane Interactions: Mechanisms for Imposing Patterns on a Fluid Bilayer Membrane. *Langmuir* **1998**, 14, 3347-3350.

[10] Janshoff, A. and Kunneke, S. Micropatterned solid-supported membranes formed by micromolding in capillaries. *European Biophysics Journal* **2000**, 29, 549-554.

[11] Kunneke, S. and Janshoff, A. Visualization of molecular recognition events on microstructured lipid-membrane compartments by in situ scanning force microscopy. *Angewandte Chemie, International Edition* **2002**, 41, 314-316.

[12] Mao, H.; Yang, T. and Cremer, P. S. Design and Characterization of Immobilized Enzymes in Microfluidic Systems. *Anal. Chem.* **2002**, 74, 379-385.

[13] Yang, T.; Jung, S. y.; Mao, H. and Cremer, P. S. Fabrication of Phospholipid Bilayer-Coated Microchannels for On-Chip Immunoassays. *Anal. Chem.* **2001**, 73, 165-169.

[14] Yoshina-Ishii, C. and Boxer, S. G. Arrays of mobile tethered vesicles on supported lipid bilayers. *Journal of the American Chemical Society* **2003**, 125, 3696-3697.

[15] Kielian, M. and Rey, F. A. Virus membrane-fusion proteins: more than one way to make a hairpin. *Nat Rev Micro* **2006**, 4, 67-76.

[16] Eckert, D. M. and Kim, P. S. Mechanisms of viral membrane fusion and its inhibition. *Annual Review of Biochemistry* **2001**, 70, 777-810.

[17] Malashkevich, V. N.; Chan, D. C.; Chutkowski, C. T. and Kim, P. S. Crystal structure of the simian immunodeficiency virus (SIV) gp41 core: Conserved helical interactions underlie the broad inhibitory activity of gp41 peptides. *Proceedings of the National Academy of Sciences* **1998**, 95, 9134-9139.

[18] Chan, D. C. and Kim, P. S. HIV Entry and Its Inhibition. *Cell* **1998**, 93, 681-684.

[19] Dalgleish, A. G.; Beverley, P. C. L.; Clapham, P. R.; Crawford, D. H.; Greaves, M. F. and Weiss, R. A. The CD4 (T4) antigen is an essential component of the receptor for the AIDS retrovirus. *Nature* **1984**, 312, 763-767.

[20] Wyatt, R. and Sodroski, J. The HIV-1 Envelope Glycoproteins: Fusogens, Antigens, and Immunogens. *Science* **1998**, 280, 1884-1888.

[21] Moore, J. P. and Doms, R. W. The entry of entry inhibitors: A fusion of science and medicine. *Proceedings of the National Academy of Sciences* **2003**, 100, 10598-10602.

CHAPTER II

2 MOTIVATION AND OBJECTIVES

2.1 BIOSENSOR CONCEPT

The scope of this work focuses on the development of a novel biosensor approach based on coiled coil lipopeptides to screen highly potent antagonists for viral mediated membrane fusion. Therefore, we aimed to mimic the pre-hairpin intermediate of gp41 by coupling N-peptides originating from the NHR region of SIV-1 and HIV-1 covalently to a lipid molecule, anchored in a solid supported artificial biomembrane. The general concept and functionality of the sensor approach is shown in figure 2.1.

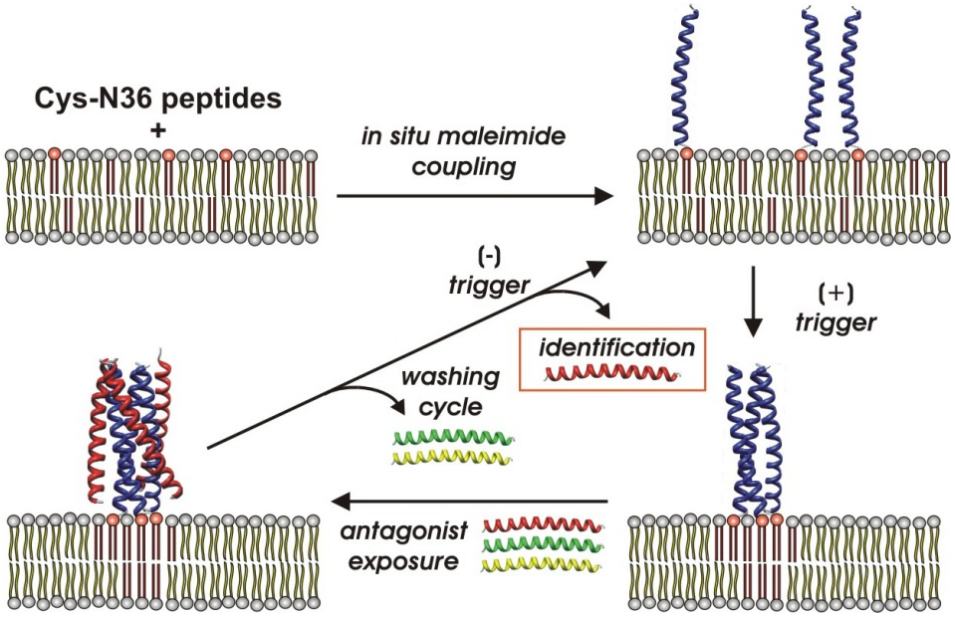

Scheme 2.1. Scheme of the biosensor approach.

Initially, viral peptides are coupled covalently to a reactive lipid bilayer in situ to produce a lipopeptide functionalized bilayer. Upon an external (+) trigger signal, lipopeptides are forced into clusters via phase separation of the lipid bilayer and therefore form coiled coil lipopeptides. A coiled coil assembly of peptides from the NHR region of gp41 results in the formation of conserved hydrophobic groves, which represent the active drug target of modern fusion inhibitors. Clustering of lipopeptides increases the local concentration of

peptides to an extent that formation of coiled coil lipopeptides can be expected and specific antagonist binding can occur. In the next step, screening of potent antagonists can be selected as follows. Exposure of antagonists to the lipopeptide assembly leads to specific adsorption of potent fusion inhibitors. Subsequently to adsorption, a washing cycle enables the separation of potent, specifically bound fusion inhibitors from the non-specific or unbound peptides. Finally, a (-) trigger, for instance heat, releases the specifically adsorbed fusion inhibitor by breaking the coiled coil assembly of the lipopeptides and antagonist identification can occur in the final step.

Certainly, a wealth of preliminary tests, novel experimental methods and reliable model systems need to be developed and validated to gain sufficient experience in order to accomplish and to understand each individual steps during the course of events of inhibitor screening based on coiled coil lipopeptides in artificial biomembranes. Experiments include structural investigation of phase separated lipid bilayers during phase transition and lipopeptide based ligand-receptor studies. Especially, parameterization of the in situ coupling reaction and detailed investigation of the functionality, as well as biophysical properties of lipopeptide-based receptors were aspired to be investigated in great detail, before experiments with delicate viral peptides can be carried out.

2.2 EXPERIMENTAL APPROACH

In order to investigate clustering of ligands due to lipid sorting in phase separated lipid bilayers, a simple method needed to be employed to track functional lipids in a phase separated binary lipid mixture. Therefore AFM analysis of a lipid mixtures consisting of DOPC / DPPC or DOPC / C15-PC doped with biotinylated DOPE or biotinylated DPPE were employed to show that sorting of lipids occurs in the fluid phase or in the gel phase, depending on the hydrocarbon backbone of the used biotinylated lipid. Detection of biotinylated lipids is accomplished by specific recognition of streptavidin. Further, lipid sorting could be readily detected by AFM in mixed hydrocarbon-fluorocarbon lipid bilayers and results in the formation of patterned self assembly structures. At first sight, nanoscale patterns of mixed hydrocarbon / fluorocarbon phospholipid bilayers raised many questions and we aspired to shed some light onto the formation of such extraordinary self assembly

structures by structural and thermotropic analysis of these synthetic fluorocarbon lipid analogs.

Reactive lipids used for in situ coupling reactions of peptides to lipid bilayers need to fulfill certain requirements, i.e. selective terminal binding of the peptide to the bilayer under ambient conditions in aqueous solution and the possibility to passivate the reactive lipid after coupling to prevent undesired reactions with adsorbents, possibly containing reactive groups. Maleimide functionalized lipids were chosen, as they selectively bind sulfhydryl groups and as the maleimide head group of the lipids can easily be hydrolyzed at pH > 8, which leaves the lipids inactive for further reactions. For lipopeptide formation, synthesized peptides were terminally functionalized by a terminal cysteine moiety and a short spacer sequence (gly-gly or gly-trp). As the chemical synthesis of the viral peptides is rather challenging, we employed smaller receptor peptides and investigated the in situ coupling reaction by a multiplicity of methods. Investigation of the functionality of lipopeptides was accomplished by specific binding of functional liposomes to lipopeptides containing bilayers.

Finally, viral terminal cysteine modified N-peptides of HIV and SIV needed to be coupled to the reactive lipid bilayer, followed by determination of the lipopeptides secondary structure and detailed investigation of the binding properties towards modern fusion inhibitors, such as T20 or C34, both derived from the corresponding CHR region of gp41. Thereby, the crucial question was, whether coiled coil formation of N-lipopeptides can be induced and if specific inhibitor recognition can be observed.

CHAPTER III

3 MATERIALS AND EXPERIMENTAL PROCEDURES

3.1 LIPIDS

3.1.1 STRUCTURE OF PHOSPHOLIPIDS

Phospholipids are the major constituents of native biological membranes. They are amphiphilic molecules as they consist of a polar, hydrophilic head group and a non polar, hydrophobic hydrocarbon chains, conjugated via the central glycerol backbone. The head group **R** is bound via a phosphoric acid ester to the *sn*-1 position and the hydrocarbon moieties are esterified at *sn*-1 and –*sn*-2 position of the glycerol backbone. A representative structure of a phospholipid is given in figure 3.1.

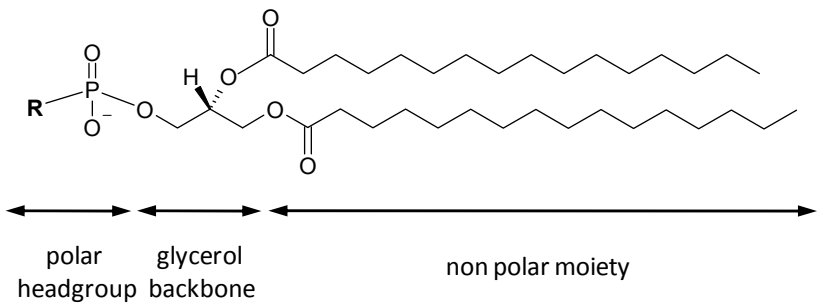

Figure 3.1. Representative structure of a phospholipid consisting of the hydrophilic headgroup and the hydrophobic hydrocarbon moiety, connected via a glycerol backbone.

The physical properties of phospholipids are mainly determined by the structure of the hydrophobic moiety, in terms of chain length, chain substituents and number or position of double bonds. Between pH 6-8 the free hydroxyl group of the phosphoric acid is deprotonated and the net charge is then determined by the head group. Typical native head groups are choline (net neutral), serine (net negative), glycerol (net negative) or

ethanolamine (net neutral for pH<8) and the chain length typically varies from 10 to 20 methylene groups. A list of the used phospholipids is given in table 3.1.

lipid	abbreviation	chains	T_M [°C]
1,2-Dioleyl-*sn*-glycero-phosphocholine	DOPC	18:1-18:1	-18,3
1,2-Dipentadecanoyl-*sn*-glycero-3-phosphocholine	C15-PC	15:0-15:0	33.8
1,2-Dimyristoyl-*sn*-glycero-3-phosphocholine	DMPC	14:0-14:0	23,6
1,2-Dipalmitoyl-*sn*-glycero-3-phosphocholine	DPPC	16:0-16:0	41,3
1-Palmitoyl-2-oleyl- *sn*-glycero-3-phosphocholine	POPC	16:0-18:1	< 0
1-Palmitoyl-2-oleyl-phosphatidylglycerol	POPG	16:0-18:1	< 0

Table 3.1. Summary of the used non functional lipids, including common abbreviation, carbon number of the chain segments and main phase transition temperature T_M.[1]

In water lipid molecules self-assemble into lipid bilayers. The main driving force for this rapid and spontaneous process is referred to as the hydrophobic effect. Since the hydrogen bonds are lost at the interface between water and hydrocarbons, a higher free energy state for the water molecules at the interface results. Therefore, it is energetically favorable for hydrocarbons to associate (self-assemble) and thus, minimizing the contact area with the surrounding water. For amphiphilic molecules, this self-assembly process results in the formation of micelles or bilayers, for which the hydrophilic head groups are pointed towards the water and the hydrocarbon moieties are buried in the interior of a micelle or in the hydrophobic core region of a bilayer. Figure 3.2 shows a representative scheme of a lipid bilayer and a hydrophobicity profile as a function of distance from the center of the bilayer. Besides the hydrophobic effect, van der Waals interactions between the associated hydrocarbon tails and hydrogen binding attractions between the polar head groups and water molecules further stabilize the self assembled lipid bilayer structure.

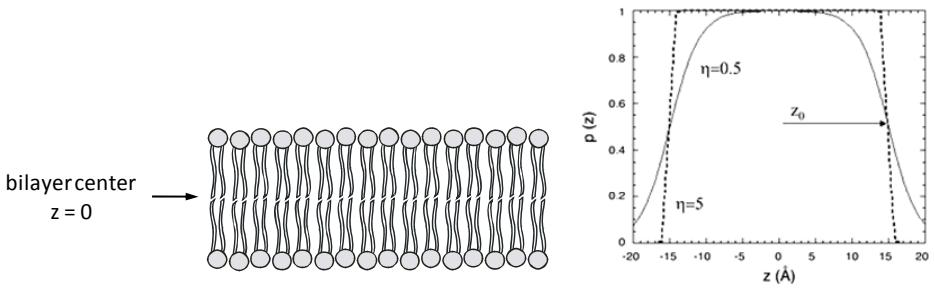

Figure 3.2. Scheme of a lipid bilayer and the hydrophobicity profile as a function of distance from the center of the bilayer (z = 0). Hydrophobicity is denoted as *p*.[2]

3.1.2 PHASE BEHAVIOR

Phospholipid bilayers exhibit a distinctive polymorphism, whereby the occurrence and stability of the several phases is a function of pressure and temperature and is mainly determined by degree of saturation, length and symmetry of the acyl chains, as well as on the head group. The gel phase can therefore be divided in a whole set of phases (e.g. L_C = gel or lamellar crystalline, $L_{\beta'}$ = tilted gel, $P_{\beta'}$ = ripple gel), which usually exhibit low transition enthalpies as compared to the main phase transition and are referred to as pre transitions. According to the *all trans* conformation of the acyl chains in the gel phase, strong van der Waals interaction between the chains result. Gel phases are characterized by a reduction of rotational motion and particularly lateral diffusion of the lipid molecules and high compression modules. The main phase transition denotes the transition from the pre-transition into the fluid, or fluid crystalline phase L_α and is characterized by the pronounced changes in physical properties, such as membrane thickness, lateral mobility of the lipid molecules, elasticity and compressibility of the bilayer. A schematic illustration of the different thermotropic phases is given in figure 3.3.

Figure 3.3. Schematic illustration of different thermotropic phases of lipid bilayers.

3.1.3 FUNCTIONAL ARTIFICIAL LIPIDS

Lipid head group functionalization is usually achieved by coupling of heterobifunctional crosslinkers or functional receptors to reactive lipids (phosphoethanolamines), by carbodiimid coupling reactions. Therefore, a large variety of functional artificial lipids for conjugation or receptor binding studies is commercially available.

3.1.3.1 BIOTINYLATED LIPIDS

Biotinylated lipids (figure 3.4) were employed for receptor-binding studies of streptavidin to lipid bilayers. Streptavidin is a tetrameric protein which binds selective to biotin. The binding constant is one of the strongest non covalent couplings in nature.

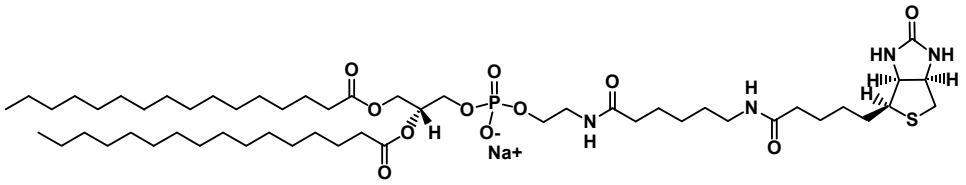

16:0 Biotinyl Cap PE

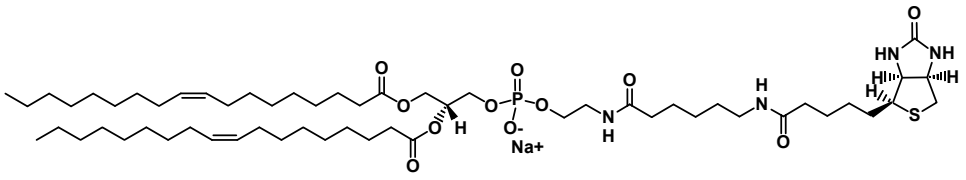

18:1 Biotinyl Cap PE

Figure 3.4. Structure of the used biotinylated lipids 16:0 Biotinyl Cap PE (1,2-Dipalmitoyl-*sn*-glycero-3-phosphoethanolamine-N-(Cap Biotinyl)) and 18:1 Biotinyl Cap PE (1,2-Dioleoyl-*sn*-glycero-3-phosphoethanolamine-N-(Cap Biotinyl).

3.1.3.2 MALEIMID FUNCTIONALIZED LIPIDS

For covalent conjugation of peptides to lipid bilayers, maleimide functionalized lipids were employed as cysteine-, or more precisely, thiol-selective coupling reagents. The maleimide group exhibits specific reactivity towards the thiol group of the cysteine side chain by 1,2 addition to α,β-unsaturated ketons. In this work, mostly commercially available MCC-DOPE

was incorporated into the bilayer to immobilize peptides via an in situ coupling reaction. Furthermore, we have synthesized a cost efficient alternative to MCC-DOPE by a variety of carbodiimid based coupling reactions. Figure 3.5 displays the used maleimide lipids MCC-DOPC and MCS-DOPE. Synthesis of MCS-DOPE was accomplished by three different methods, employing different coupling strategies (cp. 8.2).

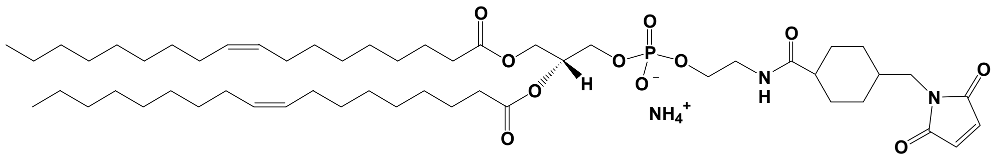

MCC-DOPE

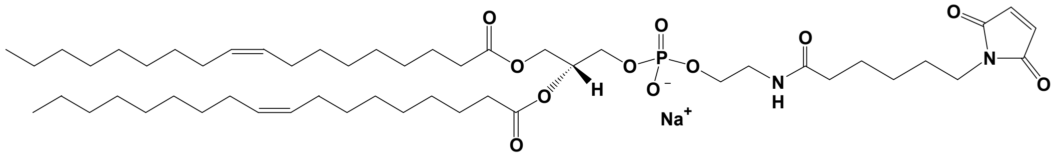

MCS-DOPE

Figure 3.5 Molecular structures of the maleimide functionalized lipids MCC-DOPE (1,2-Dioleoyl-*sn*-glycero-3-phosphoethanolamine-N-[4-(p-maleimidomethyl)cyclohexane-carboxamide]) and MCS-DOPE (1,2-Dioleoyl-*sn*-glycero-3-phosphoethanolamine-[N-maleimidohexyl-carboxamide]).

3.1.3.3 FLUORESCENT LIPID PROBES AND FLUORESCENT LIPOPEPTIDES

In this work, fluorescent probes are conjugated to a lipid molecule and can therefore be integrated into vesicles or SSLB. Texas Red (TexasRed®-1,2-dihexadecyl-sn-glycero-3-phosphoethanolamine, triethylammonia-salt (TexasRed® DHPE)) and BODIPY (2-(4,4-Difluoro-5-methyl-4-bora-3a,4a-diaza-s-indacen-3-dodecyl)-1-hexadecyl-*sn*-glycero-3-phosphocholine (β-BODIPY® 500/510 C12-HPC)) were employed to stain microstructured lipid bilayers, for investigation by means of CLSM. Furthermore, fluorescently labeled peptides (TAMRA-labeled peptides) were coupled in situ to maleimide lipid containing SSLBs to obtain fluorescent labeled lipopeptides. Synthetic details of peptide labeling and the in situ coupling reaction are given in 3.4 and 3.5, respectively. The structure of the fluorescent

probes, as well as the structure of 5(6)-Carboxytetramethylrhodamine (5(6)-TAMRA), including the corresponding absorption and the emission spectra are given in figure 3.6.

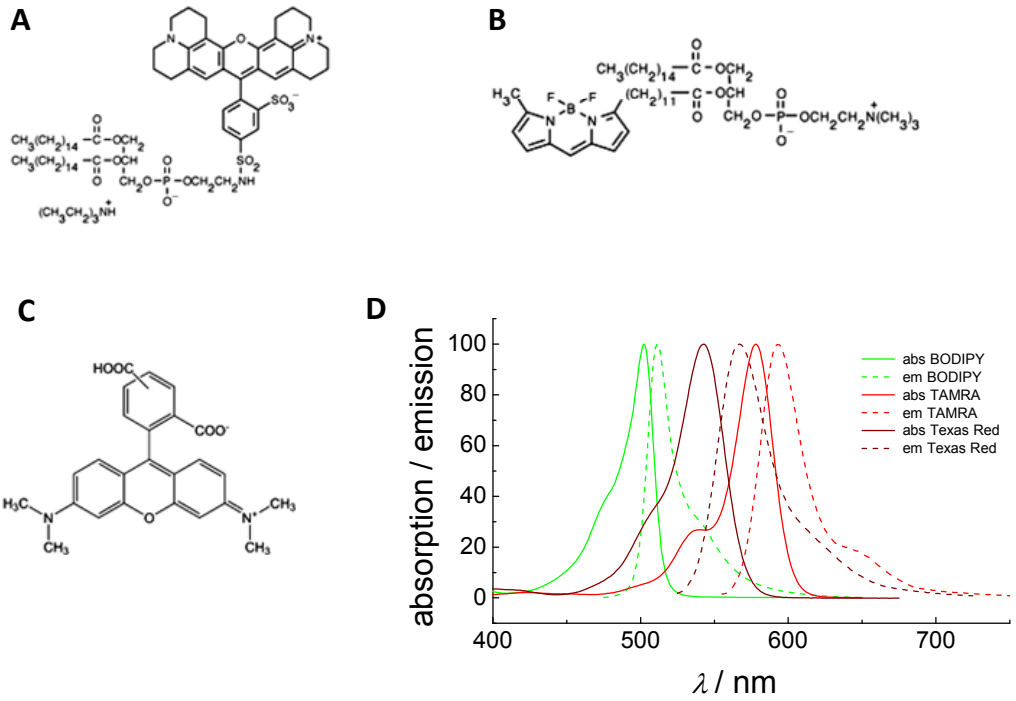

Figure 3.6. Structures and corresponding absorption / emission spectra of the used fluorescent probes. A) Texas Red, B) BODIPY, C) 5(6)-TAMRA D) Adsorption and emission of BODIPY, TAMRA and Texas Red.

3.1.3.4 FLUORINATED LIPIDS

In this work, a new class of fluorinated lipids (F6-DPPC and F4-DPPC) was investigated. The fluorinated lipids were provided by the working group of Prof. Krishna Kumar and synthesized as described by Yoder et al..[3] Structure and properties of the used lipids are discussed in great detail in 5.5 and chapter VI.

3.2 PREPARATION OF SOLID SUPPORTED LIPID BILAYERS (SSLB)

Several methods are available to form solid supported lipid bilayer. The most prominent method, besides Langmuir-Blodgett techniques and self organization of the lipids on a solid support, is the technique of vesicle spreading, first described by Brain and McConnell.[4] Therefore a liposome suspension, consisting of small unilamellar vesicles is placed directly on the hydrophilic solid support. By adhesion, vesicles are initially immobilized on the surface and if the temperature is elevated beyond T_M, vesicles rupture and spread to form the solid supported bilayer. Depending on the substrate a so called "critical" concentrations of vesicles on the surface might be necessary to initiate spreading.[5]

3.2.1 PREPARATION OF SMALL UNILAMELLAR VESICLES (SUV)

Initially, lipids were dissolved in chloroform or chloroform / methanol mixtures with concentrations between 1 – 10 mg / ml and mixed in the desired ratio. The solution is then transferred in a test tube and the solvent is evaporated in a stream of nitrogen at a temperature, well above T_M of the highest melting lipid, resulting in a lipid film, deposited on the glass wall of the test tube. The film is further dried under vacuum at the same temperature for at least 3 h. For storage of the lipid film, the test tube was flushed with nitrogen, sealed with parafilm and stored at 4°C. Multilamellar vesicles (MLV) were produced by swelling the lipid film in buffer at temperatures above T_M for 15 minutes and vortexing it periodically. The resulting MLV suspension was transferred into SUVs by sonication (50 W, 0.4 s puls, 20 min) in a vessel resonator (Sonoplus HD 2070,Bandelin, Berlin, Germany). Experimental details (buffers, temperatures, concentrations, lipid compositions or special treatments of the liposome solution) are given throughout the text.

3.2.2 PREPARATION OF SOLID SUPPORTED LIPID BILAYERS

Here the general procedure for the preparation of SSLBs is described. Experimental details are given in the materials and method section of the corresponding chapters.

Glass: Glass slides were hydrophilized by repeated sonication (2x) in 1% Hellmanex solution at 70°C for 15 min, followed by repeated sonication (2x) in MQ water at 70°C for 15 min. Clean, hydrophilic glass slides could be stored in water for 24h or were used immediately. SSLB on glass were exclusively prepared as microstructured membranes. Experimental procedures are therefore given below.

Mica: For AFM measurements on mica, liposome concentration was adjusted to 0.1 mg/ml SUVs in buffer, containing 3 mg/ml Ca^{2+}. The SUV suspension was deposited on freshly cleaved mica and incubated for 2 hours. Subsequently the sample was heated to 65°C for 10 minutes and cooled down to room temperature. Excess vesicles were removed by a flow wash with at least 100 ml of buffer.

Silicon: Silicon substrates (26 x 76 mm²) as used for ellipsometric measurements were cut from silicon wafers. Organic contaminants were removed by rinsing with first i-propanol and second chloroform. Silicon slides were pre cleaned in 1% aqueous HF solution (*v*/*v*) for 20 minutes to remove SiO_2. Hydrophilization was accomplished by a treatment of the silicon slides with a solution consisting of water / hydrogenperoxide solution (35% *w*/*v*) / ammonia (28% *v*/*v*) in the volume ratio 5:1:1 at 75°C for 20 min. The hydrophilic, oxidized substrates were thoroughly rinsed with water and used immediately.

3.3 MICROSTRUCTURING OF LIPID BILAYERS

3.3.1 SOFT LITHOGRAPHY

Soft lithography was first developed by George M. Whitesides and denotes a variety of lithographic processes for nano- and microstructuring, whereby a structured elastomer, i.e. mold, stamp or mask is employed to transfer the desired structure onto a surface.[6] Microstructured membranes as first envisioned by Boxer,[7-11] Cremer,[12-15] and Janshoff[16-18] employing soft lithography and more recently dip-pen lithography[19] opened the field to chip-based array technology.

3.3.2 MICROMOLDING IN CAPILLARIES (MIMIC)

In this work we employed micromolding in capillaries (MIMIC)[20] in order to fabricate individually addressable microstructured lipid membranes. Therefore, a poly-dimethylsiloxane (PDMS) mold is brought into contact with the substrate (glass or silicon), forming a closed microfluidic network, which channels are filled with vesicle suspension. By adhesion, followed by rupturing and spreading of the vesicles microstructured membranes are formed within the channels. Figure 3.7 displays the schematic preparation of microstructured bilayers. The geometric design of the master structure and details of the structuring process were described previously.[16-18, 21]

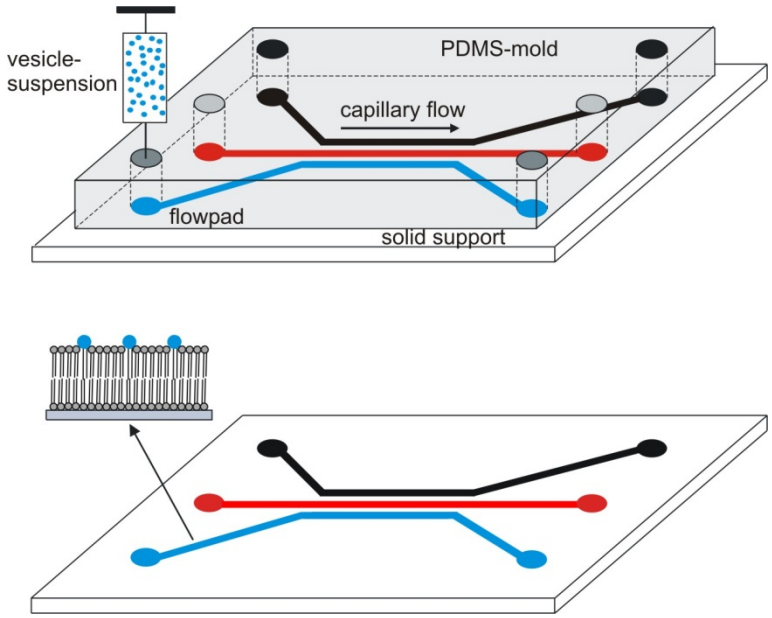

Figure 3.7: Preparation of individually addressable microstructured lipid bilayers on a glass substrate by micromolding in capillaries (MIMIC).

3.4 PEPTIDES

Peptides are linear oligomers of α-amino acids in a defined order. The amino acid residues are linking via amid bonds, resulting from the condensation reaction of the amino group and the carboxy group. Solution based synthesis is difficult to control, since already a small number of amino acids can be combined in numerous ways. In 1963 Bruce Merrifield developed a peptide synthesis on a solid phase (polymeric resin), referred to as solid phase

peptide synthesis (SPPS).[22] By synthesizing peptides on a solid support the isolation of the intermediate products could be realized by simple filtration of the resin and therefore the reaction time, as compared to solution based synthesis was largely reduced. In 1984 Merrifields research on SPPS was honored with a Nobel prize for it is up to now the leading method for peptide synthesis.

3.4.1 SOLID PHASE PEPTIDE SYNTHESIS (SPPS)

In general SPPS the resin consist of amino functionalized polystyrene beads, about 50 µm in diameter. *Spacer* molecules between the growing peptide chain and the resin, advantage the availability of the amino terminal end of the growing chain and therefore improve reaction kinetics. Further *linker* molecules such as esters or ethers are located between the spacer and the growing chain and serve as cleavable segments in order to release the synthesized peptides. The reaction sequence for coupling reaction of the amino acid to the growing peptide chain is shown in figure 3.8.

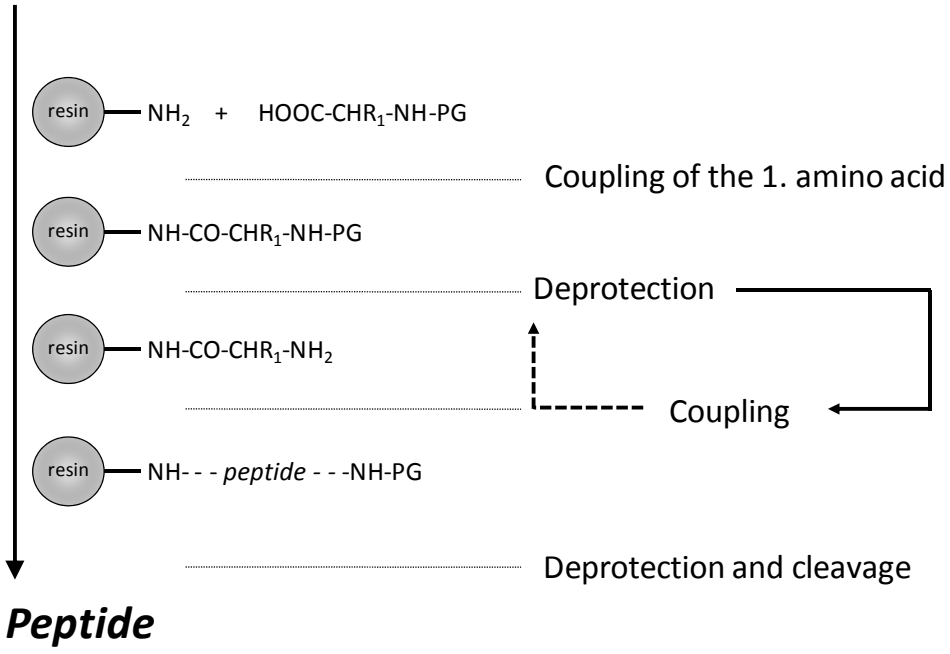

Figure 3.8. Reaction sequence for solid phase peptide synthesis.

Chain assembly of the peptides occurs in SPPS from the C-terminus to the N-terminus by **activation** of the carboxy group of the free N-protected amino acid via active esters and subsequent **coupling** to the free amino group of the resin bound growing peptide chain. Release of the temporary N-protection group (PG) of the resin bound peptide chain (**deprotection)**, washing and subsequent **coupling** of the next N-terminal protected amino acid is accomplished in repeated cycles until the desired peptide is produced. Monitoring of the coupling efficiency was determined by ninhydrin-staining of small resin aliquots (cp. 3.4.3). Cleavage from the resin and further purification by HPLC of the crude peptide are the final steps in SPPS, yielding peptides with high yield and purity.

3.4.2 PROTECTION GROUPS IN SPPS

In general, protection groups (PG) are divided in two classes, i.e. *temporary* and *permanent* protection groups. Temporary PGs are utilized for blocking temporarily the functionality of the molecule, which first couples the next amino acid in the following step of SPPS. Permanent PGs protect the functional amino acid side chains during SPPS.PERMANENT PROTECTION GROUPS (SIDE CHAIN PROTECTION)

Side chain protection groups or permanent protection groups stay intact during SSPS and protect the side chains of the amino acid from reacting with the activated amino acids, used for chain extension. Permanent protection groups are in general cleaved from the peptide in one step using the same conditions as the peptide is cleaved from the resin. For certain amino acids, the use of *scavengers*, e.g. anisol, triethylsilane or ethanedithiol is crucial to suppress side reactions of the side chains during cleavage reactions.

3.4.2.2 TEMPORARY PROTECTION GROUPS (PROTECTION OF THE AMINO GROUP)

The most important properties of temporary amino PGs are the highly selective deprotection of the amino group after a coupling reaction under mild conditions. In modern SPPS two classes of temporary PGs, i.e. the tert. Butyloxycarbonyl group (*t*Boc) and the 9-fluorenylmethyloxycarbonyl group (Fmoc) are predominantly used.

Fmoc

The base labile 9-Fluorenylmethyloxycarbonyl protecting group was first described by Carpino in 1972.[23] Deprotection of the amino group occurs by exposure to piperidine, usually 20% - 30% in DMF. Mechanistically the deprotection of the amino group results from a β-elimination reaction by abstracting the H-9 proton of the fluorenyl ring, followed by elimination of dibenzofulven and CO_2.

Boc

The acid labile the tert. butyloxycarbonyl group (Boc) was developed by Mc Kay and Albertson in 1957.[24] Treatment with strong acids, such as trifluoroacetic acid leads to elimination of the Boc group by decomposing into tert.-butylcations and the free carbamine acid, latterly decomposing into CO_2 and the free amine. Due to the strong acid conditions, the amine group of the growing peptide chain is protonated after deprotection, which must be neutralized before further couplings. Modern synthesis protocols favor in situ neutralization by addition of DIEA.

3.4.3 PROTOCOLS FOR MANUAL PEPTIDE SYNTHESIS

3.4.3.1 FMOC SYNTHESIS

In this work standard Fmoc chemistry, following the protocols of Montanari et al.[25] was used for the synthesis of the small, receptor peptides Ac-KKKKKKKKWGC (K8) and Ac-HHHHHHGGC (H6) (chapter 8). The synthesis was performed on a 0.2 mmol scale, using acid labile Rink Amide MBHA resin (~ 0.6 – 0.8 mmol NH_2 / g). Side chains were protected by acid labile permanent groups, such as tert-buthyloxycarbonyl (Boc) and Trityl (Trt). Initially the resin was swelled for 45 min in DMF. Coupling reactions were carried out by dissolving 4 eq of the Fmoc protected amino acid derivate, 3.6 eq HBTU as a coupling reagent in DMF (~5 ml) and 6 eq DIEA and subsequent addition of the solution to the resin. The reaction mixture was then allowed to shake for 30 min and after thorough rinsing with DMF, the coupling efficiency was monitored by ninhydrin staining (Kaiser test).[26] In case of positive Kaiser test, indicated by a blue coloring of the beads, the coupling was repeated with eventually 8 eq scale. If Kaiser test were negative, indicated by a transparent beads, the amino groups were deprotected, followed by coupling of the next amino acid. Deprotection was accomplished

by treatment with 30% piperidine in DMF twice for 15 min. After the SPPS was completed, peptides were end capped by acetylation. Therefore, the resin was shaken twice for 30min in 5 ml of a 10% acetic anhydride solution in DMF to which 3 drops DIEA were added. Finally peptides were cleaved from the resin using TFA / TIS / EDT / H2O (94:1:2.5:2.5) for 3h in three steps. In step one and two the resin was exposed to the cleavage cocktail and shaked for 45 min and additional 90 min in the third step. The cleavage solutions were collected, crude peptides were precipitated in cold diethylether (-20°C) and collected on a medium porosity frit. Crude peptides was redissolved in an aqueous solution of 1% AcCN/0.075% TFA (RP-A) and lyophilized. Purification of the peptides was accomplished by a combination of RP-HPLC and IEC as described in 3.6.

3.4.3.2 BOC SYNTHESIS

Viral peptides (cp. chapter 9) were synthesized manually using tert.-butyloxycarbonyl (Boc) chemistry on 4-methylbenzhydrylamine (MBHA) resin on a 0.2 mmol scale following the in situ neutralization protocols of Schnölzer et al..[27] First the resin was swollen in DMF for 45 min. Coupling reactions were carried out by addition of 4 eq t-Boc-amino acid derivates with standard side chain protection groups, 3.6 eq HBTU as a coupling reagent and 6 eq DIEA in DMF (~5ml). Reaction times were 12 – 14 min for amino acid number 1 – 10, 15 - 18 min for amino acid 11 – 20, 18-21 min for amino acid 21 – 30 and 30 min for amino acid 31 – 39. The coupling reaction was monitored by Ninhydrin staining (Kaiser test). In case of positive Kaiser test the coupling was repeated with extended coupling times (30 min) on a 8 eq scale (8 eq amino acids, 7.2 eq HBTU and 12 eq DIEA) until Kaiser test was found negative. If repeated recoupling (3 times) failed to give negative Kaiser tests, peptides were acetylated before deprotection and further couplings. Deprotection was accomplished by shaking the resin twice in concentrated TFA for 90 sec. In situ neutralization was accomplished by thorough rinsing with DMF, followed by additional swelling of the resin in DMF for 5 min prior to the next coupling reaction. Importantly, in case of asparagine and glutamine, both protected by xanthenyl (xan) as a permanent protection group, TFA was removed by thorough rinsing of the resin with DCM prior to the in situ neutralization. After chain assembly was completed, all viral peptides were acetylated using 10% acetic anhydride in DMF for 30 min (2x). Peptides were cleaved from the resin using high hydrofluoric acid (HF) conditions (90%

anhydrous HF / 10% anisole at 0°C for 1.5 h). After cleavage, HF was removed under reduced pressure and peptides were precipitated in cold Et2O. Peptides were collected on a medium porosity frit, dissolved and lyophilized.

Crude acetylated peptides were dissolved in 75% H2O / 25% AcCN / 0.1% TFA and purified by RP-HPLC on Grace Vydac C18 columns as described in 4.6.

Peptides used for IR measurements were lyophilized from 0.05 M aqueous HCl solution (5x) to remove the trifluoroacetate counterions.[28]

3.4.4 TAMRA LABELING OF THE PEPTIDES.

TAMRA labeling of the peptides with 5(6)-Carboxytetramethyl-rhodamine (TAMRA) was carried out to obtain fluorescently labeled peptides. Labeling procedure is described in 8.2.

3.5 LIPOPEPTIDES

Initially, lipopeptides were synthesized by a detergent assisted coupling reaction as described in Elliott et al. in order to isolate the desired lipopeptide as a pure substance (not shown).[29] In brief, lipid films, consisting of MCS-DOPE and 50 eq detergent (n-Octyl-ß-D-glucopyranoside (OGP) or triton X were dissolved in PBS 6.8 and after addition of the peptide, the mixture was stirred for 90 min. Identification of the lipopeptide formation was determined by MALDI-Tof analysis and detergent extraction was applied. However, precipitation of the lipopeptides with methanol in case of OGP-reactions or even detergent extraction with diethylether in case of Triton X-reactions failed to quantitatively separate the detergent from the lipopeptide. As a result, lipopeptides were strongly contaminated by a large excess of detergent and standard purification methods, such as RP-HPLC or IEC failed to yield appropriate purified products. Therefore, we employed in situ functionalization of a maleimide lipid containing bilayer, as described by Svedhem et al. to overcome the complication, associated with detergent assisted reactions.[30]

3.5.1 IN SITU COUPLING REACTION

In situ coupling reactions were employed to functionalize a bilayer with lipopeptide. In general, lipid bilayers containing 10 % of the maleimide lipid were exposed to terminal

cysteine modified peptides in PBS 6.8. After reaction was found complete, typically after 60 to 90 minutes the sample was rinsed and measured. Investigation of the in situ coupling reaction of small receptor peptides or viral peptides to liposomes and to bilayers, including all experimental details (bilayer formation, concentration, reaction conditions, etc.) are described in chapter 8 and 9.

3.6 PURIFICATION OF PEPTIDES BY HPLC

3.6.1 PURIFICATION OF SMALL RECEPTOR PEPTIDES BY USING IEC

His_6Tag peptides (H6) and oligo-lysine peptides (K8) are highly positively charged in aqueous solutions at neutral pH values and RP-HPLC could not be applied to purify the crude peptides. Hence, purification of small receptor peptides was achieved by strong cation exchange chromatography (IEC) using linear ionic strength gradients. Both peptides, H6 and K8, including TAMRA-labeled peptides were purified by similar purification protocols.

3.6.1.1 GENERAL PURIFICATION PROTOCOL BY USING IEC

For IEC, crude lyophilized peptides were dissolved in RP-A (99% H_2O, 1% AcCN, 0.075% TFA), injected onto the column (Shodex, IEC SP-825, 8.0 x 75 mm) and purified with the linear gradient of 30 to 100% B over 40 min at 1.4 ml/min; mobile phase A (IEC-A), 20mM PBS pH = 4.0; mobile phase B (IEC-B), 20mM PBS pH 4.0, 1 M NaCl. Table 3.2 shows the applied linear ionic strength gradient. Eluation of the peptides was followed by UV detection at 220 nm wavelength for unlabeled peptides and 555 nm wavelength for TAMRA labeled peptides.

Initially, a small aliquot (0.5 mg) of the stock solution of the crude peptide (5 mg / ml) was injected and the eluation time of the peptide was determined by collecting fractions, followed by MALDI-Tof analysis. After peak identification, the amount of injected peptide was increased to a maximum of 5 mg. Figure 3.9 shows a representative IEC chromatogram of H6 (3 mg) in RP-A.

t / min	*IEC-A* / vol%	*IEC-B* / vol%
0	70	0
40	0	100
48	0	100
49	70	0
55	70	0

Table 3.2. Linear ionic strength gradient for purification of H6, K8 and TAMRA-labeled derivatives.

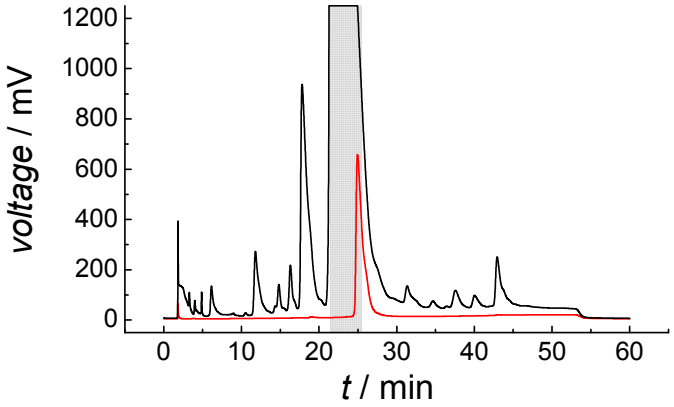

Figure 3.9. Purification of H6 by using IEC. Chromatogram shown in black displays the crude peptide (3 mg) and red chromatogram shows the purified peptide. Collected fraction from crude peptide is highlighted in grey.

Collected fractions were lyophilized and desalted on a preparative C18 HPLC column (Grace Vydac, Protein & Peptide C18, 22mm x 250mm). For desalting, lyophilized peptides were dissolved in a minimal amount of RP-A and injected on the preparative RP-HPLC column using the gradient shown in table 3.3. The purity of the resulting peptides as estimated from analytical ion exchange chromatography was greater than 95%.

t / min	*RP-A* / vol%	*RP-B* / vol%
0	100	0
10	100	0
20	60	40
21	0	100
28	0	100
29	100	0
35	100	0

Table 3.3. Gradient of RP-A and RP-B used for desalting of peptides on a preparative C18 RP-HPLC column.

3.6.2 PURIFICATION OF VIRAL PEPTIDES BY USING RP-HPLC

Purification of viral peptides (S-N36, H-N36, S-C34, H-C34) was achieved by reversed phase HPLC (RP-HPLC) using linear polarity gradients of water and AcCN. All viral peptides were purified by similar purification protocols.

3.6.2.1 GENERAL PURIFICATION PROTOCOL BY USING RP-HPLC

For preparative RP-HPLC, crude lyophilized peptides were dissolved in a 3:1 mixture of RP-A (99% H_2O, 1% AcCN, 0.075% TFA) and RP-B (10% H_2O, 90% AcCN, 0.1% TFA), injected onto the column (Grace Vydac, Protein & Peptide C18, 22mm x 250mm) and purified with the linear concentration gradient of RP-B over 20 min at 8.0 ml/min; mobile phase A (RP-A); mobile phase B (RP-B). Table 3.4 shows the applied linear polarity gradient for H-N36. Eluation of the peptides was followed by UV detection at 220 nm wavelength.

Aliquots (5 mg) of crude peptide in solution (c = 10 mg / ml) was injected and the eluation time of the peptide was determined by collecting fractions, subject to MALDI-Tof analysis. After optimization of the solvent gradient, the amount of injected peptide was increased to 20 mg for the preparative column. Figure 3.10 shows representative RP-HPLC chromatograms of H-N36 (3 mg) in RP-A / RP-B 3:1 for each purification step.

t / min	*RP-A* / vol%	*RP-B* / vol%
0	65	35
20	35	65
21	0	100
28	0	100
29	65	35
35	65	35

Table 3.4. Linear polarity gradient for purification of S-N36 peptides by a preparative column.

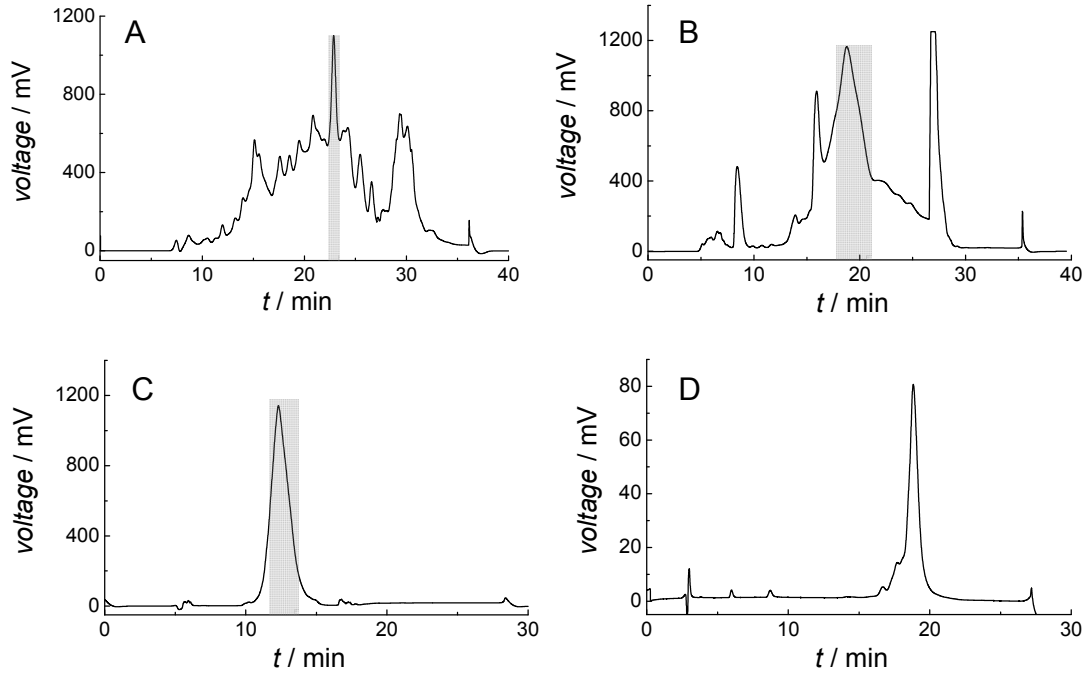

Figure 3.10. Purification of H-N36 by using A) preparative RP-HPLC (20 mg, gradient 0 – 20 min, 35 – 65% RP-B); B) semi-preparative RP-HPLC (4 mg, gradient 0 – 20 min, 45 – 54% RP-B); C) second semi-preparative RP-HPLC (2.5 mg, gradient 0 – 20 min, 48 – 54% RP-B); D) analytical RP-HPLC (gradient 0 – 20 min, 43 – 47% RP-B). Collected fraction are highlighted in grey.

Collected fractions from the preparative purification were lyophilized and repeatedly purified on a semi-preparative C18 HPLC column (Grace Vydac, Protein & Peptide C18, 10mm x 250mm) two times. In general, linear polarity gradients during 0 – 20 min were applied for all chromatographic steps, using RP-HPLC. For semi-preparative columns, the

increase in vol% of RP-B during the linear polarity gradient was in the range of 7 – 10 % and gradients for analytical RP-HPLC were as small as 5-7 %. The purity of the resulting peptides as estimated from analytical RP-chromatography (Grace Vydac, Protein & Peptide C18, 4.6 mm x 250mm) was greater than 80% for each peptide.

3.7 REFERENCES

[1] Huang, C.-h. and Li, S. Calorimetric and molecular mechanics studies of the thermotropic phase behavior of membrane phospholipids. *Biochimica et Biophysica Acta (BBA) - Reviews on Biomembranes* **1999**, 1422, 273-307.

[2] Kessel, A.; Shental-Bechor, D.; Haliloglu, T. and Ben-Tal, N. Interactions of Hydrophobic Peptides with Lipid Bilayers: Monte Carlo Simulations with M2{delta}. *Biophys. J.* **2003**, 85, 3431-3444.

[3] Yoder, N. C.; Kalsani, V.; Schuy, S.; Vogel, R.; Janshoff, A. and Kumar, K. Nanoscale Patterning in Mixed Fluorocarbon-Hydrocarbon Phospholipid Bilayers. *J. Am. Chem. Soc.* **2007**, 129, 9037-9043.

[4] Brian, A. A. and McConnell, H. M. Allogeneic Stimulation of Cytotoxic T Cells by Supported Planar Membranes. *PNAS* **1984**, 81, 6159-6163.

[5] Reimhult, E.; Hook, F. and Kasemo, B. Intact Vesicle Adsorption and Supported Biomembrane Formation from Vesicles in Solution: Influence of Surface Chemistry, Vesicle Size, Temperature, and Osmotic Pressure. *Langmuir* **2003**, 19, 1681-1691.

[6] Xia, Y. and Whitesides, G. M. Soft Lithography. *Annual Review of Materials Science* **1998**, 28, 153-184.

[7] Groves, J. T. and Boxer, S. G. Micropattern Formation in Supported Lipid Membranes. *Acc. Chem. Res.* **2002**, 35, 149-157.

[8] Groves, J. T.; Ulman, N. and Boxer, S. G. Micropatterning Fluid Lipid Bilayers on Solid Supports. *Science* **1997**, 275, 651-653.

[9] Groves, J. T.; Ulman, N.; Cremer, P. S. and Boxer, S. G. Substrate-Membrane Interactions: Mechanisms for Imposing Patterns on a Fluid Bilayer Membrane. *Langmuir* **1998**, 14, 3347-3350.

[10] Hovis, J. S. and Boxer, S. G. Patterning Barriers to Lateral Diffusion in Supported Lipid Bilayer Membranes by Blotting and Stamping. *Langmuir* **2000**, 16, 894-897.

[11] Hovis, J. S. and Boxer, S. G. Patterning and Composition Arrays of Supported Lipid Bilayers by Microcontact Printing. *Langmuir* **2001**, 17, 3400-3405.

[12] Cremer, P. S.; Groves, J. T.; Kung, L. A. and Boxer, S. G. Writing and Erasing Barriers to Lateral Mobility into Fluid Phospholipid Bilayers. *Langmuir* **1999**, 15, 3893-3896.

[13] Cremer, P. S. and Yang, T. Creating Spatially Addressed Arrays of Planar Supported Fluid Phospholipid Membranes. *J. Am. Chem. Soc.* **1999**, 121, 8130-8131.

[14] Yang, T.; Jung, S. y.; Mao, H. and Cremer, P. S. Fabrication of Phospholipid Bilayer-Coated Microchannels for On-Chip Immunoassays. *Anal. Chem.* **2001**, 73, 165-169.

[15] Yang, T.; Simanek, E. E. and Cremer, P. Creating Addressable Aqueous Microcompartments above Solid Supported Phospholipid Bilayers Using Lithographically Patterned Poly(dimethylsiloxane) Molds. *Anal. Chem.* **2000**, 72, 2587-2589.

[16] Janshoff, A. and Kunneke, S. Micropatterned solid-supported membranes formed by micromolding in capillaries. *European Biophysics Journal* **2000**, 29, 549-554.

[17] Kunneke, S. and Janshoff, A. Visualization of molecular recognition events on microstructured lipid-membrane compartments by in situ scanning force microscopy. *Angewandte Chemie, International Edition* **2002**, 41, 314-316.

[18] Schuy, S. and Janshoff, A. Microstructuring of phospholipid bilayers on gold surfaces by micromolding in capillaries. *Journal of Colloid and Interface Science* **2006**, 295, 93-99.

[19] Lenhert, S.; Sun, P.; Wang, Y.; Fuchs, H. and Mirkin, C. A. Massively Parallel Dip-Pen Nanolithography of Heterogeneous Supported Phospholipid Multilayer Patterns. *Small* **2007**, 3, 71-75.

[20] Kim, E.; Xia, Y. and Whitesides, G. M. Polymer microstructures formed by moulding in capillaries. *Nature* **1995**, 376, 581-584.

[21] Schuy, S. and Janshoff, A. Thermal expansion of microstructured DMPC bilayers quantified by temperature-controlled atomic force microscopy. *ChemPhysChem* **2006**, 7, 1207-1210.

[22] Merrifield, R. B. Solid Phase Peptide Synthesis. I. The Synthesis of a Tetrapeptide. *J. Am. Chem. Soc.* **1963**, 85, 2149-2154.

[23] Carpino, L. A. and Han, G. Y. 9-Fluorenylmethoxycarbonyl function, a new base-sensitive amino-protecting group. *J. Am. Chem. Soc.* **1970**, 92, 5748-5749.

[24] McKay, F. C. and Albertson, N. F. New Amine-masking Groups for Peptide Synthesis. *J. Am. Chem. Soc.* **1957**, 79, 4686-4690.

[25] Montanari, V. and Kumar, K. A fluorous capping strategy for Fmoc-based automated and manual solid-phase peptide synthesis. *European Journal of Organic Chemistry* **2006**, 874-877.

[26] Kaiser, E.; Colescott, R. L.; Bossinger, C. D. and Cook, P. I. Color test for detection of free terminal amino groups in the solid-phase synthesis of peptides. *Analytical Biochemistry* **1970**, 34, 595-598.

[27] Schnölzer, M.; Alewood, P.; Jones, A.; Alewood, D. and Kent, S. In Situ Neutralization in Boc-chemistry Solid Phase Peptide Synthesis. *International Journal of Peptide Research and Therapeutics* **1992**, 13, 31-44.

[28] Andrushchenko, V. V.; Vogel, H. J. and Prenner, E. J. Optimization of the hydrochloric acid concentration used for trifluoroacetate removal from synthetic peptides. *Journal of Peptide Science* **2007**, 13, 37-43.

[29] Elliott, J. T. and Prestwich, G. D. Maleimide-Functionalized Lipids that Anchor Polypeptides to Lipid Bilayers and Membranes. *Bioconjugate Chemistry* **2000**, 11, 832-841.

[30] Svedhem, S.; Dahlborg, D.; Ekeroth, J.; Kelly, J.; Hoeoek, F. and Gold, J. In situ peptide-modified supported lipid bilayers for controlled cell attachment. *Langmuir* **2003**, 19, 6730-6736.

CHAPTER IV

4 INSTRUMENTATION

Here, brief descriptions of the main instrumental techniques (AFM, Ellipsometry, IR-Spectroscopy, CD-Spectroscopy and Liquid Chromatography) are presented. techniques with a minor importance for this work, such as quartz crystal microbalance (QCM), fluorescence spectroscopy, matrix assisted laser desorption ionization mass spectrometry (MALDI-Tof) and confocal laser scanning microscopy (CLSM) will only be mentioned in terms of experimental details prior to the discussion of the obtained results without providing a theoretical background.

4.1 ATOMIC FORCE MICROSCOPY

The first atomic force microscope (AFM) was introduced by Binnig, Quate und Gerber in 1986 capable of imaging the topography of a surface with atomic resolution.[1] Contrast results the interaction between a sharp tip and the sample surface. The setup permits to measure tip sample interaction forces in the pico Newton regime. A schematic set up of a AFM is shown in figure 4.1.

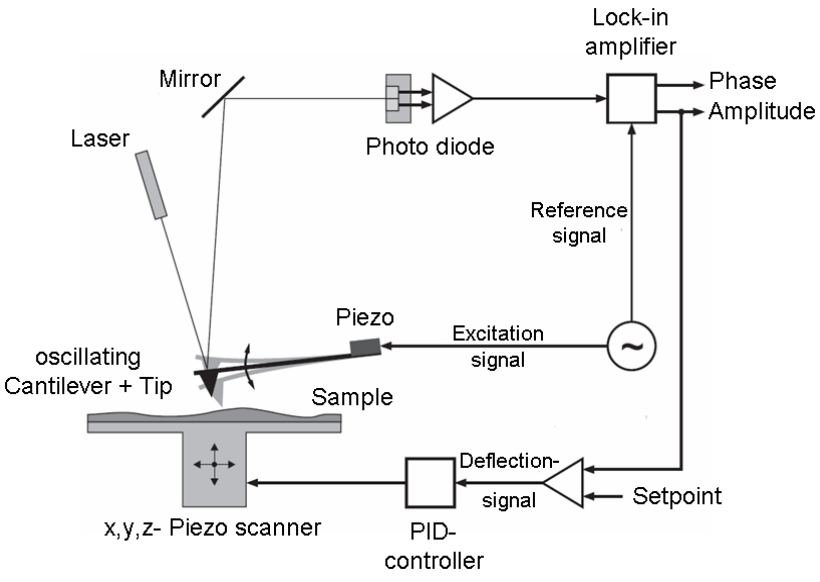

Figure 4.1: Scheme of an AFM.

4.1.1 BASICS

A very sharp needle with a tip diameter of only several nanometers is mounted at the end of a cantilever and probes the interaction between the tip and the sample surface. For imaging, the cantilever is scanned in xy-direction and the deflection in z-direction is monitored via reflection of a laser beam directed on the reflective side of the cantilever. Combining the scanning information with the deflection of the cantilever at each pixel yields the topographical image of the surface. While typical resolutions in z-direction can be as low as 1 Å, the lateral resolution in xy-direction is typically 1-10 nm and usually limited by the tip diameter. The imaging modes are divided into static (contact mode) and dynamic modes (tapping mode, non contact mode). Typical control parameters are constant deflection for static modes or constant amplitudes for dynamic modes. Control parameters are kept constant during imaging (constant force mode) by a feedback loop and the control current of the z-piezo measures the height. For a precise measurement of the topology of the sample surface, the scanning speed must be adjusted to the response of the feedback control loop.

4.1.2 IMAGING MODES

Imaging modes are usually classified by the forces between the tip and the sample. Figure 4.2 shows a representative course of the forces acting on the tip. In first approximation tip sample interaction can be described by superposition of attractive van der Waals interactions and the repulsive hard core potential.

4.1.2.1 CONTACT MODE

In contact mode, the tip is in the repulsive regime of the Lenard-Jones potential and scanning is performed with a constant deflection (constant force) or with a defined distance of the z-piezo (constant height mode). In constant force mode the resulting reflections during scanning are monitored by the segmental photo diode and compensated by the feedback control. According to Hooks law $F(z) = k_C * z_F$ the force F(z) is directly related to the cantilever deflection z_F and kept constant by the feedback loop. A computer combines the scanning information with the signal of the photo diode (deflection (error image)) or the control current of the z-piezo (height image) to record the topographical image of the surface. In general, constant force mode is easy to realize, but the continuous mechanical

contact of the tip with the surface can cause damage of the sample or, in case of fluid lipid bilayers, the tip can penetrate the thin film without measuring the actual bilayer.

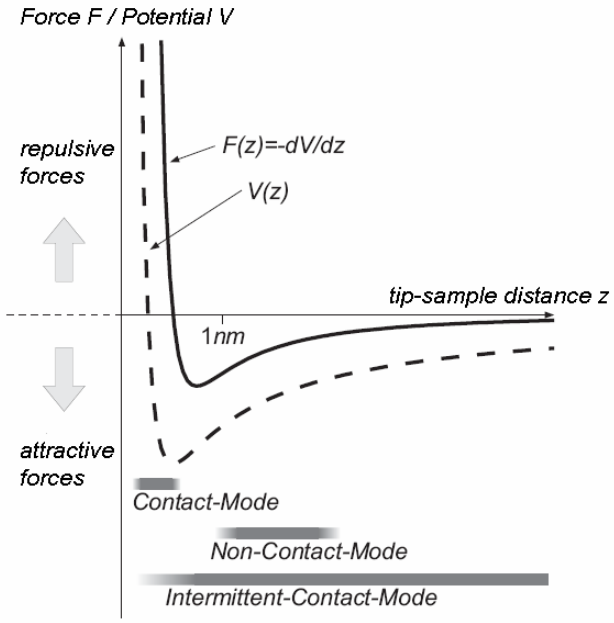

Figure 4.2: Schematic course of the potential V (z) and the resulting force F (z) as a function of tip sample distance.

4.1.2.2 TAPPING MODE.

In tapping mode (intermittent contact mode) the cantilever is excited by the z-piezo to oscillate close to its resonance frequency and high amplitudes (~ 100 nm in air). Within each oscillation cycle the tip penetrates the entire interaction potential and therefore maps both, the attractive and the repulsive regime. Normally, tapping mode is performed in constant force mode, which means that the damping of the amplitude is kept constant. The ratio of the damped amplitude A_{set} and the free amplitude A_0 determines the set point during imaging. Besides height information of the sample topography, valuable material properties can be extracted by measuring the phase shift between the excited oscillation and the actually resulting oscillation of the cantilever. The phase shift is a material dependent measure of the dissipation of energy by the sample and can be related to the viscoelasticity of the sample surface and the adhesion between tip and sample.[2]

4.2 ELLIPSOMETRY

Ellipsometry is a non invasive, well established method for the characterization of ultra thin films in terms of layer thickness and refractive indices. In principle the changes of polarization of monochromatic parallel light upon reflection of a film-covered surface is measured. The resulting changes in the state of polarization can be expressed and quantified by the ellipsometric angles Delta (Δ) and Psi (Ψ). The ellipsometry angles are sensitive to the interfacial architecture and thus, they can be related to the layer thickness for homogeneous thin films by means on model calculations based on Fresnel equations.

4.2.1 POLARIZATION OF LIGHT

Light is a self-propagating transverse electromagnetic wave, consisting of an electric and a magnetic field vector, mutually oriented perpendicular to each other and to the direction of propagation of light. The polarization of light is determined by the direction of oscillation of the electric field vector in the plane perpendicular to the direction of propagation. In general, common light sources emit *non-polarized* light and all components of the electric field vector are statistically distributed. *Polarized* light, however, consists of electric field vectors that all exhibit the same direction. All states of polarized light can further be described by superposition of two linear polarized light waves E_S and E_P (parallel or perpendicular orientation of the electric field vector towards a fixed plane) with the same wavelength and the same direction of travel. The phase shift δ between the superposed light waves determines the state of polarization and is therefore an important parameter for ellipsometric measurements.

Three different cases of polarization can be distinguished:

1) **Linear polarized light**. Light, whose electric field vector oscillates only in one plane is referred to as linear polarized light. This occurs, if the phase shift between the superposed electromagnetic waves E_S and E_P, exhibits $\delta = N \cdot \pi$ with N = 0, 1, 2, … .

2) **Circular polarized light**. If two linear polarized electromagnetic waves with the same amplitude and wavelength are superposed with a phase shift $\delta = \left\{N + \frac{1}{2}\right\}\pi$ with N =

0, 1, 2, …, the resulting electric field vector describes a circular orbit that is characteristic for circular polarized light.

3) **Elliptically polarized light**. For all other superpositions of two linear polarized light waves with same amplitude, wavelength and direction of propagation elliptically polarized light results and the electric field vector describes an elliptical orbit.

4.2.2 ELLIPSOMETRY EQUATIONS

When light reaches the interface between two media with differing refractive indices, some of the light is reflected and some becomes refracted. This results in a partial polarization of the reflected, as well as of the refracted light beam. By using Fresnels reflection coefficients r_{12}^{S} (for light with an electric field vector perpendicular to the plane of incidence) and r_{12}^{P} (for light with an electric field vector parallel to the plane of incidence) it is possible to describe the ratio of the amplitudes of the reflected to the incident light. The square of the Fresnel reflection coefficients gives the reflectance, or the intensity ratio of the wave perpendicular or parallel to the plane of incidence, R^S or R^P, respectively. In particular, the actual film thickness is derived from the film phase thickness β from Fresnels equations for multiple interfaces.

Ellipsometry measures the ratio of reflectance, since the dependence of the intensity of light is therefore eliminated. The fundamental equation of ellipsometry is:

$$\rho = \frac{R^P}{R^S} = \tan\Psi \cdot e^{-i\Delta} \qquad (4.1)$$

The two ellipsometric angles are Delta (Δ) and Psi (Ψ). Delta is mathematically expressed by

$$\Delta = \delta_1 - \delta_2 \qquad (4.2)$$

and measures the phase difference between the incident and the reflected wave, that occurs upon reflection.

Psi measures the change in amplitudes and is described as the ratio of the reflectance for the two waves before and after reflection.

$$\tan\Psi = \frac{|R^P|}{|R^S|} \quad . \qquad (4.3)$$

4.2.3 INSTRUMENTAL SET UP

A schematic set up of a modern ellipsometer is shown in figure 4.3.

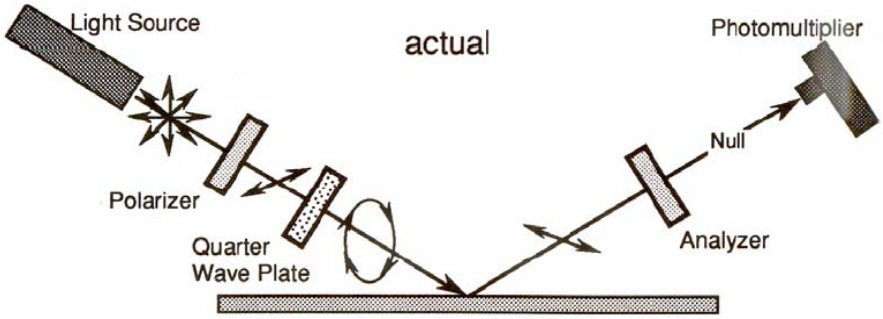

Figure 4.3. Schematic instrumental set up of a modern ellipsometer, like the EP^3-SW.[3]

The instrument consists of a Nd:YAG laser (λ = 532 nm) as a light source, a polarizer and a quarter wave plate before the actual reflection. Therefore the light is already elliptically polarized before reflection occurs and the ellipticity of the incident light is adjusted such that after reflection linear polarized light results. A rotary analyzer is set to zero intensity and from the rotational positions of the polarizer and the analyser the ellipsometric angles Delta and Psi can be calculated. The detection of the spatially resolved zero intensity procedure, a CCD camera in combination with an objective (20x) is used and therefore the sample thickness can be imaged at a lateral resolution of 1 µm.

Null positing results from several combinations of the rotary polarizer and analyzer, which are usually reduced to either two or four zones. In case of the EP^3-SW ellipsometer, which was exclusively used in this work the 4 zones are defined as:

Zone 1: $-45° < P_1 < 135°$, $0° < A_1 < 90°$, $C = 45°$

Zone 2: $135° < P_2 < 45°$, $-90° < A_2 < 90°$, $C = 45°$

Zone 3: $45° < P_3 < -135°$, $0° < A_3 < 90°$, $C = -45°$

Zone 4: $-135° < P_4 < 135°$, $-90° < A_4 < 0°$, $C = -45°$

(P: Polarizer, A: Analyzer, C: Compensator = quarter wave plate)

The resulting ellipsometry angles Delta and Psi are thereby calculated, using following equations:

$\Delta_1 = 270° - 2 \cdot P_1, \quad \Psi_1 = A_1$

$\Delta_2 = 90° - 2 \cdot P_2, \quad \Psi_2 = - A_2$

$\Delta_3 = 90° + 2 \cdot P_3, \quad \Psi_3 = A_3$

$\Delta_4 = 270° + 2 \cdot P_4, \quad \Psi_4 = - A_4.$

4.2.4 OPTICAL MODELS

Determination of the layer thickness by ellipsometry resulted from fitting of the ellipsometry angles on a standard theory based on Fresnels equations employing a parallel layer model as shown in figure 4.4.

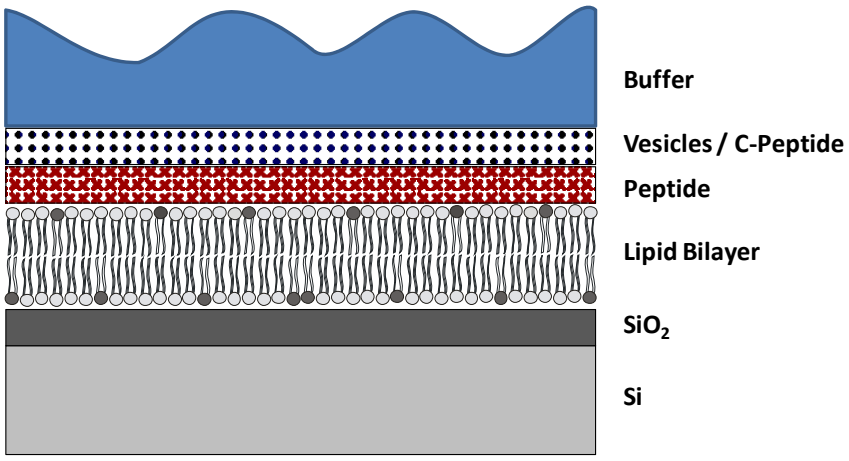

Figure 4.4. Schematic layer model of an ellipsometry sample. Lipid bilayer, bound lipopeptides and adsorbed vesicles or C-peptides are modeled as thin films.

All experiments were performed on chemically oxidized silicon. In kinetic experiments the monitoring of the bilayer formation, in situ functionalization and peptide or vesicle adsorption was performed by one-zone nulling procedure at 6 data points/min. Experimental details (buffer, concentrations, rinsing procedures, etc.) are described prior to the results in the corresponding chapters. Precise thickness determinations were obtained from 4-zone nulling procedures after complete formation of each single layer. Common layer

thickness and refractive indices of the applied materials at 532 nm wavelength are presented in Table 3.1.

Material	Layer Thickness *d* / nm	Refractive index *n*
H_2O / Buffer		1.335
doped Si		$4.1132 + 0.0538 \cdot i$
SiO_2	0.1 – 1.3	1.461
DOPC Bilayer[4]	3.5 – 3.8	1.533
Fluorinated Lipids[5]	3.1 – 4.5	1.400
Peptide / Protein[6]	0.4 – 1.3	1.500

Table 4.1. Common layer thicknesses and refractive indices of the applied materials.

Calculation of the layer thicknesses results from fitting the ellipsometric angles Δ and Ψ to the optical model using the given refractive indices. Figure 4.5 shows a simulation of the dependency of Δ and Ψ on the layer thickness of SiO_2 and a lipid bilayer, deposited on a 1 nm SiO_2 layer.

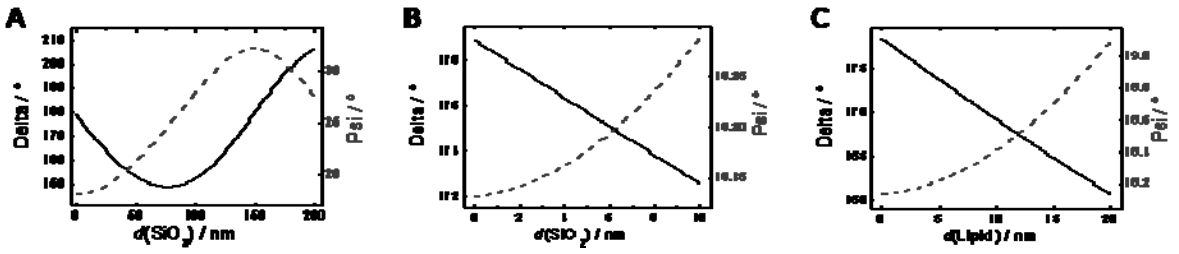

Figure 4.5. Dependency of the ellipsometric angles Δ and Ψ on the layer thickness of silicondioxide (A, B) and the layer thickness of a lipid bilayer (C), assuming a typical layer thickness of the underlying SiO_2 of 1 nm.

Figure 4.5 indicates that calculation of the layer thickness using only one ellipsometric angle is not possible. Same values of delta or psi occur in the range of 0 – 200 nm at different layer thicknesses. However, if only thin layers (0 – 10 nm) are monitored, the thickness can be determined from using exclusively delta as an ellipsometric angle. Moreover, delta shows a more distinct dependency on the layer thickness than psi, which is linear for thicknesses that do not exceed ~ 25 nm. Simulation of the delta course on the thickness change of a lipid bilayer shows the same linear relationship.

4.3 IR-SPECTROSCOPY

In the following, a brief description of polarized attenuated total internal reflection infrared spectroscopy (ATR-IR) is provided. ATR-IR is used for the determination of lipid tilt angles (chapter 6) and transmission IR spectroscopy is used for structural studies of peptides based on the sensitivity of the amide I band to the secondary structure (chapter 9). For details on IR spectroscopy (theory of infrared red absorption, instrumentation, experimental techniques, and applications in life science) the reader is referred to a comprehensive text book from Siebert and Hildebrandt.[7]

4.3.1 POLARIZED ATTENUATED TOTAL INTERNAL REFLECTION INFRARED SPECTROSCOPY (ATR-IR)

In order to obtain ATR-IR spectra the sample is directly deposited on an ATR-IR crystal, referred to as an internal reflection element (IRE). The most common design of such an IRE is a trapezoidal plate, which allows to determine molecular orientation of the sample by means of linear dichroism. A scheme of the IRE and the light pathway is given in figure 4.6. The infrared beam is directed into the ATR crystal (high refractive index medium), which is transparent for IR radiation. Above a critical angle, the light beam is completely reflected, when it impinges the surface of the IRE. By superimposition of the incoming and the reflected wave, leading to a standing wave within IRE, an evanescent field is created which penetrates the sample. The presence of the evanescent field enables the interaction of the infrared light with the sample and IR spectra of very thin films can be obtained. By using polarized ATR-IR spectroscopy and measuring the dichroic ratio of the polarized IR spectra obtained for polarization parallel and perpendicular to the surface to the plane of incidence,

molecular orientation measurements, such as measurements of lipid tilt angles or orientations of α-helices within the bilayer are possible.[8-12] Experimental details of tilt angle determinations of fluorinated lipid bilayers are given in chapter 6.

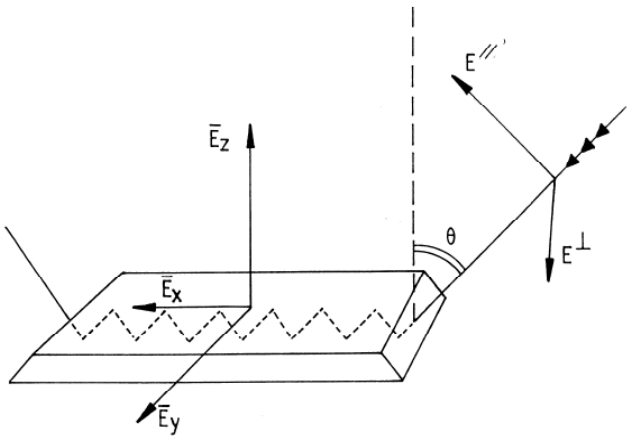

Figure 4.6: Schematic representation of the internal reflection element and the light pathway. Electric field components of the incident light are given in cartesian coordinates E_x, E_y, E_z. The two planes of polarization are indicated as $E_{||}$ and $E_{\perp}$.[8]

4.3.2 AMIDE I INFRARED SPECTRA

Backbone amide vibrations of peptides and proteins are conformational-sensitive and are therefore used to determine their secondary structure. The amide I band (1600 – 1700 cm^{-1}) consists of C=0 stretching vibrations with minor contributions of NH bending and is by far the most widely used amide vibration to measure the secondary structure of peptides and proteins. A listing of typical amide I bands and their correlation to proteins secondary structure is given in table 4.2. Each secondary structure gives rise to different C=O stretching vibrations, due to their unique molecular geometry and hydrogen bonding pattern. However, individual components of the amide I region are usually extensively overlapped and cannot be resolved instrumentally. Therefore, mathematical resolution –enhancement techniques, such as FSD-curve fitting or second order derivative analysis need to be applied to resolve the individual bands. In this work, second order derivative analysis was employed to deconvolute the amide I region of N36-lipopeptides and it allows the identification of the secondary structure. [13]

Secondary structure	Amide I frequency / cm^{-1}
Antiparallel β-sheets / aggregated strands	1675 – 1695
Turns	1660 – 1685
3_{10} Helix	1660 – 1670
α-Helix	1648 – 1660
Random coil	1652 – 1660
β-Sheets	1625 – 1640
Aggregated strands	1610 - 1628

Table 4.2. Common protein secondary structures and their corresponding amide I frequency.[7]

4.4 CIRCULAR DICHROISM (CD-SPECTROSCOPY)

CD spectroscopy is a special mode of UV / Vis absorption spectroscopy. In principle the interaction between linear polarized light upon penetration of an optical active media is measured. Circular dichroism exists if both of the circular polarized superposed waves, which build the linear polarized wave (cp. 3.2), exhibit a wavelength dependece and additionally a dichroic absorption.

4.4.1 BASICS

When linear polarized light passes an optical active media, the velocity of light as well as the extinction coefficient ε_L and ε_R of the circular polarized components (ε_L = left handed components, ε_R = right handed components) can differ, resulting in the formation of elliptical polarized light. Figure 4.7 displays the formation of elliptical polarized light by superposition of circular polarized light exhibiting opposite direction of rotation and unequal amplitudes. The difference $\Delta\varepsilon = \varepsilon_L - \varepsilon_R$ is thereby the actual measure in CD-spectroscopy, although in practical CD-spectroscopy the *ellipticity Θ*

$$\theta_{(\lambda)} = \frac{ln10 \cdot 180}{4\pi} \cdot \left(\varepsilon_L - \varepsilon_R\right) \cdot c \cdot d \qquad (4.4)$$

is usually provided, where *d* is the layer thickness in cm, *c* is the concentration in g / L and *ε* is the extinction coefficient in cm^2 / g.

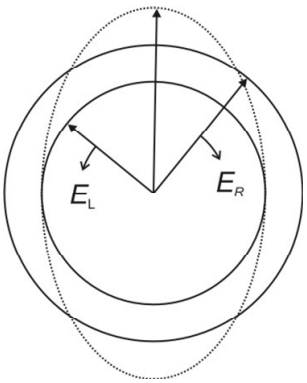

Figure 4.7: Indicator diagram shows the formation of elliptical polarized light by superposition of two circular polarized waves.

In relation to the molecular mass of the optical active molecule, the *molar ellipticity* $[\Theta]_\lambda$ is expressed by

$$[\theta]_{(\lambda)} = \frac{M_r \cdot \theta_{(\lambda)}}{100 \cdot c \cdot d} \qquad (4.5)$$

where M_r is the molecular mass in g/mol.

The dependency of the ellipticity from the wavelength of light determines the CD-spectra. CD spectra exhibit the shape of an absorption spectra, but discriminates a positive and negative circular dichroism, depending on whether the left or the right handed cicular polarized component of the wave is stronger absorbed.

4.4.2 ANALYSIS OF THE SECONDARY STRUCTURE OF PEPTIDES AND PROTEINS

The band shape of a CD spectrum is changes characteristically with the conformation of a peptide or a protein. Figure 4.8 displays the characteristic spectra obtained for peptides with high contents in random coil, ß-sheet, ß-turn or α-helical conformations.

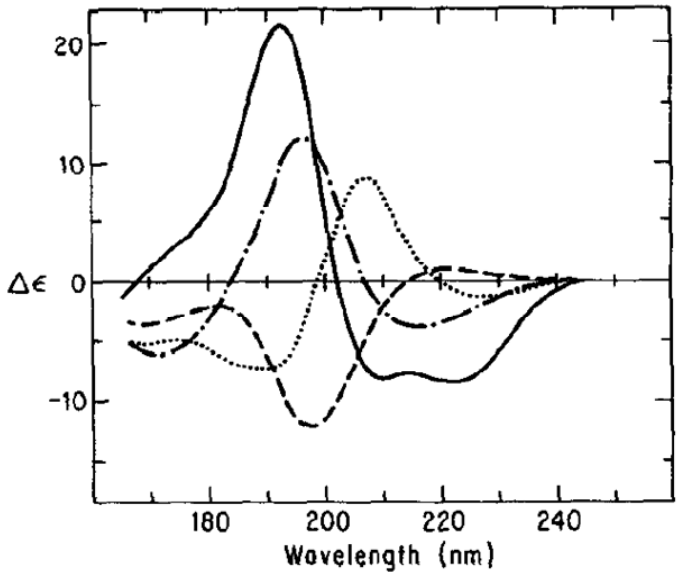

Figure 4.8. CD spectra for peptides and proteins with mainly α-helical (solid), ß-sheet (dots and dashes), ß-turn (dotted line) or random coil conformations (dashed line).[14]

A straightforward determination of the secondary structure elements from a CD spectra is to employ a linear combination of reference CD spectra for pure secondary structures, as first described by Greenfield & Fasman who measured the CD spectra for synthetic poly-lysines in the α-helical, ß-sheet and random coil form.[15] However, determination of the secondary structure content exhibits a number of problems and it is crucial to extend the CD spectra into the far UV region (~ 180 nm wavelength).[16] Due to the strong buffer conditions (50 mM PBS) and the low solubility of the peptides measured in this work, truncation of the CD spectra occurred near 200nm wavelength. Even so, analyses of the CD spectra measured to 200 nm wavelength give a good indication of the fraction of α-helix, because the circular dichroism of this secondary structure element dominates the longer wavelength region between 200 nm and 230 nm wavelength.[16, 17] Typically, a double minima at 208 nm (π -> π*) and 222 nm (n -> π*) wavelength is characteristic for α-helical secondary structures (cp. figure 4.8).

4.5 HIGH PERFORMANCE LIQUID CHROMATOGRAPHY (HPLC)

Liquid chromatography, mainly reversed phase high performance liquid chromatography (RP-HPLC) and ion exchange chromatography (IEC) was used in this work for the purification of the synthesized peptides.

4.5.1 BASICS

Liquid chromatography is a common separation method for molecules that are dissolved in a solvent (mobile phase) by utilizing different partitioning behavior of the sample components (dissolved in the mobile phase) with the stationary phase, resulting in separate eluation with well defined eluation times. The partitioning behavior of the sample mixture depends on the polarity of the sample and the sample solvent, as well as on the polarity of the column. Consequently, the mobile and the stationary phase must be adjusted for the desired separation. In peptide science, reversed phase high performance chromatography employing gradient eluation has become a widely used and well established tool for purification of crude peptides. However, for highly charged peptides, such as oligolysines or small His_6 Tag peptides, insufficient quality of separation might occur and ion exchange chromatography (IEC) must be employed to achieve an appropriate purification of the desired peptide. Gel filtration or more precisely gel permeation chromatography (GPC) was used for the separation of in situ lipopeptide modified vesicles form excess peptide.

Figure 4.9 displays a schematic setup of a HPLC instrument, mainly consisting of a solvent reservoir, pump, injection port, column and detector. The eluent mixture is controlled by a valve and is pumped at high pressure (typically ~100 bar) through the column. The sample is injected into a sample loop, connected to a Rheodyne fluid valve at low pressure. Turning the valve, injects the sample into the high pressure system and the column gets loaded with the sample. Eluation of the fractions is commonly detected ba a UV / Vis detector. In this work, peptide bonds were detected at 220 nm wavelength and in case of TAMRA labled peptides, detection occurred at 555 nm. Peak identification was accomplished by MALDI-Tof and collected fractions were eventually lyophilized.

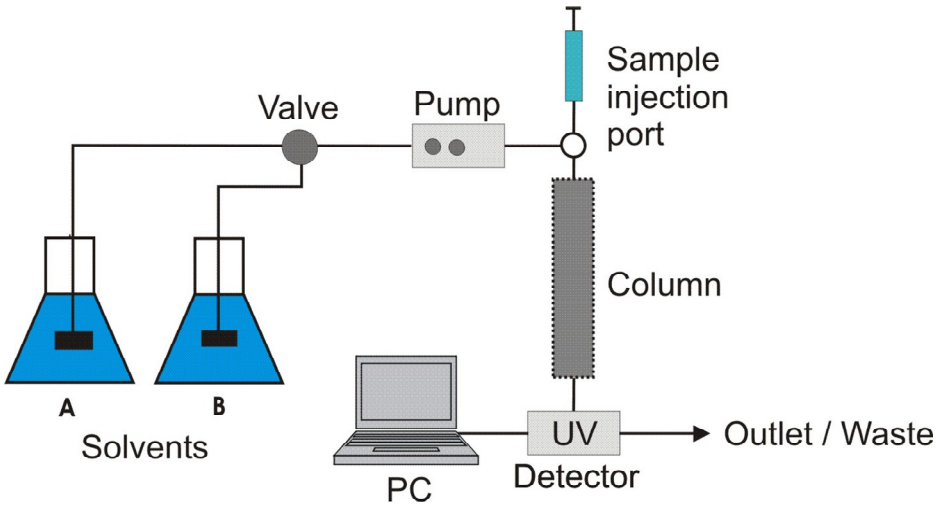

Figure 4.9. Schematic set up of a HPLC instrument.

4.5.2 REVERSED PHASE-HPLC

RP-HPLC was employed to purify viral peptides and additionally, to desalt smaller, receptor peptides subsequent to purification by IEC. In general, RP-HPLC separates peptides due to the hydrophobic nature. The stationary phase is therefore unpolar and consists of a hydrocarbon modified silica gel. Peptides adsorb on the hydrophobic surface of the stationary phase after entering the column and remain adsorbed until the polarity of the mobile phase reaches a critical value necessary to cause desorption. Linear solvent gradients are thus, adjusted to shift the polarity from polar to unpolar to improve the separation. In this work, C18 HPLC columns in combination with linear water / acetonitrile gradients were employed to purify the viral peptides (cp. chapter 3.6).

4.5.3 ION EXCHANGE CHROMATOGRAPHY

Ion exchange chromatography (IEC) allows separation of ions and polar molecules based on charge-charge interaction, using linear ionic strength gradients. Depending on the charge of the sample, IEC is commonly separated into cation and anion exchange chromatography. Here, IEC is always referred to cation exchange chromatography, since all peptide were positively charged at the applied conditions (pH < 7). In cation exchange chromatography, the stationary phase consists of PMMA beads functionalized with sulfonic acid groups, resulting in a negatively charged surface even at low pH values (pH > 1). Positively charged

analyte molecules, such as receptor peptides retain on the functionalized PMMA beads due to electrostatic interactions. The eluation time of the molecule depends on the number of its positive charges and on the concentration of positive counter ions, such as Na^+. Using linear ionic strength gradients up to a final NaCl concentration of 1 M in 20 mM PBS buffer at pH 4.0 the separation is greatly improved and receptor peptides were obtained at high purities (> 95%). A brief description of the purification method of His_6Tag-peptides used in this study is presented in 3.6.

4.5.4 GEL FILTRATION

Gel filtration is a chromatographic process, which separates the analytes by size. The stationary phase consists of a porous material, commonly hydrophilic poly-saccaroids such as dextran- or agarose-gel. The size distribution of the pores determines whether the analyte can diffuse into the pores, whereby the eluation time increases. In this work, gel filtration was applied to desalt liposomes or to separate liposomes form excess peptide. Liposomes are considered to be very large in comparison to the peptide molecules and therefore liposomes elute earlier.

4.6 REFERENCES

[1] Binnig, G.; Quate, C. F. and Gerber, C. Atomic Force Microscope. *Physical Review Letters* **1986**, 56, 930.

[2] Magonov, S. N.; Elings, V. and Whangbo, M. H. Phase imaging and stiffness in tapping-mode atomic force microscopy. *Surface Science* **1997**, 375, L385-L391.

[3] Tompkins, H. C. A user's guide to Ellipsometry. *Academic Press, Inc.* **1993**, San Diego.

[4] Faiss, S.; Schuy, S.; Weiskopf, D.; Steinem, C. and Janshoff, A. Phase Transition of Individually Addressable Microstructured Membranes Visualized by Imaging Ellipsometry. *J. Phys. Chem. B* **2007**, 111, 13979-13986.

[5] Tamada, K.; Ishida, T.; Knoll, W.; Fukushima, H.; Colorado, R.; Graupe, M.; Shmakova, O. E. and Lee, T. R. Molecular Packing of Semifluorinated Alkanethiol Self-Assembled Monolayers on Gold: Influence of Alkyl Spacer Length. *Langmuir* **2001**, 17, 1913-1921.

[6] Voros, J. The Density and Refractive Index of Adsorbing Protein Layers. *Biophys. J.* **2004**, 87, 553-561.

[7] Siebert, F. and Hildebrandt, P. Vibrational spectroscopy in life science. *Wiley-VCH, Weinheim, Germany* **2008**.

[8] Goormaghtigh, E.; Raussens, V. and Ruysschaert, J. M. Attenuated total reflection infrared spectroscopy of proteins and lipids in biological membranes. *Biochimica et biophysica acta* **1999**, 1422, 105-185.

[9] Harrick, N. J. Internal Reflection Spectroscopy. *John Wiley & Sons, New York* **1967**.

[10] Nabet, A.; Boggs, J. M. and Pezolet, M. Study by Infrared Spectroscopy of the Interdigitation of C26:0 Cerebroside Sulfate into Phosphatidylcholine Bilayers. *Biochemistry* **1996**, 35, 6674-6683.

[11] Pierre-Alain, C.; Jean, M. and Charles, R. Infrared determination of the orientation of molecules in stearamide monolayers. *The Journal of Chemical Physics* **1976**, 64, 1042-1050.

[12] Tamm, L. K. and Tatulian, S. A. Infrared spectroscopy of proteins and peptides in lipid bilayers. *Quarterly reviews of biophysics* **1997**, 30, 365-429.

[13] Kong, J. and Yu, S. Fourier Transform Infrared Spectroscopic Analysis of Protein Secondary Structures. *Acta Biochimica et Biophysica Sinica* **2007**, 39, 549-559.

[14] Brahms, S. and Brahms, J. Determination of protein secondary structure in solution by vacuum ultraviolet circular dichroism. *Journal of Molecular Biology* **1980**, 138, 149-178.

[15] Greenfield, N. J. and Fasman, G. D. Computed circular dichroism spectra for the evaluation of protein conformation. *Biochemistry* **1969**, 8, 4108-4116.

[16] Manavalan, P. and Johnson, W. C. J. Protein secondary structure from circular dichroism spectra. *J. Biosci.* **1985**, 8, 141-149.

[17] Johnson, W. C. Secondary Structure of Proteins Through Circular Dichroism Spectroscopy. *Annual Review of Biophysics and Biophysical Chemistry* **1988**, 17, 145-166.

CHAPTER V

5 DOMAIN FORMATION AND CLUSTERING OF LIGANDS IN LIPID BILAYERS MONITORED BY TEMPERATURE CONTROLLED ATOMIC FORCE MICROSCOPY

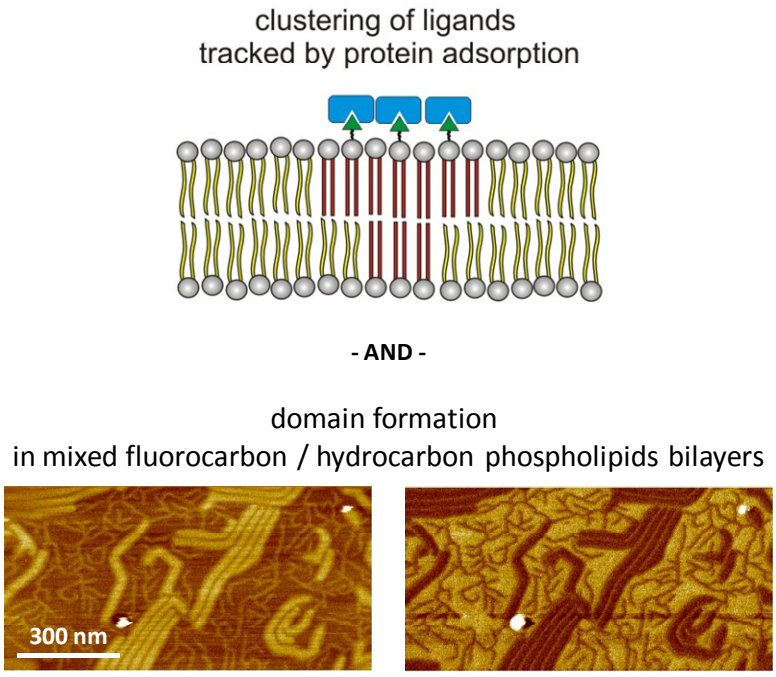

ABSTRACT

We investigated the phase separation of different lipid mixtures in order to analyze whether reversible clustering of ligands can be achieved by sorting anchor-lipids into distinctive domains, followed by specific recognition. A reversible switching of the receptor distribution, resulting in either clustering or dispersion of ligands could be applied as a (+ / -) trigger in order to assemble or disassemble coiled coil structures of lipopeptides as desired for the biosensor concept. In addition to phase separated hydrocarbon lipid mixtures, a novel class of perfluoroalkylated lipids, F6-DPPC and F4-DPPC will be presented. Domain formation based on the hydrocarbon / fluorocarbon immiscibility occurs due to the strong hydrocarbon / fluorocarbon mismatch, resulting in nano scale patterns of the phase separated mixtures.

5.1 INTRODUCTION

Domain formation in heterogeneous mixtures of lipid bilayers has recently attracted an immense attention and is believed to play a key role in molecular cell recognition, signal transduction and conformational changes in membrane proteins.[1, 2] Ideal binary lipid mixtures with a strong mismatch in their hydrophobic backbone tend to exhibit a broad two phase coexistence region. The phase separation process often results in the formation of micro and nano domains of the phase separated lipids, whereby lateral organization of the lipids occurs. This phase separation process facilitates the possibility to laterally organize anchor lipids within the gel- or within the fluid phase, accordant to the structure of the hydrophobic lipid backbone. Here, we investigated the phase separation of different lipid mixtures in order to analyze whether reversible clustering of ligands can be achieved by sorting anchor-lipids into distinctive domains, followed by specific recognition. A reversible process of ligand-clustering could be applied as a (+ / -) trigger in order to assemble or disassemble coiled coil formation of lipopeptides as desired for the biosensor concept (cp. 2.1). Thereby, if lateral mobility of ligands or anchor-lipids is desired, ligand sorting must be directed into the fluid phase by using appropriate anchors. The proof of principle that lateral clustering of ligands occurs due to lipid sorting in phase separated solid supported lipid bilayer is achieved by the irreversible binding of streptavidin to a biotinylated anchor-lipids, analyzed by means of temperature controlled atomic force microscopy. In addition to phase separated hydrocarbon lipid mixtures, a novel class of perfluoroalkylated lipids, F6-DPPC and F4-DPPC will be presented. Domain formation based on the hydrocarbon / fluorocarbon immiscibility occurs due to the strong hydrocarbon / fluorocarbon mismatch, resulting in nano scale patterns of the phase separated mixtures. [1]

[1] Mixed fluorocarbon / hydrocarbon phospholipid bilayers were investigated in close collaboration with Nicolas Y. Yoder, Tufts University, Boston, USA (Group of Prof. Krishna Kumar). Figure 5.8 is printed with permission.

5.2 MATERIALS AND METHODS

5.2.1 TEMPERATURE CONTROL STAGE

The temperature control stage, consisting of a set of two individually addressable Peltier elements, which are positioned on the opposite side of a heat conducting metal plate, is directly mounted on the wafer table of the AFM. The whole top of the brass fluid cell is coated with a thin layer of PTFE and the uncoated back side is coated with a thermally conductive paste. The fluid cell is placed on top of a metal plate, which covers one of the Peltier elements. A heat sink on top of the other Peltier element, pointing away from the AFM enables in cooling mode a heat flow from the fluid cell to the outer environment. The temperature of the fluid cell is monitored via an embedded thermo couple inside of the fluid cell, which is located 0.5 mm underneath the sample surface. The data from the thermocouple is read out by a multimeter, which is connected to a PC. The temperature adjustment is achieved by a homemade program which also holds the control circuit to maintain the present temperature. Since a comparison of three different thermo couples and three different multimeters with a calibrated mercury thermometer had shown temperature offsets of ± 1.7°C (results not shown), we used a high precision Pt100 sensor. The precise temperature of the liquid in the fluid cell is measured by an external Testo 735-2 temperature measuring instrument (Testo, Lenzkirch, Germany) equipped with a Pt100 surface probe (accuracy 0.1°C). The data from the temperature measuring instrument is read out by the PC and saved with a frequency of 1 count/s. This temperature control stage allows us to reach any temperature between 6°C to 50°C within 10 minutes and maintain it with an accuracy of ± 0.2°C.

5.2.2 TEMPERATURE CONTROLLED AFM IMAGING

Experiments were carried out in aqueous solutions using a commercial scanning force microscope (Dimension 3100 with Nanoscope IIIa+A/D controller, Veeco Digital Instruments, Santa Barbara, CA, USA) equipped with a Q-control. Silicon nitride cantilevers (OMCL-TR400PSA, Olympus, Japan), exhibiting nominal spring constants of 0.08 N / m were used for tapping mode in aqueous solution. After adjustment of the temperature the sample was allowed to equilibrate for at least 10 minutes. To compensate the vaporization of the buffer at temperatures over 30°C, 400 µl of Milli Q water were added directly into the fluid cell

before the new temperature was set. The corresponding temperature was recorded via a high precision Pt100 surface probe, which was placed inside the homemade AFM fluid cell.

5.2.3 SAMPLE PREPARATION

5.2.3.1 VESICLE PREPARATION

SUVs were prepared as described in chapter 3. In brief, SUVs were obtained by sonication of multilamellar vesicles (vessel resonator, 50 W, 0.4 s Puls, 20 min) in Tris-buffer (10 mM Tris, 100 mM NaCl, 0.3 mM $CaCl_2$, pH = 7.4).

5.2.3.2 MIXED PHOSPHOLIPID BILAYERS

SSLB were prepared as described in chapter 3, with minor modifications. We observed that the surface coverage of SSLBs with high contents of DPPC or C15 PC exhibited large defects if SUVs were incubated for only 2h. Therefore, SUVs composed of lipid compositions, exceeding more than 30 mol% DPPC or C15-PC were allowed to incubate for 4 h before heating the sample to 65°C, followed by rinsing.

5.2.3.3 PROTEIN ADSORPTION

Streptavidin stock solutions (c = 1mg / ml) were prepared from Tris-buffer by gentle vortexing. For monitoring protein adsorption, streptavidin stock solutions were either injected to the sample, incubated for 30 min, and finally rinsed before imaging or injected directly into the fluid cell during imaging. Final protein concentrations were in the range of 5 nM.

5.2.3.4 MIXED FLUOROCARBON / HYDROCARBON LIPID BILAYERS

SSLB were prepared by using standard protocols as described in chapter 3.2.

5.3 PHASE SEPARATION IN MIXED PHOSPHOLIPID BILAYERS

5.3.1 PHASE SEPARATION IN DOPC / DPPC MIXTURES

We studied phase separated SSLBs composed of DOPC / DPPC by means of AFM imaging in contact mode. This mixture serves a prototype of a gel-fluid phase separated bilayer mixture, since the main phase transition temperatures of the used lipids are strongly differing and such ideal mixtures exhibit distinctive fluid - solid phase separation as can be depicted from the respective phase diagram.[3] AFM imaging of SSLBs composed of either DOPC / DPPC 3:1 or DOPC / DPPC 1:3 at room temperature revealed domain formation due to phase separation for each sample (Figure 5.1).

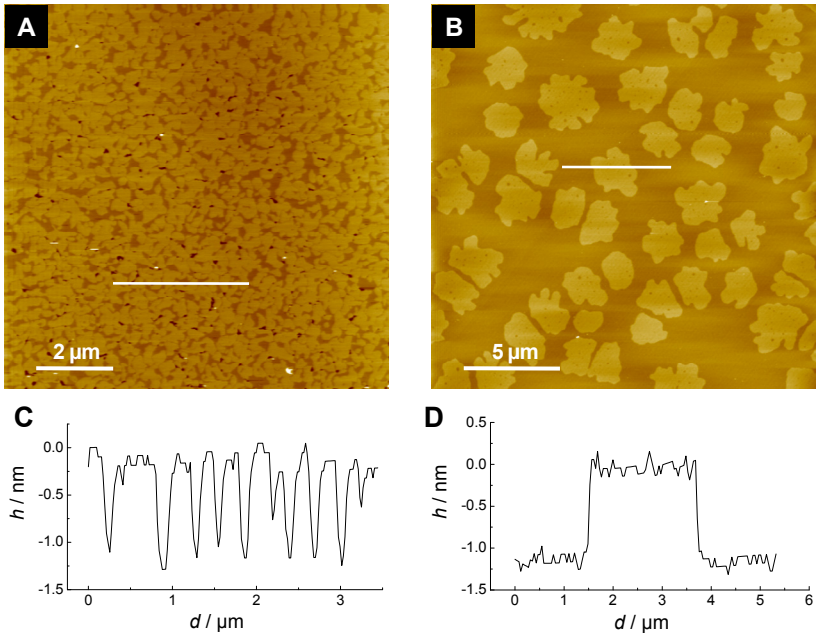

Figure 5.1. Contact mode AFM images at room temperature of a SSLB consisting of A) DOPC / DPPC 1:3 (molar ratio); B) DOPC / DPPC 3:1; C and D) Height profiles along the white line in image A and B, respectively. The average height difference between the DOPC and the DPPC rich domains was determined to be (1.2 ± 0.2) nm. The SSLB was prepared on mica and imaged in Tris-buffer.

The DPPC enriched gel phase domains can be readily observed for both samples on the basis of the (1.2 ± 0.2) nm height above the fluid DOPC matrix. Shape and distribution of the domains, as well as the measured height difference is very similar to AFM measurements preformed by others.[4-6] For a high content of DPPC (figure 5.1 A) the bilayer is homogeneously protruded by partially connected fluid DOPC enriched domains, whereas in

case of low content of DPPC (figure 5.1 B), DPPC enriched domains form globular islands of about ~1 µm in size.

5.3.2 MELTING OF PHASE SEPARATED IN DOPC / C15-PC MIXTURES

We employed temperature controlled AFM imaging to investigate the melting process of a fluid / gel phase separated bilayer mixture composed of DOPC and C15-PC. Figure 5.2 displays a set of AFM images of a SSLB composed of DOPC / C15-PC 1:4 (molar ratio) during a heating cycle. The height of the C15-PC enriched domains determined at the defect areas measured (5.2 ± 0.2) nm. DOPC rich domains were (1.4 ± 0.2) nm lower than the gel phase domains.

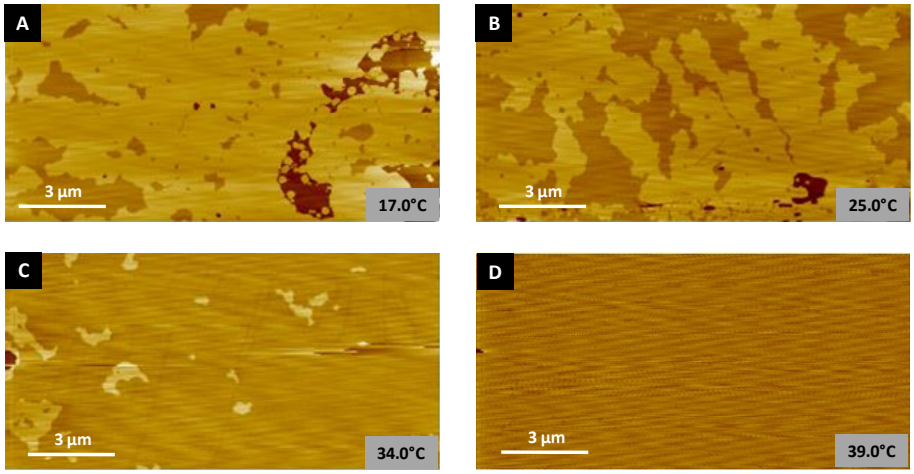

Figure 5.2. Temperature controlled AFM images in tapping mode of SSLB consisting of A) DOPC / C15-PC in a molar ratio of 1:4 at A) T = 17.0°C; B) T = 25.0°C; C) T = 34.0°C; D) T = 39°C in Tris buffer.

Upon heating of the sample C15-PC enriched domains melted. A homogeneous flat surface resulted at 39°C and defect areas disappeared. Disappearance of defect areas are related to a pronounced thermal expansion of more than 25 % of gel phase lipids during the main phase transition. Thermal expansion and changes in bilayer thickness during T_M utilizing the concept of microstructured lipid bilayers was latterly intensively investigated to measure the phase transition temperature of solid supported lipid bilayers consisting of DMPC, DPPC, F6-DPPC or F4-DPPC (cp. chapter 6, 7 and[7]).

5.4 LIPID SORTING AND CLUSTERING OF LIGANDS

Reversible switching of a lateral organization of ligands, leading either to a clustering or dispersion of ligands was aspired in order to trigger lipopeptides reversibly into a coiled coil assembly upon an external trigger. As a test bed, we first investigated the lateral organization of streptavidin binding to biotinylated lipids that were geometrically confined within a phase separated lipid bilayer. The scheme shown in figure 5.3 envisions this approach. The model system was primarily employed to study reversible lateral segregation of ligands, as desired for the biosensor concept. Temperature controlled AFM enables the investigation of ligand distribution in solid supported lipid bilayer systems at nanometer resolution.

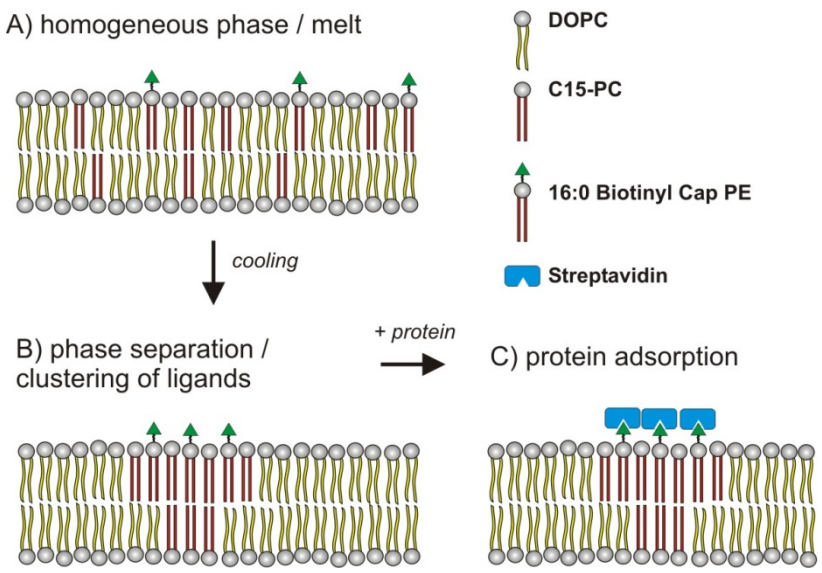

Figure 5.3. Scheme of the lateral organization of ligands due to lipid sorting and concentration in phase separated lipid bilayers to examine the lateral distribution of anchor-lipids. Sorting of anchor-lipids into gel or fluid phases occurs according to their hydrophobic tail and specific recognition of proteins is employed to follow the segregation process.

We used biotinylated lipids, 16:0 biotinyl-cap PE (bio-DPPE) and 18:1 biotinyl-cap PE (bio-DOPE) as headgroup-labeled lipidic ligands incorporated in binary lipid mixtures composed of DOPC and C15-PC. Receptor lipids are expected to segregate into gel phase domains embedded into a fluid phase, or vice versa depending on the chemical nature of the

hydrophobic tail of the anchor-lipid. Distribution of ligands is tracked by monitoring the distribution of proteins on the surface (figure 5.4).

5.4.1 LIGAND SORTING INTO FLUID PHASES

The following experiments show the different steps of the envisioned approach. Within a minor fluid phase a small amount of receptor bearing lipids were incorporated and by freezing out the system, well below T_M of C15-PC, the relative surface concentration of bio-DOPE was enhanced substantially.

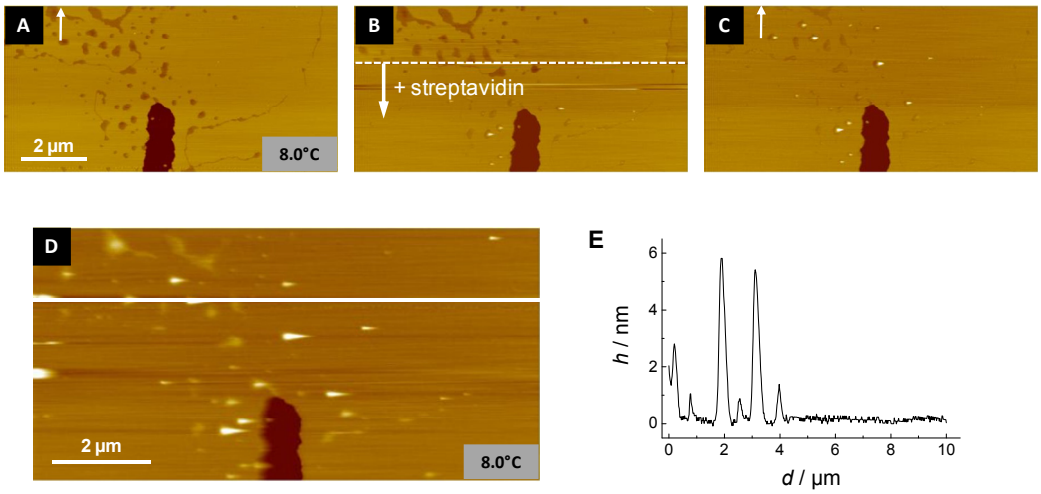

Figure 5.4. Atomic force microscopy image of a lipid bilayer consisting of 95% C15-PC, 5% DOPC and 0.2% biotinylated DOPE at 8°C. Slow scan axis is indicated by an arrow. A to C) Time lapsed images including injection of 50 µl streptavidin stock solution (1 mg / ml). Addition of streptavidin is indicated by a dashed line in image B. D) 20 min after addition of streptavidin; E) Height profile across the white line in image D.

Figure 4.5 shows a lipid mixture consisting of 95% C15-PC, 5% DOPC and 0.2% bio-DOPE at 8°C, while streptavidin was injected into the measurement chamber during imaging. The bright area corresponds to the C15-PC enriched gel phase and the less bright spots are the phase separated fluid DOPC micro domains, in which an enrichment of ligands is expected (image A). The dark area corresponds to a defect in the lipid bilayer. Distribution of ligand

lipids into DOPC enriched phases is determined by an increase of height of these domains after addition of streptavidin solution (image B, C and D). After protein adsorption fluid domains were found to be ~5 nm higher than the gel phase, indicating that biotinylated DOPE lipids have sorted into the fluid DOPC enriched domains. Consequently, lipid sorting and thereby clustering of biotinylated lipids occurred due to phase separation, tracked by the specific recognition of streptavidin.

5.4.2 LIGAND SORTING INTO GEL PHASES

Lipid sorting into gel phase domains was accomplished by the sorting of biotinylated DPPE into the C15-PC enriched gel phase domains within a DOPC matrix, followed by addition of streptavidin at low temperatures. Figure 5.5 displays the resulting AFM images.

After addition of streptavidin to a SSLB composed of 85% DOPC, 15% C15-PC and 0.6% bio-DPPE at 15°C the protein adsorbs preferentially on the biotinylated DPPE enriched gel phase domains as indicated by the ratio of surface coverage. Both images reveal that the suface coverage with proteins, calculated from the ratio of A_2 / A_1 (0.17 for image A and 0.14 for image B) correlates reasonably well with the content of C15-PC (15 mol%). Protein adsorption resulted in the formation of rectangular shaped protein domains with a length of ~ 2 µm and a width of about 300 nm, reminiscent of two-dimensional streptavidin crystals grown on biotinylated lipid bilayers as modeled Kasemo et al. utilizing Monte Carlo simulations.[8] In order to clarify, whether anchored streptavidin molecules can serve as a model system for reversible switching of a lateral organization of ligands upon an external trigger, we heated the sample to 35°C, well above T_M of C15-PC (31°C). The average height of the proteins was determined from histogram analysis to be (8.4 ± 1.8 nm) at T = 15°C and (4.5 ± 2.4 nm) at T = 35°C in good agreement with others. Kaasgard et al. determined a step height of the protein of 6 – 7 nm, adsorbed to a gel-gel phase separated lipid bilayer consisting of DPPC / C20-PC 1:1 doped with 0.7% biotinylated DPPE.[9] However, if proteins were adsorbed on fluid SSLB or monolayers doped with biotinylated lipids two-dimensional streptavidin crystals exhibited a height between 3.8 nm and 4,7 nm.[10, 11]

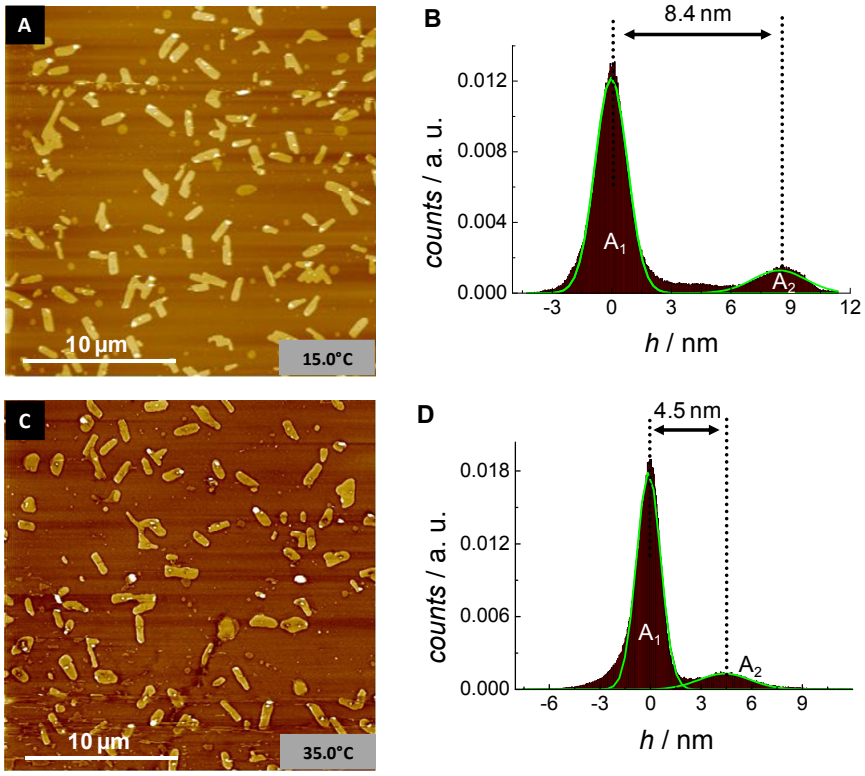

Figure 5.5: AFM images of a lipid bilayer consisting of 85% DOPC, 15% C15-PC and 0.6% biotinylated DPPE A after the streptavidin adsorption. Streptavidin was injected directly into the fluid cell at 15°C, incubated for 30 min, rinsed and imaged. A) T = 15°C; B) Histogram analysis of figure A; C) after heating the sample to 35°C for 20 min; D) Histogram analysis of figure C. The ratio of the surface coverage A_2 / A_1 was determined from the fitted histograms and measured 0.17 for image A and 0.14 for image C.

Finally, ligand-receptor based anchored lipids on the basis of biotin-streptavidin interactions failed to be a valuable model for triggering reversible lateral segregation as desired for the biosensor concept. Due to the strong lateral interaction of the streptavidin, resulting in lateral protein crystallization, domains stayed intact, even if the sample was heated to temperatures exceeding the melting temperature of the C15-PC.[10] We instead observed a significant decrease in height of ~ 4 nm, too high to be fully accounted to the melting of the underlying C15-PC enriched domains. Presumably, indentation of the protein layer resulting from tip-sample interactions during scanning, accompanied by a distortion of the protein crystal latter at elevated temperatures contribute to the unexpected decrease in height.

5.5 NANOSCALE PATTERING IN MIXED HYDROCARBON / FLUOROCARBON LIPID BILAYERS

Fluorocarbon functionalized DPPC phospholipid analogs, F6-DPPC and F4-DPPC (figure 5.6) can direct self assembly within a hydrocarbon DPPC lipid bilayer. In case of DPPC / F6-DPPC mixtures temperature controlled AFM analysis of these model membranes reveal composition and temperature dependent domain structures consisting of ~ 50 nm stripes, separated by ~ 1 µm sized domains for low contents of fluorinated lipids. Stripes can be melted at elevated temperatures above T_M of the fluorinated lipid, resulting in globular domain morphology similar to other gel-liquid phase separated lipid bilayers as shown in chapter 5.3. However, fluid fluid immiscibility can also be expected due to the unfavorable hydrocarbon / fluorocarbon interactions but has not been observed by temperature controlled AFM imaging. Interestingly, although the length per lipid molecule is not expected to be significantly altered by fluorination, the height differences between the fluorinated lipid enriched domains and the DPPC rich domains is significant. We found that DPPC enriched domains are (1.1 ± 0.1) nm higher than the fluorinated lipid enriched domains, independent of the state of the fluorinated lipid enriched domains.

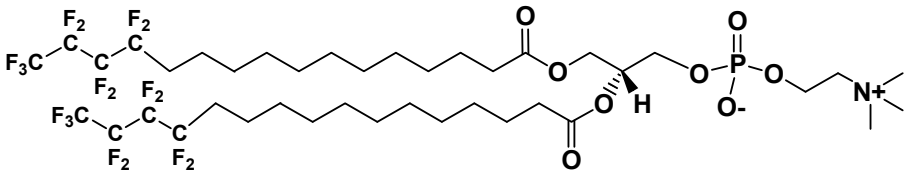

F4-DPPC

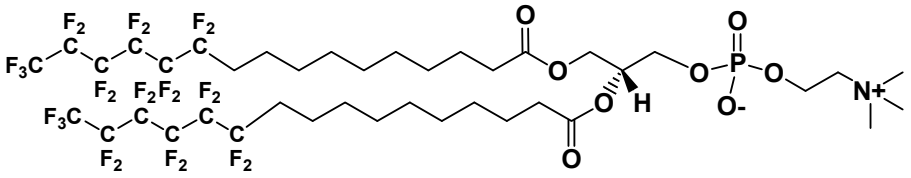

F6-DPPC

Figure 5.6. Molecular structure of the partial perfluoroalkylated DPPC analogs, referred to as F4-DPPC and F6-DPPC.

These findings provoked detailed structural and thermotropic analysis of neat fluorinated lipid bilayers by means of temperature controlled ellipsometry and attenuated total internal

reflection IR spectroscopy as described in chapter 6. In the following, investigations of SSLBs composed of DPPC / F6-DPPC mixtures (5.5.1) and neat F6-DPPC bilayers (chapter 6) are compared to F4-DPPC in order to gauge the impact of fluorination on the bilayer morphology. The phase transition temperature of the fluorinated lipids was determined by DSC to be 25°C for F6-DPPC and 18°C for F4-DPPC, both being significantly lower than the T_M of DPPC (41°C).

5.5.1 DPPC / F6-DPPC MIXTURES

SSLBs composed of DPPC and F6-DPPC at various ratios were readily fabricated on mica from vesicular suspensions in buffer and imaged at room temperature.[12] Figure 5.7 reveals that incorporation of F6-DPPC into DPPC SSLB leads to drastic changes in bilayer morphology. The maximal thickness of the bilayer d_{DPPC} = (5.3 ± 0.2) nm was measured at bilayer defects, corresponding well with the thickness of neat DPPC as measured by ellipsometry (cp. 6.3).

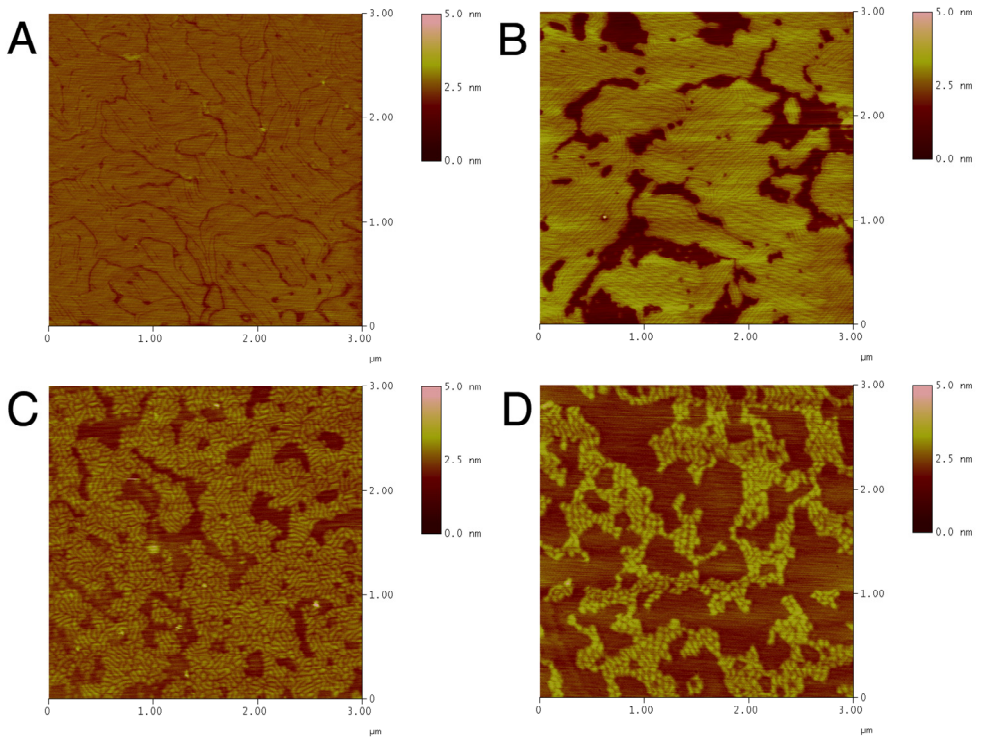

Figure 5.7. AFM images of solid supported lipid bilayers composed of various DPPC / F6-DPPC ratios: A) 85:15; B) 65:35; C) 45:55; D) 25:75.[12]

Domains lower by an average of (1.1 ± 0.1) nm were found to increase in coverage with increasing the mol fraction of F6-DPPC and are thus, referred to F6-DPPC enriched domains. More strikingly, these bilayers exhibited a quasi-ordered morphology, reminiscent of ripple phases, which we referred to as “stripes”. Bilayer morphology was altered by increasing the mol fraction of F6-DPPC from 15% to 75% (figure 5.7). At low contents of F6-DPPC (15%) the domains were elongated and the bilayer surface was protruded with parallel clusters about 40 nm apart. Figure 5.7 B (35 % F6-DPPC) reveals that almost all DPPC rich domains (higher domains) are protruded with extended, parallel stripes with well defined spacings. Parallel arrangement and extended stripe formation disappears at higher mol ratios of F6-DPPC and DPPC rich domains are broken into smaller, circular domains protruded by larger F6-DPPC enriched areas.

Ripple phases in SSLB consisting of neat DPPC bilayer has been reported by Mou et al. but morphology contributed to Tris-based buffers with concentrations > 50 mM.[13] However, we observed identical ripple formation when experiments were carried out in HEPES buffer (10 mM HEPES, 100 mM NaCl, pH 7.4) and we observed no ripple formation when imaging SSLB consisting of neat DPPC, despite the presence of 10 mM Tris. Formation of ripples in one- or two-component bilayer systems has further be described for solid supported mulit bilayer systems, attributed to the $P_{\beta'}$ phase, but periodicity and ripple amplitude is distinct from those we observed using DPPC / F6-DPPC SSLBs.[14, 15] In order to further investigate the mechanism of domain and stripe formation as a function of temperature and phase state of the F6-DPPC enriched domains we employed temperature controlled AFM analysis.

Temperature controlled imaging above T_M of F6-DPPC of a SSLB consisting of a 1:1 mixure of DPPC / F6-DPPC at 32°C as shown in figure 5.8 reveals that “stripes” are no longer present. The lipid bilayer exhibited a circular domains similar to other phase separated bilayers (cp. 5.2).[4, 5] Height differences between the F6-DPPC enriched and the DPPC enriched domains stayed constant at approximately 1.2 nm with DPPC being the elevated phase.

Domain extension (solid circle) and melting (dotted circle) of the higher domains indicate that at temperatures above the main phase transition temperature, F6-DPPC enriched domains melt into a conventional fluid phase, whereas the DPPC enriched domains remain in the gel phase. Interestingly, the height difference between domains was not altered by the melting of the F6-DPPC enriched domains, although lipid bilayers in the fluid phase are

expected to be significantly lower than gel phase bilayers (cp. chapter 6). Detailed structural analysis of the thermotropic phase behavior of neat F6-DPPC and neat F4-DPPC as presented in chapter 6, reveal that differences in height are caused by an increased tilt angle of the fluorinated lipids as compared to the hydrocarbon chain and melting has only minor impact on the thickness of fluorinated lipid bilayers.

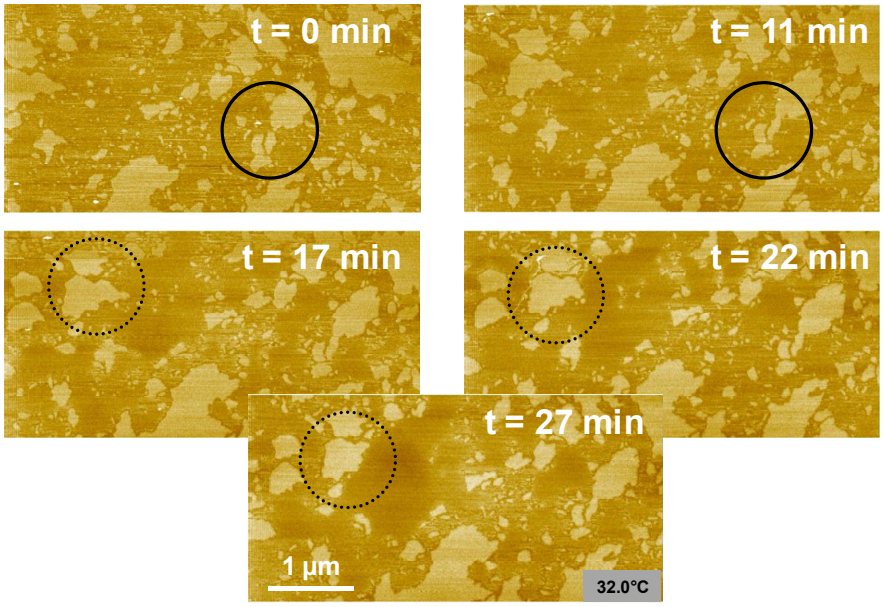

Figure 5.8. Temperature dependent AFM images of SLB composed of 1:1 mixtures of DPPC/F6-DPPC at 32°C. The higher domains (lighter color) are believed to be DPPC-rich. The solid circle highlights lateral diffusion of a DPPC-rich domain fragment and its subsequent fusion with a neighbor. The dashed circle indicates the partial melting of a DPPC-rich fragment.

Subsequently, we studied the nanoscale patterning of DPPC / F6-DPPC mixtures at temperatures well below T_M of F6-DPPC to investigate whether phase separation can be detected if both lipids are apparently in the gel phase. AFM imaging at 8°C of a SSLB consisting of DPPC / F6-DPPC 3:1 reveals that extended stripes are still present (Figure 5.9). The periodicity of the stripes was determined to be ~ 35 nm and their height measures (0.5 ± 0.2) nm. Due to the finite tip size we believe that the height determination might be underestimated, since the tip does not fully reach to the bottom of the stripes.

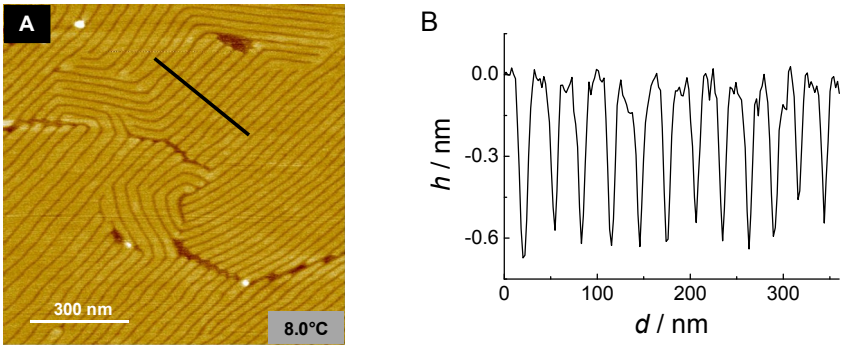

Figure 5.9. Low temperature AFM image of solid supported lipid bilayer composed of DPPC/F6-DPPC at a molar ratio of 3:1.

In following experiments we discovered that stripes in gel phase DPPC / F6-DPPC mixtures can be realigned by an annealing process (figure 5.10). Therefore, a SSLB consisting of DPPC / F6-DPPC at a molar ratio of 1:1 was prepared by standard sample preparation and held at 60°C for 30 minutes, well above T_M of both lipid components. The sample was then quenched for 30 min to 16°C and continuously imaged at 16°C for 30 min, resulting in realignment of the high DPPC rich domains into parallel oriented stripes regularly separated by lower groves and surrounded by low domains presumably composed of mainly F6-DPPC.

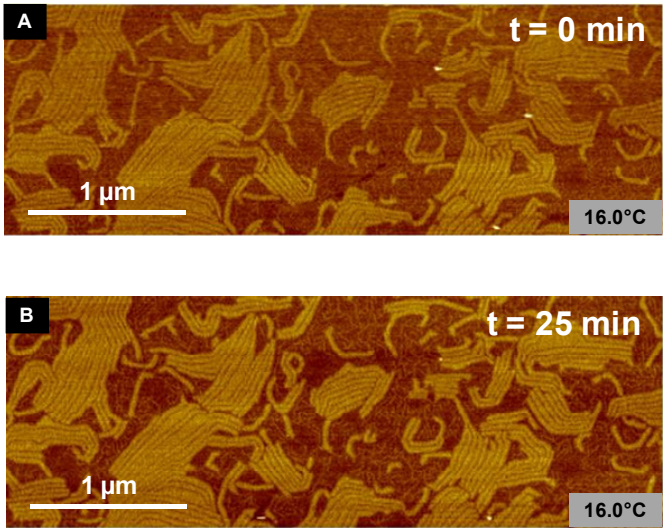

Figure 5.10. Time elapsed scan at 16°C of an annealed bilayer composed of DPPC / F6-DPPC 1:1. A) 0 min after quenching to 16°C for 30 min. B) after 30 min of continuous scanning.

As known for phase separated hydrocarbon lipid bilayers the domain size can be altered by the quenching rate, but resulting domains exhibit a more globular morphology, in contrast to the present case, in which largely periodic stripes result.[3]

High resolution imaging of this sample (figure 5.11) reveals the existence of small, dendritic stripes, slightly lower (0.9 nm) then the major stripes. Additionally we note, that the overall morphology and the step height of stripe were preserved over the time course of the continuous scanning procedure.

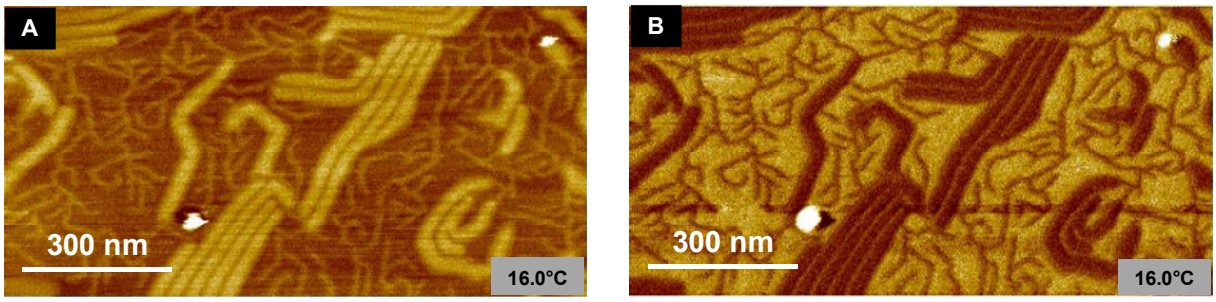

Figure 5.11. High resolution AFM images at 16°C of the annealed bilayer composed of DPPC / F6-DPPC 1:1 after continuous imaging for 30 min (cp. figure 5.10). A) Height image, B) phase image.

We conclude that the intrinsic morphology observed for mixed gel phases of DPPC and F6-DPPC is a specific feature of fluorinated lipids. Although AFM imaging does not provide a explicit map of the chemical composition of the domains, the provided images strongly suggest that lower phases are mainly composed of F6-DPPC and elevated domains are DPPC enriched. AFM phase imaging of a DPPC / F6-DPPC 1:1 mixture supports this hypothesis (figure 5.11 B). Qualitative local stiffness maps can be extracted by measuring the phase shift between the damped cantilever oscillation and the exiting oscillation of the piezo element at each point of the sample. Since both lipids are apparently in the gel phase at 16°C and thus, are expected to show comparable mechanical properties in terms of stiffness, however, a significant contrast was observed for phase imaged DPPC / F6-DPPC mixtures. The phase lag between the two domains was to be + 1.2°. By comparison, measurements at defect sites revealed phase lags of + 1.4° between the DPPC enriched domains and the rigid mica surface. The rigidifying effect of backbone semifluorination of phospholipids has been

previously suggested by Riess et al. and is consistent with our system, showing a higher stiffness for F6-DPPC than the hydrocarbon analog counterpart.[16]

In fact, cumulating evidence by structural analysis of the lipid structure and thermotropic phase behavior as presented in chapter 6 clearly reveals that the lower domains are composed of mainly F6-DPPC. As a result we measured, that tilt angles of the lipids increased from 21° for neat DPPC to 39° for neat F6-DPPC, which translates into an apparent thickness change between F6-DPPC and DPPC of 0.9 nm, in good agreement with the measured step height between the domains observed for DPPC / F6-DPPC mixtures. Additional structural investigation of neat fluorinated lipids is provided in chapter 6.

The observed intrinsic morphology of mixtures of DPPC / F6-DPPC is reminiscent of "modulated phases".[17] Such a model was previous utilized to describe elaborate, periodic morphologies, attributed between forces favoring mixing and separation as observed for ferromagnetic crystals, microphase-seperated block copolymer films or Langmuir films composed of dimyristoylphosphatic acid / cholesterol mixtures. Further, Schneider et al. speculated that modulated phases can be considered as possible explanation for the stripe formation in Langmuir monolayers consisting of pure fluorinated amphiphiles.[18] However, in the present case we observed microscale domains and nanometer sized stripes, whereto Schneider observed 2-8 µm stripes.[18] We speculate, that lipid mixtures of DPPC and F6-DPPC may form distinct regions of strict phase separation (domains) and modulated phases (stripes). It should be noted, that stripe like morphologies observed here are very similar to microphase separated block copolymers, which can also be realigned by annealing.[19]

5.5.2 DPPC / F4-DPPC MIXTURES

Rippled phases as observed for DPPC / F6-DPPC mixtures are also found if bilayers are fabricated from F4-DPPC and DPPC mixtures. Figure 5.12 displays a set of AFM images of a SSLB composed of DPPC / F4-DPPC 3:1 at 8°C. Image A reveals that the lipid bilayer is protruded by lower, elongated domains in which a similar stripe-like morphology can be detected. From ATR-IR and ellipsometric measurements we conclude, that the lower phases are presumably F4-DPPC enriched (cp. chapter 6). For lipid bilayers composed of neat F4-

DPPC, we measured a bilayer thickness of 3.9 nm, which translates into a theoretical step height between F4-DPPC and DPPC of about 1.5 nm.

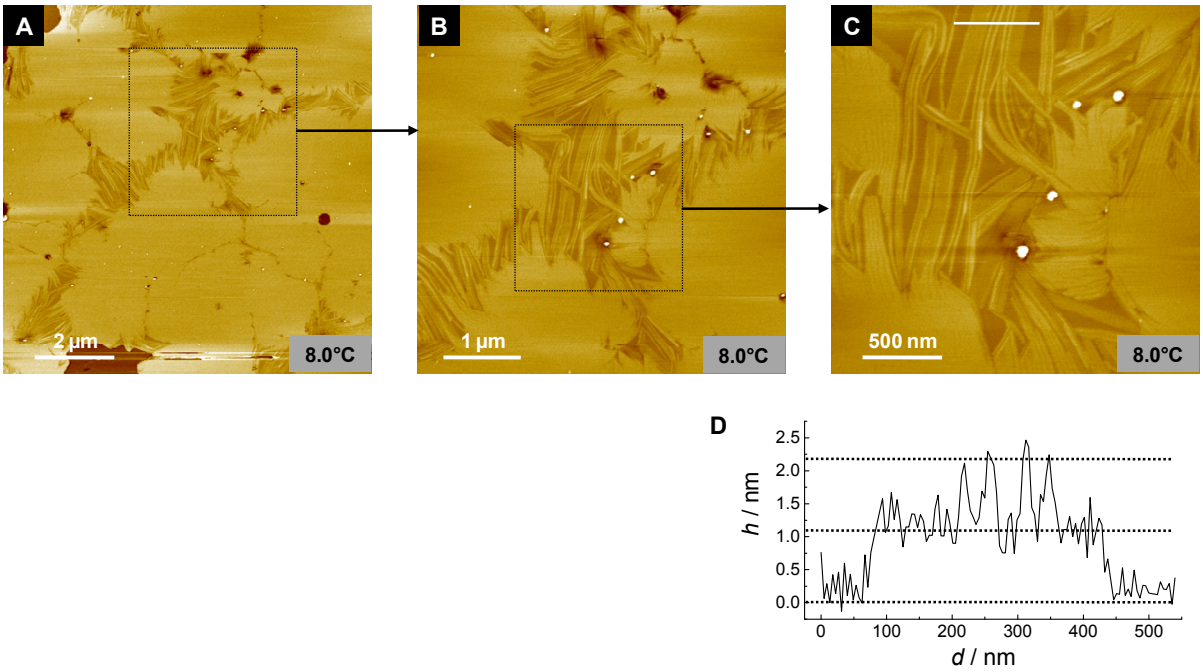

Figure 5.12. Temperature controlled AFM images of a SSLB consisting of DPPC / F4-DPPC in a molar ratio of 3:1 at 8.0°C. A to C) AFM images of the SSLB with varying scan sizes. Magnified areas are indicated by a dotted line. D) Height profile across the white line in C. Two distinctive thicknesses of the stripes were determined from image C to be (1.0 ± 0.2) nm and (2.0 ± 0.3) nm.

However, observed stripes exhibit two distinctive depths, which measure (1.0 ± 0.2) nm and (2.0 ± 0.3) nm (figure 5.12 D) and their distance of separation is rather broadly distributed in contrast to mixtures of DPPC / F6-DPPC. Noteworthy, stripes are only present in F4-DPPC rich domains, unlike stripes resulting from F6-DPPC that protrude the entire bilayer in form of regularly parallel clusters (cp. figure 5.7 A, B).

We speculate that the shorter perfluoroalkylated chain segment of F4-DPPC suppresses the formation of modulated phases and the formation circular F4-DPPC enriched domains is favored. At elevated temperature 20°C (figure 5.13) and 35°C (figure 5.14) no stripes are observed and we detected a globular domain formation similar to other gel-liquid phase separated bilayer mixtures.

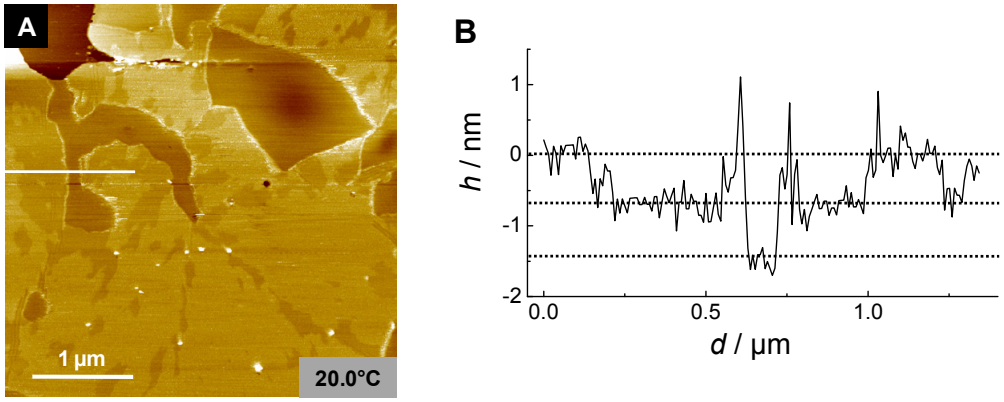

Figure 5.13. A) Temperature controlled AFM images of a SSLB consisting of DPPC / F4-DPPC in a molar ratio of 3:1 at 20.0°C. B) Height profile across the white line in image A. Two distinctive thicknesses of the globular domains were determined to be (0.9 ± 0.2) nm and (1.8 ± 0.2) nm.

Interestingly, at 20°C only 2°C above the main phase transition temperature of F4-DPPC, stripes were no longer present, but a distinctive three phase coexistence was detected. The domain step height was found to be (0.9 ± 0.2) nm for the intermediate and (1.8 ± 0.2) nm for the lowest phase, in good agreement with stripe step height measured in figure 5.12.

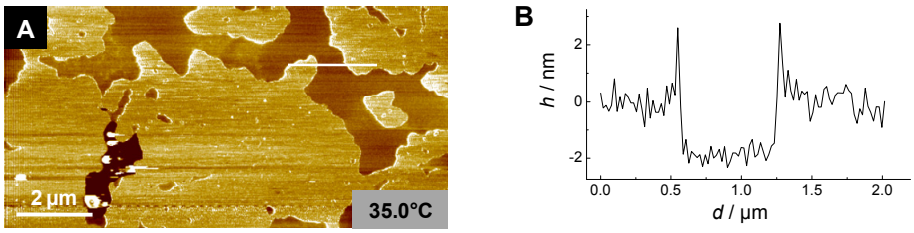

Figure 5.14. A) Temperature controlled AFM images of a SSLB consisting of DPPC / F4-DPPC in a molar ratio of 3:1 at 35.0°C. B) Height profile across the white line in image A.

At 35°C, well above T_M of F4-DPPC globular F4-DPPC enriched domains have extended and the domains are reminiscent of phase separated lipid bilayers as presented in 5.3.

5.6 CONCLUSIONS

Lateral lipid sorting due to phase separation leads to a clustering of ligands. We detected specific recognition of streptavidin in phase separated lipid bilayers doped with biotinylated lipids. Distribution of ligands could be triggered into the fluid or into the gel phase accordant the chemical nature of the anchor-lipid chain segment. However, reversible “switching” as desired for the biosensor concept leading to clustering or dispersion of anchored proteins could not be induced by melting of the phase separated bilayer, due to the strong lateral interaction of streptavidin.

Phase separation of mixed fluorocarbon / hydrocarbon lipid bilayers investigated by temperature controlled AFM imaging, allows us to explore the unusual stripe morphology. Furthermore, these stripes exhibit an ordered realignment upon annealing, giving a fingerprint texture reminiscent of microphase-separated block copolymer films. In many ways the simplest possible application of fluorocarbon-hydrocarbon immiscibility is related to self-assembly. The remarkable structures obtained, in an aqueous, inherently biocompatible[20] context, suggests that this principle may be widely applicable to the design of amphiphiles for biomaterials.

5.7 REFERENCES

[1] Anderson, R. G. W. and Jacobson, K. A Role for Lipid Shells in Targeting Proteins to Caveolae, Rafts, and Other Lipid Domains. *Science* **2002**, 296, 1821-1825.

[2] Simons, K. and Toomre, D. Lipid rafts and signal transduction. *Nat Rev Mol Cell Biol* **2000**, 1, 31-39.

[3] Milhiet, P. E.; Giocondi, M.-C. and Le Grimellec, C. AFM Imaging of Lipid Domains in Model Membranes. *The Scientific World Journal* **2003**, 3, 59-74.

[4] Leonenko, Z. V.; Finot, E.; Ma, H.; Dahms, T. E. S. and Cramb, D. T. Investigation of Temperature-Induced Phase Transitions in DOPC and DPPC Phospholipid Bilayers Using Temperature-Controlled Scanning Force Microscopy. *Biophys. J.* **2004**, 86, 3783-3793.

[5] Schneider, J.; Dufrene, Y. F.; Barger, W. R., Jr. and Lee, G. U. Atomic Force Microscope Image Contrast Mechanisms on Supported Lipid Bilayers. *Biophys. J.* **2000**, 79, 1107-1118.

[6] Burns, A. R. Domain Structure in Model Membrane Bilayers Investigated by Simultaneous Atomic Force Microscopy and Fluorescence Imaging. *Langmuir* **2003**, 19, 8358-8363.

[7] Faiss, S.; Schuy, S.; Weiskopf, D.; Steinem, C. and Janshoff, A. Phase Transition of Individually Addressable Microstructured Membranes Visualized by Imaging Ellipsometry. *J. Phys. Chem. B* **2007**, 111, 13979-13986.

[8] Zhdanov, V. P.; Höök, F. and Kasemo, B. Simulation of two-dimensional streptavidin crystallization. *Proteins: Structure, Function, and Genetics* **2001**, 43, 489-498.

[9] Kaasgaard, T.; Mouritsen, O. G. and Jorgensen, K. Lipid domain formation and ligand-receptor distribution in lipid bilayer membranes investigated by atomic force microscopy. *FEBS Letters* **2002**, 515, 29-34.

[10] Reviakine, I. and Brisson, A. Streptavidin 2D Crystals on Supported Phospholipid Bilayers: Toward Constructing Anchored Phospholipid Bilayers. *Langmuir* **2001**, 17, 8293-8299.

[11] Scheuring, S.; Muller, D. J.; Ringler, P.; Heymann, J. B. and Engel, A. Imaging streptavidin 2D crystals on biotinylated lipid monolayers at high resolution with the atomic force microscope. *Journal of Microscopy* **1999**, 193, 28-35.

[12] Yoder, N. C.; Kalsani, V.; Schuy, S.; Vogel, R.; Janshoff, A. and Kumar, K. Nanoscale Patterning in Mixed Fluorocarbon-Hydrocarbon Phospholipid Bilayers. *J. Am. Chem. Soc.* **2007**, 129, 9037-9043.

[13] Mou, J.; Yang, J. and Shao, Z. Tris(hydroxymethyl)aminomethane (C4H11NO3) Induced a Ripple Phase in Supported Unilamellar Phospholipid Bilayers. *Biochemistry* **1994**, 33, 4439-4443.

[14] Kaasgaard, T.; Leidy, C.; Crowe, J. H.; Mouritsen, O. G. and Jorgensen, K. Temperature-Controlled Structure and Kinetics of Ripple Phases in One- and Two-Component Supported Lipid Bilayers. *Biophys. J.* **2003**, 85, 350-360.

[15] Meyer, H. W. Pretransition-ripples in bilayers of dipalmitoylphosphatidylcholine: undulation or periodic segments? A freeze-fracture study. *Biochimica et Biophysica Acta (BBA) - Lipids and Lipid Metabolism* **1996**, 1302, 138-144.

[16] Santaella, C.; Vierling, P. and Riess, J. G. Highly stable liposomes from fluoroalkylated glycerophosphoquinolines. *Angew. Chem., Int. Ed.* **1991**, 30, 567-568.

[17] Seul, M. and Andelman, D. Domain Shapes and Patterns: The Phenomenology of Modulated Phases. *Science* **1995**, 267, 476-483.

[18] Schneider, M. F.; Andelman, D. and Tanaka, M. Stripes of partially fluorinated alkyl chains: Dipolar Langmuir monolayers. *The Journal of Chemical Physics* **2005**, 122, 094717-094715.

[19] Hahm, J.; Lopes, W. A.; Jaeger, H. M. and Sibener, S. J. Defect evolution in ultrathin films of polystyrene-block-polymethylmethacrylate diblock copolymers observed by atomic force microscopy. *The Journal of Chemical Physics* **1998**, 109, 10111-10114.

[20] Andersson, A. S.; Glasmastar, K.; Sutherland, D.; Lidberg, U. and Kasemo, B. Cell adhesion on supported lipid bilayers. *Journal of Biomedical Materials Research Part A* **2003**, 64A, 622-629.

CHAPTER VI

6 STRUCTURE AND THERMOTROPIC PHASE BEHAVIOR OF FLUORINATED PHOSPHOLIPID BILAYERS: A COMBINED ATTENUATED TOTAL REFLECTION IR SPECTROSCOPY AND IMAGING ELLIPSOMETRY STUDY

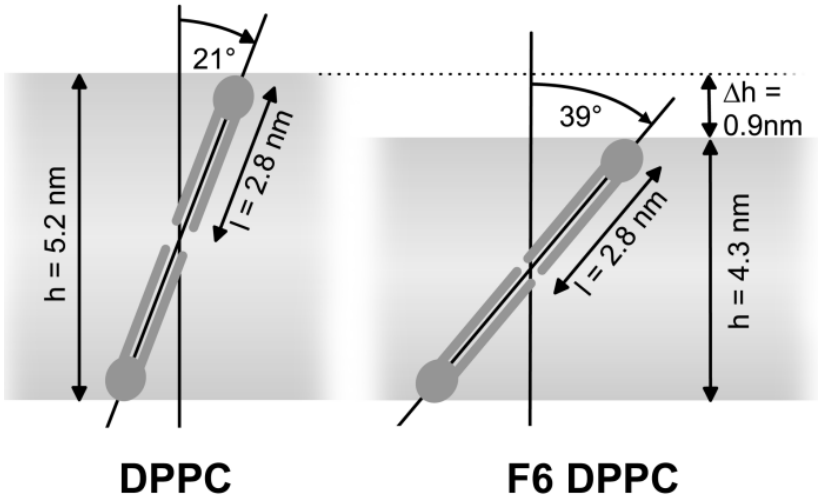

ABSTRACT

Lipid bilayers consisting of lipids with terminally perfluoroalkylated chains have remarkable properties. They exhibit increased stability and phase separated nanoscale patterns in mixtures with non-fluorinated lipids. In order to understand the bilayer properties that are responsible for this behavior, we have analyzed the structure of solid supported bilayers composed of 1,2-Dipalmitoyl-sn-glycero-3-phosphocholine (DPPC) and of a DPPC analogue with 6 terminal perfluorinated methylene units (F6-DPPC). Polarized attenuated total reflection Fourier-transform infrared (ATR-FTIR) spectroscopy indicates that for F6-DPPC the tilt of the lipid acyl chains to the bilayer normal is increased to 39° as compared to 21° for native DPPC, for both lipids in the gel phase. This substantial increase of the tilt angle is responsible for a decrease of the bilayer thickness from 5.4 nm for DPPC to 4.5 nm for F6-DPPC, as revealed by temperature-controlled imaging ellipsometry on microstructured lipid

bilayers and solution atomic force microscopy (AFM). During the main phase transition from the gel to the fluid phase, both the relative bilayer thickness change and the relative area change are substantially smaller for F6-DPPC than for DPPC. In light of these structural and thermotropic data, we propose a model in which the higher acyl chain tilt angle in F6-DPPC is the result of a conformational rearrangement to minimize unfavorable fluorocarbon-hydrocarbon interactions in the center of the bilayer due to chain staggering.[2]

[2] ATR-IR analysis were performed in collaboration with PD Dr. Reiner Vogel (Universität Freiburg). Figures (6.1 and 6.2) and schemes are printed with permission.

6.1 INTRODUCTION

Bilayers made of terminally perfluoroalkylated phosphatidylcholines (PCs) show remarkable differences in their structural and physical properties compared with bilayers composed of their pure hydrocarbon analogs. Santaella and coworkers have synthesized a series of F-alkyl modified phosphatidylcholines, that formed highly stable liposomes and are promising in biomedical applications.[1, 2] Subsequent studies revealed several interesting properties of the perfluoroalkylated phospholipids, such as polymorphic phase behavior,[3] reduced membrane permeability,[4, 5] a rigidifying effect of the fluorinated bilayer core,[6] and high detergent resistance.[7] Models describing molecular packing of highly fluorinated phospholipid monolayers were proposed by Rolland *et al*., who observed an increase in the area per molecule upon partial substitution of hydrocarbon chain segments with fluorocarbons.[8] McIntosh *et al*. have reported structural data on highly fluorinated phospholipid bilayers using X-ray diffraction and described different physical properties as compared to conventional bilayers.[9] Based on their data on the bilayer thickness of the fluorinated analogs, they further proposed a considerably increased chain tilt angle of the lipids to the bilayer normal. While there is a lack of experimental data on the chain arrangement in fluorinated bilayers, a large number of researchers have analyzed the structure of self assembled monolayers (SAMs) containing partially fluorinated alkyl chains,[10-16] from which insights into the physical driving forces for the distinct packing in fluorinated lipid bilayers can be derived. In all cases, fluorination of chain segments alters the tilt angle as compared to the pure hydrocarbon analogs, yet both direction and degree of the change also depended strongly on the alkyl spacer length, the head group of the molecule and on the metal on which the SAM is deposited.[10-16]

This work focuses on determining tilt angles of both the hydrocarbon and the fluorocarbon segments in bilayers of 1,2-dipalmitoyl-*sn*-glycero-3-phosphocholine (DPPC) and of a partially fluorinated analogue of DPPC with 6 terminal perfluorinated methylene units (F6-DPPC) (cp. 5.5), using polarized attenuated total reflection fourier-transform infrared (ATR-FTIR) spectroscopy, and relating these results to data obtained for the bilayer thickness, using imaging ellipsometry and in-situ atomic force microscopy (AFM). The results complement the findings of a recent study, in which a distinctive nanoscale domain patterning was found in supported lipid bilayers consisting of mixtures of hydrocarbon and

fluorocarbon phospholipids, using atomic force microscopy.[17] This domain patterning consisted of regularly spaced stripes and constitutes a promising tool for the clustered display of ligands on surfaces of vesicles and on live cells.[18-21] In addition, several other phenomena were observed that required further investigation, such as a conspicuous height difference of 1.1 nm between fluorinated and unfluorinated lipid domains, although both lipids were apparently in the gel phase. Furthermore, a puzzling thermotropic behavior was observed, in which the absence of defects in a heating and cooling cycle posed questions concerning the change in lipid area during the main phase transition.[22-26] These questions are now tackled by scrutiny of bilayer thickness and the relative area change $\Delta A/A$ during the main phase transition using temperature-controlled imaging ellipsometry on microstructured bilayers.

6.2 MATERIALS AND METHODS

6.2.1 VESICLE PREPARATION

Lipids were dissolved in chloroform and transferred into a test tube. After evaporation of the solvent in a stream of nitrogen at 55°C for DPPC and 40°C for F6-DPPC (all temperatures well above the main phase transition temperatures), the resulting lipid film was dried for 3 h in a vacuum oven at 55°C. Large multilamellar vesicles (MLV) of DPPC were formed from 1 mg lipid film by hydrating the film in deionized water for 20 min at 60°C and thorough vortexing. For the formation of MLVs from F6-DPPC an extended hydration time of at least 45 min at 65 °C was necessary to obtain homogeneous suspensions. This step was repeated once with a reduced hydration time of 15 min., resulting in a homogeneous, turbid suspension. Small unilamellar vesicles (SUVs) were formed from MLVs of DPPC and F6-DPPC in standard buffer (10 mM Tris, 100 mM NaCl, pH 7.4) by sonification (50 W, 0.4 s pulse, 20 min) in a vessel resonator (Sonoplus HD 2070, Bandelin, Berlin, Germany), resulting in a clear opalescent suspension. The final lipid concentration (MLVs or SUVs) was 1 mg/ml in all experiments.

6.2.2 ATR-FTIR EXPERIMENTS

ATR-FTIR experiments were performed using a Bruker Vertex FTIR spectrometer. Spectra were acquired at 2 cm^{-1} resolution with 1 minute sampling time.

Multilamellar films were produced by drying MLVs prepared from 1 mg of lipid in deionized water under reduced pressure on a 85 mm x 6 mm side of a trapezoidal germanium internal reflection element and were then mounted in a thermostatted custom made ATR cell. Films were examined either in dry state or were hydrated from the vapor phase and equilibrated prior to the experiments.

For analysis of polarized spectra, we used the Harrick thick film approximation[27] that was developed for films substantially thicker than the penetration depth of the evanescent field (~0.4 µm in our setup), which was the case in all experiments. Absorption spectra A_p and A_s were acquired with polarizations parallel (p) and perpendicular (s) to the plane of incidence using a KRS-5 12000 grid polarizer (Graseby Specac, UK) on a rotatable mount. For visual inspection, these absorption spectra were converted into absorption spectra polarized in the xy plane parallel to the surface of the ATR crystal and in the z direction perpendicular to it, A_{xy} and A_z, respectively. This was achieved by decomposing the p- and s-polarizations into their x-, y-, and z-electric field components with respect to the crystal surface in the Harrick thick-film formalism.[27-29] Using refractive indices n = 4.01 for germanium, n = 1.48 for DPPC,[30] and n = 1.40 for the fluorinated lipids,[14] the resulting equations for these conversions were $A_{xy} = A_s / j$, with j = 2.310 for DPPC and j = 2.274 for the fluorinated lipids, and $A_z = (A_p - k \cdot A_s) / l$, with k = 0.845 and l = 2.667 for DPPC and k = 0.863 and l = 2.582 for the fluorinated lipids.

The orientation of the transition dipole moment of a vibration was calculated directly from the dichroic ratio R.[27-29] R was determined by a previously developed formalism, which is relatively insensitive to baseline distortions.[31] The accuracy of the measured tilt angles was primarily limited by the achieved order parameter of the lipid films and is estimated to be approximately ± 2°. All tilt angles are averages obtained from three independent measurements. Tilt angles were further used to extract the height differences by a simple model (Figure 6.6). The apparent lipid length of 2.8 nm was calculated using the steric bilayer thickness d_B = 4.78 nm of hydrated DPPC bilayers and a chain tilt of 31°.[32, 33]

6.2.3 FORMATION OF MICROSTRUCTURED LIPID BILAYERS

Structured solid supported lipid bilayers were fabricated by micromolding in capillaries. Therefore the poly-dimethyl-siloxane (PDMS) (explain) mold was attached to a hydrophilic substrate (glass or silicon), forming a hydrodynamic network. Capillaries were filled with a suspension of SUVs in buffer to form a planar supported bilayer. After bilayer formation the stamp was peeled off and the surface was extensively rinsed with buffer. Without drying the substrate was mounted into the accordant fluid measurement cells. A detailed description on the formation of microstructured lipid bilayers on glass or silicon and imaging via temperature controlled atomic force microscopy and temperature controlled imaging ellipsometry, as well as the geometric design of the PDMS mold are given elsewhere.[34-38]

6.2.4 ELLIPSOMETRY

Ellipsometry is a non invasive, well established method for the characterization of ultra thin films in terms of layer thickness and refractive indices.[39-42] In principle the change of the state of the polarization of monochromatic parallel light upon reflection of a film-covered surface is measured. The resulting changes in the state of polarization can be expressed and quantified by the ellipsometric angles Delta (Δ) and Psi (Ψ). These angles are related to the complex reflectance ratio ρ:

$$\rho = R_P / R_S = \tan\Psi \cdot e^{i\Delta} \qquad (1)$$

where R_P and R_S are the overall refractive coefficients parallel and perpendicular to the surface, respectively. The ellipsometry angles are sensitive to the interfacial architecture and thus, they can be related to the layer thickness for homogeneous thin films by means of model calculations based on Fresnel equations. In this study a commercially available imaging ellipsometer (EP^3-SW, Nanofilm Technologie, Göttingen, Germany) was used to determine the thickness d and the relative area change $\Delta A/A$ during the main phase transition of the structured lipid bilayers. Data acquisition and analysis followed previous protocols,[38] using refractive indices n = 1.53 for a fully hydrated DPPC bilayer[38] and n = 1.40 for F6-DPPC.[14] In brief, the average bilayer thickness was first measured by a four-zone nulling procedure in several sections or regions of interests (ROIs), using the silica substrate as a reference, and the thickness calculations were accomplished by employing the

respective layer model. For the determination of the thermal expansion of a bilayer $\Delta A/A$ during the main phase transition microstructured bilayers consisting of DPPC or F6-DPPC were imaged at different temperatures by ellipsometry, resulting in a "Delta-map", which displays the ellipsometric angle Delta over the whole image with approximately 1 µm resolution and from which the thickness for each pixel was computed. From the Delta-maps for each temperature we determined the fractional area change $\Delta A/A$ by a histogram analysis of the image section. For illustration, the Delta-maps obtained from imaging ellipsometry of microstructured F6-DPPC and DPPC bilayers in the gel and in the fluid phase are given as insets in Figure 6.3 (cp. appendix A).

6.2.5 ATOMIC FORCE MICROSCOPY

Experiments were carried out in aqueous solutions using a commercial scanning force microscope (Dimension 3100 with Nanoscope IIIa+A/D controller, Veeco Digital Instruments, Santa Barbara, CA, USA) with silicon nitride cantilevers (OMCL-TR400PSA, Olympus, Japan), exhibiting nominal spring constants of 0.08 N/m. Imaging was performed in tapping mode at controlled temperature in aqueous solution. The ratio of the damped and free cantilever oscillation amplitude A_{sp}/A_0 during imaging was adjusted to 0.85.

6.3 RESULTS

6.3.1 ORIENTATION OF FLUORINATED DPPC IN DRY MULTILAMELLAR BILAYERS

To determine the tilt angle of the hydrocarbon side chains in partially perfluorinated DPPC analog (F6-DPPC) with respect to the bilayer normal, we used polarized ATR-FTIR spectroscopy on oriented multilamellar stacks of bilayers deposited on the surface of the ATR crystal. Polarized absorption spectra were measured with polarizations parallel and perpendicular with respect to the plane of incidence and were decomposed into absorption spectra polarized parallel and perpendicular to the crystal surface, A_{xy} and A_z, respectively, as detailed in the Materials and Methods section.

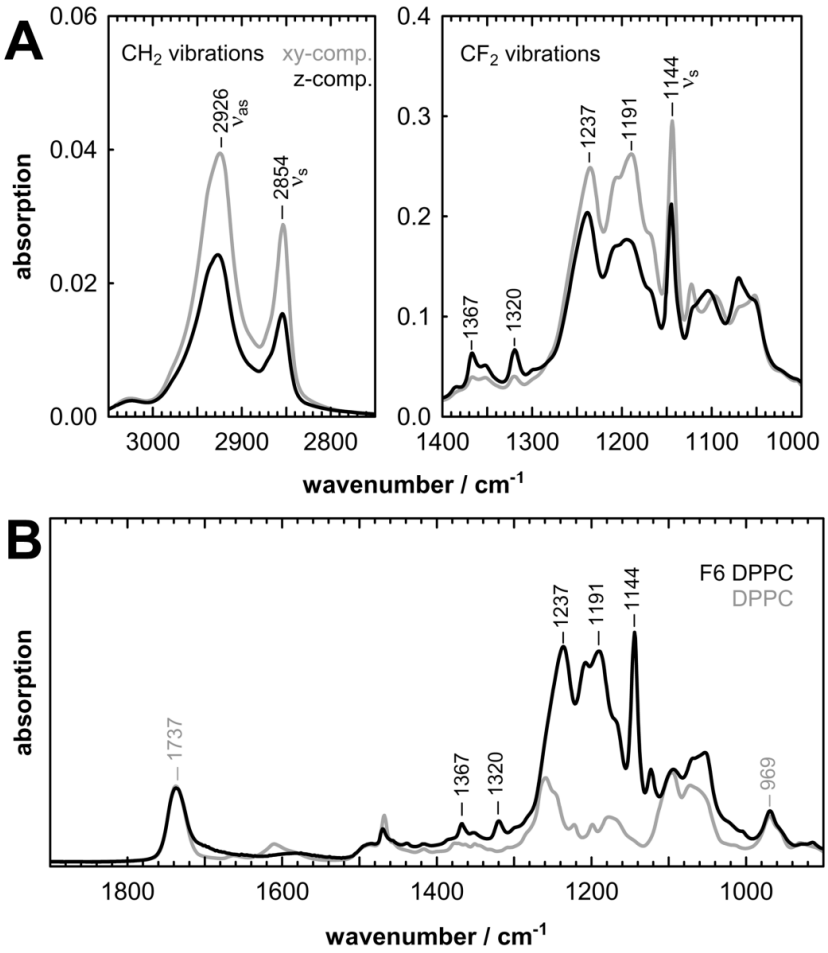

Figure 6.1. ATR-FTIR spectra of dry F6-DPPC multilamellar films in the gel phase. A. Polarized ATR-FTIR absorption spectra of dry gel phase F6-DPPC films were decomposed into the xy-component polarized in the plane parallel to the surface of the ATR crystal and the z-component polarized perpendicular to the surface. The spectra are shown in the absorption range of the CH_2 and CF_2 vibrations and allow determination of the orientations of the molecular groups with respect to the crystal surface and thus, the plane of the bilayer. B. Unpolarized ATR-FTIR spectra of dry F6-DPPC films are compared with those of DPPC, revealing the bands being due to the fluorocarbon moiety (marked with black labels).

In Figure 6.1 A, absorption spectra polarized parallel A_{xy} and perpendicular A_z to the plane of the ATR crystal are shown in the range of the hydrocarbon and fluorocarbon stretching vibrations for dry F6-DPPC multilamellar films in the gel phase (L_C) at room temperature, revealing the dichroic nature of these absorption bands. Absorption bands at 2854 and 2926 cm^{-1} are assigned to the symmetric and antisymmetric CH_2 stretch of the hydrocarbon moiety, respectively, with the transition dipole moment of these vibrations oriented

perpendicular to the chain axis. By comparing absorption spectra of F6-DPPC with those of DPPC (Figure 6.1 B), the fluorocarbon associated bands in the range between 1100 and 1400 cm^{-1} could be distinguished. Based on previous studies on fluorinated fatty acids,[16] the F6-DPPC band at 1144 cm^{-1} was assigned to the symmetric CF_2 stretch, while the bands at 1237 and 1191 cm^{-1} contain the antisymmetric CF_2 stretch. The bands at 1320 cm^{-1} and 1367 cm^{-1} were assigned to the symmetric and antisymmetric CF_3 stretches. In contrast to the CF_2 stretch, the transition dipole moment of the CF_3 stretch is oriented parallel to the chain axis, yielding therefore a dichroism inverse to that of the CF_2 stretching vibrations as can be easily discerned in the right panel of Figure 6.1 A.

lipid	Θ / ° [1] (gel, dry film)	*h* / nm (ellipsometry)	*h* / nm (AFM)	*h* / nm [2] (calculated)
DPPC	21	5.4	5.4	5.2
F6-DPPC	39	4.5	4.5	4.3

Table 6.1. Tilt angles and thicknesses of DPPC and F6-DPPC bilayers at room temperature.

[1] measured by ATR-FTIR, estimated error is ±2°.

[2] calculated from the tilt angle Θ and the model shown in figure 6.5.

Focusing on the symmetric stretch vibrations of the CH_2 groups at 2854 cm^{-1} and of the CF_2 groups at 1144 cm^{-1}, the orientation of the transition dipole moment of the vibration can be determined from their dichroic ratio with respect to the crystal surface. Assuming an orientation of the bilayer plane parallel to the crystal surface and of the transition dipole moment perpendicular to the molecular chain axis, apparent tilt angles of the chain axis with respect to the bilayer normal can be independently calculated for the hydrocarbon and the fluorocarbon moieties. Evaluation of the respective stretching bands of F6-DPPC yields an apparent tilt angle of 38° for the hydrocarbon chain and a slightly larger angle of 41° for the fluorocarbon chain. By averaging these values weighted by the approximate length of the respective chain moiety, a tilt of the F6-DPPC side chain of 39° is obtained in dry gel phase

lipid, which compares to a tilt of 21° for DPPC measured under the same conditions (table 6.1).

6.3.2 THERMOTROPIC PHASE BEHAVIOR OF SUPPORTED FLUORINATED DPPC BILAYERS

The phase transition of fluorinated DPPC analogs was also followed using ATR-FTIR spectroscopy, with the positions of the CH_2 stretching vibrations being sensitive indicators for the occurrence of *gauche* conformations during chain melting. At 15 °C, hydrated F6-DPPC films are in the gel phase and the position of the symmetric CH_2 stretch is similar as in dry films at the same temperature (Figure 6.2).

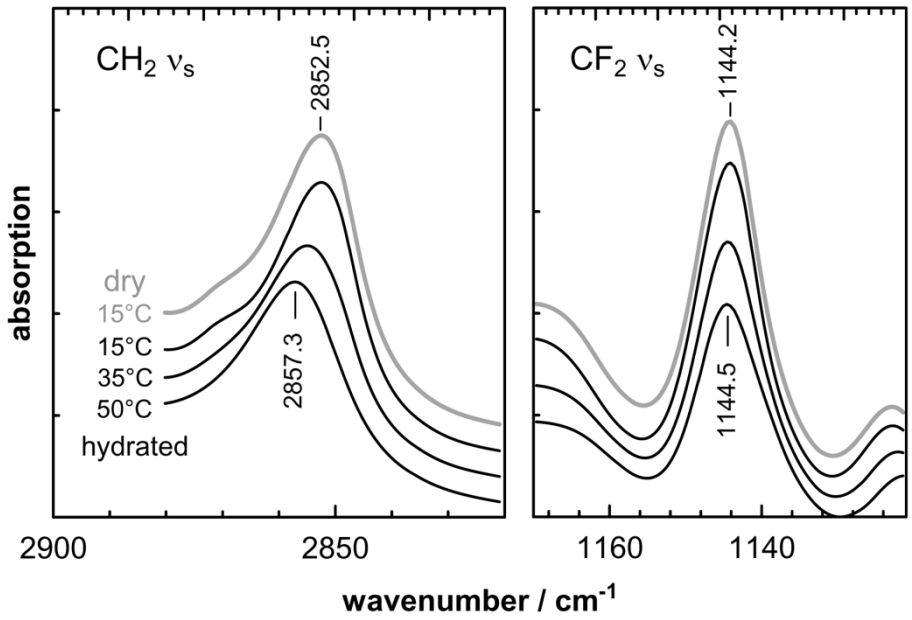

Figure 6.2. ATR-FTIR spectra of the phase transition of F6-DPPC films. Spectra obtained from hydrated films at different temperatures are stacked and compared to those of a dry film at 15 °C. The symmetric CH2 stretch (ν_s) of the hydrocarbon moiety reveals a shift from 2852.5 cm^{-1} in the gel phase to 2857.3 cm^{-1} in the fluid phase, due to the increasing occurrence of gauche conformations in the melted phase. The symmetric CF2 stretch vibration of the fluorocarbon moiety, on the other hand, reveals an absorption decrease and slight broadening, but no significant band shift. The band positions measured in hydrated bilayers in the gel phase at 15°C correspond to those measured in dry films at the same temperature. Tickmarks are 20 and 100 mOD in the left and right panels, respectively.

As the temperature is raised past the T_M, an unusually large upshift of the peak by 4.8 cm^{-1} is observed indicating the formation of melted hydrocarbon chain segments in the fluid phase (L_α). Interestingly, no significant shift is observed for the absorption peak of the symmetric stretch of the CF_2 moiety.

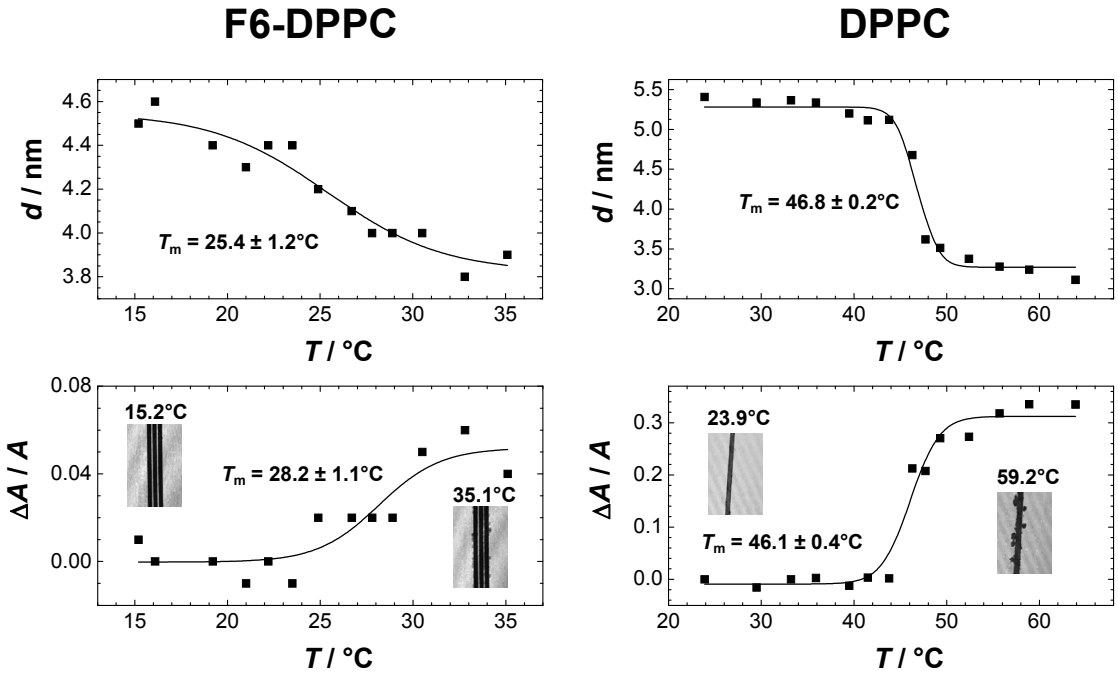

Figure 6.3. Decrease of bilayer thickness *h* and relative area change Δ*A*/*A* of microstructured F6-DPPC compartments during the phase transition measured by imaging ellipsometry. A sigmoidal fit to the ellipsometric data provides temperature and width of the phase transition during a heating cycle of hydrated DPPC and F6-DPPC bilayers. Both *h* and Δ*A*/*A* data reveal a broadening of the phase transition of F6-DPPC as compared with DPPC. F6-DPPC displays a significantly lower change in thickness (0.6 nm in F6-DPPC) as compared to neat DPPC (1.9 nm in DPPC) and lower thermal expansion (5% for F6-DPPC and 33% for DPPC bilayers) by crossing the phase transition.

In further experiments, the impact of the phase transition on the apparent tilt angles of F6-DPPC was studied. In dry multilamellar films, an increase of the apparent tilt angle by approximately 5° was observed upon heating from 10 °C to 50 °C, accompanied by a shift of the absorption peak of the CH_2 stretching vibration similar as in hydrated multilamellar films (data not shown). A similar analysis of the tilt angle in hydrated films is complicated by the decrease of the order parameter of the multilamellar films upon hydration, which reduces

the reliability of such measurements.In our previous study, the phase transition temperature, T_M, for multilamellar F6-DPPC vesicles was determined by differential scanning calorimetry (DSC) to be 25 °C, and a substantially reduced melting enthalpy compared to pure DPPC was found,[17] corresponding reasonably well to the data reported by Santaella and coworkers for similar fluorinated lipids.[3]

In order to investigate further the gross structural changes which occur in the bilayer during phase transition, we employed two high resolution, variable temperature techniques: imaging ellipsometry and AFM. Microstructured DPPC and F6-DPPC bilayers were imaged during a heating cycle, starting at temperatures well below the phase transition temperature of the respective phospholipids (Figure 6.3). During the heating cycle, the temperature was varied from 15.2°C to 35.1°C for F6-DPPC and from 23.9°C to 63.9°C for neat DPPC bilayers. The ellipsometric data reveal a decrease of the bilayer thickness during the transition from the gel to the fluid phase from 5.4 nm (23.9°C) to 3.4 nm (52.4°C) in DPPC, while the thickness of F6-DPPC bilayers decreased only marginally from 4.5 nm (15.2°C) to 3.9 nm (35.1°C) (table 6.1 and 6.2). The bilayer thickness obtained for DPPC in the gel and in the fluid phase are in good agreement with previously published results determined independently by AFM.[25, 43]

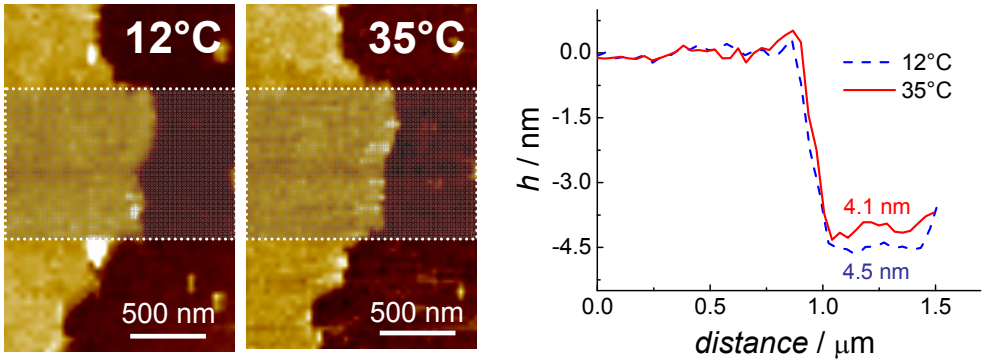

Figure 6.4. Determination of bilayer thickness by AFM. AFM images of microstructured bilayers of F6-DPPC on glass were recorded in the gel phase and in the fluid crystalline phase. Averaged line scans were taken from the highlighted areas in the center of the images.

Additional experiments employing temperature controlled AFM on microstructured solid supported F6-DPPC bilayers confirmed the membrane thickness data measured by ellipsometry (Figure 6.4). These experiments were conducted by microstructuring bilayers (as described in the Methods section) and measuring the layer thickness by averaged line scan over the edges of the bilayer. We obtained an average thickness of 4.5 nm for the L_C phase (12°C) and 4.1 nm for the L_α phase (35°C) in agreement with the ellipsometric data.

Imaging ellipsometry further revealed a very low relative area change $\Delta A/A$ during the phase transition of only 0.05 ± 0.01 for F6-DPPC bilayers, whereas DPPC exhibited a relative area change of 0.33 ± 0.02 (Figure 6.3 and Table 6.2). The main phase transition of the F6-DPPC bilayer spans over a temperature range of nearly 15°C and is thereby substantially broader than for DPPC bilayers (~ 8°C), as determined by the ellipsometric data (Figure 6.3). The main phase transition temperature was computed from the changes in bilayer thickness and from the relative area change $\Delta A/A$, to be 25.4 ± 1.2°C and 28.2 ± 1.1°C, respectively, using an empirical sigmoidal fitting function, in agreement with the values obtained by DSC. Interestingly, F6-DPPC exhibits a strong hysteresis effects between cooling and heating cycle in the regime of T_M.[34] The ellipsometric measurements of both the membrane thickness and the relative area of the F6-DPPC bilayer did not completely recover their initial values after a heating/cooling cycle (not shown).

lipid	T / °C	h / nm (ellipsometry)	h / nm (AFM)	$\Delta A/A$ (ellipsometry)
DPPC	60	3.4	-	0.35
F6-DPPC	35	3.9	4.1	0.05

Table 6.2. Thickness and relative area change during phase transition of DPPC and F6-DPPC bilayers

6.4 DISCUSSION

We have studied the structural elements of multilamellar bilayers of the fluorinated DPPC analog (F6-DPPC) in terms of hydrocarbon and fluorocarbon chain tilt angles using polarized ATR-FTIR spectroscopy and examined further the relative area change and the membrane thickness during the main phase transition of single solid supported bilayers of the respective lipids by means of temperature controlled ellipsometry and atomic force microscopy.

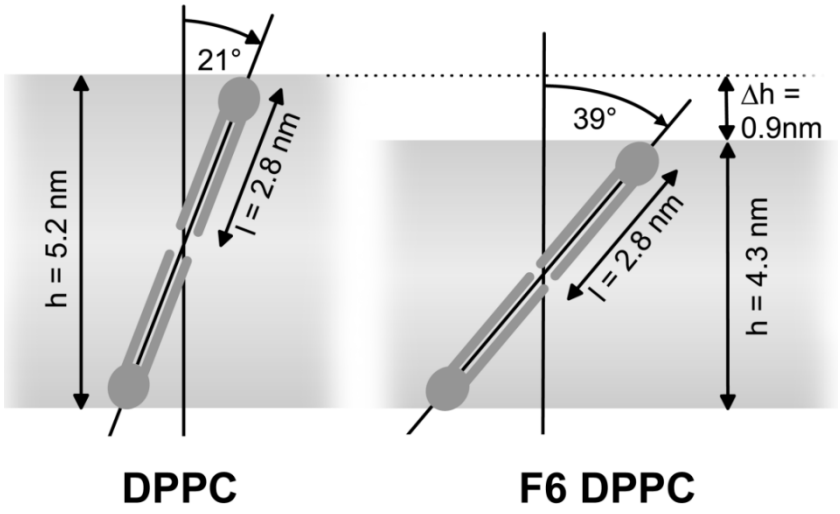

Figure 6.5. A simplified geometric model to relate the bilayer thickness *h* of DPPC and F6-DPPC with the apparent tilt angle Θ. Assuming the same empirical linear length *l* of 2.8 nm for both the DPPC and F6-DPPC lipid molecules the bilayer thickness *h* is calculated in this simplified model as 2·*l*cos Θ.

A major structural difference between DPPC and its fluorinated analogs with respect to the bilayer structure is the strongly increased chain tilt angle θ relative to the bilayer normal. Polarized ATR-FTIR data indicate a chain tilt angle of 39° in F6-DPPC bilayers, which is 18° higher than that found for DPPC bilayers (21°). The chain tilt angle of 21° for dry multilamellar DPPC bilayers agrees with previously published data provided by Katsaras et al.[32, 44] who reported a tilt angle of the DPPC chain segment of 22° at 0% relative humidity (RH) using X-ray diffraction.

This increase of the tilt angle was accompanied by a reduction of bilayer thickness. Both imaging ellipsometry and AFM on single bilayers indicate a step height approximately 1 nm

lower in F6-DPPC than in DPPC bilayers. Using as a rough approximation very simple geometric considerations as depicted in Figure 6.5, this decreased bilayer thickness of F6-DPPC can be fully accounted for by the increased chain tilt angle (Table 6.1).

What is the physical reason for this altered lipid arrangement in the fluorinated DPPC bilayer as compared with DPPC? A likely explanation of this is depicted in the cartoon shown in Figure 6.6. It is well known, that the β (sn-1) and the γ (sn-3) hydrocarbon chains of diacyl phosphatidylcholines adopt a staggered conformation, resulting in a mutual offset of the terminal methyl groups of 0.25 nm.[45] In the fluorinated DPPC analogs such a staggered arrangement of β- and γ-chains would result in partial overlap of the terminal fluorocarbon moieties and the adjacent hydrocarbon segments of the chains and would thus, lead to the presence of a mixed fluorocarbon/hydrocarbon layer Δ in the lipid bilayer. Due to unfavorable fluorocarbon/hydrocarbon interaction, such a staggered conformation would be energetically unfavorable. We therefore propose that the chains adopt a different arrangement in the perfluoroalkylated lipids as compared to the non-fluorinated lipids to minimize these unfavorable interactions by avoiding chain staggering, which is commonly referred to as microphase separation. We assume that such a rearrangement of the chains can be achieved by specific rotamer populations in the glycerol moiety of the fluorinated lipids. In general, rotation about the glycerol backbone results in changes of chain staggering and possibly also leads to variations of the head group orientation.[46] Note that the increased tilt angle in the fluorinated DPPC analogs cannot be explained on the mere basis of an altered cross-sectional area of the fluorocarbon chain segments. Based on data provided by Tamada et al. [14] the cross sectional area of the fluorocarbon chain segment is increased to 30 Å2 compared to 20 Å2 for the cross sectional area of a hydrocarbon chain segment. An increase of the cross sectional area of the chains relative to that of the headgroups should, however, lead to a decrease of the tilt angle, in contradiction to the experimental findings.

An astonishing property of the fluorinated lipids is the large upshift of the CH2 stretching vibration during chain melting. The observed shift of 4.7 cm^{-1} during the phase transition of F6-DPPC is relatively large as compared with unfluorinated PCs, which are reported to be less than 3.0 cm^{-1} for egg PC [47] and DPPC [48, 49], covering a similar temperature difference. Since the fluorocarbon moiety of the chain has a larger cross-sectional area than the adjacent hydrocarbon moiety, the free volume for the hydrocarbon segments of the chains

can be assumed to be substantially larger than in unfluorinated bilayers. This increased free volume in the fluorinated bilayers increases the probability of gauche conformations in the hydrocarbon segments relative to bilayers of lipids with pure hydrocarbon chains, which is directly related to the increased band shift of CH2 stretching vibrations during the transition from the gel to the fluid phase. Molecular dynamic simulations of DPPC further revealed that the probability of gauche conformations is enhanced near the glycerol backbone.[50] This may further add to an increased relative population of gauche defects in F6-DPPC (where the 5 distal methylene groups per chain are replaced by CF2 groups) as compared with DPPC. In the CF2 chain, however, gauche conformations are inhibited due to steric clash of the larger fluorine substituents.[51]

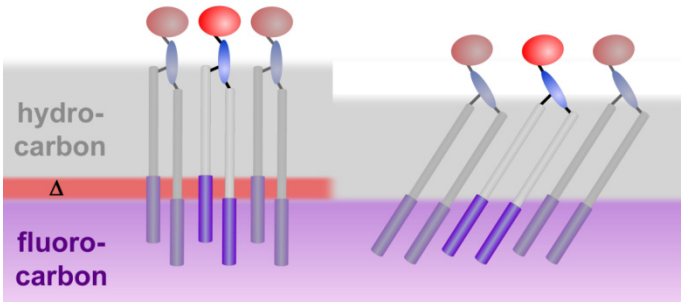

Figure 6.6. A staggered chain conformation as it is assumed in DPPC would involve unfavorable interactions in the fluorinated analogs due to mismatch between hydrocarbon and fluorocarbon moieties of the chains and hence the presence of a mixed hydrocarbon/fluorocarbon layer Δ. This mismatch is minimized by a change of the chain arrangement, presumably involving changes in the glycerol moiety as well. The increased chain tilting in fluorinated DPPC is therefore suggested to be driven by unfavorable hydrocarbon/fluorocarbon interactions.

The unusual thermotropic properties of the fluorinated PCs can as well be understood in terms of an increased free volume of the hydrocarbon segments due to the increased cross-sectional area of the adjacent fluorocarbon segments as compared to the hydrocarbon analog. The relative area change $\Delta A/A$ of lipid bilayers during the main phase transition is mainly caused by the occurrence of tgt kinks and gauche defects. In the fluid phase, DPPC chains are expected to have 3.9 gauche defects per chain at 50°C,[52] resulting in a relative area change of more than 30% during TM. In the F6-DPPC bilayers, the perfluoroalkylated chain segments appear to provide enough free volume for gauche populations in the

adjacent hydrocarbon segments to diminish the relative area change substantially, such that a $\Delta A/A$ of only 5% is observed for F6-DPPC during the transition to the fluid phase. The same effect, a larger free volume accessible to the hydrocarbon segment in the fluorinated bilayer should also interfere with the usually occurring tight packing of the chains in the gel phase and decrease the enthalpy penalty for gauche conformations, thereby contributing to the considerable lowering of both the temperature and enthalpy of the phase transition of F6-DPPC as compared to DPPC.

6.5 CONCLUSIONS

Lipids with terminally perfluoroalkylated chains have interesting bilayer properties, such as formation of highly stable vesicles[1, 2] and a very distinctive domain formation in mixtures,[17, 53] which make them promising candidates for a range of biomedical applications[1, 9, 17, 54] and possible tools for clustering of ligand on liposome surfaces.[18-21] Using polarized ATR-FTIR, imaging ellipsometry, and AFM in fluids, we have investigated structural and physical properties of bilayers of a fluorinated DPPC analog. The considerably increased tilt angle of the chains and the resulting reduced thickness of the fluorinated bilayers is presumably related to the minimization of unfavorable fluorocarbon/hydrocarbon interaction, leading to microphase separation. The decreased phase transition temperature on the one hand and the drastically reduced thermal expansion and thickness change during the main phase transition of the fluorinated bilayers, on the other hand, can be understood in terms of an increased free volume accessible to the hydrocarbon chain segments due to the larger cross-sectional area of the adjacent fluorocarbon segments.

6.6 REFERENCES

[1] Santaella, C.; Vierling, P. and Riess, J. G. Highly stable liposomes from fluoroalkylated glycerophosphoquinolines. *Angew. Chem., Int. Ed.* **1991**, 30, 567-568.

[2] Santaella, C.; Vierling, P. and Riess, J. G. New perfluoroalkylated phospholipids as injectable surfactants: synthesis, preliminary physicochemical and biocompatibility data. *New Journal of Chemistry* **1991**, 15, 685-692.

[3] Santaella, C.; Vierling, P.; Riess, J. G.; Gulik-Krzywicki, T.; Gulik, A. and Monasse, B. Polymorphic phase behavior of perfluoroalkylated phosphatidylcholines. *Biochimica et Biophysica Acta (BBA) - Biomembranes* **1994**, 1190, 25-39.

[4] Frezard, F.; Santaella, C.; Vierling, P. and Riess, J. G. Permeability and stability in buffer and in human serum of fluorinated phospholipid-based liposomes. *Biochimica et Biophysica Acta, Biomembranes* **1994**, 1192, 61-70.

[5] Frezard, F.; Santaella, C.; Montisci, M. J.; Vierling, P. and Riess, J. G. Fluorinated phosphatidylcholine-based liposomes: H+/Na+ permeability, active doxorubicin encapsulation and stability in human serum. *Biochimica et Biophysica Acta, Biomembranes* **1994**, 1194, 61-68.

[6] Santaella, C. and Vierling, P. Molecular order and mobility within liposomal membrane made from highly fluorinated phospholipids. *Chemistry and Physics of Lipids* **1995**, 77, 173-177.

[7] Gadras, C.; Santaella, C. and Vierling, P. Improved stability of highly fluorinated phospholipid-based vesicles in the presence of bile salts. *Journal of Controlled Release* **1999**, 57, 29-34.

[8] Rolland, J.-P.; Santaella, C. and Vierling, P. Molecular packing of highly fluorinated phosphatidylcholines in monolayers. *Chemistry and Physics of Lipids* **1996**, 79, 71-77.

[9] McIntosh, T. J.; Simon, S. A.; Vierling, P.; Santaella, C. and Ravily, V. Structure and interactive properties of highly fluorinated phospholipid bilayers. *Biophysical Journal* **1996**, 71, 1853-1868.

[10] Allara, D. L. and Swalen, J. D. An infrared reflection spectroscopy study of oriented cadmium arachidate monolayer films on evaporated silver. *J. Phys. Chem.* **1982**, 86, 2700-2704.

[11] Chau, L.-K. and Porter, M. D. Composition and structure of spontaneously adsorbed monolayers of n-perfluorocarboxylic acids on silver. *Chemical Physics Letters* **1990**, 167, 198-204.

[12] Frey, S.; Heister, K.; Zharnikov, M.; Grunze, M.; Tamada, K.; Colorado, R., Jr.; Graupe, M.; Shmakova, O. E. and Lee, T. R. Structure of self-assembled monolayers of semifluorinated alkanethiols on gold and silver substrates. *Israel Journal of Chemistry* **2000**, 40, 81-97.

[13] Naselli, C.; Swalen, J. D. and Rabolt, J. F. Order--disorder transitions in Langmuir--Blodgett films. IV. Structure of $(F(CF_2)_8(CH_2)_{10}COO^-)_2$ Cd^{2+} multilayers at ambient and elevated temperatures. *The Journal of Chemical Physics* **1989**, 90, 3855-3860.

[14] Tamada, K.; Ishida, T.; Knoll, W.; Fukushima, H.; Colorado, R.; Graupe, M.; Shmakova, O. E. and Lee, T. R. Molecular Packing of Semifluorinated Alkanethiol Self-Assembled Monolayers on Gold: Influence of Alkyl Spacer Length. *Langmuir* **2001**, 17, 1913-1921.

[15] Tsao, M. W.; Hoffmann, C. L.; Rabolt, J. F.; Johnson, H. E.; Castner, D. G.; Erdelen, C. and Ringsdorf, H. Studies of Molecular Orientation and Order in Self-Assembled Semifluorinated n-Alkanethiols: Single and Dual Component Mixtures. *Langmuir* **1997**, 13, 4317-4322.

[16] Ren, Y.; Iimura, K. i.; Ogawa, A. and Kato, T. Surface Micelles of CF3(CF2)7(CH2)10COOH on Aqueous La3+ Subphase Investigated by Atomic Force Microscopy and Infrared Spectroscopy. *J. Phys. Chem. B* **2001**, 105, 4305-4312.

[17] Yoder, N. C.; Kalsani, V.; Schuy, S.; Vogel, R.; Janshoff, A. and Kumar, K. Nanoscale Patterning in Mixed Fluorocarbon-Hydrocarbon Phospholipid Bilayers. *J. Am. Chem. Soc.* **2007**, 129, 9037-9043.

[18] Rai, P. R.; Saraph, A.; Ashton, R.; Poon, V.; Mogridge, J. and Kane, R. S. Raftlike Polyvalent Inhibitors of the Anthrax Toxin: Modulating Inhibitory Potency by Formation of Lipid Microdomains. *Angewandte Chemie International Edition* **2007**, 46, 2207-2209.

[19] Rai, P.; Padala, C.; Poon, V.; Saraph, A.; Basha, S.; Kate, S.; Tao, K.; Mogridge, J. and Kane, R. S. Statistical pattern matching facilitates the design of polyvalent inhibitors of anthrax and cholera toxins. *Nat Biotech* **2006**, 24, 582-586.

[20] Nam, J. M.; Nair, P. M.; Neve, R. M.; Gray, J. W. and Groves, J. T. A Fluid Membrane-Based Soluble Ligand-Display System for Live-Cell Assays. *ChemBioChem* **2006**, 7, 436-440.

[21] Gege, C.; Schneider, M. F.; Schumacher, G.; Limozin, L.; Rothe, U.; Bendas, G.; Tanaka, M. and Schmidt, R. R. Functional Microdomains of Glycolipids with Partially Fluorinated Membrane Anchors: Impact on Cell Adhesion (ChemPhysChem 2/2004). *ChemPhysChem* **2004**, 5, 157.

[22] Charrier, A. and Thibaudau, F. Main Phase Transitions in Supported Lipid Single-Bilayer. *Biophys. J.* **2005**, 89, 1094-1101.

[23] Feng, Z. V.; Spurlin, T. A. and Gewirth, A. A. Direct Visualization of Asymmetric Behavior in Supported Lipid Bilayers at the Gel-Fluid Phase Transition. *Biophys. J.* **2005**, 88, 2154-2164.

[24] Keller, D.; Niels, B. L.; Ian, M. M. and Ole, G. M. Decoupled Phase Transitions and Grain-Boundary Melting in Supported Phospholipid Bilayers. *Physical Review Letters* **2005**, 94, 025701.

[25] Leonenko, Z. V.; Finot, E.; Ma, H.; Dahms, T. E. S. and Cramb, D. T. Investigation of Temperature-Induced Phase Transitions in DOPC and DPPC Phospholipid Bilayers Using Temperature-Controlled Scanning Force Microscopy. *Biophys. J.* **2004**, 86, 3783-3793.

[26] Xie, A. F.; Yamada, R.; Gewirth, A. A. and Granick, S. Materials Science of the Gel to Fluid Phase Transition in a Supported Phospholipid Bilayer. *Physical Review Letters* **2002**, 89, 246103.

[27] Harrick, N. J. Internal Reflection Spectroscopy. *John Wiley & Sons, New York* **1967**.

[28] Tamm, L. K. and Tatulian, S. A. Infrared spectroscopy of proteins and peptides in lipid bilayers. *Quarterly reviews of biophysics* **1997**, 30, 365-429.

[29] Goormaghtigh, E.; Raussens, V. and Ruysschaert, J. M. Attenuated total reflection infrared spectroscopy of proteins and lipids in biological membranes. *Biochimica et biophysica acta* **1999**, 1422, 105-185.

[30] Yi, P. N. and MacDonald, R. C. Temperature dependence of optical properties of aqueous dispersions of phosphatidylcholine. *Chemistry and Physics of Lipids* **1973**, 11, 114-134.

[31] Fahmy, K.; Siebert, F.; Grossjean, M. F. and Tavan, P. Photoisomerization in bacteriorhodopsin studied by FTIR, linear dichroism, and photoselection experiments combined with quantum chemical theoretical analysis. *Journal of Molecular Structure* **1989**, 214, 257-288.

[32] Katsaras, J. Structure of the Subgel and Gel Phases of Oriented Dipalmitoylphosphatidylcholine Multibilayers. *J. Phys. Chem.* **1995**, 99, 4141-4147.

[33] Nagle, J. F. and Tristram-Nagle, S. Structure of lipid bilayers. *Biochimica et Biophysica Acta (BBA) - Reviews on Biomembranes* **2000**, 1469, 159-195.

[34] Schuy, S. and Janshoff, A. Thermal expansion of microstructured DMPC bilayers quantified by temperature-controlled atomic force microscopy. *ChemPhysChem* **2006**, 7, 1207-1210.

[35] Schuy, S. and Janshoff, A. Microstructuring of phospholipid bilayers on gold surfaces by micromolding in capillaries. *Journal of Colloid and Interface Science* **2006**, 295, 93-99.

[36] Janshoff, A. and Kunneke, S. Micropatterned solid-supported membranes formed by micromolding in capillaries. *European Biophysics Journal* **2000**, 29, 549-554.

[37] Kunneke, S. and Janshoff, A. Visualization of molecular recognition events on microstructured lipid-membrane compartments by in situ scanning force microscopy. *Angewandte Chemie, International Edition* **2002**, 41, 314-316.

[38] Faiss, S.; Schuy, S. and Janshoff, A. Phase Transition of Individually Adressabe Microstructured Membranes Visualized by Imaging Ellipsometry. *J. Phys. Chem. (in press)* **2007**.

[39] Gang, J.; Roger, J. and Hans, A. Imaging ellipsometry revisited: Developments for visualization of thin transparent layers on silicon substrates. *Review of Scientific Instruments* **1996**, 67, 2930-2936.

[40] Kim, Y. T.; Allara, D. L.; Collins, R. W. and Vedam, K. Real-time spectroscopic ellipsometry study of theelectrochemical deposition of polypyrrole thin films. *Thin Solid Films* **1990**, 193-194, 350-360.

[41] Reiter, R.; Motschmann, H.; Orendi, H.; Nemetz, A. and Knoll, W. Ellipsometric microscopy. Imaging monomolecular surfactant layers at the air-water interface. *Langmuir* **1992**, 8, 1784-1788.

[42] Vedam, K. Spectroscopic ellipsometry: a historical overview. *Thin Solid Films* **1998**, 313-314, 1-9.

[43] Ganchev, D. N.; Hasper, H. E.; Breukink, E. and deKruijff, B. Size and Orientation of the Lipid II Headgroup As Revealed by AFM Imaging. *Biochemistry* **2006**, 45, 6195-6202.

[44] Katsaras, J.; Yang, D. S. and Epand, R. M. Fatty-acid chain tilt angles and directions in dipalmitoyl phosphatidylcholine bilayers. *Biophys. J.* **1992**, 63, 1170-1175.

[45] Wiederschain, G. Y. The structure of biological membranes, edited by P.L. Yeagle *(2nd edn., CRC Press, Boca Raton-London-New York-Singapore)*. **2005**; Vol. 71, p 345.

[46] Hauser, H.; Pascher, I. and Sundell, S. Preferred conformation and dynamics of the glycerol backbone in phospholipids. An NMR and x-ray single-crystal analysis. *Biochemistry* **1988**, 27, 9166-9174.

[47] Popova, A. V. and Hincha, D. K. Intermolecular Interactions in Dry and Rehydrated Pure and Mixed Bilayers of Phosphatidylcholine and Digalactosyldiacylglycerol: A Fourier Transform Infrared Spectroscopy Study. *Biophys. J.* **2003**, 85, 1682-1690.

[48] Nabet, A.; Boggs, J. M. and Pezolet, M. Study by Infrared Spectroscopy of the Interdigitation of C26:0 Cerebroside Sulfate into Phosphatidylcholine Bilayers. *Biochemistry* **1996**, 35, 6674-6683.

[49] Binder, H. Infrared dichroism investigations on the acyl chain ordering in lamellar structures III. Characterisation of the chain tilt and biaxiality in the solid phases of

dipalmitoylphosphatidylcholine as a function of temperature and hydration using molecular order parameters. *Vibrational Spectroscopy* **1999**, 21, 151-163.

[50] Smondyrev, A. M. and Berkowitz, M. L. Molecular dynamics study of Sn-1 and Sn-2 chain conformations in dipalmitoylphosphatidylcholine membranes. *Journal of Chemical Physics* **1999**, 110, 3981-3985.

[51] Rabolt, J. B. and Fanconi, B. Longitudinal acoustic mode in helical polymers: poly(oxymethylene) and isotactic polypropylene. *Journal of Polymer Science, Polymer Letters Edition* **1977**, 15, 121-127.

[52] Douliez, J. P.; Leonard, A. and Dufourc, E. J. Restatement of order parameters in biomembranes: calculation of C-C bond order parameters from C-D quadrupolar splittings. *Biophys. J.* **1995**, 68, 1727-1739.

[53] Schneider, M. F.; Andelman, D. and Tanaka, M. Stripes of partially fluorinated alkyl chains: Dipolar Langmuir monolayers. *The Journal of Chemical Physics* **2005**, 122, 094717-094715.

[54] Ravily, V.; Santaella, C. and Vierling, P. Membrane permeability and stability in buffer and in human serum of fluorinated di-O-alkylglycerophosphocholine-based liposomes. *Biochimica et Biophysica Acta, Biomembranes* **1996**, 1285, 79-90.

6.7 APPENDIX AND ADDITIONAL DATA

A

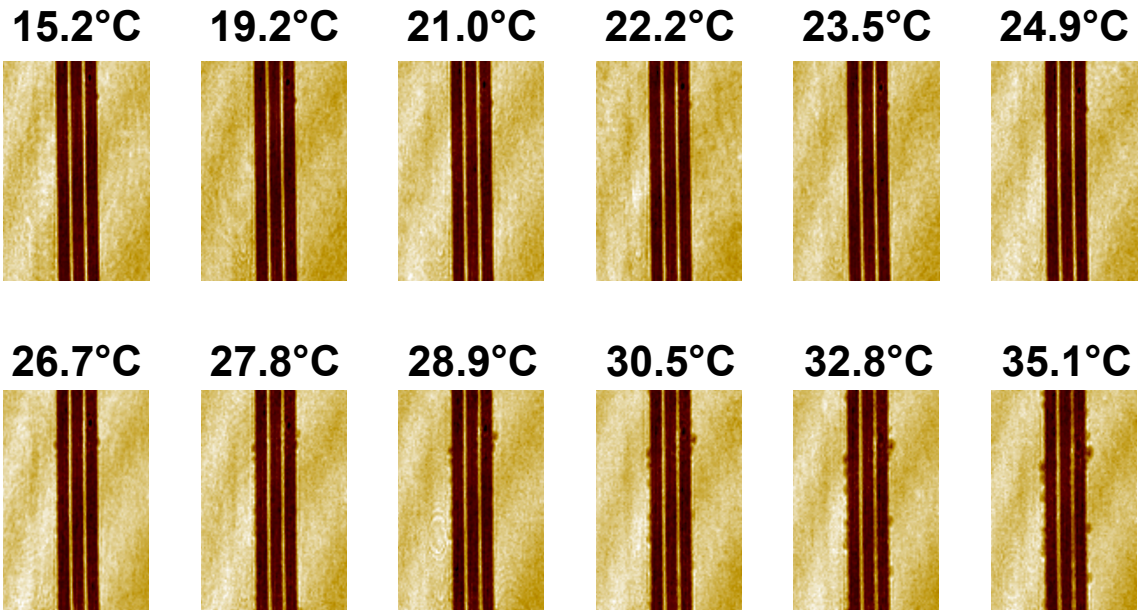

Appendix A. Delta-maps obtained from imaging ellipsometry of microstructured F6-DPPC bilayers in Tris buffer (10 mM Tris, 100 mM NaCl, pH = 7.4) at rising temperatures.

B

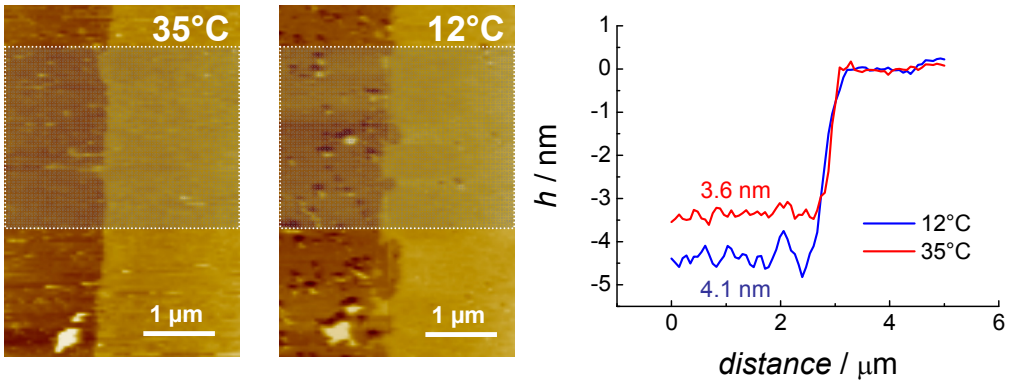

Appendix B. AFM images of microstructured F4-DPPC on glass at a microstructured lipid bilayer taken at 12°C and 35°C assuming that the bilayer is in the gel-phase or in the fluid crystalline phase respectively. The highlighted area in the center of the image marks the area from with the averaged line scan was calculated.

C

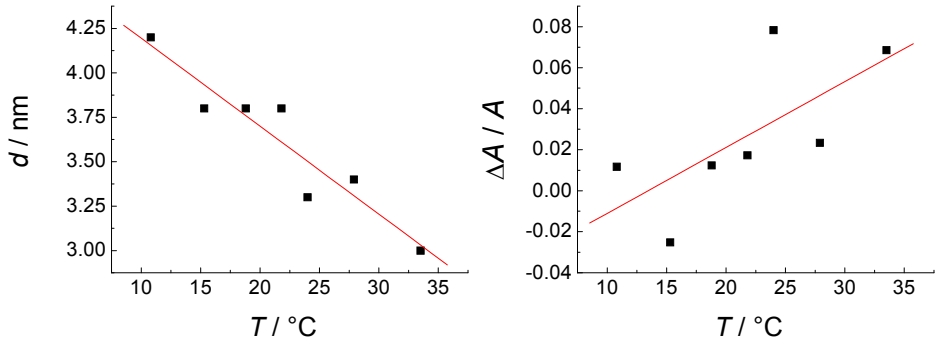

Appendix C. Absolute change in bilayer thickness *d* and relative area change Δ*A*/*A* of microstructured F4-DPPC compartments upon heating. Melting of the bilayer exhibits virtually no cooperativity and transition temperatures can not be determined accurately. The decrease in the bilayer thickness from the gel to the fluid phase was estimated to be 0.6 nm and the maximal thermal expansion was 8 %.

D

lipid	Θ / ° [1] (gel, dry film)	*h* / nm (ellipsometry)	*h* / nm (AFM)	*h* / nm [2] (calculated)
F4-DPPC	40	3.9	4.1	4.3

Appendix D. Tilt angles and thickness of F4-DPPC bilayers at room temperature.

E

lipid	*T* / °C	*h* / nm (ellipsometry)	*h* / nm (AFM)	Δ*A*/*A* (ellipsometry)
F4-DPPC	35	3.1	3.6	0.08

Appendix E. Thickness and relative area change of F4-DPPC bilayers during phase transition.

CHAPTER VII

7 THERMAL EXPANSION OF MICROSTRUCTURED DMPC BILAYERS QUANTIFIED BY TEMPERATURE CONTROLLED ATOMIC FORCE MICROSCOPY

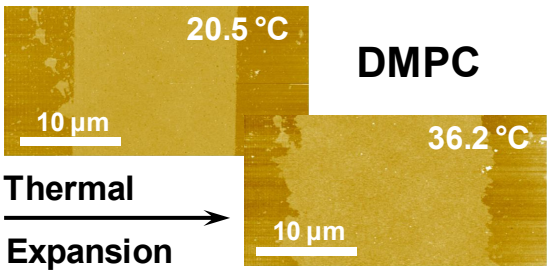

ABSTRACT

We have analyzed the thermal expansion of a 1,2-dimyristoyl-*sn*-glycero-3-phosphocholine (DMPC) bilayer by means of temperature controlled atomic force microscopy, utilizing the concept of microstructured lipid bilayers. Our experiment elucidates the strong increase in area per lipid molecule from the gel to the fluid phase transition, resulting in an increase of fractional area ΔA / A_{ave} of the lipid bilayer of 0.24 and a decrease in bilayer thickness of 1 nm. The main phase transition temperature was extracted from the relative area change ΔA / A_{ave} in the region of T_m. We could show that the main phase transition temperature of the solid supported DMPC bilayer was shifted to higher temperatures, accompanied by a strong broadening of T_M. Furthermore, we have analyzed the fluctuation amplitude of the boundaries of the bilayer structure, revealing a distinctive increase, matching the transition point.

7.1 INTRODUCTION

Solid supported membranes (SSMs) are an invaluable tool to study protein adsorption, peptide-membrane-interactions, ion transport, lateral inhomogeneities, phase transitions, and mechanical properties with the objective to mimic processes that usually occur at cellular membranes. As a prerequisite it is necessary to determine and control the physical and chemical properties of the model membranes in which fluidity, lateral organization, main phase transition temperature and composition play a pivotal role in imitating biological membranes to the highest possible extend. It was found that confined lipid bilayers exhibit significantly different thermomechanical and electrical properties as compared to free-standing bilayers due to pronounced lipid substrate interactions.[1-4] Recently, a series of papers has been published on the measurement of the main phase transition temperature (T_m) of solid supported phospholipid bilayers by means of temperature controlled atomic force microscopy.[5-13] Knowledge of T_M is pivotal if lateral organization, fluidity and elasticity are of interest or need to be adjusted. The findings so far are contradictory. Melting temperature and broadness of the melting transition of SSMs are reported to either perfectly reproduce the results obtained from vesicular systems[6, 8] or in contrary display a substantial increase in T_m accompanied by a large broadening of the transition of a few degrees.[7, 9, 11] Decoupling of the two leaflets as reported by Feng et al.[5] might explain the occurrence of the broad transition of various phosphocholine membranes. The authors found two independently melting monolayers, in which the T_M value of the surface confined monolayer is shifted to higher temperatures (5°C) employing atomic force microscopy (AFM) height analysis. Bilayer thickness as a function of temperature is frequently used as a measure of the chain melting process during the main phase transition from the gel phase (L_C) to the fluid crystalline phase (L_α).[5, 8-12] Apart from height analysis, thermal expansion during the heating or the cooling of the SSMs, which can be detected as a closing or opening of defect areas within the SSM, is also used to extract thermodynamic quantities from temperature controlled AFM.[5-13] Measuring thermal expansion directly upon heating is, however, hampered by lack of free area and only few studies provide quantitative information.[7, 8]

Our approach targets detection and quantification of the thermal expansion of SSMs during the main phase transition by means of temperature controlled AFM utilizing microstructured bilayers. The great benefit of a microstructured bilayer is the distinct geometry on a large length scale (~ 1 mm), which allows us to precisely determine the thermal expansion of the lipid over a large temperature interval as well as to quantify fluctuations at the boundary as a function of temperature. Moreover, microstructured bilayers exhibit the required free area for the bilayer to expand upon heating.

7.2 MATERIALS AND METHODS

7.2.1 LIPIDS AND VESICLE PREPARATION

Lipids were used without further purification to prepare films consisting of 1,2-dimyristoyl-*sn*-glycero-3-phosphocholine (DMPC, Avanti Polar Lipids, Alabaster, Al, USA) doped with 1 mol% Texas-Red DHPE (Molecular Probes, Eugene, Ore., USA). Small unilamellar vesicles were prepared by tip sonification of multilamellar vesicles in Tris-buffer (10 mM Tris, 100 mM NaCl, 0.2 mM $CaCl_2$, pH = 7.4) for 2 $\times$ 20 min (cp. 3.2).

7.2.2 MICROSTRUCTURING OF DMPC BILAYERS ON GLASS

PDMS stamps displaying a hydrodynamically coupled network of capillaries were prepared following the general procedure established by Whitesides and coworkers [14, 15]. Separate trenches were molded into a polydimethylsiloxane (PDMS) elastomer using a silicon wafer as the master structure. For further description of the geometric design of the master structure, please refer to.[16, 17] Briefly, the capillary structures in the experiments are 15 µm wide, 3 µm in height and 2 mm long. The 5 parallel aligned capillaries are divided by a 5 µm spacing ending on either side in flow pads of 2.13 $\times$ 2.13 mm. For replication of the master structure a 10:1 mixture of Sylgard 184 and curing agent was cured at 60°C for 2 h. Injection of merely 0.05 µl solution was necessary to fill the capillaries.

The surface of the PDMS stamp was activated, in order to achieve a strong but reversible binding of the mold to the gold surface. For this purpose, reactive hydroxyl groups were formed on the PDMS surface by exposing the elastomer to oxygen plasma for 30 seconds. Immediately after plasma oxidization the stamp was placed under slight load forces on a

cover slip (Plano, Wetzlar, Germany). Prior the cover slip was treated two times in an ultra sonic bath with aqueous 1% Hellmanex solution at 65°C for 15 minutes and thoroughly rinsed with deionized water. The pretreatment of the PDMS stamp and the glass substrate enables a strong but reversible seal between stamp and glass.

7.2.3 ATOMIC FORCE MICROSCOPY

Imaging was performed in liquid tapping mode at steady temperature on a commercial scanning force microscope (Dimension 3100 with Nanoscope IIIa+A/D controller, Veeco Digital Instruments, Santa Barbara, CA, USA) as described previously (cp. 5.2). The ratio of the damped and free cantilever oscillation amplitude A_{sp}/A_0 during imaging was adjusted to 0.85 after the probe engagement of the sample surface. All images were 30 µm × 30 µm in size and taken at a scan rate of 2 Hz and were post-processed using SPIP^{TM} image processing software (Version 2.2002, Image Metrology, Lyngby, Denmark). All images were cut to 15 µm × 30 µm prior to image processing at one specific position and data acquisition to yield a comparable sector of the image.

7.2.4 FLUCTUATION ANALYSIS

Fluctuation analysis was carried out using Tracer 1.7 software, which provides a listing of relevant (x,y) data points extracted from the image in ascii format. Therefore, all images were converted into 1 bit black and white images using Corel Draw 11.0 software and the interesting area was analyzed by the Tracer software, obtaining analyzable boundary fluctuations (figure 7.4 A). The squared standard deviation (σ^2) of the fluctuation amplitude was determined by statistical analyses using Origin 6.1 software

7.3 RESULTS AND DISCUSSION

A microstructured 1,2-dimyristoyl-*sn*-glycero-3-phospocholine (DMPC) bilayer prepared by micromolding in capillaries[16, 17] was imaged by means of temperature controlled AFM while exposed to heating and cooling cycles. Figure 7.1 displays a set of AFM images of a microstructured DMPC bilayer taken at different temperatures, i.e. heating the sample from 15.6°C to 36.2°C followed by cooling it from 32.1°C to 16.6°C.

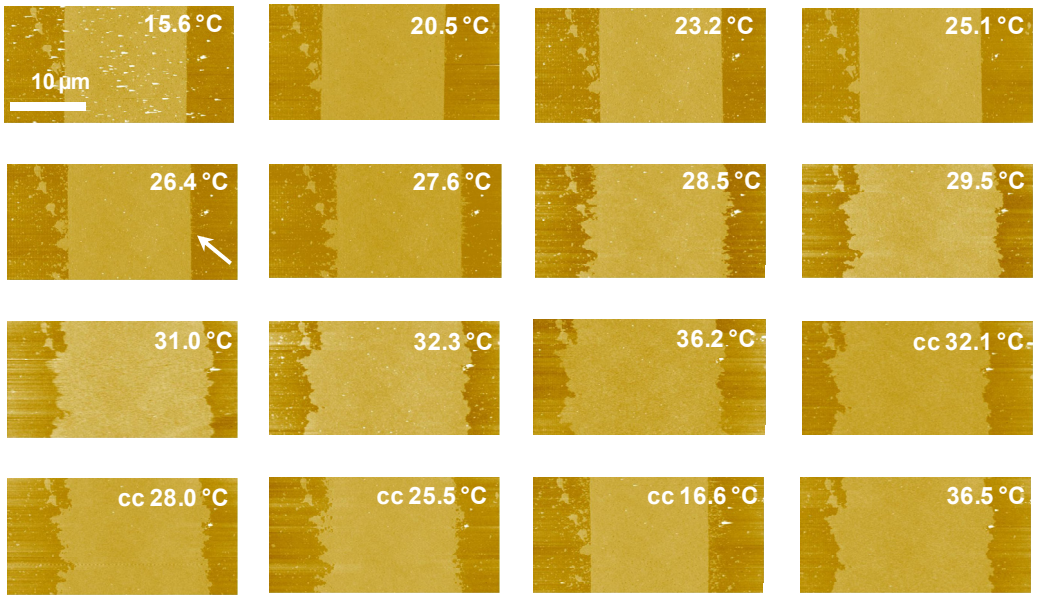

Figure 7.1. Tapping-mode AFM images (size: 30 µm × 15µm, z-scale: 30 nm) of a microstructured DMPC bilayer in Tris-Buffer (10 mM Tris, 100 mM NaCl, 0.2 mM CaCl2, pH = 7,4) following a given temperature profile. All images show the same sector of the sample at different temperatures.

The average width of the structure at low temperatures was determined to be (15.6 ± 0.1) µm in good agreement with the nominal channel width of the microfluidic network (15.0 µm). Characteristic lipid patches, visible on the left hand side of the bilayer stripe facilitate to locate the exact position of the image and its the magnification, producing images of the same size and position (figure 7.1). The values for the surface coverage, i.e. the area occupied by the DMPC bilayer, were determined through histogram analysis of the image (figure 7.2).

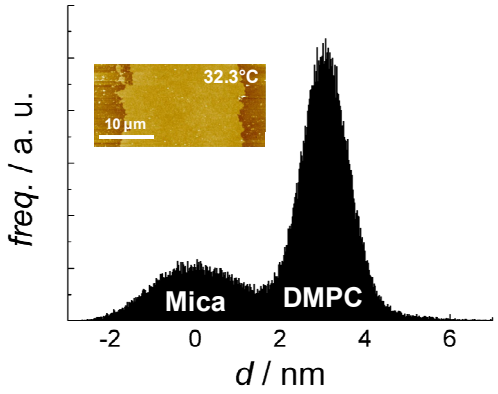

Figure 7.2. Representative height histogram of the image taken at 32.3°C. The original AFM image is shown in the inset.

At low temperature (15.6°C) we found an average bilayer thickness d_{ave} of (4.70 ± 0.02) nm in good agreement with a study of Kolb and coworkers who found a bilayer thickness of 4.8 nm in the gel phase also employing AFM.[9, 12, 18] Upon heating, the structured bilayer maintains its initial surface coverage of (0.59 ± 0.03) and average thickness of (4.7 ± 0.02) nm up to 26.4°C. However, the AFM image at 26.4 °C shows already weak structural changes of the microstructured bilayer (arrow). For instance, the boundaries of the microstructured bilayer show first signs of fluctuations that grow in amplitude with temperature. From the AFM images we determined the fractional area $\Delta A/A_{ave} = (A_{ave}\text{-}A(T))/A_{ave}$ with A_{ave} the mean area of the DMPC bilayer measured at 15.6 °C and $A(T)$ the actual area at a given temperature. An average normalized area of $A_{ave}/A_{tot} = 0.51$ was found at 15.6 °C. Figure 7.3 A shows the change of $\Delta A/A_{ave}$ and the average bilayer thickness $d(T)$ as a function of temperature.

The bilayer thickness decreases during the transition from the L_C- to the L_α-phase from 4.7 nm (15 °C) to 3.6 nm (30 °C) in good accordance with data from literature. For instance, Nagle et al. found $d_{L\alpha} = 3.6$ nm for the bilayer in the fluid state using X-ray diffraction,[19, 20] while Tokumasu and Dvorak[9] reported an average thickness of 4.3 nm for DMPC in the gel phase but only 3.4 nm for the membrane in the fluid state using temperature controlled AFM. However, it is important to mention that indentation of the bilayer with the AFM tip is typically higher when the bilayer is the softer fluid-state as compared to the more rigid gel-

state. This might lead to an overestimation of the real height difference between the two phases.

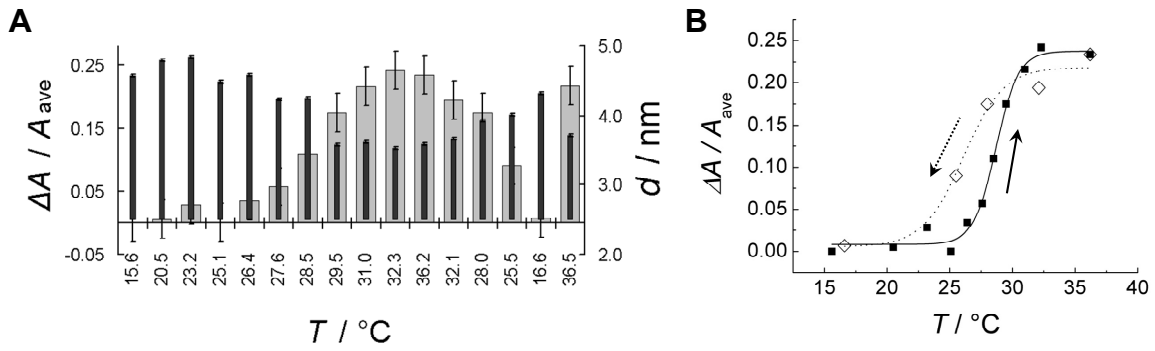

Figure 7.3. (A) Thermal expansion of the microstructured DMPC bilayer $\Delta A/A_{ave}$ (grey columns) and average bilayer thickness (black columns) of the bilayer as a function of temperature. The temperature axis displays the exact measured temperatures. (B) Relative area change of the DMPC bilayer during the gel-liquid phase transition upon heating (■) and cooling (◇). The lines correspond to empirical sigmoidal fits providing the transition temperature and the width of the phase transition. The phase transition temperature T_M obtained from the heating cycle amounts to (28.9± 0.1)°C (black line), while the T_M value extracted from the cooling cycle (dotted line) is substantially lower ((26.6 ± 1.4)°C).

Figure 7.3 B shows the fractional area $\Delta A/A_{ave}$ of the microstructured bilayer as a function of temperature in the region of the phase transition temperature. Heating the sample to higher values than 36 °C has little impact on the surface coverage suggesting that the melting of the DMPC bilayer is complete. We found a maximal relative area change $\Delta A_{max}/A_{ave}$ between the fluid and the gel-state of the membrane of (0.242 ± 0.03). The area-related thermal expansion during the main phase transition of 1,2-dipalmitoyl-*sn*-glycero-3-posphocholine (DPPC) has been determined independently to be 0.246[21, 22] in very good agreement with our values using temperature controlled AFM of microstructured bilayers.

The main phase transition temperature can be readily determined from the relative area change $\Delta A/A_{ave}$ using a sigmoidal fitting function

$$\Delta A/A_{ave} = \Delta A_{max}/A_{ave}\left(1-\left(1+\exp(T-T_M/\Delta T_M)\right)^{-1}\right). \quad \textbf{(1)}$$

We found a T_M value at $\Delta A_{max}/2A_{ave}$ of (28.9 ± 0.1) °C with a width of $\Delta T_M = (0.9 \pm 0.1)°C$ for heating the DMPC bilayer (closed symbols). The transition region spans over a temperature interval of roughly 8 °C. The phase transition temperature of confined DMPC bilayers is shifted substantially to higher temperature as compared with calorimetric data for non-confined DMPC liposomes providing a main phase transition temperature of merely 22°C. Moreover, non-confined DMPC-bilayers exhibit a much sharper transition of over a temperature interval of only 1 °C as opposed to bilayers attached to a solid support. Therefore we attribute the broadening of the of the main phase transition largely to the interaction of the lipids with the glass substrate as argued by others.[8, 11,5, 9,5, 11, 23] Subsequent to the heating cycle the sample was cooled down back to low temperature conditions (16.6 °C) while taking AFM images in discrete temperature steps. The images obtained during the cooling cycle are labeled “cc” (figure 7.1). The change of the relative area as a function of temperature (figure 7.3 B) shows a distinct hysteresis between heating (closed symbols) and cooling (open symbols) of the sample. A shift in T_m of 1–2 °C to lower values is observed if the transition temperature is determined from the cooling cycle. Similar observations were reported by others using non structured membranes.[9, 11, 24, 25]

Alternatively to the relative area change one might as well use the bilayer thickness $d(T)$ as a measure of the phase transition temperature. Fitting the corresponding data with a sigmoidal equation provides a T_M value of (28.3 ± 0.4) °C and a transition width of ΔT_M = (0.9 ± 0.4) °C rendering both methods equally suited to extract the melting point of the lipid bilayer.

The formation of the ripple gel phase $P_{\beta'}$ as a pre-melting transition[12, 13] has not been detected throughout the experiment. The large image sizes and the surface roughness of the glass substrate impede the visualization of ripple phases, but we have experimental evidence from lipid patch analysis on mica at higher magnification that the $P_{\beta'}$ phase occurs during the melting process (results not shown) in accordance with the results of Kolb and coworkers.[12]

It is instructive to monitor not only changes in bilayer thickness and surface coverage, but also to evaluate fluctuations of the membrane / glass boundary. Figure 7.4 B shows that the

variance σ^2 obtained from contour line analysis of the boundary increases considerably within the phase transition regime (figure 7.4 A).

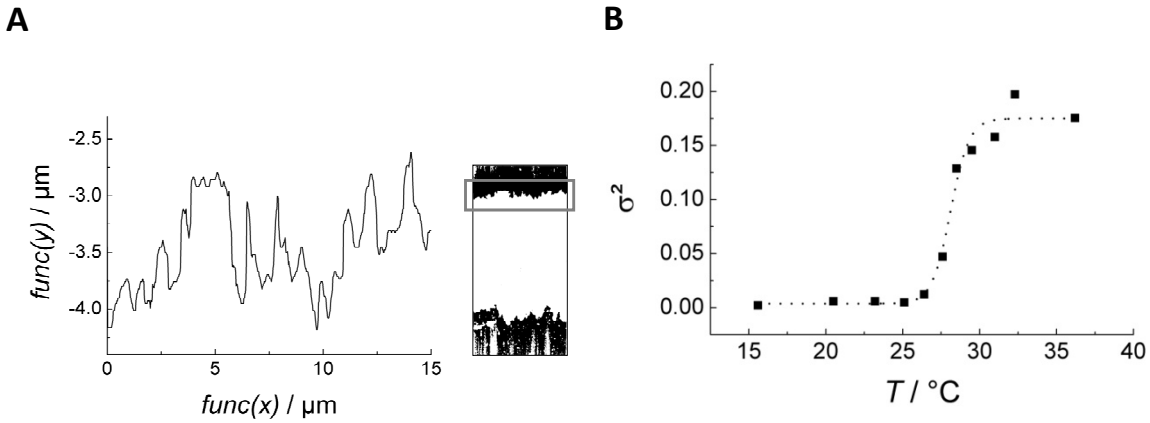

Figure 7.4. (A) Representative fluctuation analysis of the boundaries of the microstructured DMPC bilayer at 30°C. The inset shows the 1 bit black and white image of the original AFM image. The grey box highlights the area of interest, which was analysis to obtain the boundary fluctuations.

In fact, this type of analysis provides a reliable and slightly more accurate means to determine the transition temperature than employing changes in surface coverage or bilayer thickness. We found a main phase transition temperature of T_M = (28.1 ± 0.2) °C and $\Delta T_M = (0.6 \pm 0.2)°C$ using essentially the same empirical fitting function as for the surface coverage and bilayer thickness. Upon cooling, the fractal boundary of the liquid-crystalline DMPC bilayer shrinks back to adopt its initial shape exhibiting straight and well-defined margins with a bilayer thickness of (4.30 ± 0.02) nm. Back at low temperature (16.6 °C), the microstructured bilayer and the lipid patches on the left hand side of the structure occupy their initial shape, size and surface coverage of 0.56 ± 0.03. This indicates that the expansion of the microstructured DMPC bilayer is reversible and results from the thermal expansion of the lipid molecules in the membrane due to their strong increase of the degrees of freedom of the melted chain and thus, a less dense packing of the molecules.

Noteworthy, we found that thermal expansion of the bilayer is maximal if the area has been scanned with the AFM-tip for a few times. If we abolish tip-sample interaction by employing

non-contact mode by enhancing the *Q*-factor of the oscillation (*Q*-control) thermal expansion of the microstructured bilayer is rather small. This means that a finite tip bilayer interaction is necessary to overcome an energy barrier to allow the full thermal expansion of the bilayer. The origin of the energy barrier might be the lipid-substrate interaction, residual PDMS from the microfluidic network changing the surface tension of the glass substrate or the line tension of the bilayer. Hence, we expect the area expansion to be larger than computed from the area per molecule of the corresponding states of the bilayer due to excess of lipid originating from the lipid reservoir provided by the microstructured bilayer. As a consequence care must be taken when extraction thermodynamic data from the area expansion of the bilayer. However, the tip sample interaction does not affect the reversibility of expansion. Interestingly, the thickness of the bilayer is decreased upon heating above T_M to the same value whether expansion is observed or not. A closer look at the AFM-images reveals that the bilayer displays shape memory. Comparing the AFM images (figure 7.1) taken at 36.2°C with the one obtained at 36.6°C after experiencing a cooling cycle and heated back to elevated temperature, roughly the same shape of the boundary can be observed at the micrometer scale. The same behavior is found when comparing images taken at low temperatures. After heating the sample and cooling back down to ~ 16 °C the shape of the membrane stripe resembles – on the micrometer scale - that taken prior to the heating cycle (figure 7.1). In fact the image shows the same isolated patches as before (figure 7.1, upper left corner). It is conceivable that the individual patches are immobilized due to strong adsorption on particular pinning points. Occurrence of shape memory indicates the presence of preferred adsorption sites for the bilayer (pinning points) and a boundary influenced by the tip sample interaction, which ultimately limits the maximal expansion of the membrane.

7.4 CONCLUSIONS

In conclusion, the concept of microstructured lipid bilayers on solid supports in combination with temperature controlled AFM provides are versatile means to measure the structural changes, i.e. surface coverage, height and boundary fluctuations of bilayers as a function of temperature allowing for a precise determination of the phase transition temperature of solid supported membranes.

7.5 REFERENCES

[1] Heimburg, T. Mechanical aspects of membrane thermodynamics. Estimation of the mechanical properties of lipid membranes close to the chain melting transition from calorimetry. *Biochim. Biophys. Acta* **1998**, 1415, 147-162.

[2] White, S. H. and King, G. I. Molecular packing and area compressibility of lipid bilayers. *Proc. Natl. Acad. Sci. USA* **1985**, 82, 6532-6536.

[3] Lee, C.-H.; Lin, W.-C. and Wang, J. Using differential confocal microscopy to detect the phase transition of lipid vesicle membranes. *Opti. Engine.* **2001**, 40, 2077-2083.

[4] Raudino, A.; Zuccarello, F.; La Rosa, C. and Buemi, G. Thermal expansion and compressibility coefficients of phospholipid vesicles: experimental determination and theoretical modeling. *J. Phys. Chem.* **1990**, 94, 4217-4223.

[5] Feng, Z. V.; Spurlin, T. A. and Gewirth, A. A. Direct visualization of asymmetric behavior in supported lipid bilayers at the gel-fluid phase transition. *Biophys. J.* **2005**, 88, 2154-2164.

[6] Yarrow, F.; Vlugt, T. J. H.; van der Eerden, J. P. J. M. and Snel, M. M. E. Melting of a DPPC lipid bilayer observed with atomic force microscopy and computer simulation. *J. Cryst. Growth* **2005**, 275, e1417-e1421.

[7] Leonenko, Z. V.; Finot, E.; Ma, H.; Dahms, T. E. S. and Cramb, D. T. Investigation of temperature-induced phase transitions in DOPC and DPPC phospholipid bilayers using temperature-controlled scanning force microscopy. *Biophys. J.* **2004**, 86, 3783-3793.

[8] Xie, A. F.; Yamada, R.; Gewirth, A. A. and Granick, S. Materials Science of the Gel to Fluid Phase Transition in a Supported Phospholipid Bilayer. *Phys. Rev. Lett.* **2002**, 89, 246101-246104.

[9] Tokumasu, F.; Jin, A. J. and Dvorak, J. A. Lipid membrane phase behaviour elucidated in real time by controlled environment atomic force microscopy. *J. Elec. Micros.* **2002**, 51, 1-9.

[10] Keller, D.; Larsen, N. B.; Moeller, I. M. and Mouritsen, O. G. Decoupled Phase Transitions and Grain-Boundary Melting in Supported Phospholipid Bilayers. *Phys. Rev. Lett.* **2005**, 94, 025701/025701-025701/025704.

[11] Charrier, A. and Thibaudau, F. Main phase transitions in supported lipid single-bilayer. *Biophys. J.* **2005**, 89, 1094-1101.

[12] Enders, O.; Ngezahayo, A.; Wiechmann, M.; Leisten, F. and Kolb, H. A. Structural calorimetry of main transition of supported DMPC bilayers by temperature-controlled AFM. *Biophys. J.* **2004**, 87, 2522-2531.

[13] Kaasgaard, T.; Leidy, C.; Crowe, J. H.; Mouritsen, O. G. and Jorgensen, K. Temperature-controlled structure and kinetics of ripple phases in one- and two-component supported lipid bilayers. *Biophys. J.* **2003**, 85, 350-360.

[14] Xia, Y. and Whitesides, G. M. Soft Lithography. *Annual Review of Materials Science* **1998**, 28, 153-184.

[15] Kim, E.; Kia, Y. and Whitesides, G. M. Micromolding in Capillaries: Applications in Materials Science. *J. Am. Chem. Soc.* **1996**, 118, 5722.

[16] Schuy, S. and Janshoff, A. Microstructuring of phospholipid bilayers on gold surfaces by micromolding in capillaries. *J. Coll. Interf. Sci.* **2006**, 295, 93-99.

[17] Janshoff, A. and Kunneke, S. Micropatterned solid-supported membranes formed by micromolding in capillaries. *Euro. Biophys. J.* **2000**, 29, 549-554.

[18] Kucerka, N.; Kiselev, M. A. and Balgavy, P. Determination of bilayer thickness and lipid surface area in unilamellar dimyristoylphosphatidylcholine vesicles from small-angle neutron scattering curves: a comparison of evaluation methods. *Euro. Biophys. J.* **2004**, 33, 328-334.

[19] Nagle, J. F. and Tristram-Nagle, S. Structure of lipid bilayers. *Biochim. Biophys. Acta* **2000**, 1469, 159-195.

[20] Petrache, H. I.; Tristram-Nagle, S. and Nagle, J. F. Fluid phase structure of EPC and DMPC bilayers. *Chem. Phys. Lip.* **1998**, 95, 83-94.

[21] Nagle, J. F.; Zhang, R.; Tristram-Nagle, S.; Sun, W.; Petrache, H. I. and Suter, R. M. X-ray structure determination of fully hydrated L.a phase dipalmitoylphosphatidylcholine bilayers. *Biophys. J.* **1996**, 70, 1419-1431.

[22] Sun, W. J.; Tristram-Nagle, S.; Suter, R. M. and Nagle, J. F. Structure of gel phase saturated lecithin bilayers: temperature and chain length dependence. *Biophys. J.* **1996**, 71, 885-891.

[23] Yang, J. and Appleyard, J. The Main Phase Transition of Mica-Supported Phosphatidylcholine Membranes. *J. Phys. Chem. B* **2000**, 104, 8097-8100.

[24] Koynova, R. and Caffrey, M. Phases and phase transitions of the phosphatidylcholines. *Biochim. Biophys. Acta* **1998**, 1376, 91-145.

[25] Toombes, G. E. S.; Finnefrock, A. C.; Tate, M. W. and Gruner, S. M. Determination of La-HII phase transition temperature for 1,2-dioleoyl-sn-glycero-3-phosphatidylethanolamine. *Biophys. J.* **2002**, 82, 2504-2510.

CHAPTER VIII

8 IN SITU SYNTHESIS OF LIPOPEPTIDES AS VERSATILE RECEPTORS FOR THE SPECIFIC BINDING OF NANOPARTICLES AND LIPOSOMES TO SOLID SUPPORTED MEMBRANES

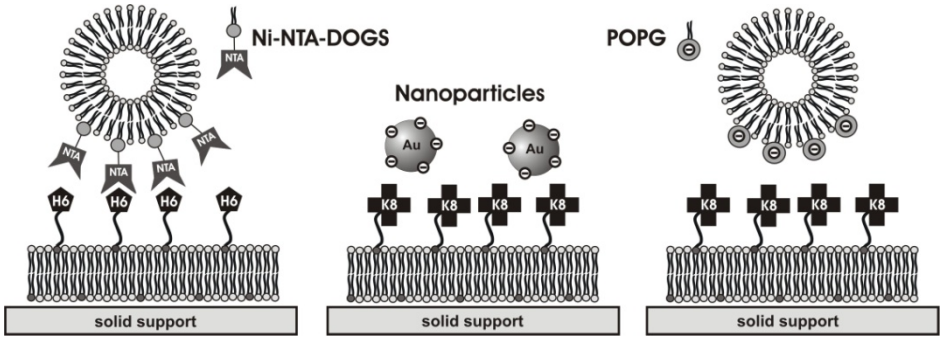

ABSTRACT

A detailed study of the in situ coupling of small peptides, such as $CGGH_6$ (H6) and $CGWK_8$ (K8) to maleimide functionalized phospholipid bilayers is presented. Surface reactions are monitored by quartz crystal microbalance, ellipsometry and atomic force as well as confocal laser scanning microscopy. Individually addressable microstructured membranes were employed to unequivocally probe the conjugation. We show that the in situ coupling of peptides via terminal cysteine moiety to maleimide functionalized phospholipids is a convenient and versatile way to selectively fabricate peptide modified phospholipid bilayers serving as specific receptor platforms for functionalized vesicles and nanoparticles. Specific adsorption of functional vesicles on the peptide modified bilayers is either achieved by means of histidine complexation with Ni-NTA-DOGS containing vesicles or electrostatic interaction between positively charged oligolysine bearing lipopeptides and negatively charged POPC/POPG vesicles. Furthermore, we found by means of fluorescence spectroscopy that peptide receptors are easily accessible from the aqueous phase and not buried within in the membrane interior.

8.1 INTRODUCTION

Biological membranes are mainly composed of phospholipids, sterols, proteins and glycolipids forming complex two dimensional aggregates that provide the structural and functional prerequisites for the existence of living cells. Membranes are the native environment for cell surface receptors and are thus, desired entities for quantifying ligand-receptor interactions and designing biosensor applications. Modeling of this sophisticated interface in a robust and versatile way requires strategies that involve highly advanced techniques that allow facile incorporating of receptor structures.

A large variety of different solid supported membranes have been developed since their invention in 1984.[1-5] Besides various different attachment schemes, microstructured lipid bilayers as first envisioned by Boxer,[6-12] Cremer,[13-19] and Janshoff[20-23] employing soft lithography and more recently dip-pen lithography[24] opened the field to chip-based array technology. While some of the above mentioned systems are routinely used for biophysical investigations of membrane-protein interactions, the main challenge is still the functional insertion of receptors with the goal to quantify the interaction of ligands with biological membranes. Transmembrane proteins are delicate to handle and rarely integrated in artificial bilayers. However, in most cases it is not necessary to integrate large proteins into lipid bilayers to display receptor moieties such as oligosaccharides or small peptide sequences serving as epitopes for ligands such as antibodies, toxins, or lectins. Instead, it is conceivable to create a platform based on preformed lipid bilayers on an arbitrary support that allows covalent coupling of the desired peptide sequence in situ, while monitoring the successful surface derivatization. A similar approach, employing membrane bound oligonucleotide for creating spatially encoded tethered vesicles on a solid supported fuid lipid bilayer, has recently been successfully established by Boxer and coworkers,[25-27] as well as by Höök and coworkers.[28] Both groups envision the strategy of tethered vesicles to be a direct route for preparing arrays of integral transmembrane proteins, allowing the investigation of integral transmembrane protein interactions with membranes under conditions that approach a native environment.

Since lipid bilayers are the native environment for cellular receptors, they ensure the integration of highly oriented receptors by coupling of the corresponding epitope to either lipid or protein anchors. Apart from orientation, solid supported lipid bilayers are known to

efficiently abolish unwanted adsorption of proteins to a much higher extend than PEGylated surfaces.[29, 30] Suppression of non-specific adsorption is further enhanced by the natural high packing density and surface coverage of lipid bilayers on solid supports due to self-organization of lipids in two dimensions. These properties render supported lipid bilayers ideal candidates for studying ligand-receptor interactions with unprecedented signal to noise ratio. The presentation of cell adhesion molecules, such as synthetic lipopeptides at controlled amounts on a culture surface would greatly facilitate the control of cell growth and differentiation. For instance, Jensen et al. successfully employed a series of lipidated peptides, displaying RGD binding motives for controlled cell adhesion and utilized the load percentage of lipopeptides in the monolayer, to discriminate non-spreading KG-1a cells from adhesive HUEC cells.[31] Another prominent example of peptide/protein lipidation, as presented by Bader et al., involves the covalent coupling of carboxy-terminally truncated non-lipidated proteins to lipidated peptides representing the C-terminus of the proteins. This strategy has successfully used to display Ras protein constructs.[32] This particular conjugation of the truncated protein with the lipidated peptide exhibits properties very similar to the full Ras protein and thus, is operative in biophysical and cellular assay systems. However, solid phase lipopeptide synthesis involves sophisticated synthetic methods and elaborated purification methods.

Maleimide functionalized lipids have been successfully employed for the in situ coupling of terminal cysteine bearing peptides to detergent micelles,[33] lipid vesicles,[34] and, more recently, for in situ coupling of peptides to lipid bilayers for controlled cell attachment.[35] Hence, the conjugation of synthetic peptides via a terminal cysteine moiety to maleimide functionalized surfaces represents a versatile and robust method to derivatize preformed solid supported lipid bilayers with peptide moieties by forming membrane-anchored lipopeptides. Here, the process of covalent in situ coupling, as well as the subsequent binding of functionalized vesicles and gold nanoparticles to lipopeptide containing bilayers is scrutinized by a large variety of techniques such as ellipsometry, quartz crystal microbalance (QCM), atomic force microscopy (AFM), confocal laser scanning microscopy (CLSM), fluorescence recovery after photobleaching (FRAP) and fluorescence spectroscopy. Thereby, we seek to draw a detailed and comprehensive picture of the coupling and binding process, while carrying out each step in situ. We want to stress the fact that this approach allows a fast and highly sensitive, as well as selective establishment of binding assays involving

peptide epitopes as potential receptor moieties, opening an alternative fabrication method of tethered vesicles or bilayers and lipopeptide based screening devices.

8.2 MATERIALS AND METHODS

8.2.1 MATERIALS

Abbreviations. AcCN: Acetonitril; BisTris: Bis(2-hydroxyethyl)amino-tris(hydroxymethyl)methane; BODIPY: 2-(4,4-Difluoro-5-methyl-4-bora-3a,4a-diaza-s-indacene-3-dodecanoyl)-1-hexadecanoyl-sn-glycero-3-phosphocholine; CLSM: Confocal Laser Scanning Microscopy; DCC: N,N'-Dicyclohexylcarbodiimide; DIEA: N,N-Diisopropylethyl-amine; DMAP: 4-(Dimethylamino)pyridine; DMF: N,N-Dimethylformamide; DOGS-NTA-Ni: 1,2-Dioleoyl-sn-glycero-3-{succinyl} (Nickel salt); DOPC: 1,2-Dioleoyl-sn-glycero-3-phosphocholine; DOPE: 1,2-Dioleoyl-sn-glycero-3-phosphoethanolamine; EDC: N-(3-Dimethylaminopropyl)-N'-ethyl-carbodiimide hydro-chloride; EDT: Ethanedithiole; FRAP: Fluorescence Recovery after Photo Bleaching; HBTU: 2-(1H-Benzotriazole-1-yl)-1,1,3,3-tetramethylaminium hexafluorophosphate; H_2O_2: Hydrogen peroxide solution (35 wt %); HF: aqueous hydrofluoric acid (35wt%); HOBT: 1-Hydroxybenzotriazole; IEC: Ion Exchange Chromatography; MCA: 6-Maleimidohexanoic acid; MCC-DOPE: 1,2-Dioleoyl-sn-glycero-3-phosphoethanolamine-N-[4-(p-maleimidomethyl) cyclohexane-carboxamide]; MCS-DOPE: N-(6-Maleimidohexanoyl)-1,2-dioleoyl-sn-glycero-3-phosphoethanol-amine; NH_4OH: Ammonia solution (28%); NHS: N-Hydroxysuccinimide; PDMS: Poly(dimethylsiloxane); POPC: 1-Palmitoyl-2-oleoyl-sn-glycero-3-phosphocholine; POPG: 1-Palmitoyl-2-oleoyl-sn-glycero-3-[phospho-rac-(1-glycerol)] (Sodium salt); QCM: Quartz Crystal Microbalance; RP-HPLC: Reversed Phase – HPLC; TAMRA: 5(6)-Carboxytetramethyl-rhodamine; TFA: Triflouroaceticacid; TIS: Triisopropylsilan; Texas Red: Sulforhodamine 101 DHPE.

Materials. Unless stated otherwise all chemicals were of HPLC grade and used without further purification. Lipids were purchased from Avanti Polar Lipids (Alabaster, AL, USA). N-α-Fmoc-α-S-amino acid derivates with standard side chain protecting groups, HBTU, TAMRA, Rink Amide MBHA resin and all Fmoc-amino acids were from Novabiochem (Darmstadt,

Germany). All other chemicals and solvents were purchased from Sigma-Aldrich (Hamburg, Germany).

Instrumentation. AFM, Dimension 3100, Nanoscope IIIa+A/D controller, Veeco Digital Instruments (Santa Barbara, CA, USA); CLSM, Leica TCS SL, Leica Microsystems (Bensheim, Germany); Fluorescence Spectrometer, Jasco FP-6500 (Groß-Umstadt, Germany); Imaging Ellipsometer EP3-SW, Nanofilm Technologie (Göttingen Germany); HPLC, L-6200A Intelligent Pump and L-4200 UV/VIS Detector, Merck-Hitachi (Darmstadt, Germany); MALDI-TOF, TofSpec-E, Micromass (Manchester, GB)

8.2.2 SYNTHESIS OF PEPTIDES AND MALEIMIDE FUNCTIONALIZED-LIPIDS

Solid Phase Peptide Synthesis. All peptides were synthesized manually using N-Fluorenylmethoxycarbonyl (Fmoc) chemistry on acid labile Rink Amide MBHA resin following the procedures of Montanari et al.[36] with slight variations. Briefly, couplings were carried out using 4 eq Fmoc-amino acid derivates, 3.6 eq HBTU as a coupling reagent and 6 eq DIEA in DMF for 30 min. The coupling reaction was monitored by Ninhydrin staining (Kaiser test). In case of positive Kaiser test the coupling was repeated. Deprotection was accomplished by 30% piperidine in DMF (2 x 15 min). All non fluorescent labeled peptides were acetylated using 10% acetic anhydride in DMF for 30 min. Peptides were cleaved from the resin using TFA/TIS/EDT/H_2O (94:1:2.5:2.5) for 2-3 h. After cleavage, peptides were precipitated in cold Et_2O and collected on a medium porosity frit, redissolved in aqueous solution of 1% AcCN/0.075% TFA (RP-A) and eventually lyophilized. Peptides were identified by MALDI-TOF (TofSpec-E, Micromass (Manchester, GB). Mass deviation of the peptides was smaller than 0.2%.

TAMRA labeling of the peptides. Coupling of the 5(6)-Carboxytetramethyl-rhodamine (TAMRA) dye to the resin-bound peptides was accomplished by shaking the resin with a solution of 1.5 eq TAMRA, 1.5 eq HOBt and 1.7 eq DIEA in minimal amount of DMF/DMSO (5:1) for 18 h. Cleavage and purification of the TAMRA labeled peptides followed the identical protocol of the precipitation of acetylated peptides.

Purification of the peptides. Crude acetylated peptides and TAMRA labeled peptides were purified by strong cation exchange chromatography using a linear ionic strength gradient. The crude peptides were dissolved in RP-A and injected onto an ion exchange column (Shodex, IEC SP-825, 8.0 x 75 mm) and purified with the linear gradient of 30 to 100% B over 40 min at 1.4 ml/min; mobile phase A, 20mM PBS pH = 4.0 (PBS 4.0); mobile phase B, 20mM PBS 4.0, 1 M NaCl. Collected peaks were lyophilized and desalted on a preparative C18 HPLC column (Grace Vydac, Protein & Peptide C18, 22mm x 250mm) with 0% RP-B for 10 min followed by the gradient of 0 to 40% RP-B from 10 to 20 min; mobile phase RP-A, 1% AcCN/0.075% TFA; mobile phase RP-B 90% AcCN/0.1% TFA. The purity of the resulting peptides as estimated from analytical ion exchange chromatography was greater than 95%.

Synthesis of MCS-DOPE. Synthesis of **2** (MCS-DOPE) was accomplished by three different methods, employing different coupling strategies (cp. 3.1).

Synthesis of MCS-DOPE using EDC as a coupling reagent (Method A). 6-Maleimidohexanoic acid (22 mg, 0.1 mmol) and DOPE (75mg, 0.1 mmol) were dissolved in $CHCl_3$ (15ml) and cooled to 0°C. EDC (23 mg, 0.12 mmol) and DIEA (36µl, 0.2mmol) were added. The clear reaction mixture was stirred over night at room temperature and the reaction was monitored by TLC (mobile phase $CHCl_3$/MeOH (5:1); KMnO4 and Ninhydrin staining), revealing that DOPE was transformed into a faster running product with R_f = 0.35. After completion of the reaction the reaction mixture was concentrated in a rotavap and purified by flash chromatography on silica gel (mobile phase $CHCl_3$/MeOH (2:1)). Minor impurities of 6-maleimidohexanoic acid were removed by flash column chromatography on aluminum oxid (activated, basic, Brockmann I; mobile phase $CHCl_3$/MeOH/H_2O (65:25:4)). Freeze drying from benzene yielded MCS-DOPE as a white solid (63 mg, 67%) with R_f = 0.35 ($CHCl_3$/MeOH 5:1); MALDI-TOF for $C_{51}H_{88}N_2NaO_{11}P$, MH^+ at m/z = 940.4 (calcd 940.2);

Synthesis of MCS-DOPE using DCC as a coupling reagent (Method B). 6-Maleimidohexanoic acid (32 mg, 0.15 mmol) and DOPE (75mg, 0.1 mmol) were dissolved in $CHCl_3$ (15ml) and cooled to 0 °C. DCC (33 mg, 0.16 mmol) and DMAP (10 mg, 0.08mmol) were added from stock solutions in $CHCl_3$. Monitoring, general work up and purification are essentially identical to method A with minor changes, i.e. solvent of collected fractions from silica flash chromatography was removed and the precipitate was dissolved in benzene. Insoluble

dicyclohexylurea was removed by syringe filtration (Millex LCR, 0.45µm) and the product was lyophilized from benzene followed by flash column chromatography on basic aluminum oxid. MCS-DOPE was obtained as a white solid (52 mg, 54%) with R_f = 0.34 ($CHCl_3$/MeOH 5:1); MALDI-TOF for $C_{51}H_{88}N_2NaO_{11}P$, MH^+ at m/z = 940.1 (calcd 940.2).

Synthesis of MCS-DOPE via NHS ester of 6-maleimidohexanoic acid (Method C). 6-Maleimidohexanoic acid (106 mg, 0.5 mmol) and NHS (63 mg, 0.55 mmol) were dissolved in 10 ml THF and cooled to 0 °C. DCC (114 mg, 0.55 mmol) was added from a stock solution in THF. After 90 min a white precipitation due to insoluble dicyclohexylurea was observed. The turbid suspension was stirred over night at room temperature and the reaction was monitored by TLC (mobile phase $CHCl_3$/MeOH (5:1); KMnO4 staining), revealing that 6-maleimidohexanoic acid was transformed into a faster running product R_f = 0.71. Insoluble dicyclohexylurea was removed by syringe filtration (Millex LCR, 0.45µm) and the reaction solvent was evaporated in a rotavap. The product was dissolved in 10 ml $CHCl_3$ and used without further purification. 2.5 ml of the NHS-maleimidohexanoic-ester solution (~ 0.12 mmol NHS ester) was added to DOPE (75 mg, 0.1 mmol) and diluted to 10 ml with $CHCl_3$. The reaction was stirred over night and monitored by TLC. Purification and work up followed method A. MCS-DOPE was received as a white solid (73 mg, 78%) with R_f = 0.34 ($CHCl_3$/MeOH 5:1); MALDI-TOF for $C_{51}H_{88}N_2NaO_{11}P$, MH^+ at m/z = 940.2 (calcd 940.2).

8.2.3 SAMPLE PREPARATION AND IN SITU LIPOPEPTIDE SYNTHESIS

Vesicle preparation. Vesicle preparation of maleimide functionalized lipids was carried out according to Brain and McConnell.[1] In brief, functionalized DOPC multilamellar vesicles (MLVs) were prepared by swelling a lipid film deposited on a glass wall in 50 mM PBS, pH = 5.9 (PBS 5.9) for 20 minutes above the main phase transition temperature of the lipids and vortexing the suspension periodically. The resulting multi lamellar vesicle suspension was transformed into small unilamellar vesicles (SUVs) by sonification (50 W, 0.4 s Puls, 20 min) in a vessel resonator (Sonoplus HD 2070, Bandelin, Berlin, Germany).

SSLB preparation. Membranes on solid supports (silica, glass, quartz resonators) were prepared as described previously (cp. 3.2).[22, 37, 38]

In situ coupling reaction. All in situ coupling reactions were performed in 50 mM PBS pH = 6.8 (PBS 6.8) on maleimide functionalized solid supported lipid bilayers (SSLB). SSLBs were obtained by vesicle spreading in PBS 5.9 on the respective solid support. Immediately after rinsing with PBS 6.8 the fresh peptide dissolved in PBS 6.8 was added, yielding peptide concentrations of at least 0.01 µmol/ml. In general, the reaction was completed after 60 to 90 min and residual unreacted peptides were removed by rinsing thoroughly with PBS 6.8.

Lipopeptide mediated adsorption of vesicle and gold nanoparticles. Adsorption of functionalized vesicles and gold nanoparticles was carried out on peptide modified solid supported lipid bilayers. Vesicle concentrations were in the range of 0.1 mg/ml. Details of the lipopeptide mediated coupling conditions are given in the text.

Microstructuring of individual addressable lipid bilayers. PDMS stamps displaying a hydrodynamically coupled network of capillaries were prepared, following the general procedure established by Whitesides and coworkers.[39, 40] Separate trenches were molded into a polydimethylsiloxane (PDMS) elastomer using a silicon wafer as the master structure. The geometric design of the master structure and details of the structuring process are described previously. [20-23] Briefly, after the hydrophilic PDMS mold was attached to the glass cover slip, individual channels were filled with 0.03 µl of unilamellar vesicle solution. Spreading of the vesicles was completed after 2 min and the sample was immediately rinsed with buffer after the stamp was removed.

8.2.4 INSTRUMENTAL METHODS

QCM Measurements. The in situ coupling reaction of the peptides to maleimide functionalized bilayers was examined by QCM measurements using 5 MHz resonators (KVG, Neckarbischofsheim, Germany). The experimental set up is given elsewhere.[37] Briefly, the functionalization of the gold electrode by a hydrophobic monolayer of octanethiol (OT) was achieved by incubation of the electrode with a solution of 2 mM OT in ethanol for 60 min and subsequent rinsing with buffer. Then SUVs composed of DOPC/**1** were injected into QCM cell at a final concentration of 1 mg/ml and incubated for 30 min at room temperature

followed by heating at 65°C for 15 min and rinsed with PBS 6.8, which results in a second phospholipid monolayer on the SAM. The quality of the SAM and the deposition of the final phospholipid monolayer were monitored by impedance spectroscopy following the protocols of Steinem et al.[41] Finally, after the peptides were injected into the reaction camber at a final concentration of 0.05 µmol/ml, the time course of the in situ coupling reaction was monitored by QCM.

Ellipsometry. In this study a commercial available imaging ellipsometer (EP^3-SW, Nanofilm Technologie, Göttingen, Germany) was used (cp. 6.2) to determine the changes in layer thicknesses during the in situ coupling of peptides to lipid bilayers and vesicle adsorption by lipopeptide mediation. Initially, the layer thickness of the SiO_2 layer was determined by four-zone nulling procedures and all given layer thicknesses were SiO_2 corrected. In general, all thickness measurements presented throughout the text were carried out by four-zone nulling procedures after thorough rinsing with buffer. Kinetic studies of the change of the ellipsometric angle delta during the experiment were recorded by one-zone nulling procedures at a higher sample rate of 6 data points/min.

Atomic force microscopy. Experiments were carried out in aqueous solutions as described previously (cp. 5.2) using a commercial scanning force microscope (Dimension 3100 with Nanoscope IIIa+A/D controller, Veeco Digital Instruments, Santa Barbara, CA, USA).

Fluorescence spectroscopy. All fluorescence emission spectra were recorded on a Jasco FP-6500 fluorescence spectrometer (Groß-Umstadt, Germany). The tryptophan fluorescence was monitored from 300 nm to 450 nm with excitation at 280 nm wavelength, a 5 nm bandpass filter, and 0.2 nm data pitch. Samples were measured at room temperature. The peptide concentration in all experiments was 5 mM.

Confocal Laser Scanning Microscopy. All CLSM and FRAP measurements were carried out with a Leica LCS SL confocal laser scanning microscope (Leica Microsystems, Bensheim, Germany) using a 20x water immersion objective (∞/0.17/D, HC PL FLUOTAR, 20x0.50). A 50 mW Argon Laser with a wavelength of λ = 488 nm was used for bleaching and for scanning.

In FRAP experiments, a small spot on a fluorescent surface is photobleached by a brief exposure to an intense focused laser beam. Intact fluorophore from the surrounding surface diffuses into the spot by lateral transport and the resulting recovery of the fluorescence intensity is monitored by the same, but attenuated, laser beam. The characteristic time for fluorescence recovery, τ_D, is defined by the expression

$$\tau_D = \omega^2 / 4D \qquad (2)$$

where D is the lateral diffusion coefficient of the fluorescent labeled molecules. ω represents the half-width at e^{-2} height of the Gaussian intensity profile of the laser beam.

The sample was bleached for 0.5 s with a focused laser beam at 100% laser activity followed by taking time elapsed images at 6% laser activity and a scanning frequency of 1000 Hz every 1.3 s. Time elapsed CLSM images were analyzed with a home written analysis program in Igor Pro based on the theory of Axelrod et al. and Soumpasis.[42, 43] The intensity profile, $I(r)$ of the bleaching spot on the first image upon bleaching was fitted to a Gaussian function

$$I(r) = \left(\frac{2P_0}{\pi\omega^2} \right) \exp\left(-\frac{2r^2}{\omega^2} \right) \qquad (3)$$

where P_0 is the total laser power and ω is the half-width at e^{-2} height. The average Gaussian radius of a bleaching spot was 4.4 ± 0.6 µm. In order to obtain the course of fluorescence intensity in the bleached region over time, a circular region of interest (ROI) was marked on the first image and the average fluorescence intensity within the ROI was determined for each image. Additionally, a ROI from far outside the bleached area was defined and the course of its fluorescence intensity was determined as described above providing the background bleaching over the time period of a FRAP experiment by the scanning laser beam. The fluorescence recovery curve was then corrected by the background bleaching. The fluorescence recovery curve was normalized and a series function

$$F_K(t) = (qP_0C_0/A)\sum_{n=0}^{\infty}\left[(-K)^n/n!\right]\cdot\left[1+n(1+2t/\tau_D)\right]^{-1} \quad (4)$$

Is fitted to the data as described by Axelrod et al. (equation 4). The characteristic time for fluorescence recovery τ_D provides the lateral diffusion coefficient according to equation 2. P_0 is the total laser power, *t* is time, C_0 the initial concentration of the fluorophore, and τ_D is the characteristic time for fluorescence recovery. The parameter *q* is the product of all the quantum efficiencies of light absorption, emission and detection and *A* is the attenuation factor of the beam during observation of recovery. The extend of bleaching induced in time *T* is expressed by the parameter *K* which is defined as $K \equiv \alpha TI(0)$.

In all FRAP experiments the initial microstructured lipid bilayer on glass was composed of 90% DOPC and 10% **1**. Lipopeptides were formed in an in situ coupling reaction by exposing 0.1 µmol non fluorescently labeled peptide K8 and H6, respectively, in 3 ml PBS 6.8 to the sample for 60 min, followed by thorough rinsing with PBS 6.8. Prior to lipopeptide mediated adsorption of functionalized vesicles, the SSLB was incubated in BSA solution (0.25 mg/ml in PBS 6.8) for 30 min to minimize non-specific vesicle adsorption on the glass substrate. Vesicle adsorption to K8 lipopeptide was performed in 10 mM Tris·HCl buffer at pH 7.0 (Tris 7.0) containing 0.5 mM EDTA in order to avoid calcium mediated aggregation of negatively charged vesicles. Vesicles composed of 30%POPC, 69% POPG and 1% BODIPY were added to the sample at a concentration of 0.1 mg lipid/ml in Tris 7.0 for 30 min followed by thorough rinsing. H6 lipopeptide mediated vesicle adsorption was carried out in PBS 6.8 with small unilamellar vesicles composed of 88% DOPC, 10% Ni-NTA-DOGS and 2% BODIPY.

8.3 RESULTS AND DISCUSSION

8.3.1 GENERAL EXPERIMENTAL PROCEDURE

The general experimental procedure for the lipopeptide mediated adsorption of functionalized vesicles and functional gold nanoparticels (Nanoprobes, Yaphank, NY, USA) particles is illustrated in figure 8.1.

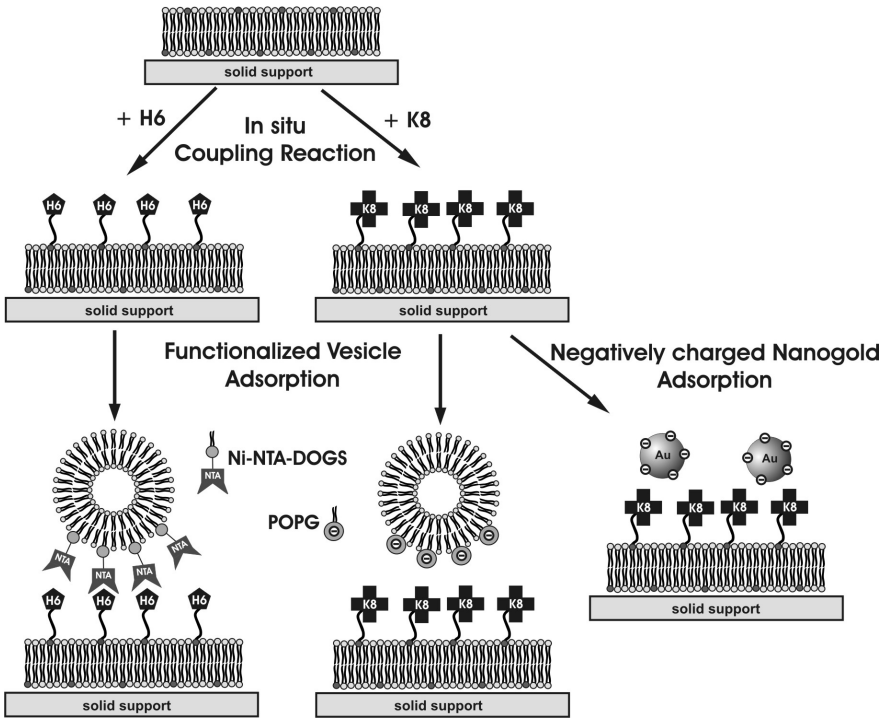

Figure 8.1. Schematic drawing of the various experimental procedures for the in situ coupling of Ac-HHHHHHGGC (H6) and Ac-KKKKKKKKWGC (K8) peptides to maleimide functionalized solid supported lipid bilayers and the corresponding lipopeptide mediated adsorption of functionalized vesicles and gold nanoparticles. Maleimide functionalized lipids are represented by dark grayish head groups. H6 and K8 peptides are drawn as black pentagons and black crosses, respectively. Ni-NTA bearing vesicles (DOPC/Ni-NTA-DOGS) and negatively charged vesicles (POPC/POPG) are represented by marked headgroups. Negatively charged gold nano-particles are drawn as solid spheres in light gray.

Initially, functionalization of the supported lipid bilayer was achieved by an in situ coupling reaction of a peptide to a maleimide lipid. Two main interactions were utilized to bind functional vesicles or gold nanoparticles to the supported lipid bilayer equipped with the

corresponding lipopeptide. The attachment is either based on the formation of a Ni^{2+} complex via specific interaction of a histidine tagged lipid (H6 lipopeptide) and vesicles doped with Ni - NTA bearing lipids or on electrostatic interactions between the poly-cationic K8 lipopeptide and negatively charged POPC/POPG vesicles. Initially, a solid supported lipid bilayer composed of DOPC with 10 mol% of the maleimide functionalized lipid **1** or **2** (figure 8.2), respectively, was prepared from unilamellar vesicle suspension.

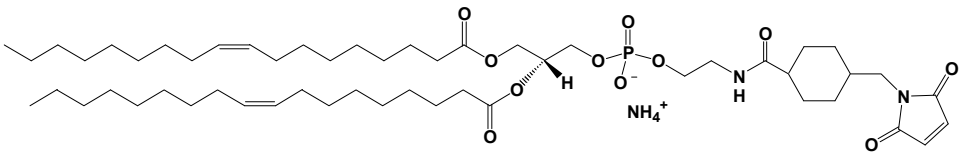

1

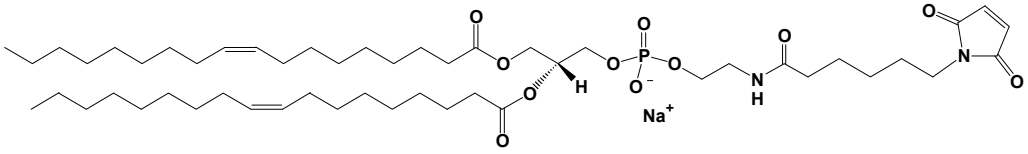

2

Figure 8.2. Molecular structures of the maleimide functionalized lipids 1 (1,2-Dioleoyl-*sn*-glycero-3-phosphoethanolamine-N-[4-(p-maleimidomethyl)cyclohexane-carboxamide]) and 2 (1,2-Dioleoyl-*sn*-glycero-3-phosphoethanolamine-[N-maleimidohexyl-carboxamide]).

To protect the reactive maleimide moiety from hydrolysis at neutral and basic pH values,[44] vesicle preparation and vesicle spreading was carried out at pH = 5.9. However, prior to the in situ coupling reaction of the peptides with the maleimide functionalized bilayer the buffer was exchanged with PBS 6.8 to improve the coupling efficiency.[44] Peptides were dissolved in PBS 6.8 from aliquots and added immediately to the solid supported lipid bilayer. The reaction mixture was allowed to equilibrate at room temperature for at least 1 h, yielding in a specific in situ coupling reaction of the C terminal cysteine moiety of the peptide to the maleimide head group of the reactive lipid via addition of sulfhydryl group to the maleimide (figure 8.3).

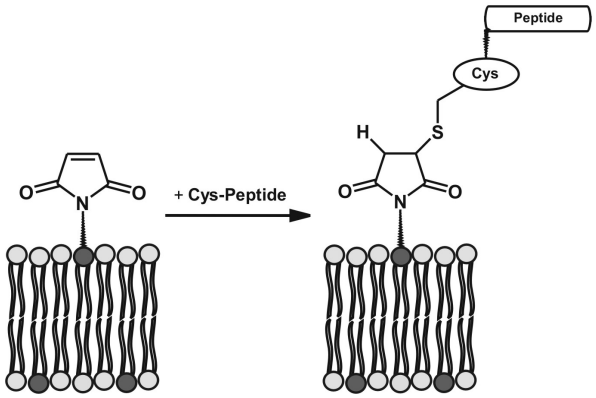

Figure 8.3. In situ coupling reaction of a peptide with a terminal cysteine moiety to a maleimide functionalized bilayer.

Subsequently, excess peptide was removed by thorough rinsing with PBS 6.8, followed by the addition of functionalized vesicles (~ 30 nm) or gold nanoparticles with an average diameter of 1.4 nm. Experiments utilizing either **1** or **2** were virtually indistinguishable. However, it should be noted that **2** is a cost efficient alternative to **1**, which can easily be synthesized at high yields.

8.3.2 IN SITU COUPLING REACTION OF H6 MONITORED BY QUARTZ CRYSTAL MICROBALANCE

QCM analysis was employed to determine the minimal fraction of the maleimide lipid within the DOPC bilayer, which is necessary to obtain a continuous, covalent bound peptide monolayer. For this purpose, we investigated the impact of the molar fraction of **1** on the maximal frequency shift obtained after the addition of the peptide. QCM analysis utilizes the resonance frequency shifts of a thickness shear mode resonator oscillating at 5 MHz in response to deposition of a foreign mass, such as a thin organic layer.[45] The frequency decrease is essentially proportional to an increase in film thickness in the case of a thin rigid monolayer. Exemplary, a time course of the resonance frequency shift monitored during the in situ coupling reaction after the addition of H6 ($CGGH_6$-Ac) to a maleimide functionalized DOPC bilayer is shown in figure 8.4 (black line). Control experiments (red line) using pure DOPC did not show a significant decrease in resonance frequency upon addition of H6.

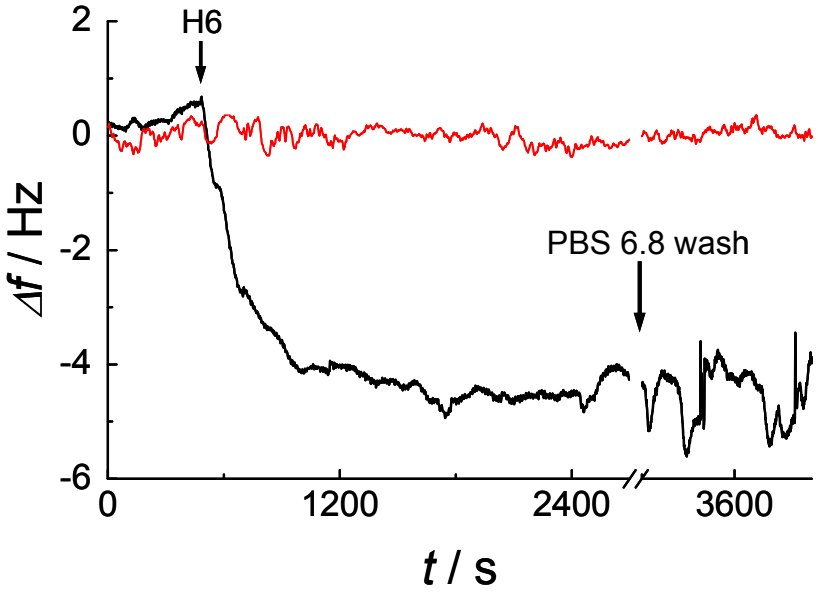

Figure 8.4: Time course of the resonance frequency shifts of a 5 MHz quartz crystal after injection of 0.2 µmol H6 in PBS 6.8 (c = 0.1 µmol peptide/ ml) to the maleimide functionalized bilayer. The outermost monolayer is composed of 90% DOPC and 10% of 1. Rinsing with PBS 6.8 as indicated did not affect the resonance frequency shift. The resonance frequency shift of the control experiment using neat DOPC is shown in red. Frequency shifts after the in situ coupling reaction of H6 to bilayers with varying composition of DOPC and 1 are compiled in table 8.1.

2 mol% maleimide functionalization of the DOPC bilayer with **1** did not reveal any significant decrease in resonance frequency, whereas 5 mol% and 10 mol% yielded a resonance frequency shift Δf of the quartz crystal of 2.4 Hz and 5.2 Hz, respectively. Stepwise increase of the molar fractions of **1** up to 40 mol% did not result in a further increase of the resonance frequency shift (table 8.1). Presumably the availability of further unreacted maleimide lipid headgroups was sterically hindered by the crowding of the in situ coupled peptides, which limits the maximal surface coverage of the membrane with peptide residues. Coupling of H6 to the maleimide lipid head groups is completed within 20 min due to the fast mass transport of the peptide towards the reactive surface of the functionalized DOPC layer achieved by a stagnation point flow geometry of the measurement chamber.[37, 46]

In conclusion, the investigation of the in situ coupling reaction of small peptides to maleimide functionalized bilayer by QCM has been proven to be a valuable and

extraordinary surface-sensitive method to detect the formation of lipopeptides at bilayer surfaces. However, it is cumbersome to extract exact quantitative data such as thickness from the frequency shift as small viscoelastic contributions arise due to bound water as discussed elsewhere.[45, 47] According to Sauerbrey[48] a frequency decrease of 2.4 Hz corresponds to a thickness change of roughly 0.75 nm assuming a density of 1 g/ml. More reliable thickness information is expected from ellipsometry in combination with AFM. Unless stated otherwise all further in situ coupling reactions were carried out using 10 mol% of maleimide functionalized lipid **1** or **2** within the DOPC matrix.

DOPC monolayer composition [% **1**]	Δf [Hz]
5	2.4
10	5.2
20	5.3
40	5.6

Table 8.1. Resonance frequency shifts of a 5 MHz quartz resonator after in situ coupling of H6 to DOPC/OT doped with various amounts of 1.

8.3.3 IN SITU COUPLING REACTION AND LIPOPEPTIDE MEDIATED ADSORPTION MONITORED BY ELLIPSOMETRY

Time elapsed ellipsometry enables us to monitor each of the individual steps of the lipopeptide mediated adsorption with sub-nanometer resolution. The entire process of the lipopeptide mediated adsorption of Ni-NTA vesicles on a DOPC bilayer is shown in figure 8.5. Initially, the experiment starts with the addition of unilamellar DOPC vesicles to the silicon wafer consisting of 90% DOPC and 10% **2**, resulting in adsorption followed by spreading of the vesicles. 20 min after vesicle addition the ellipsometric angle remained constant at Δ = 174.6°, confirming that a lipid bilayer has been formed. Excess vesicles were removed by thorough rinsing and the layer thickness was determined to be d_{DOPC} = 3.8 nm by 4 zone measurements assuming a refractive index of n = 1.53.[38] Subsequent addition of H6 at 50

min yielded a slight decrease in delta values to Δ = 174.2° as displayed in the inset of figure 8.5. Assuming a quasi continuous peptide layer with a refractive index of n_{pep} = 1.50 the layer thickness was calculated to be d_{H6} = 0.5 nm in good accordance with the thickness change obtained from QCM analysis. Exposure of Ni NTA functionalized vesicles to the H6 lipopeptide functionalized bilayers results in a significant decrease in delta of Δ = 3.0° at t_x = 310 min. After 150 min exposure time the delta values remained nearly constant at Δ = 171.2°. It is, however, difficult to quantify from ellipsometry data alone to what extend Ni-NTA functionalized vesicles attach to the bilayer as intact liposomes or spread to form a second bilayer. Hence, we carried out AFM and CLSM experiments to further elucidate this issue. From the shift in Δ – value we presume coexistence of intact vesicles and bilayer patches.

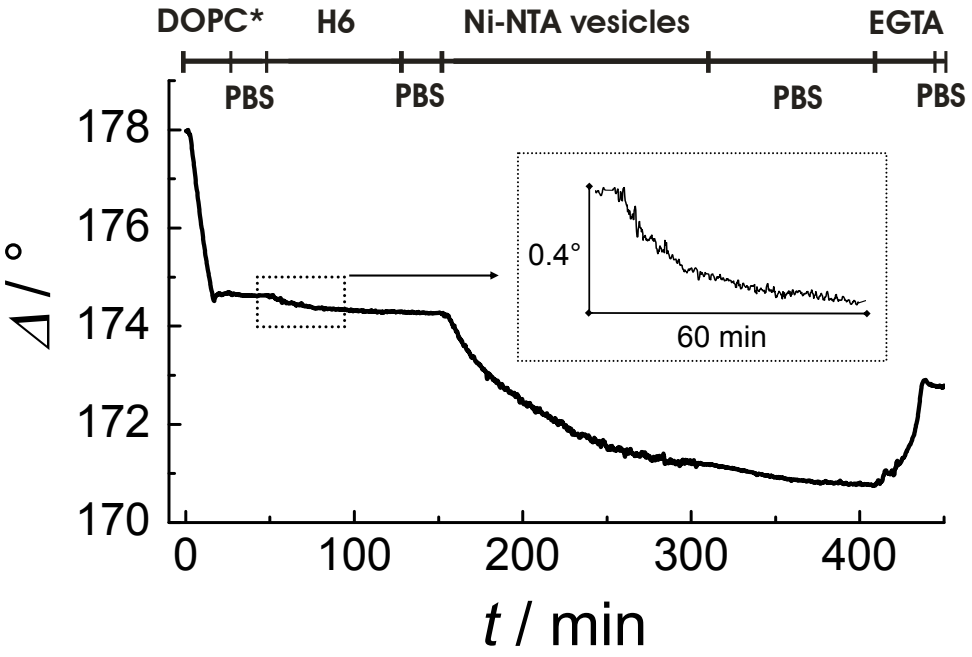

Figure 8.5. Δ values obtained from ellipsometry measurements during the in situ coupling reaction of H6 to a lipid bilayer composed of 90% DOPC and 10% of 2 (DOPC*) and subsequent Ni-NTA vesicle adsorption as a function of time. EGTA induced desorption confirms the specific binding of Ni-NTA functionalized vesicles to H6 lipopeptides in an intact manner. Inset shows the details of the in situ coupling reaction of H6 to the maleimide functionalized DOPC bilayer.

Time elapsed AFM images of the H6 lipopeptide mediated vesicle adsorption displays instantaneous adsorption of intact vesicles and subsequent vesicle spreading. Figure 8.6 A shows a maleimide functionalized bilayer after the incubation with H6 for 120 min. Special care was taken to ensure that the rather homogeneously flat surface could be assigned to a defect free, histidine tagged bilayer. Therefore, force distances curves were applied and mechanical instabilities (breakthrough events) of the lipid bilayer upon stochastic tip penetration were recorded (data not shown).[49-52] Breakthrough events were taken as an indication for the presence of a lipid bilayer on the mica substrate.

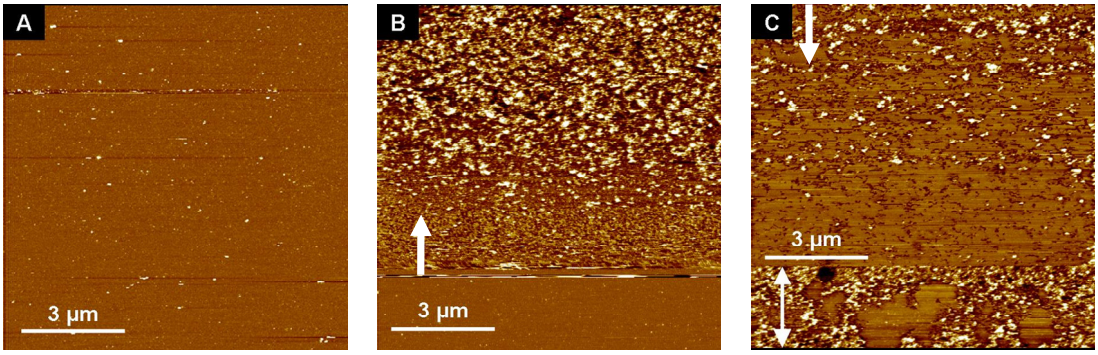

Figure 8. 6. Time elapsed AFM images of the binding of Ni-NTA functionalized DOPC vesicles on H6 functionalized DOPC bilayers. A) H6 functionalized DOPC bilayer before vesicle binding. B) Time course of vesicle binding. Addition of vesicle suspension and scan direction is marked by an arrow, which also indicates the scan direction. C) Subsequent image (scan direction indicated by an arrow) confirms the formation of a second bilayer due to vesicle rupture, which is enhanced by the tip-sample interaction. The double headed arrows indicate an area after vesicle binding, which was not subject to repeated scanning.

Along the slow scan axis (y-axis) of figure 8.6 B after Ni-NTA/DOPC vesicle addition, enrichment in vesicle density, combined with a cumulative increase in height can be detected. Since AFM imaging is a rather invasive method, tip induced vesicles rupture might occur. We found that the vesicle to bilayer ratio in the lower area of figure 8.6 C is higher than the repeatedly scanned upper area, confirming that tip induced vesicle rupture occurs upon repeated scanning due to tip-sample interactions. Further evidence that the H6 lipopeptide mediated vesicle adsorption monitored by time elapsed ellipsometry results in the coexistence of intact and ruptured vesicles on top of the H6 lipopeptide functionalized

DOPC bilayer, was obtained from experiments in which EGTA is used to remove Ni^{2+} and as a consequence trigger detachment of intact vesicles. The ellipsometric response after EGTA rinsing was determined to be constantly $\Delta = 172.9°$ at 435 min. Significant differences in the ellipsometric response before Ni-NTA vesicle adsorption and after rinsing with 1mM EGTA solution were measured to be Δ = 1.3°, implying that bilayer patches were still present on the surface.

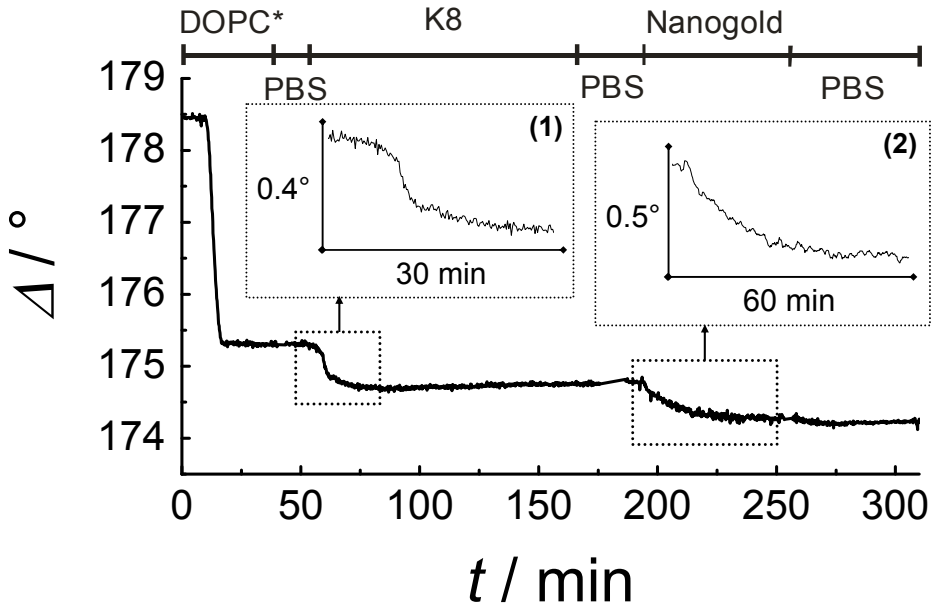

Figure 8.7. Time course of the Δ values obtained from ellipsometric measurements during the in situ coupling reaction of K8 to a lipid bilayer composed of 90% DOPC and 10% of 1 and subsequent adsorption of negatively charged gold nanoparticles as a function of time. Gold nanoparticles exhibited a nominal diameter of 1.4 nm. Inset (1) shows the details of the in situ coupling reaction of K8 to the maleimide functionalized DOPC bilayer, while inset (2) displays the details of the nanoparticle adsorption.

Besides attachment of vesicles as attoliter containers on SSLB we also selectively immobilized gold nanoparticles on bilayers. Ellipsometric measurements and AFM imaging of the adsorption of gold nanoparticles on K8 functionalized DOPC bilayers were employed to investigate, whether the binding of functional particles occurs exclusively onto the lipopeptides or is of non-specific nature. Coupling protocols were basically identical for K8 and H6 peptides. Figure 8.7 displays the ellipsometric angle Δ during the in situ coupling

reaction of K8 to a maleimide functionalized bilayer and subsequent adsorption of negatively charged gold nanoparticles as a function of time. The nominal diameter of the particles was 1.4 nm, resulting in a brownish coloring of the buffer. We found a change in Δ of 3.4° (d_{DOPC} = 3.8 nm) for the formation of the bilayer on silicon and an additional decrease of 0.4° for the coupling of K8 (d_{K8} = 0.5 nm) in perfect agreement with the thickness changes produced by covalent coupling of H6. Although the peptide concentration, the maleimide content of the bilayer, and the instrumental parameters were identical for both peptides (K8 and H6), the in situ coupling reaction of K8 to the maleimide lipids was observed to be generally faster than the kinetics of H6. After rinsing with buffer, gold nanoparticles were adsorbed on the K8 lipopeptides, resulting in a further decrease of the ellipsometric angle of 0.5°, accompanied by a clearing of the turbid, brownish particle solution. We refrain here from a calculation of the resulting gold monolayer thickness from the ellipsometry angle, due to probably incomplete coverage of the surface (cp. figure 8.8), lateral clustering and the complicated relation between the refractive index of the particles and the size, which would be far beyond the scope of this work.[53, 54]

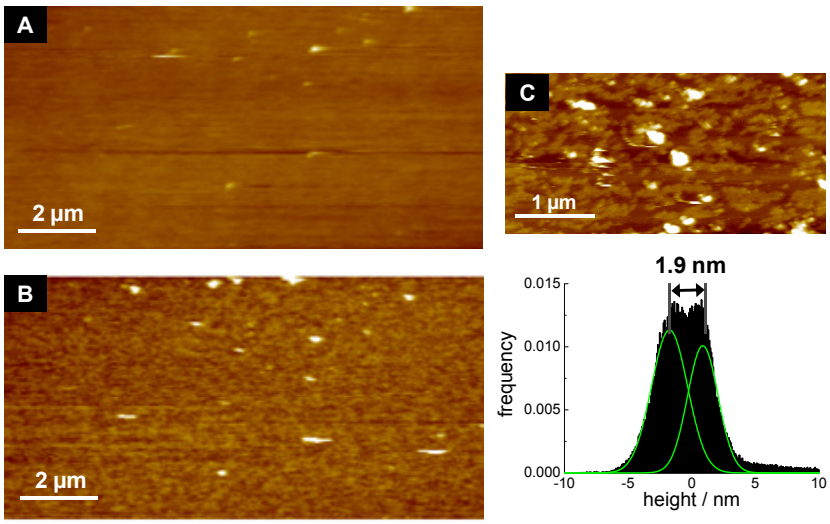

Figure 8.8. AFM images of the binding of negatively charged gold nanoparticles to a K8 functionalized DOPC bilayer on glass. A) K8 functionalized DOPC bilayer in the absence of gold nanoparticles. B) Binding of nanoparticles and subsequent rinsing with PBS 6.8. C) Details of the adsorbed gold monolayer and histogram analysis employing two Gaussian fitting functions (green), revealing an average height of the gold nanoparticles of (1.9±0.5) nm and an apparent coverage of 43 %.

AFM images could clearly resolve the submonolayer coverage with nanoparticles exhibiting a height of (1.9±0.5) nm (figure 8.8), corresponding well to the expected thickness change of 1.4 nm. Control experiments did not show a significant change in the ellipsometric angle upon addition of peptide or nanoparticles, when neat DOPC was used (cp. appendix C, D). Although there is evidence for a non-specific adsorption of oligo-polylysine, especially to gel phase lipids[55] and a weak non-specific adsorption of K8 and H6 on neat DOPC bilayers could be detected using fluorescently labeled peptides, adsorption of vesicles or gold nanoparticles on functionalized bilayers is exclusively observed for peptides covalently attached to lipid anchors.

8.3.4 FLUORESCENCE RECOVERY AFTER PHOTOBLEACHING (FRAP)

Fluorescence recovery after photobleaching (FRAP) was applied in order to determine lateral diffusion coefficients of BODIPY C_{12}-HPC stained lipid vesicles adsorbed on microstructured bilayers equipped with lipopeptides. Values and ranges of the diffusion coefficients should clarify, whether lipid vesicles stay intact upon adsorption or rupture resulting in a second bilayer on top of the lipopeptide containing SSLB.

Figure 8.9 shows representative CLSM images of a FRAP experiment of POPC/POPG/BODIPY (30:68:2) vesicles adsorbed on a K8 lipopeptide (**1**) doped microstructured DOPC bilayer (DOPC/**1,** 90:10) on glass. Figure 8.9 E shows the normalized fluorescence intensity (recovery curve) extracted from the 60 images together with the corresponding Axelrod fit employing equation 4. The average diffusion coefficient of the adsorbed POPC/POPG/BODIPY-vesicles added to the preformed K8-lipopetide containing SSLB was determined to be (3.2 ± 1.1) $\mu m^2 s^{-1}$ with an immobile fraction of (24 ± 4) %. Noteworthy, the bilayer stripes with a width of 15 µm exhibit reduced diffusion coefficients due to their confined geometry. By finite element simulation we could show the diffusion constant is by approximately 25 % smaller than on an entirely covered surface (data not shown). While the diffusion constant is only slightly smaller than expected for a lipid bilayer stripe (≈ 5-7 $\mu m^2 s^{-1}$), the immobile fraction is unusual high if we assume an intact bilayer on top of the SSLB. The data suggests the coexistence of interconnected bilayer patches and intact vesicles representing the immobile fraction. Therefore, we conclude that the strong adhesion, which is caused by attractive electrostatic interactions leads to deformation and partial rupture of vesicles on the first

bilayer. Lateral mobility of vesicles tethered to fluid supported lipid bilayers has been investigated by Yoshina-Ishii et al. using single-particle tracking[26] and by Benkoski and Höök also using FRAP,[56] both reporting on diffusion coefficients of the tethered vesicles as small as 0.2-0.4 $\mu m^2 s^{-1}$ and 0.3 $\mu m^2 s^{-1}$, respectively. Further evidence that the immobile fraction originates from adsorbed vesicles is obtained from heating the sample consisting of POPC/POPG vesicles absorbed on SSLB displaying K8 oligopeptides to 65°C for 15 min and subsequently carrying out FRAP measurements at room temperature.

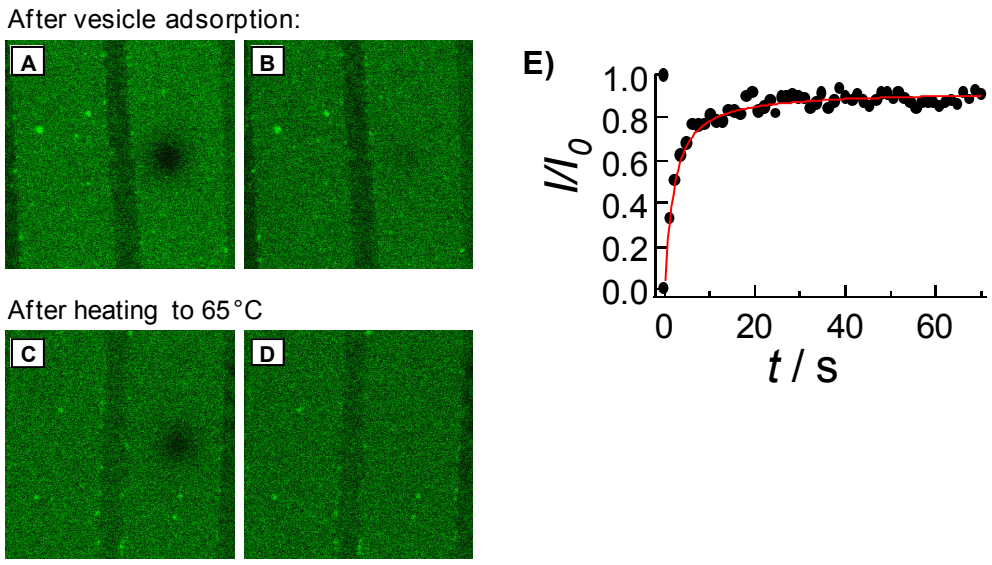

Figure 8.9. Typical confocal laser scanning microscope images of a FRAP experiment performed on microstructured bilayers. The image size is (23.4 x 23.4) µm² for every image. A) Bleached spot in a BODIPY labeled lipid vesicle layer adsorbed on a microstructured bilayer containing K8 lipopeptides (~10 mol %) immediately after bleaching. B) Image of the same bilayer section 78 s after bleaching. C, D) Same sample as shown in Figures 8.9 A, B after brief exposure to 65°C for 15min, measured at room temperature. C) Bleached spot immediately after bleaching. D) Image 78 s after bleaching. The lipid bilayer is composed of 90% DOPC and 10% MalCHex-DOPE and the small unilamellar vesicles are composed of 69% POPG, 30% POPC and 1% BODIPY. The left compartment of the microstructured bilayer is not exposed to the intense focused laser beam used for bleaching. Thus, the course of its fluorescence intensity can be used to compensate for the background bleaching over the time period of a FRAP experiment by the attenuated scanning laser beam. E: Normalized fluorescence recovery curve measured with corresponding Axelrod fit (red line).

At these conditions, adhered vesicles are expected to rupture. The FRAP experiments of these samples resulted in a slightly larger diffusion coefficient of (4.7 ± 0.9) $\mu m^2 s^{-1}$ and more significantly to a substantial reduction of the immobile fraction to (8 ± 1) %. The heating process enabled attached vesicles to reduce the energy barrier for rupture leading to larger bilayer patches, which result in less immobile fraction and higher diffusion constants.

We also investigated H6-lipopeptide mediated vesicle adsorption using FRAP. For vesicles composed of DOPC/Ni-NTA-DOGS/BODIPY (88:10:2) adsorbed on H6 lipopeptides via specific complexation, an average diffusion coefficient of (2.9 ± 1.7) $\mu m^2 s^{-1}$ with a substantial immobile fraction of (61 ± 18) % was determined. These values (cp. table 8.2) as detailed above also support the assumption that intact vesicles coexist with bilayer patches.

System	D_{System} [$\mu m^2 s^{-1}$]	immobile fraction [%]
K8 - POPC/POPG vesicles:		
before heating	3.2 ± 1.1	24 ± 4
after heating 15min at 65°C and measured at RT	4.7 ± 0.9	8 ± 1
DOPC/10% **1**	5.7 ± 0.8	10 ± 2
H6 – Ni-NTA vesicles	2.9 ± 1.7	61 ± 18

Table 8.2 Diffusion coefficient and immobile fraction of POPC/POPG vesicles adsorbed on K8 modified supported bilayers (DOPC/1, 90:10) before and after heating the sample to 65°C for 15 min measured by FRAP at room temperature. Additionally, the diffusion coefficient and the immobile fraction of pure bilayers composed of DOPC/1 (90:10), as well as the diffusion coefficient of Ni-NTA functionalized vesicles adsorbed on H6 modified bilayers are listed.

These findings are fully corroborated by the time resolved in situ AFM images of vesicle adsorption on SSLB equipped with H6 lipopeptides (figure 8.6). It will be a matter of tunable adhesion energy to control whether vesicles remain intact or rupture to form a bilayer sandwich. This can be achieved by either adjusting the number of receptor molecules in the

preformed SSLB or ligands embedded in the vesicle. Höök as well as Vogel and coworkers showed how it is possible to carefully control these parameters to accomplish defined deposition of nanocontainers on functionalized surfaces.[56-60] We believe that our study will contribute to this important issue by proving a versatile platform to use oligopeptides as universal receptors for particles, liposomes, proteins, and even nucleic acids.

8.3.5 CONFOCAL LASER SCANNING MICROSCOPY ON MICROSTRUCTURED LIPID BILAYERS

The concept of individually addressable microstructured lipid bilayers, which has been extensively used and improved by our group,[20-23] was employed to detect the lipopeptide mediated adsorption of functionalized DOPC vesicles on a solid supported bilayer while simultaneously carrying out the proper control experiments. Precisely, we are able to visualize the adsorption of functionalized vesicles on the lipopeptide displaying bilayer compartments and at the same time non-specific adherence of liposomes to neat DOPC bilayers serving as an internal control under identical experimental conditions.

Figure 8.10 shows a set of interrelated two channel confocal scanning microscope (CLSM) images, in which channel 1 (PMT 1) displays the BODIPY emission (λ_{em} = 510 nm (A, C, E)), recorded between 500 – 530 nm, while channel 2 (PMT2) shows the Texas Red emission (λ_{em} = 614 nm) and/or the TAMRA emission (λ_{em} = 580 nm), both recorded between 580 nm – 650 nm (B, D, F). The two bilayer compartments of the upper images A and B consist of either 90 mol% DOPC/10 mol% **1** (left, reactive) or 99% mol% DOPC/1 mol% Texas Red (right, control). Prior to the in situ coupling reaction of **1** with TAMRA-H6, which is supposed to occur only at the reactive lipid bilayer compartment (left stripe, without fluorescent probes), exclusively the Texas Red emission of the control bilayer compartment (right stripe) is recorded with photo multiplier tube 2 (PMT 2, B). Incubation of the sample with TAMRA-H6 (middle images) results in the formation of TAMRA-H6 lipopeptide, which renders the left lipid bilayer compartment detectable in PMT 2 (D). After the incubation of BODIPY labeled Ni-NTA functionalized vesicles with the supported bilayer compartments, vesicle adsorption is only observed on the left lipid bilayer compartment, containing covalent attached TAMRA-H6 (figure 8.10, E and F).

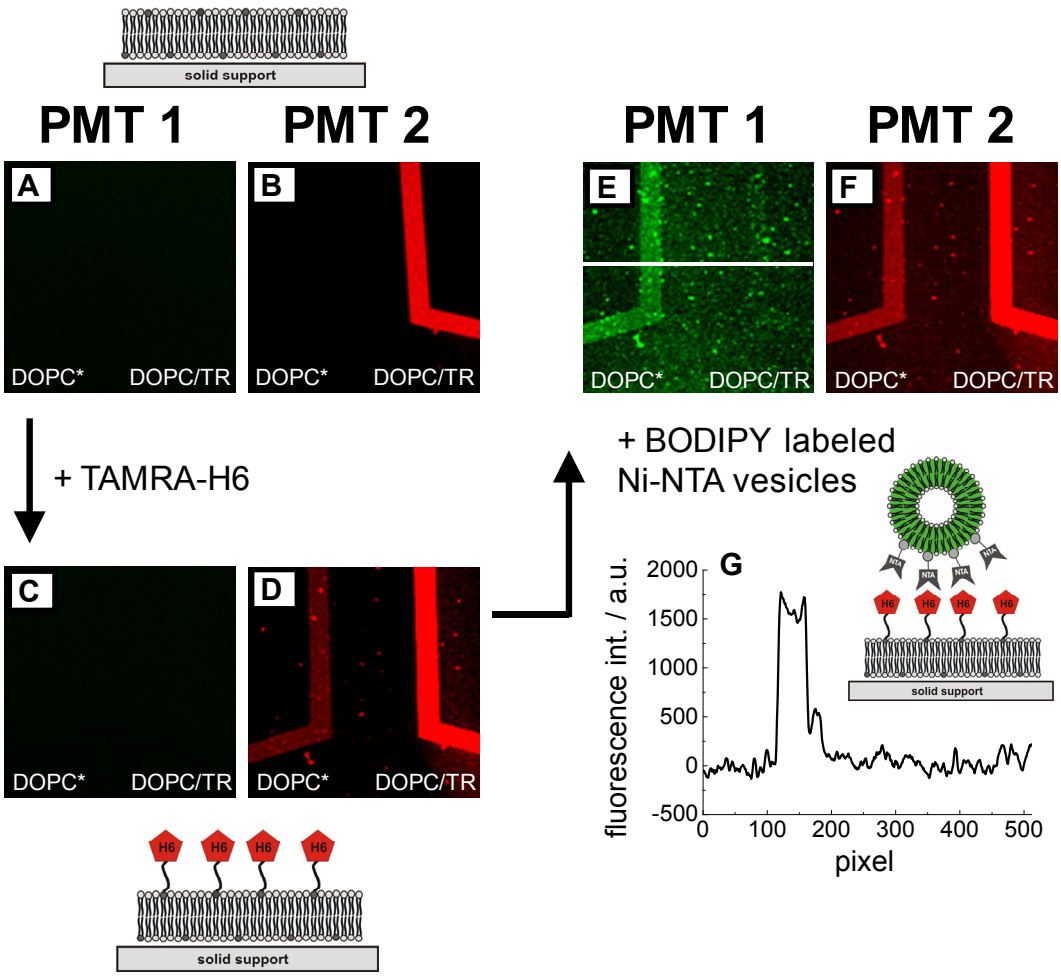

Figure 8.10. Left: Two channel confocal laser scanning microscopy images of the lipopeptide mediated binding of Ni-NTA vesicles to microstructured lipid bilayers. The schemes illustrate the in situ coupling reaction of the reactive lipid bilayer compartment including vesicle binding (left). Images were taken by two laser excitation at 488 nm and 543 nm. Photo multiplier tube 1 (PMT 1) recorded the BODIPY-C_{12}-PC (BODIPY) emission between 500 – 530 nm (green), while PMT 2 detects the rhodamine emission of TAMRA-H6 and the sulforhodamine 101 DHPE (Texas Red) emission between 580-650 nm (red). A, B) The left, non-fluorescent lipid bilayer compartment (DOPC*) is composed of 90% DOPC and 10% 1 and the right lipid bilayer compartment (DOPC/TR) is composed of 99% DOPC and 1% Texas Red. C, D) After the addition of 0.1 µmol TAMRA-H6 to the sample, resulting in an overall concentration of 0.03 mM TAMRA-H6 in PBS 6.8 for 90 min and thorough rinsing, the left compartment can be detected by the red light emission of the TAMRA labeled H6 lipopeptides. Prior to the lipopeptide mediated binding of functional vesicles, the sample was incubated in BSA solution (0.25 mg/ml in PBS 6.8) for 30 min to minimize non-specific vesicle adsorption on the glass substrate (cp. appendix A). E, F) BODIPY fluorescence after binding of Ni-NTA-DOGS containing vesicles (88% DOPC, 10% Ni-NTA-DOGS, 2% BODIPY C_{12}-HPC) at a final concentration of 0.1 mg lipid/ml in PBS 6.8 for 30 min. G) Absolute fluorescence intensity profile (indicated as a white line in E) of the BODIPY emission of image E.

Although non-specific adsorption of TAMRA-H6 occurs on the control stripe composed of neat DOPC, no significant binding of NTA bearing vesicles was observed (figure 8.10 G). Since the TAMRA-H6 is considered to be a minor hydrophobic peptide (hydrophilicity by Hopp-Woods of H6: -0.4)[61] with negligible secondary structure formation, it is conceivable that the non-specifically adsorbed peptide is partitioned into the lipid bilayer near the head group leaflet,[62] abolishing complexation of the TAMRA-H6 peptide with the Ni-NTA functionalized vesicle surface. We assume that the specific binding properties of the Ni-NTA functionalized vesicles to the histidine tagged lipid bilayers results from the hydrocarbon cyclohexyl-or n-hexyl-spacer, which seems to provide a sufficient availability of the peptide moiety to undergo complexation with the Ni-NTA headgroups. It should be noted, that lipopeptide mediated adsorption following the above described experiment was also achieved, when **2** was used as a reactive component (appendix A).

Furthermore, the lipopeptide mediated adsorption of negatively charged POPC/POPG vesicles on TAMRA-K8 modified bilayers under identical conditions, provided similar results (appendix B). We also found that the K8 lipopeptide mediated adsorption via electrostatic interactions between the polycationic K8 and negatively charged POPC/POPG only occurs if K8 is bound covalently to the lipid anchor. Non-specific adsorption of the TAMRA-K8 peptide did not result in any observable interaction of the negatively charged POPC/POPG vesicles with the bilayer, which implies that the surface charge density of the bilayer after non-specific TAMRA-K8 adsorption does not change significantly enough to permit quasi-irreversible attachment of POPC/POPG vesicles. Importantly, non-specific adsorption was exclusively detected in case of TAMRA labeled peptides, presumably due to the hydrophobic nature of the N-terminal fluorescent marker.

8.3.6 QUENCHING OF BODIPY FLUORESCENCE BY TAMRA LABELED PEPTIDES

Figure 8.11 shows the impact of TAMRA labeled peptides on the fluorescence of BODIPY labeled lipids. The fluorescence of BODIPY in the wavelength range between 570 and 600 nm was quenched upon in situ coupling as Förster resonance energy transfer (FRET) to TAMRA molecules occurs. Because images were captured during simultaneous excitation at 488 nm and 543 nm, TAMRA fluorescence detected by PMT 2 not only resulted from TAMRA directly excited by the 543 nm laser but also from TAMRA dyes excited by BODIPY via FRET. Since

FRET efficiency depends on the distance between the FRET donor acceptor pair a comparison of the extend of BODIPY quenching and increase in red fluorescence from TAMRA excited via FRET with the increase in red fluorescence from directly excited TAMRA provides information about the distance between BODIPY and TAMRA.

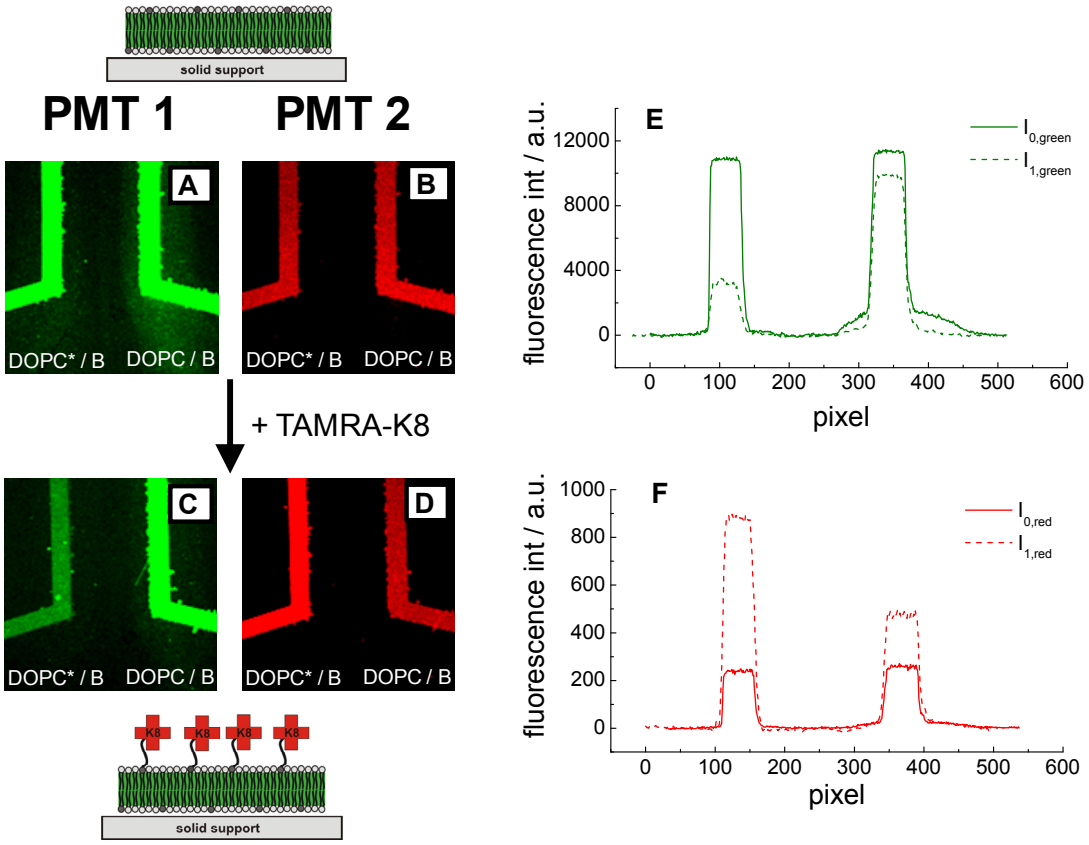

Figure 8.11. Two channel confocal laser scanning microscope images of the in situ coupling reaction of TAMRA-K8 to maleimide functionalized DOPC as illustrated by the corresponding schemes. The lipid bilayer compartments consist of 88 mol% DOPC/10 mol% 1/2 mol% BODIPY (DOPC*/B, left, reactive compartment) and 98 mol% DOPC/2 mol% BODIPY (DOPC/B, right, control compartment). A, B) Images display the two lipid bilayer compartments prior to the in situ coupling reaction with TAMRA-K8. C, D) Images taken after the exposition of the sample to 0.03 mM TAMRA-K8 solution in PBS 6.8 for 60 min, followed by thorough rinsing. E, F) Averaged fluorescence intensity profile across the lipid bilayer compartments of the BODIPY emission (E), the TAMRA K8 emission (F).

By this means, we will be able to infer to what extend the peptide moiety is buried in the membrane. For a qualitative analysis, experiments were performed in which samples

containing BODIPY labeled DOPC compartments with (left stripe) or without (right stripe) maleimide carrying lipids were excited separately at 488 nm and 543 nm, respectively, before and after in situ coupling to K8-TAMRA. Green BODIPY as well as TAMRA fluorescence was detected simultaneously by PMT 1 and PMT 2, respectively (figure 8.11).

The analysis of the change in fluorescence intensity subsequent to in situ coupling to K8-TAMRA of the reactive and the control compartment showed that for both compartments, the relative decrease in BODIPY fluorescence due to quenching and the relative increase in red fluorescence due to FRET correspond. Besides, the extend of increase in TAMRA fluorescence and of decrease in BODIPY fluorescence was much greater for the reactive compartment, which confirms that more TAMRA-K8 is covalently bound to the bilayer containing maleimide functionalized lipids than non-specifically attached to the DOPC control bilayer. However, the ratio of the increase in red fluorescence from TAMRA directly excited at 543 nm to the increase of red fluorescence from FRET was smaller for the control compartment than for the reactive compartment. This means that the FRET efficiency is higher for the control compartment than for the reactive compartment and hence we draw conclusion, that the distance between the donor BODIPY and the acceptor TAMRA is smaller if TAMRA-K8 is non-specifically interacting with the DOPC bilayer as compared to covalently coupled K8-TAMRA. Non-specific TAMRA-K8 is therefore deeper embedded in the DOPC-bilayer than the covalently coupled TAMRA peptide. Hence, the cyclohexyl-methyl-group of the crosslinker serves its function as a spacer keeping a distance between the peptide and the lipid bilayer. These results were further corroborated fluorescence spectroscopy, as detailed below.

8.3.7 TRYPTOPHAN FLUORESCENCE MEASUREMENTS

Fluorescence spectroscopy was applied in order to investigate the covalent coupling process of K8 (Cys-Gly-Trp-$(Lys)_8$-Ac) to maleimide functionalized lipid vesicles, in contrast to the binding process of the K8 peptide via non-specific electrostatic interactions with POPC/POPG vesicles. The maximum of the tryptophan fluorescence is sensitive to the dielectric environment and it is known that a blue-shift in the fluorescence maximum occurs if the peptide binds to or inserts into the lipid bilayer. It was shown that the tryptophan

fluorescence displays a maximum fluorescence emission between 335 and 343 nm if the tryptophan moiety is located near the head group region of a phospholipid bilayer.[63]

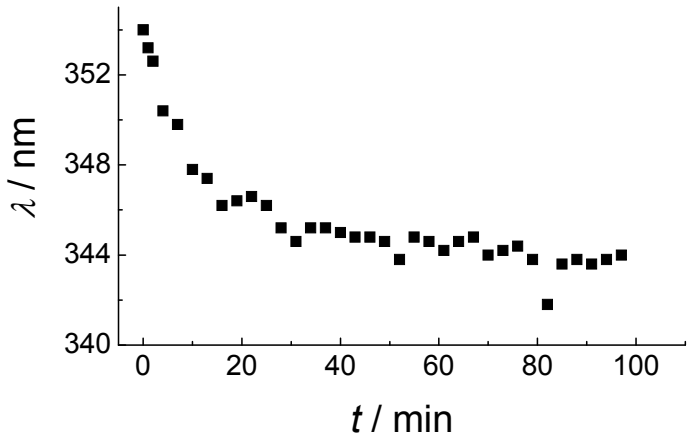

Figure 8.12. Change in tryptophan fluorescence (λ_{max}) as a function of time after adding a vesicle suspension composed of 1.4 mg/ml DOPC* SUVs (200 µl) to a peptide solution consisting of 5 mM K8 in PBS 6.8. The fluorescence spectra of the neat peptide in PBS 6.8 exhibited an emission maximum at 354 nm.

We found only a blue shift of the tryptophan emission to 344 nm upon addition of 200 µl of a 1 mg/ml vesicle solution consisting of 90 % DOPC and 10 % **1** in PBS 6.8 (figure 8.12) to the peptide (c = 5 mM). The tryptophan emission of the pure peptide solution was measured to be 354 nm. Control experiments using neat DOPC SUVs did not show a blue shift of the tryptophan fluorescence, which is probably due to lack of interaction between pure DOPC and the charged peptide. As a consequence, we investigated the non-specific adsorption of K8 on POPC/POPG vesicles form comparison to shift of the tethered peptide. We found a substantial blue shift of 14 nm upon addition of SUVs composed of 30% POPC and 70% POPG (200 µl, 1 mg/ml) to a 5 mM K8 solution in PBS 6.8 (not shown). Importantly, the shift in tryptophan emission using maleimide functionalized bilayers is 4 nm less than observed for POPC/POPG vesicles and far less than expected for deep insertion of tryptophan into the bilayer matrix. We explain these finding in terms of an increased spacing between the tryptophan residue and the bilayer head group region in the case of covalently bound peptides rendering the peptides easily accessible by ligands in solution.

8.4 CONCLUSIONS

Selective in situ coupling of oligopeptides was achieved using preformed solid supported lipid bilayers on silicon, glass, and gold doped with maleimide bearing phospholipids. By utilizing a large variety of techniques such as atomic force microscopy, confocal laser scanning techniques, quartz crystal microbalance, ellipsometry, and fluorescence spectroscopy we were able to scrutinize the process of peptide coupling and subsequent nanoparticle and vesicle deposition by ligand receptor interactions. We found that the coupling process is highly specific and that peptides are more easily accessible than those which are merely non-specifically adsorbed on the membrane. Hence, interaction of functionalized vesicles exclusively occurs on peptide displaying maleimide functionalized SSLB. The proposed in situ functionalization scheme in conjunction with microstructured membranes paves the way for exploring peptide epitopes and receptors without cumbersome reconstitution of transmembrane proteinaceous receptors.

8.5 REFERENCES

[1] Brian, A. A. and McConnell, H. M. Allogeneic Stimulation of Cytotoxic T Cells by Supported Planar Membranes. *PNAS* **1984**, 81, 6159-6163.

[2] Tamm, L. K. and McConnell, H. M. Supported phospholipid bilayers. *Biophys. J.* **1985**, 47, 105-113.

[3] Cooper, M. A. Advances in membrane receptor screening and analysis. *Journal of Molecular Recognition* **2004**, 17, 286-315.

[4] Janshoff, A. and Steinem, C. Transport across artificial membranes–an analytical perspective. *Analytical and Bioanalytical Chemistry* **2006**, 385, 433-451.

[5] Tanaka, M. and Sackmann, E. Polymer-supported membranes as models of the cell surface. *Nature* **2005**, 437, 656-663.

[6] Cremer, P. S.; Groves, J. T.; Kung, L. A. and Boxer, S. G. Writing and Erasing Barriers to Lateral Mobility into Fluid Phospholipid Bilayers. *Langmuir* **1999**, 15, 3893-3896.

[7] Groves, J. T.; Ulman, N. and Boxer, S. G. Micropatterning Fluid Lipid Bilayers on Solid Supports. *Science* **1997**, 275, 651-653.

[8] Groves, J. T.; Ulman, N.; Cremer, P. S. and Boxer, S. G. Substrate-Membrane Interactions: Mechanisms for Imposing Patterns on a Fluid Bilayer Membrane. *Langmuir* **1998**, 14, 3347-3350.

[9] Hovis, J. S. and Boxer, S. G. Patterning Barriers to Lateral Diffusion in Supported Lipid Bilayer Membranes by Blotting and Stamping. *Langmuir* **2000**, 16, 894-897.

[10] Hovis, J. S. and Boxer, S. G. Patterning and Composition Arrays of Supported Lipid Bilayers by Microcontact Printing. *Langmuir* **2001**, 17, 3400-3405.

[11] Kam, L. and Boxer, S. G. Formation of Supported Lipid Bilayer Composition Arrays by Controlled Mixing and Surface Capture. *J. Am. Chem. Soc.* **2000**, 122, 12901-12902.

[12] Kung, L. A.; Kam, L.; Hovis, J. S. and Boxer, S. G. Patterning Hybrid Surfaces of Proteins and Supported Lipid Bilayers. *Langmuir* **2000**, 16, 6773-6776.

[13] Castellana, E. T. and Cremer, P. S. Imaging large arrays of supported lipid bilayers with a macroscope. *Biointerphases* **2007**, 2, 57-63.

[14] Holden, M. A. and Cremer, P. S. Microfluidic tools for studying the specific binding, adsorption, and displacement of proteins at interfaces. *Annual Review of Physical Chemistry* 2005, 56, 369-387.

[15] Holden, M. A.; Jung, S. Y. and Cremer, P. S. Patterning Enzymes Inside Microfluidic Channels via Photoattachment Chemistry. *Anal. Chem.* **2004**, 76, 1838-1843.

[16] Holden, M. A.; Jung, S. Y.; Yang, T.; Castellana, E. T. and Cremer, P. S. Creating Fluid and Air-Stable Solid Supported Lipid Bilayers. *J. Am. Chem. Soc.* **2004**, 126, 6512-6513.

[17] Shi, J.; Yang, T.; Kataoka, S.; Zhang, Y.; Diaz, A. J. and Cremer, P. S. GM1 Clustering Inhibits Cholera Toxin Binding in Supported Phospholipid Membranes. *J. Am. Chem. Soc.* **2007**, 129, 5954-5961.

[18] Yang, T.; Jung, S. y.; Mao, H. and Cremer, P. S. Fabrication of Phospholipid Bilayer-Coated Microchannels for On-Chip Immunoassays. *Anal. Chem.* **2001**, 73, 165-169.

[19] Yang, T.; Simanek, E. E. and Cremer, P. Creating Addressable Aqueous Microcompartments above Solid Supported Phospholipid Bilayers Using Lithographically Patterned Poly(dimethylsiloxane) Molds. *Anal. Chem.* **2000**, 72, 2587-2589.

[20] Janshoff, A. and Kunneke, S. Micropatterned solid-supported membranes formed by micromolding in capillaries. *European Biophysics Journal* **2000**, 29, 549-554.

[21] Kunneke, S. and Janshoff, A. Visualization of molecular recognition events on microstructured lipid-membrane compartments by in situ scanning force microscopy. *Angewandte Chemie, International Edition* **2002**, 41, 314-316.

[22] Schuy, S. and Janshoff, A. Thermal expansion of microstructured DMPC bilayers quantified by temperature-controlled atomic force microscopy. *ChemPhysChem* **2006**, 7, 1207-1210.

[23] Schuy, S. and Janshoff, A. Microstructuring of phospholipid bilayers on gold surfaces by micromolding in capillaries. *Journal of Colloid and Interface Science* **2006**, 295, 93-99.

[24] Lenhert, S.; Sun, P.; Wang, Y.; Fuchs, H. and Mirkin, C. A. Massively Parallel Dip-Pen Nanolithography of Heterogeneous Supported Phospholipid Multilayer Patterns. *Small* **2007**, 3, 71-75.

[25] Yoshina-Ishii, C. and Boxer, S. G. Arrays of mobile tethered vesicles on supported lipid bilayers. *Journal of the American Chemical Society* **2003**, 125, 3696-3697.

[26] Yoshina-Ishii, C. and Boxer, S. G. Controlling Two-Dimensional Tethered Vesicle Motion Using an Electric Field: Interplay of Electrophoresis and Electro-Osmosis. *Langmuir* **2006**, 22, 2384-2391.

[27] Yoshina-Ishii, C.; Miller, G. P.; Kraft, M. L.; Kool, E. T. and Boxer, S. G. General Method for Modification of Liposomes for Encoded Assembly on Supported Bilayers. *Journal of the American Chemical Society* **2005**, 127, 1356-1357.

[28] Benkoski, J. J.; Jesorka, A.; Edvardsson, M. and Hoeoek, F. Light-regulated release of liposomes from phospholipid membranes via photoresponsive polymer-DNA conjugates. *Soft Matter* **2006**, 2, 710-715.

[29] Glasmastar, K.; Larsson, C.; Hook, F. and Kasemo, B. Protein Adsorption on Supported Phospholipid Bilayers. *Journal of Colloid and Interface Science* **2002**, 246, 40-47.

[30] Michel, R.; Pasche, S.; Textor, M. and Castner, D. G. Influence of PEG Architecture on Protein Adsorption and Conformation. *Langmuir* **2005**, 21, 12327-12332.

[31] Jensen, T. W.; Hu, B. H.; Delatore, S. M.; Garcia, A. S.; Messersmith, P. B. and Miller, W. M. Lipopeptides Incorporated into Supported Phospholipid Monolayers Have High Specific Activity at Low Incorporation Levels. *J. Am. Chem. Soc.* **2004**, 126, 15223-15230.

[32] Bader, B.; Kuhn, K.; Owen, D. J.; Waldmann, H.; Wittinghofer, A. and Kuhlmann, J. Bioorganic synthesis of lipid-modified proteins for the study of signal transduction. *Nature* **2000**, 403, 223-226.

[33] Elliott, J. T. and Prestwich, G. D. Maleimide-Functionalized Lipids that Anchor Polypeptides to Lipid Bilayers and Membranes. *Bioconjugate Chemistry* **2000**, 11, 832-841.

[34] Frisch, B.; Boeckler, C. and Schuber, F. Synthesis of Short Polyoxyethylene-Based Heterobifunctional Cross-Linking Reagents. Application to the Coupling of Peptides to Liposomes. *Bioconjugate Chem.* **1996**, 7, 180-186.

[35] Svedhem, S.; Dahlborg, D.; Ekeroth, J.; Kelly, J.; Hoeoek, F. and Gold, J. In situ peptide-modified supported lipid bilayers for controlled cell attachment. *Langmuir* **2003**, 19, 6730-6736.

[36] Montanari, V. and Kumar, K. A fluorous capping strategy for Fmoc-based automated and manual solid-phase peptide synthesis. *European Journal of Organic Chemistry* **2006**, 874-877.

[37] Faiss, S.; Luethgens, E. and Janshoff, A. Adhesion and rupture of liposomes mediated by electrostatic interaction monitored by thickness shear mode resonators. *European Biophysics Journal* **2004**, 33, 555-561.

[38] Faiss, S.; Schuy, S. and Janshoff, A. Phase Transition of Individually Adressabe Microstructured Membranes Visualized by Imaging Ellipsometry. **2007**.

[39] Kim, E.; Xia, Y. and Whitesides, G. M. Micromolding in Capillaries: Applications in Materials Science. *J. Am. Chem. Soc.* **1996**, 118, 5722-5731.

[40] Xia, Y. and Whitesides, G. M. Soft Lithography. *Annual Review of Materials Science* **1998**, 28, 153-184.

[41] Steinem, C.; Janshoff, A.; Ulrich, W.-P.; Sieber, M. and Galla, H.-J. Impedance analysis of supported lipid bilayer membranes: a scrutiny of different preparation techniques. *Biochimica et Biophysica Acta, Biomembranes* **1996**, 1279, 169-180.

[42] Axelrod, D.; Koppel, D. E.; Schlessinger, J.; Elson, E. and Webb, W. W. Mobility measurement by analysis of fluorescence photobleaching recovery kinetics. *Biophys. J.* **1976**, 16, 1055-1069.

[43] Soumpasis, D. M. Theoretical analysis of fluorescence photobleaching recovery experiments. *Biophys. J.* **1983**, 41, 95-97.

[44] Knight, P. Hydrolysis of p-NN'-phenylenebismaleimide and its adducts with cysteine. Implications for cross-linking of proteins. *The Biochemical journal* **1979**, 179, 191-197.

[45] Janshoff, A.; Galla, H. J. and Steinem, C. Piezoelectric Mass-Sensing Devices as Biosensors - An Alternative to Optical Biosensors? *Angewandte Chemie* **2000**, 39, 4004-4032.

[46] Luethgens, E.; Herrig, A.; Kastl, K.; Steinem, C.; Reiss, B.; Wegener, J.; Pignataro, B. and Janshoff, A. Adhesion of liposomes: a quartz crystal microbalance study. *Measurement Science and Technology* **2003**, 14, 1865-1875.

[47] Johannsmann, D. Studies of Viscoelasticity with the QCM, Springer Series on Chemical Sensors and Biosensors: Piezoelectric biosensors: Studies of Viscoelasticity with the QCM, Springer Series on Chemical Sensors and Biosensors: Piezoelectric biosensors (Editors C. Steinem and A. Janshoff)*, Springer Verlag,* Berlin Heidelberg

2007, Vol. 5.

[48] Sauerbrey, G. Verwendung von Schwingquarzen zur Wägung dünner Schichten und zur Mikrowägung. *Zeitschrift für Physik A Hadrons and Nuclei* **1959**, 155, 206-222.

[49] Butt, H.-J. and Franz, V. Rupture of molecular thin films observed in atomic force microscopy. I. Theory. *Physical Review E* **2002**, 66, 031601.

[50] Loi, S.; Sun, G.; Franz, V. and Butt, H.-J. Rupture of molecular thin films observed in atomic force microscopy. II. Experiment. *Physical Review E* **2002**, 66, 031602.

[51] Kunneke, S.; Kruger, D. and Janshoff, A. Scrutiny of the Failure of Lipid Membranes as a Function of Headgroups, Chain Length, and Lamellarity Measured by Scanning Force Microscopy. *Biophys. J.* **2004**, 86, 1545-1553.

[52] Franz, V.; Loi, S.; Muller, H.; Bamberg, E. and Butt, H. J. Tip penetration through lipid bilayers in atomic force microscopy. *Colloids and Surfaces B: Biointerfaces* **2002**, 23, 191-200.

[53] Auer, F.; Scotti, M.; Ulman, A.; Jordan, R.; Sellergren, B.; Garno, J. and Liu, G. Y. Nanocomposites by Electrostatic Interactions: 1. Impact of Sublayer Quality on the Organization of Functionalized Nanoparticles on Charged Self-Assembled Layers. *Langmuir* **2000**, 16, 7554-7557.

[54] Zhang, H.-L.; Evans, S. D. and Henderson, J. R. Spectroscopic Ellipsometric Evaluation of Gold Nanoparticle Thin Films Fabricated Using Layer-by-Layer Self-Assembly. *Advanced Materials* **2003**, 15, 531-534.

[55] Spurlin, T. A. and Gewirth, A. A. Poly-L-Lysine-Induced Morphology Changes in Mixed Anionic/Zwitterionic and Neat Zwitterionic-Supported Phospholipid Bilayers. *Biophys. J.* **2006**, 91, 2919-2927.

[56] Benkoski, J. J. and Hook, F. Lateral Mobility of Tethered Vesicle-DNA Assemblies. *J. Phys. Chem. B* **2005**, 109, 9773-9779.

[57] Pick, H.; Schmid, E. L.; Tairi, A. P.; Ilegems, E.; Hovius, R. and Vogel, H. Investigating Cellular Signaling Reactions in Single Attoliter Vesicles. *J. Am. Chem. Soc.* **2005**, 127, 2908-2912.

[58] Bolinger, P. Y.; Stamou, D. and Vogel, H. Integrated Nanoreactor Systems: Triggering the Release and Mixing of Compounds Inside Single Vesicles. *J. Am. Chem. Soc.* **2004**, 126, 8594-8595.

[59] Stadler, B.; Falconnet, D.; Pfeiffer, I.; Hook, F. and Voros, J. Micropatterning of DNA-Tagged Vesicles. *Langmuir* **2004**, 20, 11348-11354.

[60] Svedhem, S.; Pfeiffer, I.; Larsson, C.; Wingren, C.; Borrebaeck, C. and Höök, F. Patterns of DNA-labeled and scFv-antibody-carrying lipid vesicles directed by material-specific immobilization of DNA and supported lipid bilayer formation on an Au/SiO2 template. *Chembiochem* **2003**, 4, 339-343.

[61] Hopp, T. P. and Woods, K. R. Prediction of Protein Antigenic Determinants from Amino Acid Sequences. *PNAS* **1981**, 78, 3824-3828.

[62] White, S. H. and Wimley, W. C. Peptides in lipid bilayers: structural and thermodynamic basis for partitioning and folding. *Current Opinion in Structural Biology* **1994**, 4, 79-86.

[63] Chung, L. A.; Lear, J. D. and DeGrado, W. F. Fluorescence studies of the secondary structure and orientation of a model ion channel peptide in phospholipid vesicles. *Biochemistry* **1992**, 31, 6608-6616.

8.6 APPENDIX AND CONTROL EXPERIMENTS

A

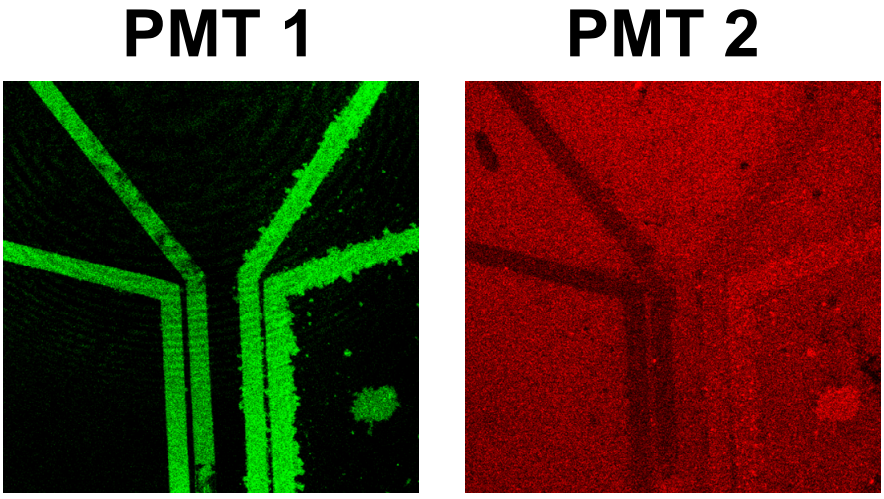

Appendix A. Two channel confocal laser scanning microscopy images of the H6 lipopeptide mediated adsorption of Texas Red labeled Ni-NTA vesicles on microstructured lipid bilayers without BSA passivation of the glass substrate. PMT 1 recorded the BODIPY emission and PMT 2 recorded the Texas Red emission. Initially the left control lipid bilayer compartment composed of 98% DOPC / 2% BODIPY and the right reactive lipid bilayer compartment composed of 88% DOPC/10% 2 / 2% BODIPY were exposed to 0.4 µmol H6 for 60 min. After rinsing the sample, it was incubated with unilamellar Texas Red labeled Ni-NTA DOPC vesicles, composed of 89% DOPC/10% Ni-NTA DOGS/1% Texas Red at a final concentration of 0.15 mg/ml for 30 min. The right H6 lipopeptide functionalized lipid bilayer compartment showed exclusively specific adsorption of Ni-NTA DOPC vesicles, whereas the control bilayer compartment remained non fluorescent in the PMT 2. Strong non-specific adsorption of Texas Red labeled Ni-NTA DOPC vesicles was observed on the glass background due to the lack of BSA passivation.

B

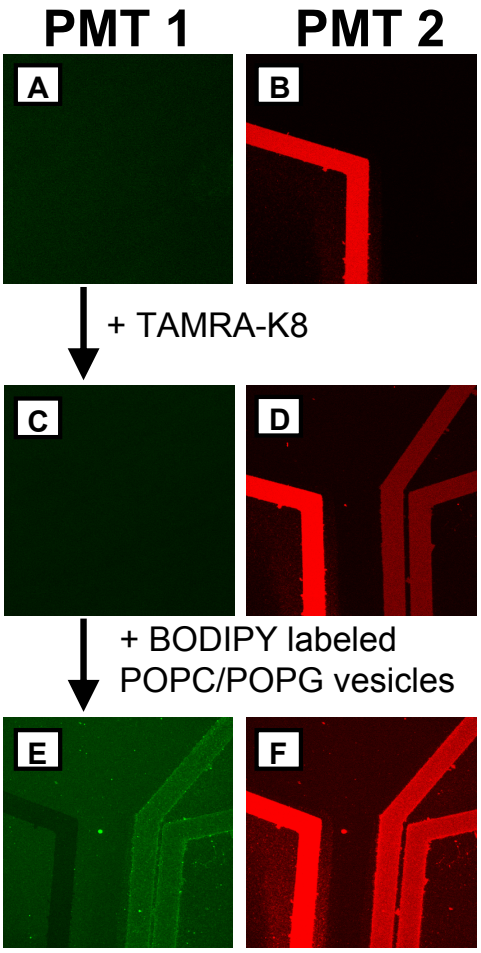

Appendix B. Two channel confocal laser scanning microscopy images of the lipopeptide mediated adsorption of POPC/POPG vesicles to microstructured lipid bilayers containing K8 lipopeptides. Images were taken by two laser excitation at 488 nm and 543 nm. Photo multiplier tube 1 (PMT 1) recorded the BODIPY-C_{12}-PC (BODIPY) emission between 500 – 530 nm, while PMT 2 detects the rhodamine emission of TAMRA-H6 and the Sulforhodamine 101 DHPE (Texas Red) emission between 580-650 nm. A, B) The right, non-fluorescent lipid bilayer compartments are composed of 90% DOPC and 10% 1 and the left lipid bilayer compartment is composed of 99% DOPC and 1% Sulforhodamine 101 DHPE (Texas Red). C, D) After the addition of 0.1 µmol TAMRA-K8 to the sample, resulting in an overall concentration of 0.03 mM TAMRA-H8 in PBS 6.8 for 60 min and thorough rinsing, the right compartments can be detected by the red light emission of the TAMRA labeled K8 lipopeptides. Prior to the lipopeptide mediated adsorption of functionalized vesicles, the sample was incubated in BSA solution (0.25 mg/ml in PBS 6.8) for 30 min. E, F) BODIPY fluorescence after adsorption of POPC/POPG vesicles (30%POPC, 68% POPG, 2% BODIPY C_{12}-HPC) at a final concentration of 0.1 mg lipid/ml in PBS 6.8 for 30 min.

C

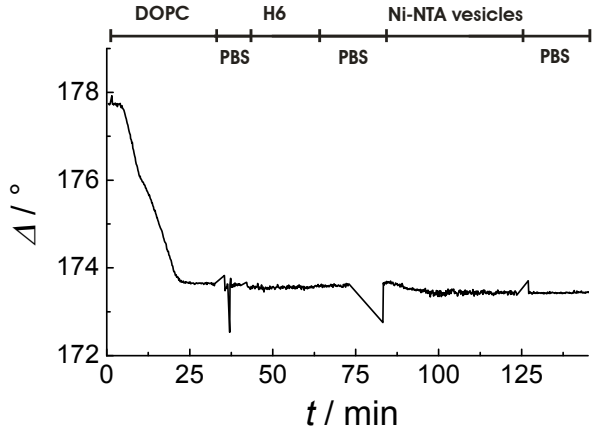

Appendix C. Time course of the ellipsometric Δ values of the H6 lipopeptide mediated adsorption of Ni-NTA DOPC vesicles on neat DOPC as a control experiment. Initially, unilamellar vesicles consistent of 100% DOPC were spread. After rinsing with buffer 0.4 µmol H6 in PBS 6.8 were added, yielding in no significant increase in layer thickness. Slight variations in the ellipsometric angle were recorded after the addition of unilamellar Ni-NTA DOPC vesicles (0.5 mg), resulting from non-specific adsorption.

D

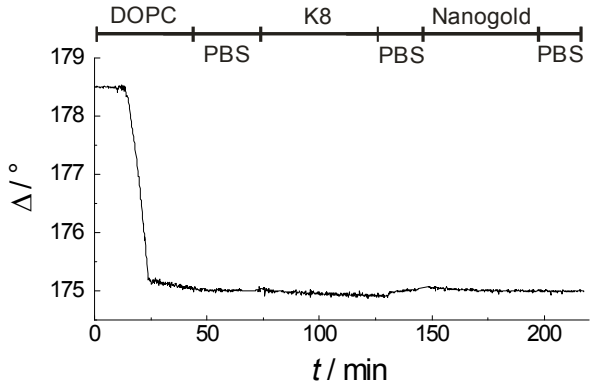

Appendix D. Time course of the ellipsometric Δ values of the control experiment for the K8 lipopeptide mediated adsorption of gold nanoparticles. Initially unilamellar vesicles consistent of 100% DOPC were spread. After rinsing 0.4 µmol K8 in PBS 6.8 were added, yielding no significant increase in layer thickness. Constant values in the ellipsometric angle were recorded after the addition of 0.5 nmol gold nanoparticles.

E

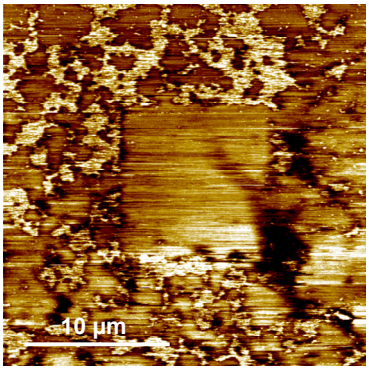

Appendix E. AFM image of H6 lipopeptide mediated adsorption of Ni-NTA functionalized DOPC vesicles. Image was taken from the surrounding scan area of figure 8.6. Bright areas in the image display intact vesicles which are adsorbed on the H6 lipopeptide functionalized bilayer. Dark areas display the second bilayer, which has formed upon vesicle rupturing.

CHAPTER IX

9 MIMICKING THE PRE-HAIRPIN INTERMEDIATE OF GP41

A SCREENING PLATFORM BASED ON COILED COIL LIPOPEPTIDES

IN ARTIFICIAL BIOMEMBRANES

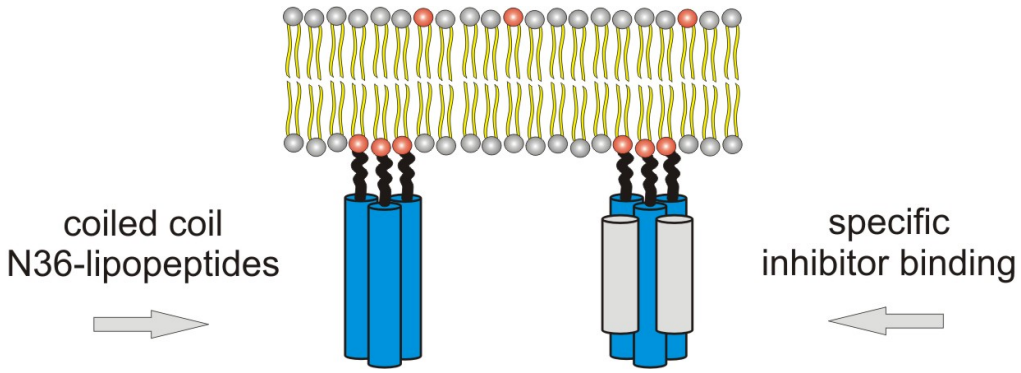

ABSTRACT

We present a novel mimetic approach of the pre hairpin intermediate of gp41, which represents the active drug target for fusion inhibitors of HIV based on membrane anchored lipopeptides. For this purpose, we have coupled terminal cysteine modified peptides originating from the NHR of SIV and HIV in situ to a maleimide functionalized DOPC bilayer and monitored the interactions with C34 and T20 by means of atomic force microscopy and ellipsometry. FT-IR analysis in conjugation with CD spectroscopy of hydrated N36-lipopeptides, incorporated in multilamellar bilayer stacks was employed to investigate their conformation. In contrast to solution studies substantial secondary structure formation of S-N36 during the in situ coupling reaction was found. We could show that S-N36 lipopeptide-aggregates in bilayers were selectively able to bind T20 or the corresponding C-peptides (C34) and similar results could be achieved by using H-N36 lipopeptides. Further, we were able to release T20, adsorbed to S-N36 lipopeptide containing bilayers by rinsing at elevated temperatures.

9.1 INTRODUCTION

Enveloped glycoprotein complexes (Env) enable the viral entry of the human- and simian-immunodeficiency virus into the target cell by viral mediated membrane fusion. Env is a homotrimeric type I integral protein, consisting of the heterodimeric subunits gp120 and gp41. The surface exposed subunit (gp120) and the transmembrane subunit (gp41), produced by the proteolytic cleavage of the highly glycosylated precursor gp160,[1, 2] are non covalently associated and control the key process of viral mediated membrane fusion (figure 9.1).

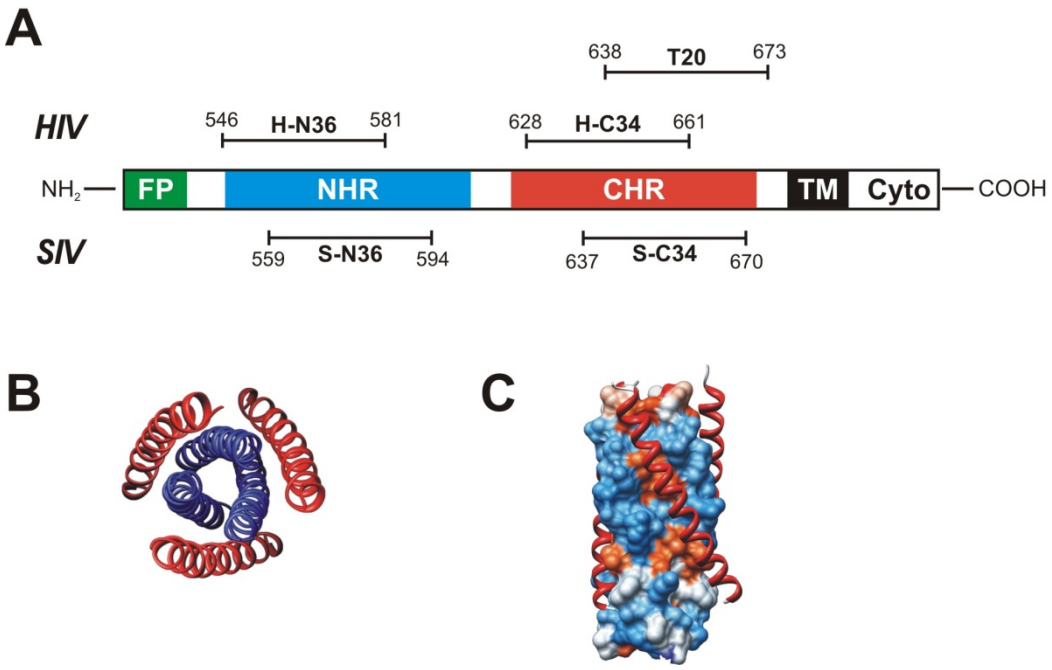

Figure 9.1. A) Ribbon diagram of gp41 of HIV and SIV (FP, fusion peptide; NHR, N-terminal heptad repeat unit; CHR, C-terminal heptad repeat unit; TM, transmembrane subunit; Cyto, cytoplasma of the virus). The residue numbers correspond to their positions in gp160 of HIV-1_{HXB2} and of SIV_{Mas239}, respectively. B, C) Core structure in the fusion active conformation of gp41 (trimer-of-hairpins) as determined by X-ray crystallography.[3] B) top view, ribbon structure. N36 peptides are shown in blue, C34 peptides are shown in red. C) Hydrophobicity plot of the interior N36 coiled coil (hydrophobicity legend: blue: polar amino acid side chains, white: small hydrophobic side chains, red: large hydrophobic side chains) and ribbon structure of C34 (red helix).

Triggered by binding of gp120 to CD4 receptors and chemokine coreceptors,[4-6] presented on the extracellular surface of T lymphocytes and macrophages, gp120 dissociates partially

from gp41. Subsequently, gp41 undergoes a sequence of conformational changes that eventually lead to membrane fusion of the host cell with the viral envelope. In the first step, conformational rearrangement of gp41 leads to an exposition and finally to insertation of the hydrophobic N-terminal fusion peptides (FP) into the host membrane, anchored via hydrophobic membrane spanning helices.[7, 8] The conformational changes of gp41 during the process of FP insertation into the host membrane are envisioned with what is referred to as the loaded spring model, known from the influenza virus.[7] In the next step of viral entry, gp120 is believed to entirely dissociate from gp41, enabling the C-terminal heptad repeat unit (CHR) to fold back towards the central N-terminal heptad repeat unit (NHR) by packing into the conserved hydrophobic groves of the trimeric coiled coil region of NHR. The formation of a six helix bundle forces the viral and the host membrane into close contact and fusion pores may induce membrane fusion.[3, 9, 10] The crystal core structure of gp41 is shown in figure 9.1.

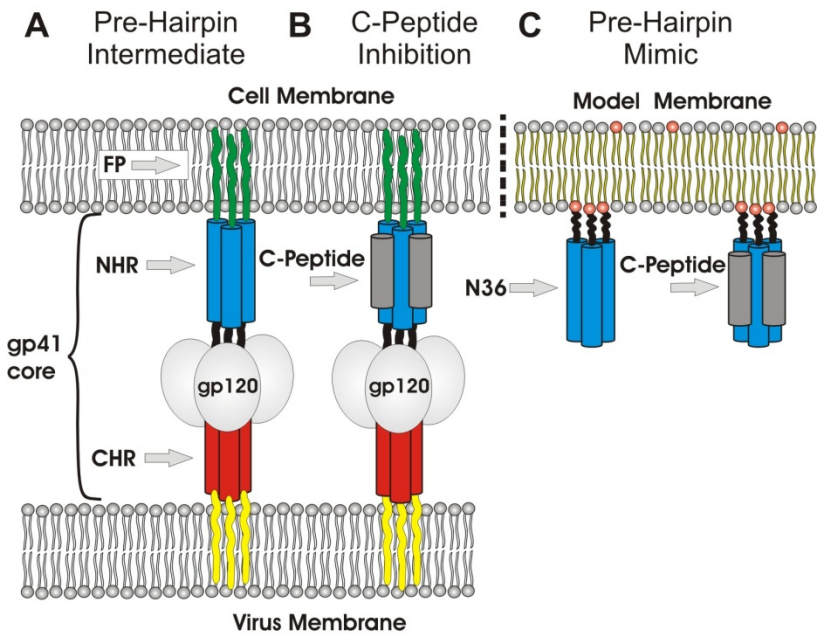

Figure 9.2. Representative scheme of the pre-hairpin intermediate and the pre hairpin mimic. A) Prior to inhibitor addition, B) Inhibitor adsorption to NHR, C) Pre hairpin mimic based on coiled coil lipopeptides in artificial biomembranes and C-peptide (inhibitor) adsorption.

The extended intermediate conformation of gp41 (figure 9.2 A), consisting of the trimeric coiled coil NHR bundle is long-lived and entry inhibitors (C-peptides or T20) can target the exposed pre-hairpin intermediate (figure 9.2 B) to inhibit the formation of the trimer-of-hairpin.[10-12]

Synthetic peptides (N36 and C34) displaying large areas of NHR and CHR, respectively, have been utilized as valuable models for the investigation of the crystal core structure of gp41, stability of the fusion active conformation and targets for entry inhibitors.[3, 12, 13] In fact, it was shown that C34, likewise T20 (Fuzeon) or other molecules targeting the hydrophobic groves of NHR, exhibit a promising potential for fusion inhibition.[12, 14-17] Our work focuses on the further structural understanding of the pre-hairpin intermediate by a mimetic approach based on synthetic N36-lipopeptides anchored in a DOPC lipid bilayer (figure 9.2 C). This sensor scheme will pave the way for antagonist screening beyond peptides derived from the native C-peptides towards small molecule inhibitors.

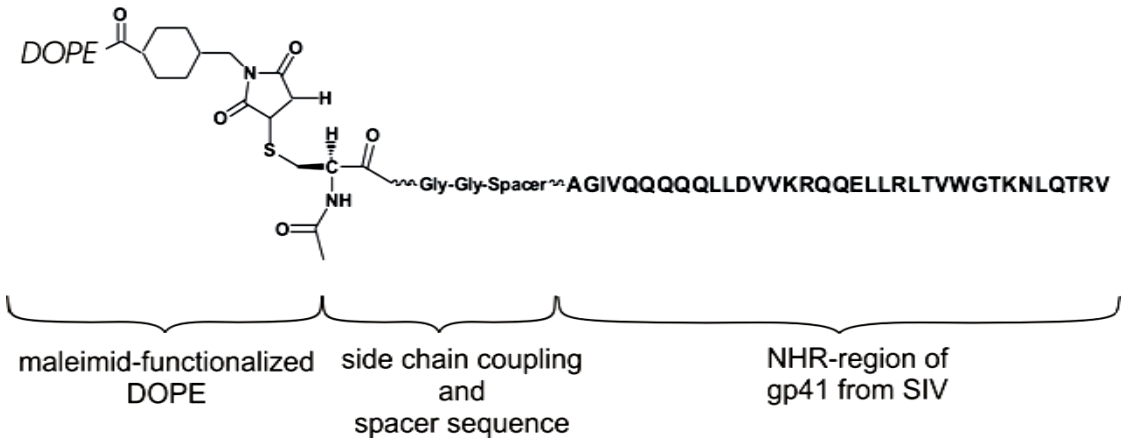

Figure 9.3. Molecular structure of the S-N36 lipopeptide (MCC-DOPE – SN36 conjugate). S-N36 is covalently bound to the reactive maleimide lipid (MCC-DOPE) by in situ synthesis of lipopeptides.

Terminal cysteine modified peptides originating from the NHR of SIV and HIV (S-N36 and H-N36, respectively) are coupled in situ to a maleimide functionalized DOPC bilayer. The reaction was monitored by means of by CD-spectroscopy, atomic force microscopy (AFM) and ellipsometry. The molecular structure of the resulting lipopeptide (e.g. MCC-DOPES-N36 lipopeptide) is shown in figure 9.3. Strikingly, we found a tendency of S-N36 to adopt a α-

helical conformation after coupling to a lipid bilayer, which indicates the formation of possible receptor structures for potential antagonists. We could show that S-N36 lipopeptides in bilayers were selectively able to bind T20 or the corresponding C-peptides (C34), whereto similar results could be achieved by using H-N36 lipopeptides. Furthermore, we were able to track a reversible binding of T20 after the inhibitor was released from the S-N36 lipopeptides by rinsing at elevated temperatures.

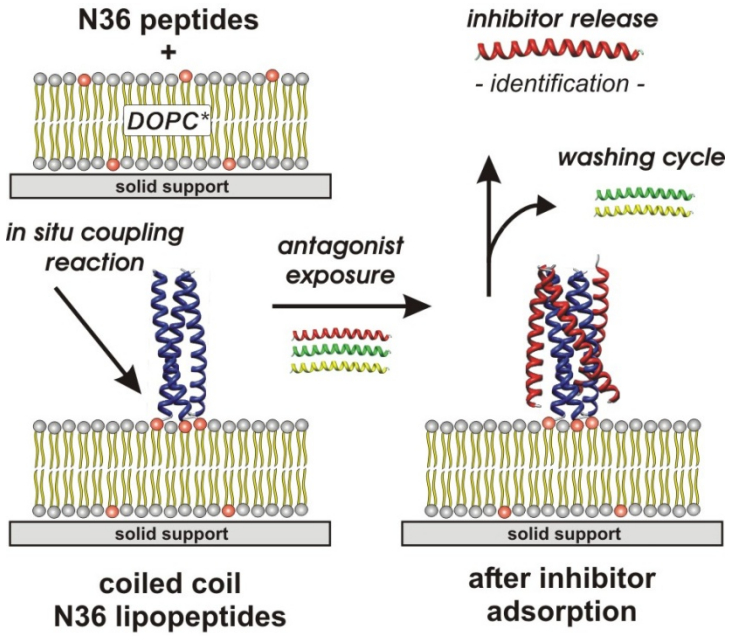

Figure 9.4. Scheme of the label free screening assay to detect potent antagonists to suppress viral mediated membrane fusion.

Mimicking the active drug target for fusion inhibitors under controllable experimental conditions, renders a label free fusion inhibitor screening assay within reach. A possible concept of the screening assay is given in figure 9.4. Specific binding of potent inhibitors is accomplished by coiled coil lipopeptides derived from the NHR unit of fusion proteins. Evaluation of the screening assay involves screening of a library of inhibitors, whereby specific interaction of potent antagonists can be identified after a washing cycle is applied. Inhibitor release can be accomplished by rinsing the assay at elevated temperatures and thus, breaking the thermodynamic stable coiled coil assembly of lipopeptides, whereby inhibitor identification can follow.

9.2 MATERIALS AND METHODS

9.2.1 VIRAL PEPTIDES

9.2.1.1 PEPTIDE SYNTHESIS AND PURIFICATION

Peptides was synthesized manually using *tert.*-butyloxycarbonyl (*t*-Boc) chemistry following the in situ neutralization protocols of Schnölzer et al. (cp. 3.4).[18] Crude acetylated peptides were purified by RP-HPLC on Grace Vydac C18 columns by using linear gradients; mobile phase RP-A, 99% H_2O / 1% AcCN / 0.075% TFA; mobile phase RP-B, 90% AcCN / 10% H_2O / 0.1% TFA (cp. 3.6). Peptides were identified by MALDI-TOF analysis. The purity of the resulting peptides as estimated from analytical RP-HPLC was greater than 85%.

T20 (Fuzeon®) was a gift from Roche Pharma (Mannheim, Germany). Before use, T20 was purified by RP-HPLC.

Peptides used for IR measurements were lyophilized from 0.05 M aqueous HCl solution (5x) to remove the trifluoroacetate counterions.[19]

9.2.1.2 PEPTIDE SEQUENCES

Peptide sequences as one letter code from N- to C- terminus (left to right).

S-N36: Ac-CGGAGIVQQQQQLLDVVKRQQELLRLTVWGTKNLQTRV

S-C34: Ac-WQEWERKVDFLEENITALLEEAQIQQEKNMYELQ

H-N36: Ac-CGGSGIVQQQNNLLRAIEAQQHLLQLTVWGIKQLQARIL

H-C34: Ac-WMEWDREINNYTSLIHSLIEESQNQQEKNEQELLGGC

T20: YTSLIHSLIEESQNQQEKNEQELLELDKWASLWNWF

9.2.1.3 PEPTIDE SOLUTIONS

Concentration of peptide stock solutions in 90% AcCN / 10% H_2O / 0.1% TFA were measured by UV absorption at 280 nm in 6M Gdn HCl solution.[20] Peptides were stored as 20 nmol and 50 nmol aliquots at -20°C. Aliquots were dissolved in 1.5 ml PBS 6.8 by gentle sonification at 70°C for 1 min and thorough vortexing. Insoluble peptide residues was removed by centrifugation and concentration of the saturated peptide solution were directly determined

from PBS 6.8 buffer. Average peptide concentrations in buffer were measured to be: (11 ± 2) µM (H-N36), (13 ± 2) µM(S-N36), (18 ± 3) µM (H-C34), (16 ± 3) µM (S-C34), (29 ± 2) µM (T20).

9.2.2 VESICLE PREPARATION AND IN SITU SYNTHESIS

9.2.2.1 VESICLE PREPARATION

In brief, multilamellar vesicles (MLVs) of the respective lipid were prepared in 50 mM PBS, pH = 5.9 (PBS 5.9) and transformed into small unilamellar vesicles (SUVs) by sonification (50 W, 0.4 s Puls, 20 min) using a vessel resonator (Sonoplus HD 2070, Bandelin, Berlin, Germany) (cp. 3.2).

9.2.2.2 IN SITU COUPLING REACTION ON SSLB

Unless stated otherwise, SSLBs were obtained by vesicle spreading in PBS 5.9 on the respective solid support. Spreading vesicles in buffer at pH 5.9 was employed to protect maleimid groups from hydrolysis during bilayer formation.[21] In situ coupling reactions on maleimide functionalized solid supported lipid bilayers (SSLB) were performed in 50 mM PBS pH = 6.8 (PBS 6.8). After rinsing the sample with PBS 6.8 fresh peptide solution was added, yielding peptide concentrations of at least 5 µM. In general, the coupling reaction was completed after 90 min and residual unreacted peptides were removed by rinsing thoroughly with PBS 6.8.

9.2.2.3 IN SITU COUPLING REACTION ON LIPOSOMES

MLVs were directly prepared in 50 mM PBS pH = 6.8 (PBS 6.8) from lipid films and transformed into SUVs via bioconjugation. In situ coupling reactions were performed in buffer on SUVs consisting of 90% DOPC / 10% MCC-DOPE. For this purpose, 300 µl of a 1.7 mg/ml liposome suspension were diluted with 700 µl of a N36 peptide solution in PBS 6.8 and stirred for 90 min. Subsequently, excess peptide was removed by gel filtration on Illustra NAP-25 columns (GE Healthcare, Buckinghamshire, UK) (1st gel filtration). Collected fractions were measured directly or incubated with 350 µl C-peptide (C34) or T20 solutions in buffer (overall concentration: $c_{C\text{-}peptides}$ ~ 5 µM, c_{T20} ~ 8 µM). In the case of C34 or T20 exposition to the lipopeptide containing vesicles, residual C-peptides were removed again by gel filtration as described above (2nd gel filtration). Average yield of vesicles after the 2nd gel filtration was determined to be 50% or less (cp. appendix G). In situ coupling reactions on liposomes were

accompanied by a slight increase of turbidity of the opalescent liposome suspension. For control experiments, vesicles consisting of neat DOPC were incubated with C34 or T20 using the same conditions and concentrations as for DOPC*, followed by gel filtration.

9.2.3 INSTRUMENTAL METHODS

9.2.3.1 ELLIPSOMETRY

Experiments were performed with an imaging ellipsometer (EP³-SW, Nanofilm Technology, Göttingen, Germany) as described previously (cp. 8.2).

Sample preparation: Hydrophilic silica substrates were prepared as described in chapter 3.2).[22] After the silicon substrate was placed in the ellipsometric measuring cell the substrate was rinsed with PBS 5.9. Subsequent addition of 0.25 mg SUVs consisting of 90% DOPC / 10% MCC-DOPE in 1.2 ml PBS 5.9 resulted in a spontaneous adsorption, as indicated by the strong decrease in Δ, followed by rupturing and spreading of the vesicles. After formation of the SSLB was completed, as indicated by constant Δ values, the sample was rinsed with PBS 6.8. For ellipsometric measurements, a large excess of N36 peptides was needed to initialize the in situ coupling reaction to the SSLB. Therefore, the first aliquot (50 nmol in 1.2 ml PBS 6.8), which was injected into the closed fluid circuit of the ellipsometric measurement cell was exchanged after 20 min reaction time with a fresh aliquot (50 nmol in 1.2 ml PBS 6.8). Note that the figure text only the overall amount of peptide is given ($c_{overall}$ ~ 12-15 µM). Adsorption of T20 or C-peptides was accomplished by adding 50 nmol of the corresponding peptide dissolved in 1.2 ml PBS 6.8 (c_{T20} ~ 10 µM).

9.2.3.2 ATOMIC FORCE MICROSCOPY

Experiments were carried out in aqueous solutions using a commercial scanning force microscope (Dimension 3100 with Nanoscope IIIa+A/D controller, Veeco Digital Instruments, Santa Barbara, CA, USA). Silicon nitride cantilevers (OMCL-TR400PSA, Olympus, Japan) exhibiting a nominal spring constants of 0.08 N/m were used for tapping mode in aqueous solution at controlled temperature.

Sample preparation: SUVs consting of 90% DOPC and 10% MCC-DOPE were prepared in Tris buffer (5 mM Tris, 3 mM $CaCl_2$, pH 5.9) as described above (4.2). Formation of the SSLB on mica was accomplished by deposition of 1 ml vesicle suspension (0.1 mg/ml) on a piece of

freshly cleaved mica, followed an incubation for 2h. After heating the sample to 65°C for 10 min, the sample was thoroughly rinsed with PBS 6.8 and measured or further functionalized.

9.2.3.3 CD-SPECTROSCOPY.

CD measurements were performed with a Jasco J-810 (Groß-Umstadt, Germany) CD Spectrometer. All spectra were acquired in a 2 mm cuvette at 25°C by using a 2 nm spectral bandwidth, 2 sec response time, 50 nm/min scanning speed. Baseline correction of the spectra obtained from peptide solutions or from lipopeptide containing vesicle suspensions was accomplished by subtraction of the spectra of the neat solvent or of a vesicle suspension consisting of neat DOPC, respectively. Spectra were accumulated (3x), averaged and smoothed. Peptide solutions and lipopeptide containing liposomes were prepared as described above.

Monitoring the band at 222 nm during the in situ coupling reaction of S-N36 on lipid vesicles consisting of 90% DOPC and 10% MCC-DOPE was accomplished by an interval scan measurement. Therefore 100 µl vesicle suspension was mixed with 250 µl S-N36 in PBS 6.8 and measured. CD spectra were recorded with a 2 min interval for 90 min. Peak evaluation at 222 nm was analyzed by using the Jasco software utility.

9.2.3.4 INFRARED SPECTROSCOPY

Fourier transform infrared spectra were measured on a Bruker Vertex 70 spectrometer with a DTGS detector at 2 cm^{-1} resolution and a sampling time of 60 s at room temperature. Absorption spectra of stacks of the lipopeptide vesicles were obtained in D_2O in a BaF_2 cuvette with 8 µm path length against pure D_2O as background.

Sample preparation: Samples were prepared by concentrating the lipopeptide vesicle suspensions in Milli Q water to ~2 mg/ml using Vivaspin 10kDa concentrators (Sartorius, Epsom, UK) and drying 50 µl of the concentrated suspensions on the IR windows under a stream of nitrogen. The sample films were covered with excess D_2O and the cuvettes were assembled. D_2O exchange was found to be complete in all samples. The amide I band pattern was decomposed into its constituent bands using second order derivative analysis to determine the positions of the bands[23] and fitted by Gaussian absorption peaks with a an empirically determined uniform 20 cm^{-1} half width (except for the 1644 cm^{-1} band of H-N36, for which a 25 cm^{-1} half width was used to improve the fit) using the Bruker Opus spectroscopy software. The relative intensities of the bands are integral intensities.

9.3 RESULTS

9.3.1 STRUCTURAL ANALYSIS OF N36 LIPOPEPTIDES INCORPORATED IN DOPC VESICLES

9.3.1.1 CD-SPECTROSCOPY

CD-spectroscopy was used to measure the changes in secondary structure formation of the viral N-peptides (S-N36, H-N36) upon binding to the maleimide groups of liposomes equipped with 10 % MCC-DOPE. Therefore, CD-spectra of the N-peptides in buffer were compared to the spectra of N36-lipopeptide containing DOPC liposomes (figure 9.5). In case of S-N36, the in situ coupling reaction of S-N36 to functionalized DOPC SUVs was additionally monitored by measuring the 222 nm band intensity of the CD-spectra over time (inset figure 9.5 A).

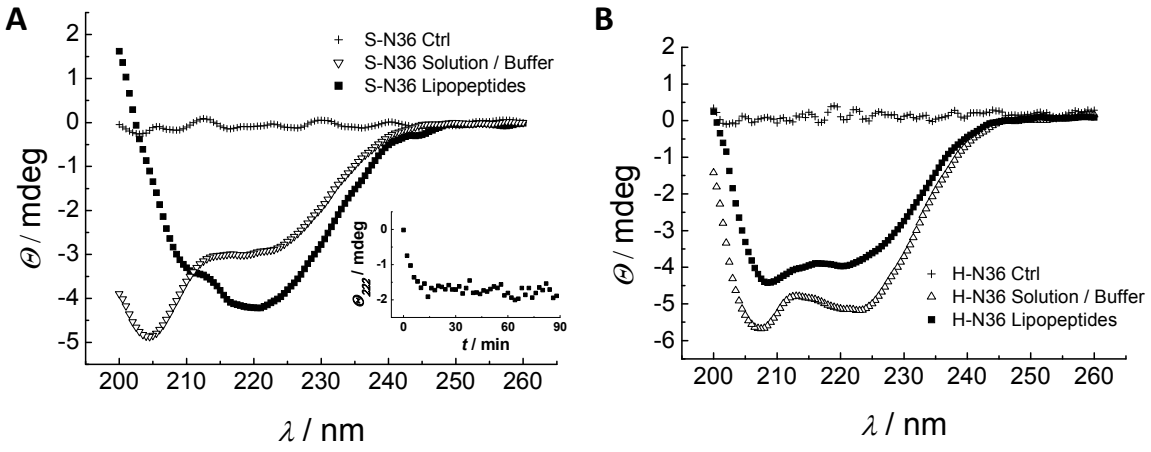

Figure 9.5. CD spectra of N36-lipopeptide containing DOPC liposomes (■) compared to N36 peptides in buffer (∇).A) S-N36 lipopeptide containing vesicles and S-N36 peptide in buffer. Control experiments (+) using neat DOPC vesicles did not show adsorption of N36. Inset displays the increase in peak intensity of the 222 nm band over time. B) H-N36 lipopeptide containing DOPC vesicles and H-N36 peptide in buffer.

Figure 9.5 A reveals that the secondary structure of S-N36 is tremendously altered by covalent anchoring of the peptide on a DOPC vesicle. In agreement with the results of Malashkevich et al., no significant helical secondary structure was detected for S-N36

peptides in solution (cp. appendix C),[3] while we observed a high propensity of S-N36 lipopeptides anchored to DOPC* liposomes to adopt α-helical conformation. The pronounced double minima of ellipticity at 208 nm and 222 nm wavelength are indicative for α-helical conformation.[23] Further, monitoring of the 222 nm band intensity during in situ synthesis as a function of time reveals a fast coupling reaction, comparable with the results obtained from in situ coupling of smaller peptides, such as oligolysines (K8) to maleimid functionalized vesicles using fluorescence spectroscopy (cp. 8.3.7).

In contrary to S-N36, the secondary structure of H-N36 was not substantially altered when coupled to DOPC liposomes (Figure 9.5 B). Clearly, α-helical secondary structure elements are already present for H-N36 peptides in solution as well as for H-N36 lipopeptides covalently coupled to DOPC* vesicles. Control experiments using neat DOPC SUVs did not show an altering of the CD-spectra when mixed with S-N36 or H-N36 (not shown), nor, non specific adsorption of N-peptides was detected (figure 9.5 (+)). Therefore, vesicles consisting of neat DOPC were incubated with S-N36 or H-N36 for 30 min, followed by gel filtration to remove the unbound peptide. The control samples did not reveal a significant CD signal.

9.3.1.2 FT-IR SPECTROSCOPY

Fourier transformed infrared spectroscopy of the amide I band of fully deuterated N36-lipopeptides in hydrated multilamellar bilayer stacks (cp. appendix A) was carried out to determine whether the N-peptides form coiled coil motives when coupled to a bilayer or vesicle in situ (figure 9.6). The spectral maxima of the amide I region of both lipopeptides, S-N36 and H-N36 (figure 9.6 A and B, respectively), anchored to a hydrated multilamellar DOPC bilayer is located well below the classical α-helical band (1651 cm^{-1}), i.e. 1643 cm^{-1} for S-N36 lipopeptides and 1645 cm^{-1} for H-N36 lipopeptides within a DOPC bilayer (table 1), indicative for coiled coil aggregatess.[24, 25]

Peak deconvolution (see experimental section for details) revealed a distinctive three band pattern for the analyzed lipopeptides, localized at 1653 cm^{-1}, 1642 cm^{-1}, 1632 cm^{-1} for S-N36 lipopeptides and 1653 cm^{-1}, 1644 cm^{-1} and 1633 cm^{-1} for H-N36 lipopeptides (table 1). In the case of S-N36 a fourth, major peak at 1615 cm^{-1} was found.

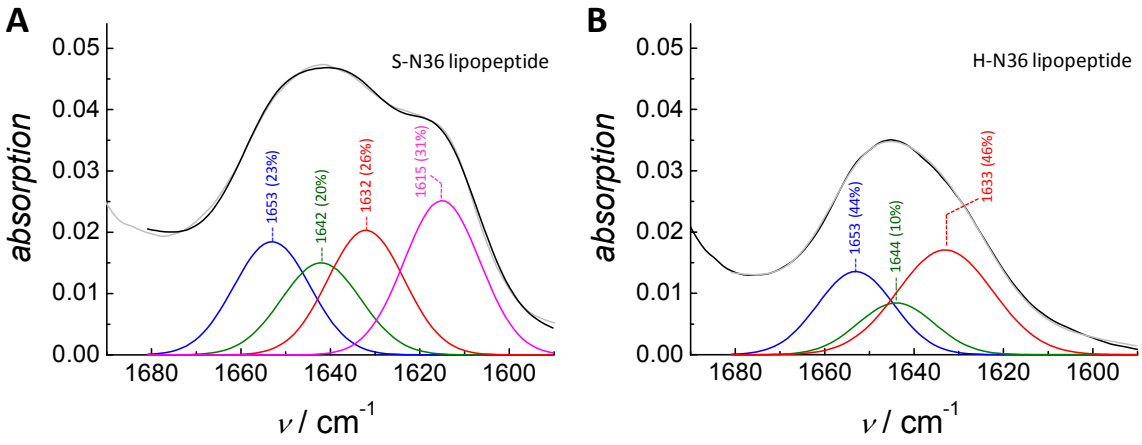

Figure 9.6. FTIR adsorption spectra of fully deuterated N36-lipopeptides incorporated into DOPC multilamellar bilayer stacks. Grey line shows the measured FT-IR spectra. Fitted spectra are shown in black. Blue, green, red and magenta lines show the deconvoluted peaks. A) S-N36 lipopeptides, B) H-N36 lipopeptides. Control experiments using neat DOPC vesicles for incubation with N36-peptides, followed by gel filtration did not exhibit a amide I band (not shown).

	band 1 [cm^{-1}]	band 2 [cm^{-1}]	band 3 [cm^{-1}]	band 4 [cm^{-1}]	spectral weight [cm^{-1}]	spectral max [cm^{-1}].
S-N36 LP	1653	1642	1632	1615	1642	1643
(area)	(23)	(20)	(26)	(31)		
H-N36 LP	1653	1644	1633	-	1641	1645
(area)	(31)	(19)	(50)	-		

Table 9.1. Band positions and areas of the deconvoluted peaks of the amide I region of coiled coil lipopeptides including the spectral weight and the spectral maxima. Spectral weights (v) are deduced from the band positions and calculated from the peaks of band 1-3 [(v) = (av_a + bv_b+ cv_c)/(a + b +c)].[25] Spectral maxima are those of the un-deconvolved amide I band.

9.3.2 ATOMIC FORCE MICROSCOPY OF N36-LIPOPEPTIDES IN DOPC SSLBS

Further indication that viral lipopeptides assemble into a higher order structure can be drawn from figure 9.7. The figure shows time elapsed AFM imaging of the in situ coupling reaction of S-N36 to maleimide functionalized solid supported DOPC bilayers revealing a clustering of lipopeptides.

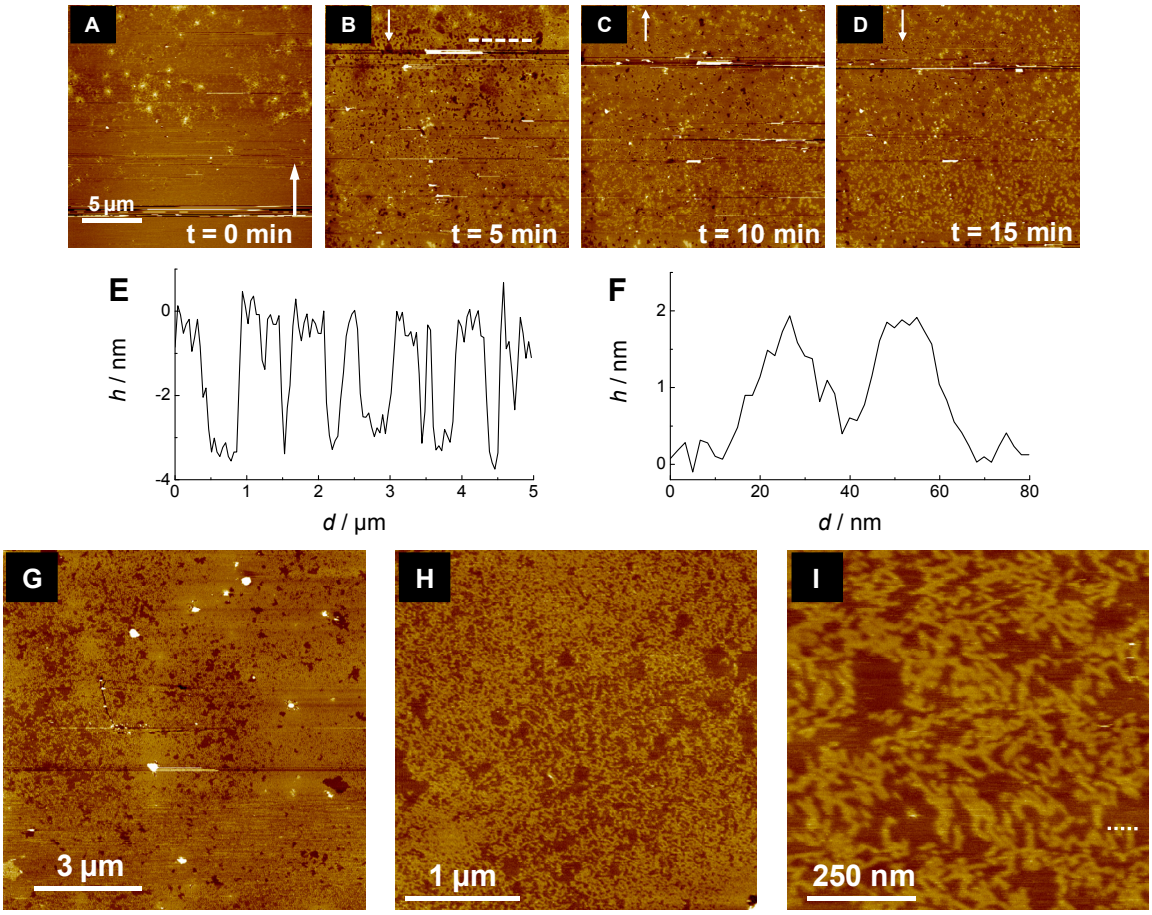

Figure 9.7. A-D) Time elapsed AFM images of the in situ coupling reaction of S-N36 to a lipid bilayer composed of 90% DOPC / 10% MCC-DOPE. Slow scan axis and addition of 50 nmol S-N36 in PBS 6.8 buffer (overall concentration: c ~ 10 µM) in image A is indicated with an arrow. The layer thickness of the bilayer, determined from the defect areas of image B was (3.4 ± 0.2) nm. E, F) Height profile along the white dashed line in image B, I, respectively. G, H, I) Images taken after 2 h coupling time and rinsing with buffer. Lipopeptide enriched domains exhibit a step height of (1.9 ± 0.3) nm on top of the bilayer (determined from image I, dashed line measures across two separated ribbon aggregates, cp. F).

In figure 9.7 A the addition of 50 nmol S-N36 in PBS 6.8 (c ~ 10 µM) to a solid supported bilayer consisting of 90% DOPC / 10% MCC-DOPE is indicated by the large arrow. Initially, S-N36 binds instantly to the bilayer surface. Subsequent images (figure 9.7 B-D) reveal that S-N36 induces randomly distributed defect areas throughout the bilayer, which heal out over time, resulting in circular lipopeptide enriched domains. After 90 min reaction time the in situ coupling reaction was found to be complete and the sample was thoroughly rinsed with buffer. Figure 9.7 G reveals that the in situ lipopeptide formation results in a dense coverage of the bilayer with lipopeptides. Higher magnification of the less lipopeptides enriched areas reveals further that the lipopeptides assemble into randomly oriented, ribbon like aggregates, exhibiting a variable ribbon length, but a distinctive height and width (figure 9.7 H and I). Ribbon aggregates of lipopeptides exhibited a step height of (1.9 ± 0.3) nm towards the bilayer and are about 15 nm wide.

9.3.3 BINDING OF FUSION INHIBITORS AND C-PEPTIDES

In the following section the specific recognition of potential antagonists of HIV and SIV, such as T20 and corresponding C-peptides are investigated by means of AFM, ellipsometry and CD-spectroscopy.

9.3.3.1 ATOMIC FORCE MICROSCOPY

Figure 9.8 A shows a S-N36 lipopeptide equipped bilayer (cp. figure 9.7) after the addition of 25 nmol T20 in PBS 6.8 (c ~ 7 µM) and subsequent rinsing. The bilayer was prepared as described in the previous section. T20 adsorption was detected by the formation of higher domains, exhibiting (2.1 ± 0.3) nm in height with respect to S-N36 lipopeptides. Clearly visible is the adsorption of T20 in the vicinity of the defect areas of the S-N36 lipopeptide layer, forming extended domains along the defect margin. The linescan in figure 9.8 B is taken across a defect area of the DOPC bilayer (figure 9.8 A, white line) and thus, revealing the height of each individual layer. S-N36 lipopeptide containing bilayers are determined to be (6.0 ± 0.4) nm in height ((3.7 ± 0.2) nm of the DOPC bilayer plus (1.9 ± 0.3) nm of the bound S-N36). The additional layer thickness of the adsorbed T20 is measured to be about (2.1 ± 0.3) nm. We note that the characteristic ribbon structure of the S-N36 lipopeptides is still visible, when T20 was added, but appears to be rather undefined and laterally expanded (cp. inset in figure 9.8 C). After heating the sample to 65°C for 20 minutes and rinsing with

hot buffer (65°C) the characteristic ribbon structure emerges again and domains, which resulted from addition of T20 completely vanished (figure 9.8 C). Hence, we conclude that heating efficiently breaks the complex as expected.[3] Repeated addition of T20 to the same sample, followed by heating and rinsing with hot buffer revealed a reversible adsorption process. Importantly, comparison of the images after addition of T20 (figure 9.8 A, D) with images after desorption (figure 9.8 C, F) due to rinsing with hot buffer solution reveals that adsorption of T20 does not lead exclusively to elevated domains with respect to the S-N36 lipopeptides, but results additionally in the formation of a rather homogeneous surface coverage of the intermediate areas between S-N36 lipopeptide aggregates, indicative for lateral expansion of the aggregates.

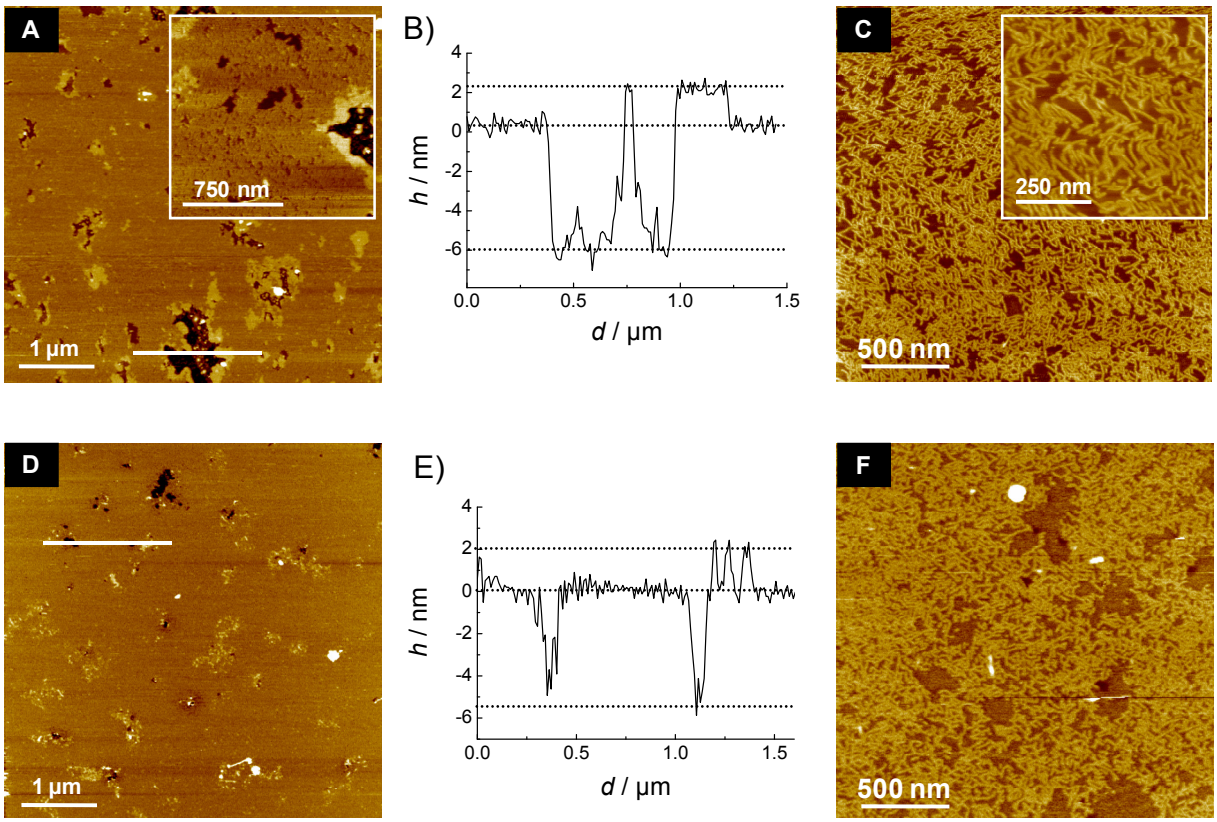

Figure 9.8. AFM images of a S-N36 lipopeptide containing solid supported DOPC lipid bilayer during one adsorption / desorption cycle of T20. A) After addition of 25 nmol T20 and rinsing with buffer (c ~ 7 µM). B) Height analysis across a defect area in image A. C) Sample after heating to 65°C for 20 min and rinsing with buffer at 65°C. D) Same sample, after second addition of 25 nmol T20 and rinsing with buffer. E) Height analysis across a defect area in image D. F) Sample after heating to 65°C for 20 min and rinsing with buffer at 65°C.

Hence, we expect that coiled coil aggregates are oriented perpendicular to the bilayer surface, laterally attached to the 3HB of NHR and lateral expansion of S-N36 lipopeptide aggregates should occur. The exact origin of extended elevated domains, found mainly in the vicinity of defect areas remains obscure.

In situ coupling of H-N36 and inhibitor adsorption revealed similar results (cp. appendix F). Ribbon aggregates of H-N36 lipopeptides measured (2.0 ± 0.3) nm, similar to S-N36 lipopeptide ribbon aggregates (cp. figure 9.7). However, T20 adsorption was irreversible. Heating the sample to 85°C and rinsing with hot buffer had no effect on the adsorbent. Control experiments, using solid supported bilayers consisting of neat DOPC did not result in the formation of the characteristic ribbon structure, but weak structural changed were detected when N-peptides were added (not shown). In contrast, T20 showed a non specific adsorption to neat DOPC bilayers in the form of larger spherical aggregates (not shown).

9.3.3.2 ELLIPSOMETRY

The entire process of the formation of SSLB, followed by in situ coupling reaction of viral N-peptides to maleimid functionalized solid supported bilayers and inhibitor adsorption / desorption cycles, was measured by time elapsed ellipsometry at sub-nanometer resolution. Figure 9.9 shows an experimental sequence, starting from a bilayer, consisting of 90% DOPC and 10 % MCC-DOPE (DOPC*) with S-N36 and H-N36 peptides (figure 9.9 A, C and B, D, respectively) and followed by binding of T20 (figure 9.9 A, B) or the corresponding C-peptides (S-C34 for a S-N36 lipopeptide containing bilayer (figure 9.9 C), and H-C34 for H-N36 lipopeptides (figure 9.9 D)), respectively. Experimental details of bilayer formation, in situ coupling reaction and C-peptide addition are given in the experimental section (9.2).

Initially, the experiment starts with the formation of a functionalized DOPC bilayer (DOPC*) on a silicon surface by addition of SUVs resulting in adsorption followed by rupturing and spreading of vesicles. After 20 min, the bilayer formation was completed and the ellipsometric angle Δ remained constant at around 175°. After excess vesicles were removed by rinsing with PBS 6.8 the layer thickness was determined to be d = (3.7 ± 0.2) nm by 4 zone nulling procedure, assuming a refractive index of DOPC* of n_{DOPC} = 1.53.[22] Subsequent addition of 100 nmol S-N36 (figure 9.9 A, C) or H-N36 (figure 9.9 B, D) resulted in a significant

decrease of the Δ values over time. Interestingly, coupling kinetics of H-N36 to the functionalized bilayer were found to be much faster than for S-N36.

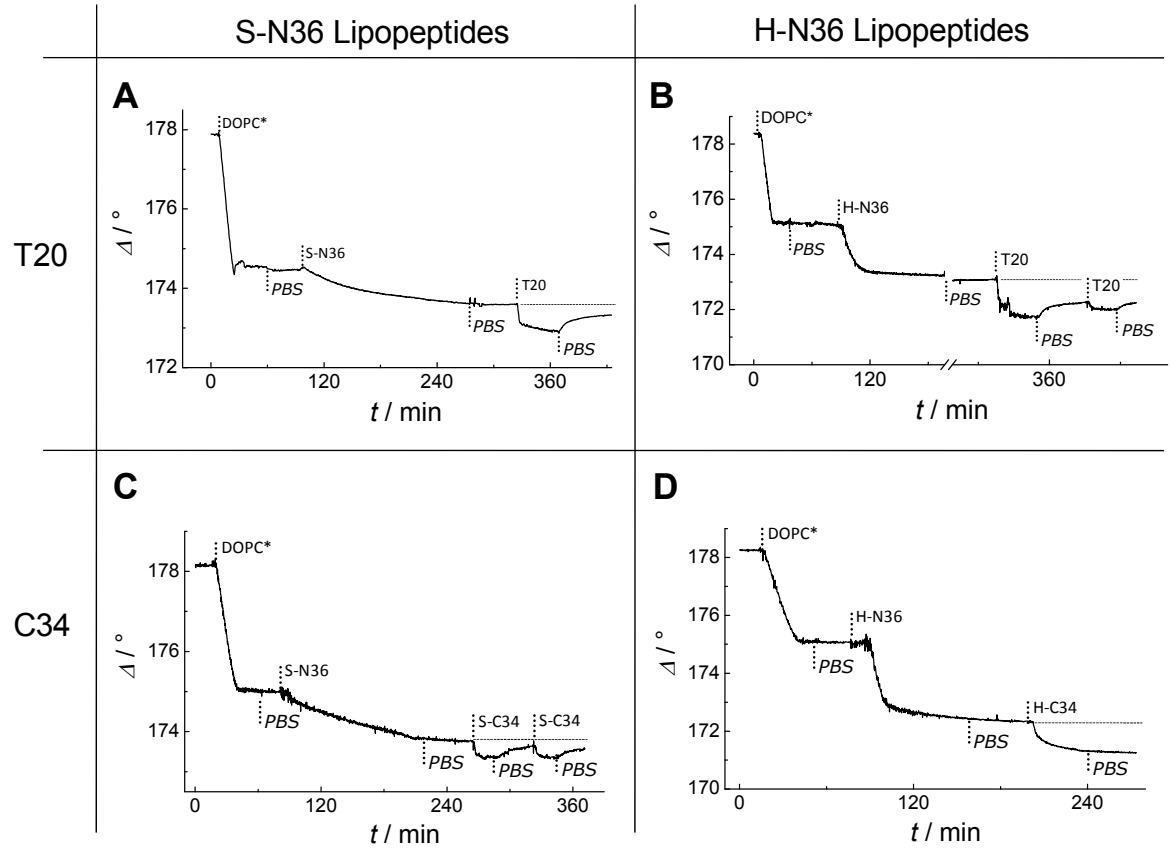

Figure 9.9. Time course of the Δ values obtained from ellipsometric measurements during the in situ coupling reaction of S-N36 (A, C) and H-N36 (B, D) to a lipid bilayer composed of 90% DOPC / 10% MCC-DOPE (DOPC*) and subsequent adsorption of T20 (A, B) or adsorption of S-C34 (C) and H-C34 (D), respectively, as a function of time. Experimental steps are marked with a vertically dashed line and labeled accordingly. Rinsing with buffer (PBS 6.8) is indicated as *PBS*. Constant Δ values, obtained after in situ coupling reaction was found to be complete, are marked with a horizontal dashed line.

In fact, coupling of S-N36 resulted in a rather linear decrease of delta values over hours, whereto in case of H-N36 a steep drop of the ellipsometric angle Δ was detected, remaining nearly constant after 60 min. Hence, we conclude that the cysteine moiety of S-N36, exhibiting a random coil / β-sheet conformation in solution, seems to be less easily available

for reacting with the functionalized bilayer. Possibly, H-N36s cysteine moiety is more accessible to maleimide head groups, due to the already extended helical structure in buffer. After rinsing the sample with buffer, the layer thickness of the N-peptides was determined to be $d_{H\text{-}N36}$ = (2.4 ± 0.4) nm and $d_{S\text{-}N36}$ = (1.3 ± 0.3) nm, assuming a continuous peptide layer (cp. figure 9.7 G) with a refractive index of n_{pep} = 1.50. Addition of C-peptides or T20 resulted in a significant decrease in delta values and subsequent rinsing with buffer lead to a partial desorption with comparable adsorption / desorption characteristics. Noteably, no desorption could be detected in the case of H-C34 after rinsing with buffer, but covalent attachment of the C-peptide to unreacted MCC-DOPE might occur as a side reaction. Taking into account the observations from AFM imaging, revealing inhibitor assembly after adsorption into extended domains (cp. figure 9.8 A,D), we refrain from quantification of the layer thickness of the adsorbent (C34 or T20), since all ellipsometric models require homogenous flat surfaces.

9.3.3.3 CD-SPECTROSCOPY OF N36-LIPOPEPTIDES AFTER INHIBITOR BINDING

CD-spectroscopy of N36-lipopeptide containing vesicles, exposed to T20 or the corresponding C-peptides (C34), was performed to monitor the overall secondary structure of the peptide after inhibitor binding. Samples were prepared as described previously (cp. 9.2.2.3) and spectra are shown as raw data after smoothing (figure 9.10).

All spectra revealed non-specific adsorption of T20 or C-peptides to neat DOPC vesicles (+). For N36-lipopeptide containing DOPC liposomes, the addition of T20 or C-peptides resulted in an increase in negative ellipticity (■) of the band at 208 nm and 222 nm waverlength as compared to the added spectra of T20 or C34 (∇). Binding of T20 or respective C34 peptides to N36-functionalized DOPC vesicles results in an increase of the helical content as deduced from the ratio $\Theta_{222\ nm}$ / $\Theta_{208\ nm}$ (table 9.2). However, precise determination of lipopeptide concentrations or the C-peptide concentrations could not be achieved by UV adsorption at 280 nm wavelength and therefore distinct quantification of secondary structure contents cannot be provided.

Importantly, the sample preparation of vesicles used for control measurements (cp. figure 9.10, denoted as C34 ctrl or T20 ctrl) required only one gel-filtration, whereby preparation of

lipopeptide containing vesicles, which were additionally incubated with C34 or T20 (denoted as N36 lipo + T20 or C34 (exp)) required two gel filtration processes. As a consequence of the peak broadening of eluting vesicles due to the 1st gel filtration, the concentration of vesicles after the 2nd gel filtration is reduced by a factor of ~ 0.5 (cp. appendix G), as compared to the to the concentration of vesicles obtained from the 1st gel filtration.

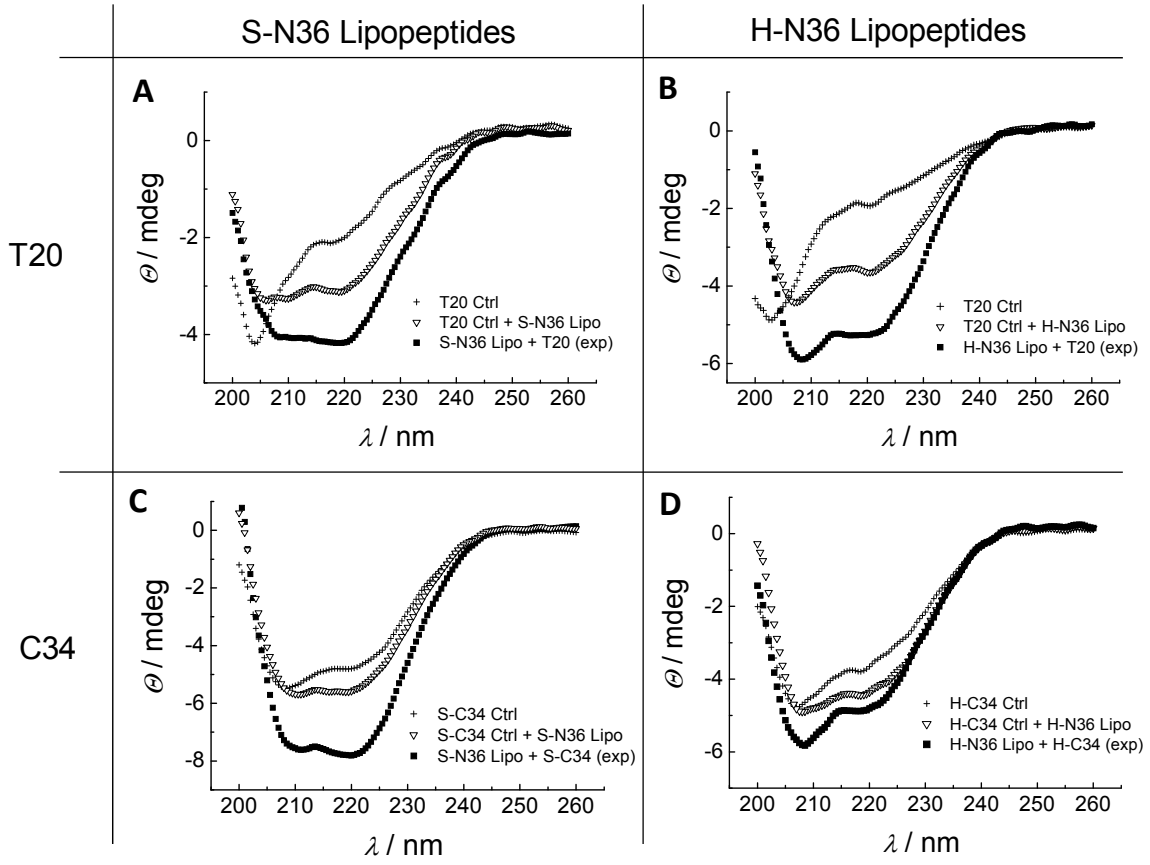

Figure 9.10. CD spectra of N36-lipopeptide containing DOPC liposomes after addition of T20 or the respective C34 peptides (■). T20 and C34 peptides, respectively, were added to the collected gel filtration fractions from the N36-lipopeptide functionalized DOPC liposomes and incubated for 20 min. Subsequently excess T20 or C34 was removed again by gel filtration and collected fractions were measured. Control experiments using neat DOPC vesicles showed non specific adsorption of T20 and C34 peptides (+). Spectra of the respective N36-lipopeptide containing liposomes were added to the spectra obtained from non-specific absorbed T20 or C34 and divided by a factor of two (∇) (see text for details). A, C) S-N36 lipopeptide containing vesicles after addition of T20 and S-C34, respectively. B, D) H-N36 lipopeptide containing vesicles after addition of T20 and H-C34, respectively.

In order to distinguish between non-specific adsorption of C34 or T20 and specific inhibitor binding to N36-lipopeptide containing vesicles, the recovery factor after 2nd gel filtration must be considered. If exposition of N36-lipopeptide containing vesicles led exclusively to non specific adsorption, the resulting spectra could be obtained by simple addition of the C34 ctrl or T20 ctrl spectra (cp. figure 9.10) and spectra of N36-lipopetide containing vesicles (cp. figure 9.5). Note that spectra of C34 ctrl or T20 ctrl and of N36 lipopeptides are then only subject of one gel-filtration and therefore, the calculated spectra (cp. figure 9.10, denoted as T20 or C34 ctrl + N36 lipo) are divided by a factor of two in order to consider the low recovery after 2nd gel filtration as valid for the case of the experimental spectra (cp. figure 9.10, N36 lipo + T20 or C34 (exp)).

System / Spectra	$\Theta_{222\ nm}$ / $\Theta_{208\ nm}$
S-N36 – T20 / Ctrl + Lipo	0.91
S-N36 – T20 / Exp	0.99
S-N36 – S-C34 / Ctrl + Lipo	0.99
S-N36 – SC34/ Exp	1.06
H-N36 – T20 / Ctrl + Lipo	0.81
H-N36 – T20 / Exp	0.88
H-N36 – H-C34 / Ctrl + Lipo	0.88
H-N36 – H-C34/ Exp	0.80

Table. 9.2. Ratios of ellipticity $\Theta_{222\ nm}$ / $\Theta_{208\ nm}$ for CD spectra of lipopeptide containing vesicles after addition of T20 or the respective C34 peptides.

9.4 DISCUSSION

The in situ coupling reaction of terminal cysteine functionalized N36-peptides to maleimide functionalized lipid bilayers results in the formation of N36-lipopeptide containing bilayers. In order to utilize N36-lipopeptides as a mimic of the prehairpin intermediate of gp41, which is a prerequisite for viral mediated membrane fusion, a detailed investigation of the lipopeptides secondary structure was aspired.[3, 8, 10, 26] Hence, we analyzed the secondary structure of N36-lipopeptide containing bilayers by means of CD- and IR spectroscopy to elucidate whether coiled coil aggregates of the viral lipopeptides were formed in the bilayer

environment. Inhibitor binding is discussed in terms of specific binding of C-peptides or T20 to the conserved hydrophobic groves of the coiled coil N36-lipopeptides.

9.4.1 COILED COIL N36-LIPOPEPTIDES IN LIPOSOMES

CD analysis reveals that the secondary structure of S-N36 peptides is tremendously affected when coupled to a bilayer in situ, whereas the secondary structure of H-N36 peptides, which already exhibit a distinctive helical structure in solution, is insignificantly altered by covalent anchoring to a DOPC bilayer (figure 9.5). CD spectra of S-N36 peptides in solution adopt a strong propensity to form a random coil conformation accompanied by β-sheets.[3] Coupling of S-N36 to functionalized bilayers results in the highly helical conformation of the lipopeptides indicative of aggregation. Li and Tamm observed a similar behavior for a peptide, originating from the gp41 fusion domain, denoted as P23H8.[27] In buffer the P23H8 fusion domain was unstructured but adopted a helical conformation when bound to a vesicle via electrostatic interactions between the functional oligolysine moiety of the peptide and POPC / POPG (4:1) vesicles.

This raises the question, whether helical lipopeptides rather assemble as coiled coils, as presented in the native fusion protein and in the pre hairpin intermediate of gp41 during viral mediated membrane fusion, or if N36-lipopeptides are merely interacting with the bilayer which switches conformation? Therefore, FT-IR analysis of multilamellar bilayer stacks doped with N36-lipopeptides was carried out to confirm that indeed a coiled coil assembly of lipopeptides is formed.

The amide I region is sensitive to the secondary structure of peptides or proteins and can be utilized to measure helical distortions, resulting from coiled coil assemblies of α-helical peptides, such as desin rods, tropomyosin or synthetic leucine zippers (GCN4).[24] Helix bending and regular axially distortion of the hydrogen bonds in a coiled coil assembly, results in a specifically vibrational characteristics of the backbone C=O and N-H groups, and can thus, be measured by IR spectroscopy. Detailed analysis of the infrared spectra of well characterized multistranded coiled coils, as shown by Heimburg et al., exhibit a amide I band with components at unusual low frequencies and further, a very distinct three band pattern after deconvolution of the amide I region.[25, 28] Characteristic band positions of a coiled coil are localized around (1651 ± 1) cm^{-1}, (1641 ± 2) cm^{-1} and (1630 ± 2) cm^{-1}. The band at 1651

cm^{-1} is assigned to classical α-helical band position in D_2O and the other two are usually regarded as indicatives of random or β-sheet structure.[29] However, coiled coils analyzed by Heimburg et al. exhibited usually 85% helicity or even higher as determined by CD-spectroscopy, NMR or X-Ray crystal structures, which stresses the fact that the bands at 1641 cm^{-1} and 1630 cm^{-1} are not related to random coil or β-sheet structures.

FT-IR spectroscopy of S-N36- and H-N36-lipopeptides in fully hydrated multilamellar bilayer stacks clearly revealed this characteristic 3 band pattern (figure 9.6). Band positions of deconvoluted FT-IR spectra of viral N36-lipopeptides are comparable to band positions obtained from well characterized multistranded coiled coil, such as leucine zippers or fibritin.[24, 25] The classical helical band of the amid I region (1651 cm^{-1}) is usually the major peak, however, the major peak of the three band pattern of N36-lipopeptides is the band around 1632 cm^{-1} (cp. table 9.1). As shown by Heimburg et al. the inverse of the pitch length of a coiled coil correlates with the spectral maximum of the amide I region.[25] Both N-peptides exhibit a pitch length of ca. 175 Å.[26] Assuming that the pitch length is not altered by lipopeptide formation, the spectral maximum of H-N36- and S-N36-lipopeptides (1645 cm^{-1} and 1643 cm^{-1}, respectively) correlates reasonably well with the spectral maximum of GCN4-p1II zippers (1644 cm^{-1}), which also exhibit a pitch length of 175 Å and assembles in trimeric coiled coils.[30] Interestingly, the spectra of S-N36 lipopeptides differs from H-N36 analogs, in terms of spectral maxima or spectral intensities of the deconvoluted peaks (cp. table 1) Moreover, deconvoluted spectra of S-N36-lipopeptides exhibit a major peak at 1615 cm^{-1}. Bands at such low frequencies of the amide I region are usually indicative of denatured or aggregated proteins, but are commonly accompanied by a band near 1685 cm^{-1}, which appears to be superposed by the maleimide C=O stretch in the FT-IR spectra of S-N36 lipopeptides (cp. appendix A).[31, 32] Since our AFM data clearly shows lateral aggregates of N36-lipopeptides into ribbons, we assume that aggregation to larger complexes is induced (figure 9.7 and 9.8).

Summarizing, we assign the peaks of the amide I region (around 1652 cm^{-1}, 1643 cm^{-1} and 1632 cm^{-1}) to the characteristic three band pattern of coiled coils and not to random coils or β-sheets, since data obtained from CD-spectroscopy clearly confirms that α-helical secondary structures is the prevailing conformation of N36-lipopeptide anchored in bilayers.

Thus, we expect that conserved hydrophobic groves are also present in case of coiled coil N36-lipopeptides anchored in DOPC bilayers and specific inhibitor binding can occur.

9.4.2 INHIBITOR BINDING

In addition to the in situ functionalization of lipid bilayers with viral N-peptides to mimic pre hairpin intermediates, we exposed the samples to viral C-peptides and measured the binding process. This experiment serves as further proof that induced coiled coil peptides have been formed. AFM data reveals that inhibitor adsorption leads to a clustering, whereby the main portion of the adsorbent is located in domain like aggregates in the vicinity of defect areas (figure 9.8). Interestingly, if imaged immediately after T20 addition before rinsing with buffer solution, adsorption of T20 resulted in smaller domains (cp. appendix B) and increased surface coverage. Inhibitor release was achieved by rinsing with pure buffer heated to 65°C and was identified by the recurring characteristic ribbon like aggregates of N36-lipopeptides. Binding and desorption were found to be reversible and thus, paves the way to probe new potent fusion inhibitors, e. g. stemming from a combinatorial library. However, for the system H-N36-lipopeptides / T20, inhibitor release was irreversible under experimental conditions, even if the sample was rinsed hot at 85°C (not shown). In fact, H-N36 lipopeptide also assembled in ribbon like domains (cp. appendix F) and adsorption of T20 was resulted in an increased surface coverage, similar to adsorption of T20 to S-N36 lipopeptides.

These finding require inhibitor binding and six helix bundle formation in buffer to be revisited and investigated in more detail. First, T20 formed stable complexes with an extended helical structure (appendix C) if mixed with equimolar amounts of H-N36, although T20 fails to induce helical structure N36 without the CGG moiety.[12] Second, specific T20 adsorption and desorption was detected on S-N36 lipopeptide containing bilayers although T20 is known to be HIV specific.[33]

Trivedi at el. has found that the LLSGIV stretch of NHR of HIV-1 gp41 is critical for binding of T20 and presented 15 mer peptides, originating from the NHR region of HIV-1 gp41, which induce strong helical structure formations if mixed with T20.[34] Considering the non polar nature of lysine and the polar nature of glutamine (following amino acid toward FP; FP---QLLSGIV---) it is conceivable that our H-N36 derivative, exhibiting a CGGSGIV stretch (polar cysteine and non polar glycine) and a CGGAGIV stretch in case of S-N36 might be critical for

binding of T20. Further indication that T20 binds strongly to H-N36 (and less strong to S-N36) is that T20 failed to be released by hot rinsing (85°C) although six helix bundles consisting of viral N-peptides and C-peptides, including T20, should dissociate between 35°C and 65°C.[3, 12, 35] Interestingly, increased thermal stability of the trimeric N36 core and therefore increased six helix bundle stability up to 89°C was measured for N36, N-terminally extended with the polar region of the fusion peptide.[36] Here, increased core stability might result from the spatial vicinity of the N-terminus of N36 towards the polar head group region of the lipid bilayer. We assume that the increased core stability is also given for coiled coil S-N36 lipopeptides and are therefore, capable of binding T20 to the extended hydrophobic groves. However, compared to H-N36 we found a rather reversible binding to S-N36 indicative of weaker affinity.

Adsorption of T20 and C-peptides to N36-lipopeptides was further monitored by time resolved ellipsometry (figure 9.9). After functionalization of the bilayer with N36-lipopeptides, inhibitor adsorption exceeded an instantaneous drop of ellipsometric delta values, which remained constant after 20 min. Rinsing of the samples with buffer resulted only in a partial desorption of the inhibitor-peptide (cp. figure 9.9, dashed horizontal line). Control experiments using neat DOPC bilayers did not show inhibitor adsorption (appendix D, E) and thus, we assume that rinsing with buffer removes not non-specifically adsorbed peptides but is rather an indication for specific reversible binding of T20 or C34 to the core of NHR. Entirely irreversible is the binding of H-C34 to H-N36 lipopeptides (figure 9.9 D). C34-peptides pack antiparallel into the hydrophobic groves of the trimeric coil of N36 and thus, the C-terminal end of C34 is located near the N-terminal end of N36.[3, 26, 37, 38] Here H-C34 is functionalized at the C-terminal end by a cysteine moiety, whereas N36 binds to the maleimid functionalized groups with the N-terminal cysteine. Antiparallel packing of H-C34 to coiled coil H-N36 lipopeptides might lead to a positioning of H-C34 near the bilayer surface, exposing the C-terminal cysteine towards the maleimide headgroups of remaining MCC-DOPE and thus, covalent coupling of H-C34 can occur.

Structural analysis of N36 lipopeptide containing vesicles by CD spectroscopy, incubated with T20 or the corresponding C-peptides reveals that helical conformation is still present as the major structural component (figure 9.10). In the case of S-N36 lipopeptides, inhibitor adsorption results in increased negative band intensity at 222 nm from which we conclude a

predominant helical conformation. Inhibitor adsorption on H-N36 lipopeptide containing liposomes, however, exhibits mainly a simple addition of the two spectra from the inhibitor and the N36 peptide. Considering the low yield of liposomes after the second gel filtration of only 50% or less (cp. appendix G), the intensity of the CD signal of N36-lipopeptides after inhibitor adsorption is significantly stronger than the corresponding addition of the individual spectra. Further, considering the coverage of a bilayer surface with N36-lipopeptides after in situ coupling, free non specific inhibitor adsorption sites on the bilayer surface are expected to be rather reduced. The large CD signal is probably a sign of peptide / inhibitor accumulation due to the high inhibitor affinity to N36-receptors. Therefore, we assume that the major fraction of the adsorbed inhibitor is bound as helices, possibly packing into the hydrophobic groves of coiled coil N36-lipopeptides and thus, contributing to the overall helical confirmation as measured by CD spectroscopy.

9.5 CONCLUSIONS

We have shown, that in situ functionalization of bilayers with peptides, originating from the NHR region of gp41 of SIV and HIV results in the formation of a pre hairpin mimetic. Thus, coiled coil lipopeptides deduced from the NHR regime of gp41 constitute promising tools for label free screening of efficient fusion inhibitors. Assembly into coiled coil structures of the synthetic lipopeptides was proven by FT-IR spectroscopy in combination with CD spectroscopy. A specific three band pattern of the amide I region for both lipopeptides (S-N36 and H-N36), accompanied by significant helical conformation was measured, indicative for the formation of extended coiled coil assemblies. Inhibitor binding (T20 and C34) to N36-lipopeptide containing bilayers was found to be specific and lead to an increased helical structure of the post fusion mimic.

9.6 REFERENCES

[1] Freed, E. O.; Myers, D. J. and Risser, R. Mutational analysis of the cleavage sequence of the human immunodeficiency virus type 1 envelope glycoprotein precursor gp160. *J. Virol.* **1989**, 63, 4670-4675.

[2] Montagnier, L.; Clavel, F.; Krust, B.; Chamaret, S.; Rey, F.; Barre-sinoussi, F. and Chermann, J. C. Identification and antigenicity of the major envelope glycoprotein of of lymphadenopathy-associated virus. *Virology* **1985**, 144, 283-289.

[3] Malashkevich, V. N.; Chan, D. C.; Chutkowski, C. T. and Kim, P. S. Crystal structure of the simian immunodeficiency virus (SIV) gp41 core: Conserved helical interactions underlie the broad inhibitory activity of gp41 peptides. *Proceedings of the National Academy of Sciences* **1998**, 95, 9134-9139.

[4] Dalgleish, A. G.; Beverley, P. C. L.; Clapham, P. R.; Crawford, D. H.; Greaves, M. F. and Weiss, R. A. The CD4 (T4) antigen is an essential component of the receptor for the AIDS retrovirus. *Nature* **1984**, 312, 763-767.

[5] Wyatt, R. and Sodroski, J. The HIV-1 Envelope Glycoproteins: Fusogens, Antigens, and Immunogens. *Science* **1998**, 280, 1884-1888.

[6] Feng, Y.; Broder, C. C.; Kennedy, P. E. and Berger, E. A. HIV-1 Entry Cofactor: Functional cDNA Cloning of a Seven-Transmembrane, G Protein-Coupled Receptor. *Science* **1996**, 272, 872-877.

[7] Eckert, D. M. and Kim, P. S. Mechanisms of viral membrane fusion and its inhibition. *Annual Review of Biochemistry* **2001**, 70, 777-810.

[8] Doms, R. W. and Moore, J. P. HIV-1 Membrane Fusion: Targets of Opportunity. *J. Cell Biol.* **2000**, 151, 9F-14.

[9] Chan, D. C. and Kim, P. S. HIV Entry and Its Inhibition. *Cell* **1998**, 93, 681-684.

[10] Chan, D. C.; Chutkowski, C. T. and Kim, P. S. Evidence that a prominent cavity in the coiled coil of HIV type 1 gp41 is an attractive drug target. *Proceedings of the National Academy of Sciences* **1998**, 95, 15613-15617.

[11] Kilby, J. M.; Hopkins, S.; Venetta, T. M.; DiMassimo, B.; Cloud, G. A.; Lee, J. Y.; Alldredge, L.; Hunter, E.; Lambert, D.; Bolognesi, D.; Matthews, T.; Johnson, M. R.; Nowak, M. A.; Shaw, G. M. and Saag, M. S. Potent suppression of HIV-1 replication in humans by T-20, a peptide inhibitor of gp41-mediated virus entry. *Nat Med* **1998**, 4, 1302-1307.

[12] Liu, S.; Lu, H.; Niu, J.; Xu, Y.; Wu, S. and Jiang, S. Different from the HIV Fusion Inhibitor C34, the Anti-HIV Drug Fuzeon (T-20) Inhibits HIV-1 Entry by Targeting Multiple Sites in gp41 and gp120. *J. Biol. Chem.* **2005**, 280, 11259-11273.

[13] Gallo, S. A.; Sackett, K.; Rawat, S. S.; Shai, Y. and Blumenthal, R. The Stability of the Intact Envelope Glycoproteins is a Major Determinant of Sensitivity of HIV/SIV to Peptidic Fusion Inhibitors. *Journal of Molecular Biology* **2004**, 340, 9-14.

[14] Welch, B. D.; VanDemark, A. P.; Heroux, A.; Hill, C. P. and Kay, M. S. Potent D-peptide inhibitors of HIV-1 entry. *Proceedings of the National Academy of Sciences* **2007**, 104, 16828-16833.

[15] Munch, J.; Standker, L.; Adermann, K.; Schulz, A.; Schindler, M.; Chinnadurai, R.; Pohlmann, S.; Chaipan, C.; Biet, T.; Peters, T.; Meyer, B.; Wilhelm, D.; Lu, H.; Jing, W.; Jiang, S.; Forssmann, W.-G. and Kirchhoff, F. Discovery and Optimization of a Natural HIV-1 Entry Inhibitor Targeting the gp41 Fusion Peptide. *Cell* **2007**, 129, 263-275.

[16] Moore, J. P. and Doms, R. W. The entry of entry inhibitors: A fusion of science and medicine. *Proceedings of the National Academy of Sciences* **2003**, 100, 10598-10602.

[17] Kliger, Y.; Gallo, S. A.; Peisajovich, S. G.; Munoz-Barroso, I.; Avkin, S.; Blumenthal, R. and Shai, Y. Mode of Action of an Antiviral Peptide from HIV-1. Inhibition at a post-lipid mixing stage. *J. Biol. Chem.* **2001**, 276, 1391-1397.

[18] Schnölzer, M.; Alewood, P.; Jones, A.; Alewood, D. and Kent, S. In Situ Neutralization in Boc-chemistry Solid Phase Peptide Synthesis. *International Journal of Peptide Research and Therapeutics* **1992**, 13, 31-44.

[19] Andrushchenko, V. V.; Vogel, H. J. and Prenner, E. J. Optimization of the hydrochloric acid concentration used for trifluoroacetate removal from synthetic peptides. *Journal of Peptide Science* **2007**, 13, 37-43.

[20] Edelhoch, H. Spectroscopic Determination of Tryptophan and Tyrosine in Proteins. *Biochemistry* **1967**, 6, 1948-1954.

[21] Knight, P. Hydrolysis of p-NN'-phenylenebismaleimide and its adducts with cysteine. Implications for cross-linking of proteins. *The Biochemical journal* **1979**, 179, 191-197.

[22] Faiss, S.; Schuy, S. and Janshoff, A. Phase Transition of Individually Adressabe Microstructured Membranes Visualized by Imaging Ellipsometry. *J. Phys. Chem. (in press)* **2007**.

[23] Dong, A.; Huang, P. and Caughey, W. S. Protein secondary structures in water from second-derivative amide I infrared spectra. *Biochemistry* **1990**, 29, 3303-3308.

[24] Heimburg, T.; Schuenemann, J.; Weber, K. and Geisler, N. Specific Recognition of Coiled Coils by Infrared Spectroscopy: Analysis of the Three Structural Domains of Type III Intermediate Filament Proteins. *Biochemistry* **1996**, 35, 1375-1382.

[25] Heimburg, T.; Schunemann, J.; Weber, K. and Geisler, N. FTIR-Spectroscopy of Multistranded Coiled Coil Proteins. *Biochemistry* **1999**, 38, 12727-12734.

[26] Chan, D. C.; Fass, D.; Berger, J. M. and Kim, P. S. Core Structure of gp41 from the HIV Envelope Glycoprotein *Cell* **1997**, 89, 263-273.

[27] Li, Y. and Tamm, L. K. Structure and plasticity of the human immunodeficiency virus gp41 fusion domain in lipid micelles and bilayers. *Biophys. J.* **2007**, biophysj.106.102335.

[28] Reisdorf, W. C. and Krimm, S. Infrared Amide I' Band of the Coiled Coil. *Biochemistry* **1996**, 35, 1383-1386.

[29] Kong, J. and Yu, S. Fourier Transform Infrared Spectroscopic Analysis of Protein Secondary Structures. *Acta Biochimica et Biophysica Sinica* **2007**, 39, 549-559.

[30] Harbury, P. B.; Kim, P. S. and Alber, T. Crystal structure of an isoleucine-zipper trimer. *Nature* **1994**, 371, 80-83.

[31] Heimburg, T. and Marsh, D. Investigation of secondary and tertiary structural changes of cytochrome c in complexes with anionic lipids using amide hydrogen exchange measurements: an FTIR study. *Biophys. J.* **1993**, 65, 2408-2417.

[32] Muga, A.; Mantsch, H. H. and Surewicz, W. K. Apocytochrome c interaction with phospholipid membranes studied by Fourier-transform infrared spectroscopy. *Biochemistry* **1991**, 30, 2629-2635.

[33] Das, A. T.; Baldwin, C. E.; Vink, M. and Berkhout, B. Improving the Safety of a Conditional-Live Human Immunodeficiency Virus Type 1 Vaccine by Controlling both Gene Expression and Cell Entry. *J. Virol.* **2005**, 79, 3855-3858.

[34] Trivedi, V. D.; Cheng, S.-F.; Wu, C.-W.; Karthikeyan, R.; Chen, C.-J. and Chang, D.-K. The LLSGIV stretch of the N-terminal region of HIV-1 gp41 is critical for binding to a model peptide, T20. *Protein Eng.* **2003**, 16, 311-317.

[35] He, Y.; Liu, S.; Jing, W.; Lu, H.; Cai, D.; Chin, D. J.; Debnath, A. K.; Kirchhoff, F. and Jiang, S. Conserved residue Lys574 in the cavity of HIV-1 GP41 coiled-coil domain is critical for six-helix bundle stability and virus entry. *J. Biol. Chem.* **2007**, M703781200.

[36] Sackett, K.; Wexler-Cohen, Y. and Shai, Y. Characterization of the HIV N-terminal Fusion Peptide-containing Region in Context of Key gp41 Fusion Conformations. *J. Biol. Chem.* **2006**, 281, 21755-21762.

[37] Tan, K.; Liu, J.-h.; Wang, J.-h.; Shen, S. and Lu, M. Atomic structure of a thermostable subdomain of HIV-1 gp41. *Proceedings of the National Academy of Sciences* **1997**, 94, 12303-12308.

[38] Weissenhorn, W.; Dessen, A.; Harrison, S. C.; Skehel, J. J. and Wiley, D. C. Atomic structure of the ectodomain from HIV-1 gp41. *Nature* **1997**, 387, 426-430.

9.7 APPENDIX AND CONTROL EXPERIMENTS

A

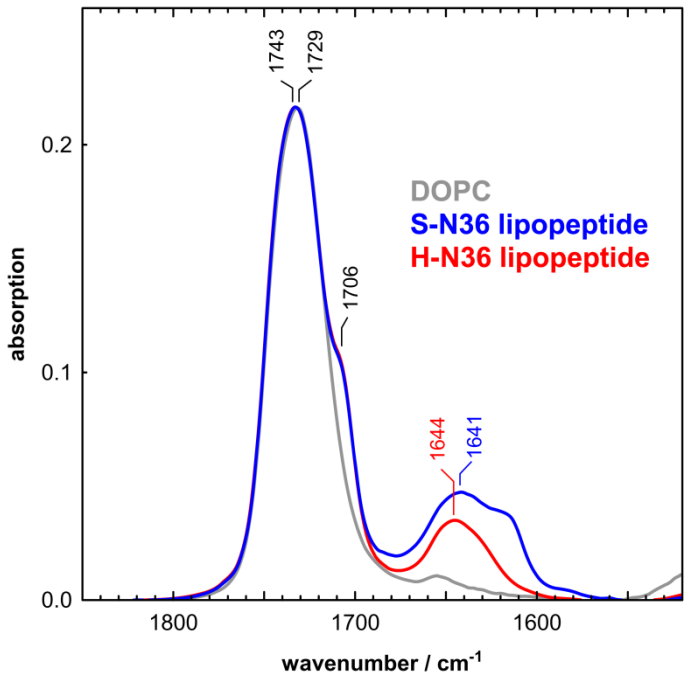

Appendix A. Amide I region of coiled coil lipopeptides.

B

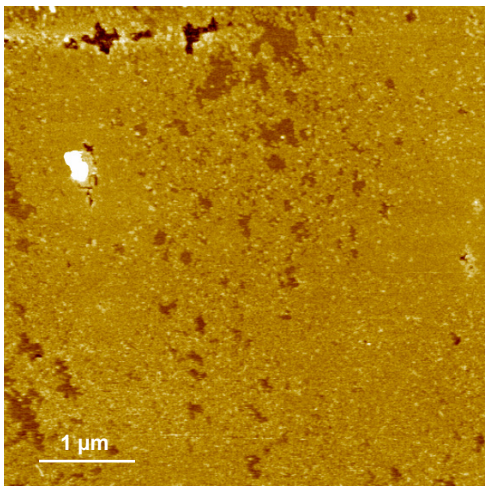

Appendix B. AFM image of a S-N36 lipopeptide containing bilayer, imaged instantaneous after T20 addition directly before rinsing with buffer solution.

C

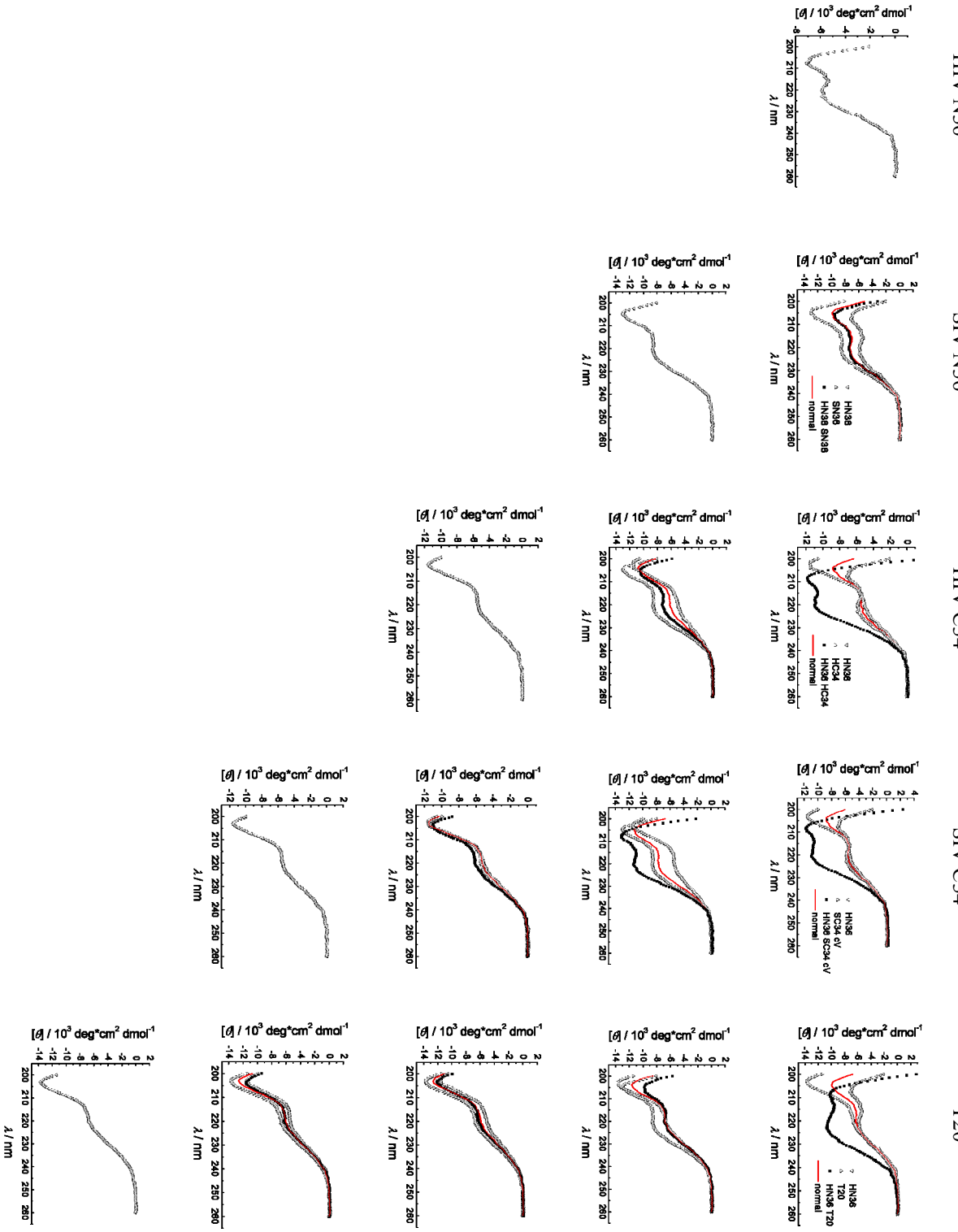

Appendix C. CD-Spectra of viral peptides in solution and their mixtures.

D

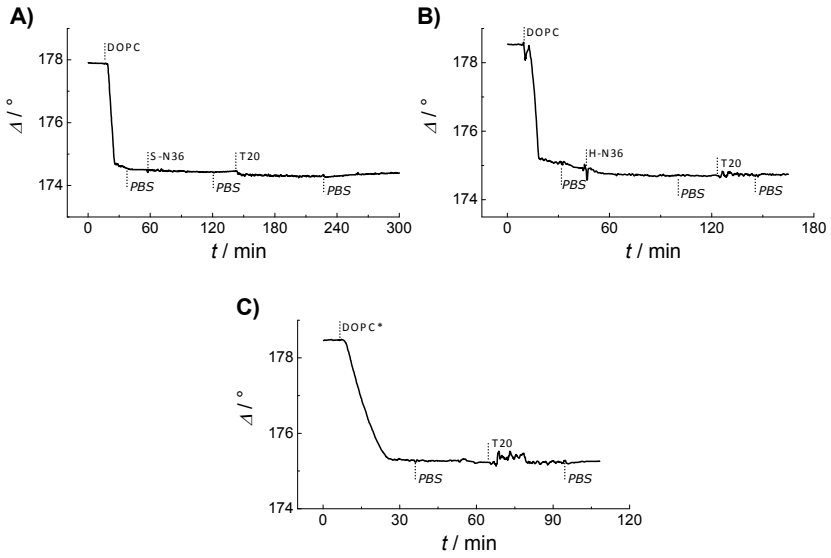

Appendix D. Time course of the ellipsometric Δ values of the adsorption of T20 on neat DOPC as a control experiment. Initially, unilamellar vesicles consistent of 100% DOPC were spread on silicon. After rinsing with buffer, 100 nmol H-N36 in PBS 6.8 were added (c ~ 12 - 15 µM), resulting in slight variations in the ellipsometric angle. No significant increase in layer thickness was found after the addition of 50 nmol T20 in PBS 6.8 (c ~ 10 µM).

E

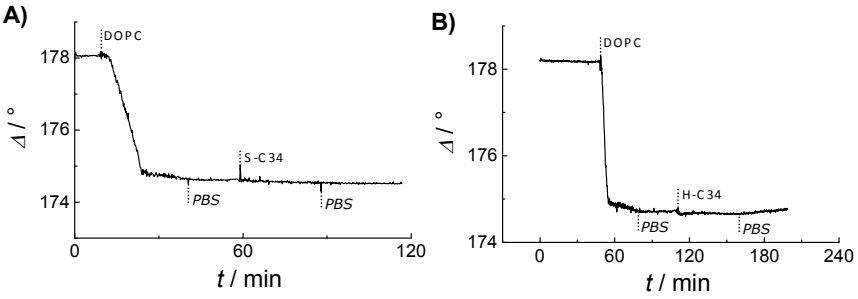

Appendix E. Time course of the ellipsometric Δ values of the adsorption of C34 peptides (A) S-C34, B) H-C34) on neat DOPC as a control experiment. Initially, unilamellar vesicles consistent of 100% DOPC were spread on silicon. After rinsing with buffer, 50 nmol C34 in PBS 6.8 were added (c ~ 10 - 12 µM), resulting in insignificant variations in the ellipsometric angle Δ.

F

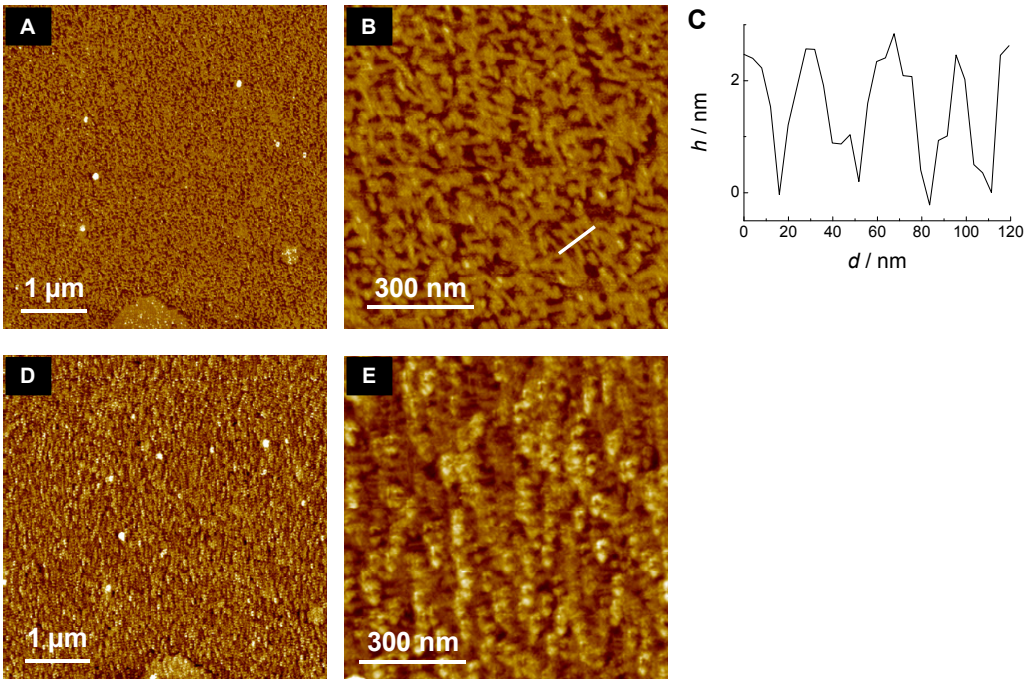

Appendix F. AFM images of a H-N36 containing bilayer A, B) H-N36 lipopeptide containing DOPC bilayer. C) Height profile along the white line in image B. D, E) Same sample, after T20 addition and rinsing at room temperature.

G

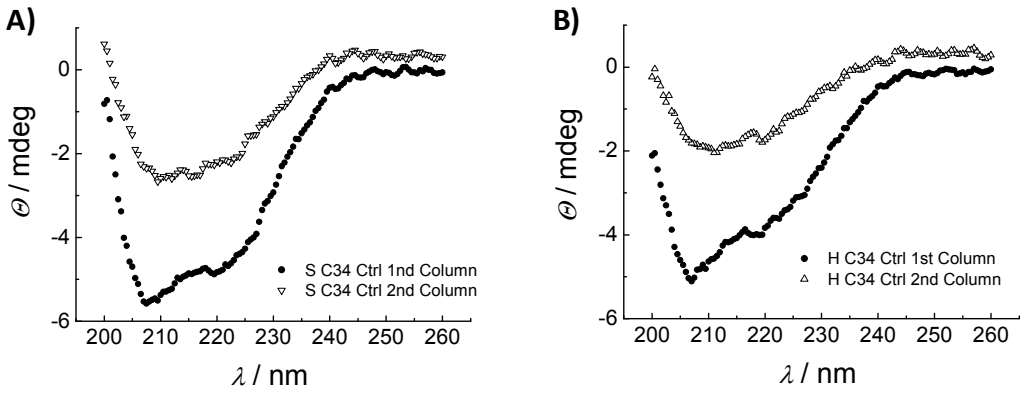

Appendix G. Determination of the vesicle-yield after first and second gel filtration. The recovery was determined to be less than 50% from the initial concentration after the second gel filtration. A) S C34 control and B) H-C34 control. Experimental details for the control experiments are described in 9.2.2.

CHAPTER X

10 SUMMARY

The aim of this work is focused on the development of a novel screening assay for potent fusion inhibitors of retroviral infection, which can be applied for high-throughput screening devices. Therefore, we aimed to mimic the pre-hairpin intermediate of gp41 of HIV and SIV on the basis of a reversibly switchable formation of coiled coil lipopeptides, originating from the NHR region of the respective retroviruses, anchored in artificial biomembranes. This switching process was at first believed to be crucial for the release of specifically bound antagonists and therefore it is essential to gain detailed knowledge about lipid organization in phase separated lipid bilayers during the main phase transition. Certainly, robust and reliable methods for peptide functionalization of a bilayer, as well as distinctive structural investigation of the secondary structure of anchored lipopeptides in biomembranes describe another essential step towards the development of such a challenging screening device.

Lateral lipid sorting was visualized by specific recognition of streptavidin of the biotinylated anchor lipids and it was shown that we can trigger the distribution of ligands specifically either into the fluid or into the gel phase of phase separated lipid bilayers. However, the strong lateral interaction of streptavidin inhibited reversible switching of ligand clustering. Additionally, a novel class of synthetic, perfluoroalkylated lipids was employed to fabricate phase separated mixed hydrocarbon / fluorocarbon bilayer systems, which display nanoscale patterns due to the hydrocarbon / fluorocarbon immiscibility. Detailed analysis of the fluorocarbon lipid structure by means of ATR-IR spectroscopy and investigation of the thermotropic phase behavior of the bilayers by ellipsometry and AFM clarified many open questions, derived from the experimental data of mixed fluorocarbon / hydrocarbon lipid bilayers. Tilt angle of the fluorocarbon lipids was found to be tremendously increased as compared to the hydrocarbon analog, resulting in reduced thickness of the bilayer. Furthermore, we found a very low relative area change as well as a low change of thickness of the fluorocarbon bilayer during the main phase transition.

Summarizing, the concept of solid supported bilayers in combination with temperature-controlled surface sensitive instrumental techniques, such as ATR-IR, AFM or ellipsometry paves the way to precisely determine the structural and thermotropic properties of bilayers directly on solid supports.

Besides in-depth investigation of novel phase separated bilayer systems, including possible applications for reversible switching of ligand clustering, two additional major goals were achieved towards construction of the biosensor scheme.

First, a reliable and robust in situ coupling method for specific covalent coupling of peptide receptors, such as His_6Tag peptides or oligolysines to a lipid bilayer was developed. The coupling reaction of terminal cysteine modified peptides to maleimide functionalized lipid bilayers was monitored by a multiplicity of characterization methods, such as ellipsometry, CLSM, AFM or fluorescence spectroscopy. Small receptor peptides served as versatile receptors for the deposition of vesicles or nanoparticles and are envisioned to open new doors towards the construction of arrays of mobile tethered vesicles. It could be shown that peptides, which were covalently bound to lipid bilayer, are more accessible than those, which were merely non-specifically associated with the membrane. Hence, lipopeptides exhibit specific receptor functionality. It can be irrevocably stated that in situ functionalization of bilayers with receptor peptides, based on maleimide lipids represents a straight-forward and reliable method. In situ synthesis paves the way to easily achievable receptor lipidation under conditions that approach a native environment without sophisticated lipidation synthesis, followed by complicated reconstitution of lipidated receptors.

Second, specific inhibitor binding based on the formation of N36 coiled coil lipopeptides is the major milestone of this work. In situ functionalization of lipid bilayers with viral N36 peptides and thus, mimicking the active drug target of modern fusion inhibitors render label-free drug screening feasible. Terminal cysteine modified peptides, originating from the NHR region of HIV and SIV were coupled to a maleimide containing DOPC bilayer in situ and interactions with potent fusion inhibitors, such as T20 or C34 were monitored by AFM, ellipsometry and CD spectroscopy. In addition, structural analysis of the lipopeptides by means of FT-IR analysis exhibited a distinctive three band pattern of the deconvoluted amide

I region, reminiscent of well characterized coiled coil peptides in solution. It was found that the in situ coupling reaction of S-N36 to DOPC bilayers alters the secondary structure of the peptide substantially and that S-N36 lipopeptide aggregates were selectively able to bind T20 and C34 peptide. Furthermore, reversible binding of T20 was detected after it was released at elevated temperature.

In summary, a new platform has been generated, which displays fully functional coiled coil aggregates of N36 lipopeptides as selective receptors for potential fusion inhibitors. The setup allows screening of large amounts of substances in almost native manner.